

A KINETIC INVESTIGATION OF THE ELECTRON-TRANSFER PATHWAYS  
ASSOCIATED WITH REGENERATION AND RECOMBINATION FOR THE  
DESIGN OF NEXT GENERATION DYE-SENSITIZED SOLAR CELLS

By

Joshua Wade Baillargeon

A DISSERTATION

Submitted to  
Michigan State University  
in partial fulfillment of the requirements  
for the degree of

Chemistry – Doctor of Philosophy

2018

## **ABSTRACT**

### **A KINETIC INVESTIGATION OF THE ELECTRON-TRANSFER PATHWAYS ASSOCIATED WITH REGENERATION AND RECOMBINATION FOR THE DESIGN OF NEXT GENERATION DYE-SENSITIZED SOLAR CELLS**

By

Joshua Wade Baillargeon

The multicomponent design of DSSCs provides the opportunity of integrating cheap materials for efficient power generation and has significant advantages over conventional silicon photovoltaics (PVs). By separating the processes of absorption, charge separation and charge collection through the use of a molecular sensitizer, a wide bandgap semiconductor and redox shuttle, dye cells are highly tunable for conducting fundamental studies leading to device optimization. Given the synergy of charge-transfer among these three components is pivotal for maximizing device performance, this dissertation will focus on understanding charge-transfer relative to the pathways of recombination and regeneration, which limit DSSC efficiencies. Use of one-electron outersphere redox shuttles (OSRSs) has provided a viable route for describing such pathways in operating dye cells through the application of Marcus Theory. A central theme has been to design novel low-spin (LS) cobalt OSRSs, which employ fast self-exchange kinetics and low reorganization energies, in an effort to optimize rates of regeneration. It is evident, however, that a balance must be struck between the reorganization energy of the redox shuttle and the driving force for recombination. We address this issue through a series of external quantum yield measurements in Chapter 3 and seek to remedy the problem by either using a tandem electrolyte as in Chapter 4 or by integrating redox shuttles with highly negative formal potentials to regenerate near IR absorbing sensitizers as in Chapter 5.

Copyright by  
JOSHUA WADE BAILLARGEON  
2018

*A dedication to two of the most important women in my life...*  
*Sally Baillargeon (Nana)*  
*&*  
*Josephine DeMarte (Grams DeMarte)*  
*Without your continued love and support I wouldn't be where I am today*  
*I thank and love you both*

## ACKNOWLEDGMENTS

There are many people I would like to thank for their help, support and friendship over the course of my graduate career at Michigan State. First and foremost, I would like to thank you Tom for being an outstanding mentor and a role model for conducting good science. Your patience and support has allowed me to persevere through failure and difficult projects in an effort to answer challenging questions. To my parents, thanks for the love and support you have provided me over the years. Your positive light has guided me through difficult times. The hard working qualities you have engrained in me have no doubt aided in my development and success as a young scientist. I would also like to extend thanks to past and present Hamannites who I have worked closely with on the dye cell project: Jesse, Suraj, Yuling, Mandal, Yujue and Austin. You all have made research in this difficult field stimulating and exciting. I have truly enjoyed talking science with each and everyone one of you and hope for the best for each of you in the future. To the rest of the group members, thanks for keeping the lab light-hearted and enjoyable to work in. Dan, I can honestly say I don't know what I would have done for five years without such a comical desk buddy. I will miss the trips to the dairy store as much as the yearly Red Wings vs. Canadiens hockey games. Lastly, I would like to thank all my great friends outside of lab whom have made the tough days of grad school bearable. Stephen, Dan, Garrett, Ben, Nick, Kelley and Sarah thanks for making the past five years the most memorable of my life. I'll never forget all the UP trips, late night volleyball games or last calls at Crunchy's after long days in the lab. You are all family and I know, wherever we all end up, we will always stay in touch. Cheers.

# TABLE OF CONTENTS

<b>LIST OF TABLES .....</b>	<b>ix</b>
<b>LIST OF FIGURES .....</b>	<b>xii</b>
<b>LIST OF SCHEMES .....</b>	<b>xx</b>
<b>KEY TO ABBREVIATIONS .....</b>	<b>xxi</b>
<b>Chapter 1. An Introduction to Dye-Sensitized Solar Cell Research .....</b>	<b>1</b>
1.1 Motivation for Renewable Energy Research .....	1
1.2 Historical Development of DSSCs .....	4
1.3 Operating Principles of DSSCs.....	7
1.4 Reliance on the $I_3^-/I^-$ Electrolyte .....	12
1.5 Device Integration of Outersphere Redox Shuttles .....	14
1.6 Modeling Recombination and Regeneration using the Principles of Marcus Theory .....	20
1.7 Dissertation Overview .....	26
REFERENCES .....	28
<b>Chapter 2. Stopped-Flow Spectroscopy: A Tool to Define the Self-Exchange Kinetics of One-Electron OSRSs .....</b>	<b>35</b>
2.1 Introduction.....	35
2.2 Results and Discussion .....	36
2.2.1 <i>Basics of Operation</i> .....	36
2.2.2 <i>Experimental Design Principles</i> .....	38
2.2.3 <i>Data Analysis and Fitting</i> .....	43
2.3 Conclusion .....	47
APPENDIX.....	48
REFERENCES .....	54
<b>Chapter 3. Kinetics of Regeneration and Recombination in DSSCs using Cobalt OSRSs.....</b>	<b>57</b>
3.1 Abstract.....	57
3.2 Introduction.....	58
3.3 Experimental.....	62
3.3.1 <i>Materials</i> .....	62
3.3.2 <i>Synthesis of Cobalt OSRS</i> .....	63
3.3.3 <i>Cross-Exchange Kinetics</i> .....	64
3.3.4 <i>Solar Cell Preparation</i> .....	65
3.3.5 <i>Solar Cell Measurements</i> .....	67
3.3.6 <i>Preparation of Sample Cells for Optical Measurements</i> .....	68
3.3.7 <i>Optical Measurements</i> .....	69
3.4 Results and Discussion .....	70

3.4.1 Determining the self-exchange kinetics of $[Co(bpy)_3]^{3+/2+}$ and $[Co(ttcn)_2]^{3+/2+}$ .....	70
3.4.2 Understanding Regeneration using Marcus Theory .....	76
3.4.3 Understanding Recombination using Marcus Theory .....	78
3.4.4 Measurements and Modeling of Regeneration .....	83
3.4.5 Effect of an Alumina Layer .....	89
3.5 Conclusion .....	94
REFERENCES .....	111
<b>Chapter 4. Bifurcation of Regeneration and Recombination in DSSCs via Electronic Manipulation of Tandem Cobalt Redox Shuttles .....</b>	<b>117</b>
4.1 Abstract .....	117
4.2 Introduction .....	117
4.3 Experimental .....	119
4.3.1 Materials .....	119
4.3.2 Synthesis of OSRSs .....	120
4.3.3 Electrochemistry .....	121
4.3.4 Cross-Exchange Kinetics .....	121
4.3.5 Solar Cell Fabrication and Characterization .....	122
4.4 Results and Discussion .....	124
4.4.1 Electrochemical Properties of $[Co(ppy)_3]$ .....	124
4.4.2 Self-Exchange Kinetics of $[Co(ppy)_3]^{+/0}$ via Stopped-Flow Spectroscopy .....	125
4.4.3 Determination of $[Co(ppy)_3]^{+/0}$ Reorganization Energy .....	129
4.4.4 $[Co(ppy)_3]$ Application in DSSCs .....	130
4.5 Conclusion .....	134
APPENDIX .....	136
REFERENCES .....	144
<b>Chapter 5. Spin-Doctoring Cobalt Redox Shuttles .....</b>	<b>148</b>
5.1 Abstract .....	148
5.2 Introduction .....	149
5.3 Experimental .....	152
5.3.1 Materials .....	152
5.3.2 Instrumentation .....	153
5.3.3 X-Ray Crystallography Methodology .....	154
5.3.4 Synthesis of Parent Cobalt $[Co(PY_5Me_2)(MeCN)](OTf)_2$ Complex .....	154
5.3.5 $[Co(PY_5Me_2)(CN)](OTf)$ Synthesis .....	155
5.3.6 $[Co(PY_5Me_2)(CN)](OTf)_2$ Synthesis .....	156
5.3.7 Synthesis of Cross-Exchange Redox Shuttles .....	157
5.3.7 Cross-Exchange Kinetics .....	158
5.3.9 Semiconductor Anode Fabrication .....	160
5.4 Results .....	161
5.4.1 Synthesis .....	161
5.4.2 X-Ray Crystallography .....	163
5.4.3 $[Co(PY_5Me_2)(CN)](OTf)$ Magnetic Properties .....	167
5.4.4 Vibrational Spectroscopy .....	168
5.4.5 UV-Vis Spectroscopy .....	170

5.4.6 Electrochemical Properties .....	171
5.4.7 Self-Exchange Kinetics of $[\text{Co}(\text{PY}_5\text{Me}_2)(\text{CN})]^{2+/+}$ via Stopped-Flow Spectroscopy .....	173
5.4.8 Recombination Kinetics .....	177
5.5 Discussion .....	179
5.6 Conclusion .....	186
APPENDIX.....	188
REFERENCES .....	204
<b>Chapter 6. Considerations for the Future Directions of DSSCs.....</b>	<b>208</b>
6.1 Integrating Near-IR Absorbing Sensitizers into Solid-State DSSC Devices for Potential Tandem Solar Cell Designs .....	208
6.2 Copper Redox Shuttles as Alternatives to Cobalt.....	212
6.3 The Quest for New Semiconductor Materials .....	214
6.4 Mechanistic Insight as to the Pathway for Dye Recombination .....	216
APPENDIX.....	221
REFERENCES .....	225

## LIST OF TABLES

Table 3.1 Summary of self-exchange rate constants, $k_{11}$ , $k_{22}$ , and $k_{33}$ , and the corresponding reduction potentials, $E^\circ$ , for $[\text{Fe}(\text{C}_5\text{H}_4\text{CH}_3)_2]^{+/0}$ , $[\text{Co}(\text{bpy})_3]^{3+/2+}$ and $[\text{Co}(\text{ttn})_2]^{3+/2+}$ in acetonitrile with 0.1 M LiTFSI at $25 \pm 0.4^\circ\text{C}$ .....	76
Table 3.2 Summary of the reorganization energies determined for the $[\text{Co}(\text{bpy})_3]^{3+/2+}$ and $[\text{Co}(\text{ttn})_2]^{3+/2+}$ redox shuttles, and the parameters used for calculation of $k_{\text{rec},R+}$ .....	82
Table 3.3 Average $J$ - $V$ characteristics of twelve DSSCs under simulated 1 sun AM 1.5G illumination ( $100 \text{ mW cm}^{-2}$ ). .....	84
Table 3.4 Fit values of $L_n$ and $\eta_{\text{inj}} \times \eta_{\text{reg}}$ for DSSCs employing $[\text{Co}(\text{bpy})_3]^{3+/2+}$ and $[\text{Co}(\text{ttn})_2]^{3+/2+}$ redox shuttles with and without 1 ALD cycle of $\text{Al}_2\text{O}_3$ as a blocking layer. Also shown is the driving force for regeneration, $-\Delta G_{\text{reg}}^0$ , for each of the two redox shuttles. ....	92
Table A3.1 Observed pseudo-first order rate constants, $k_{\text{obs}}$ , and the initial reaction mixtures for the cross-exchange between $[\text{Co}(\text{bpy})_3]^{3+}$ and $[\text{Fe}(\text{C}_5\text{H}_4\text{CH}_3)_2]$ , see Reaction (3.1) of the main text.....	98
Table A3.2 Observed pseudo-first order rate constants, $k_{\text{obs}}$ , and the initial reaction mixtures for the cross-exchange between $[\text{Co}(\text{ttn})_2]^{3+}$ and $[\text{Co}(\text{bpy})_3]^{2+}$ , see Reaction (3.2) of the main text. ....	98
Table A3.3 Kinetic summary of the cross-exchange rate constants, $k_{12}$ and $k_{21}$ , measured equilibrium constants for the forward reaction, $K_{12}$ , the nonlinear correction term, $f_{12}$ , and work term, $W_{12}$ , associated with bringing precursor complexes together for Reaction (3.1) between $[\text{Fe}(\text{C}_5\text{H}_4\text{CH}_3)_2]$ and $[\text{Co}(\text{bpy})_3]^{3+}$ in acetonitrile with 0.1 M LiTFSI at $25 \pm 0.4^\circ\text{C}$ . ....	99
Table A3.4 Kinetic summary of the cross-exchange rate constants, $k_{23}$ and $k_{32}$ , measured equilibrium constants for the forward reaction, $K_{23}$ , the nonlinear correction term, $f_{23}$ , and work term, $W_{23}$ , associated with bringing precursor complexes together for Reaction (3.2) between $[\text{Co}(\text{bpy})_3]^{2+}$ and $[\text{Co}(\text{ttn})_2]^{3+}$ in acetonitrile with 0.1 M LiTFSI at $25 \pm 0.4^\circ\text{C}$ . ....	99
Table A4.1 Elemental analysis results.....	137
Table A4.2 Observed pseudo-first order rate constants, $k_{\text{obs}}$ , and the initial reaction mixtures for the cross-exchange between $[\text{Co}(\text{ptpy})_3]$ and $[\text{Co}(\text{bpyCl}_2)_3](\text{PF}_6)_3$ .....	137
Table A4.3 Kinetic summary of the cross-exchange rate constants, $k_{12}$ and $k_{21}$ , measured equilibrium constants for the forward reaction, $K_{12}$ , the nonlinear correction term, $f_{12}$ , and work term, $W_{12}$ , associated with bringing precursor complexes together for Reaction (4.1)	

between [Co(bpyCl<sub>2</sub>)<sub>3</sub>](PF<sub>6</sub>)<sub>3</sub> and [Co(ppy)<sub>3</sub>] in acetonitrile with 0.1 M TBAPF<sub>6</sub> at 25 ± 0.1°C. .... 138

Table A4.4 Formal reduction potentials,  $E^\circ$ , of all cobalt complexes used in the stopped-flow and DSSC studies. Ferrocene (Fc), [Fe(C<sub>5</sub>H<sub>5</sub>)<sub>2</sub>]<sup>+0</sup>, is also included as a point of reference in converting from Ag/AgNO<sub>3</sub> to NHE. All formal potentials were measured using in acetonitrile with 0.1 M TBAPF<sub>6</sub> or 0.1 M LiTFSI supporting electrolyte with a platinum working electrode, a platinum mesh counter electrode and a Ag/AgNO<sub>3</sub> reference electrode (0.1 M TBAPF<sub>6</sub> acetonitrile). .... 138

Table A4.5 Average *J-V* Characteristics of four DSSCs containing a [Co(bpy)<sub>3</sub>]<sup>3+/2+</sup> electrolyte and four cells with a tandem electrolyte of [Co(ppy)<sub>3</sub>] and [Co(bpy)<sub>3</sub>]<sup>3+/2+</sup>, both paired with the D35cpdt dye, and measured under 1 sun simulated AM 1.5G illumination (100 mW cm<sup>-2</sup>). .... 139

Table 5.1 Selected bond lengths and angles for Co(PY<sub>5</sub>Me<sub>2</sub>)(CN)](OTf) and Co(PY<sub>5</sub>Me<sub>2</sub>)(CN)](OTf)<sub>2</sub>. Note– bond lengths are reported in angstroms (Å) and bond angles are in degrees (°). The standard deviations of each value are shown in parenthesis. Each of the N<sub>1</sub> – Co – N<sub>X</sub> (X = 2-5) bond angles are not listed since each value is nearly 90° (±1°–2°). .... 165

Table 5.2 Summary of cyano, CN, vibrational frequencies using Raman spectroscopy and single crystals of [Co(PY<sub>5</sub>Me<sub>2</sub>)(CN)](OTf), [Co(PY<sub>5</sub>Me<sub>2</sub>)(CN)](OTf) and the Dimer Complex. .... 170

Table A5.1 Elemental analysis summary of the cobalt complexes under investigation. Note- Complex (0): [Co(PY<sub>5</sub>Me<sub>2</sub>)(MeCN)](OTf)<sub>2</sub>, Complex (1): [Co(PY<sub>5</sub>Me<sub>2</sub>)(CN)](OTf), Complex (2): [Co(PY<sub>5</sub>Me<sub>2</sub>)(CN)](OTf)<sub>2</sub> and Complex (3): Dimer Complex. Note- single crystals of the dimer complex were used for CHN assuming two acetonitrile molecules in the lattice. It was difficult, however, to isolate only Dimer crystals for the measurement. Presumably some [Co(PY<sub>5</sub>Me<sub>2</sub>)(MeCN)](OTf)<sub>2</sub> are present, which is the source of the larger error. .... 189

Table A5.2 Single crystal X-ray diffraction data and refinement details. Note- Complex (1): [Co(PY<sub>5</sub>Me<sub>2</sub>)(CN)](OTf), Complex (2): [Co(PY<sub>5</sub>Me<sub>2</sub>)(CN)](OTf)<sub>2</sub>, Complex (3): Dimer Complex. .... 190

Table A5.3 Single crystal X-ray diffraction data and refinement details. Note- Complex (4): Cluster Complex and Complex (5): [Co(PY<sub>5</sub>Me<sub>2</sub>)(F)](OTf)<sub>2</sub>. .... 191

Table A5.4 Selected bond lengths and angles for the Dimer Complex. Note– bond lengths are reported in angstroms (Å) and bond angles are in degrees (°). The standard deviations of each value are shown in parenthesis. .... 192

Table A5.5 Formal reduction potentials,  $E^\circ$ , of [Co(PY<sub>5</sub>Me<sub>2</sub>)(X)] (X = MeCN or CN), [Co(terpy)<sub>2</sub>]<sup>3+/2+</sup> and 1,1'-dimthylferrocene, [Fe(C<sub>4</sub>H<sub>5</sub>CH<sub>3</sub>)<sub>2</sub>]<sup>+0</sup>, redox shuttles measured via CV. Ferrocene, [Fe(C<sub>5</sub>H<sub>5</sub>)<sub>2</sub>]<sup>+0</sup>, is also included as a point of reference in converting from Ag/AgNO<sub>3</sub> to NHE (Ferrocene: 0.40V vs. SCE).<sup>15</sup> All formal potentials were

measured in acetonitrile with 0.1 M tetrabutylammonium hexafluorophosphate, TBAPF<sub>6</sub>, supporting electrolyte using a platinum working electrode, a platinum mesh counter electrode and a homemade Ag/AgNO<sub>3</sub> (0.1 M TBAPF<sub>6</sub> acetonitrile) reference electrode.

..... 193

Table A5.6 Observed pseudo-first order rate constants,  $k_{obs}$ , and the initial reaction mixtures for the cross-exchange reactions between [Co(PY<sub>5</sub>Me<sub>2</sub>)(CN)](OTf) and [Co(terpy)<sub>2</sub>](PF<sub>6</sub>)<sub>3</sub>, Reaction (5.1) of the main text, in neat acetonitrile at 25 ± 0.1°C.. 193

Table A5.7 Observed pseudo-first order rate constants,  $k_{obs}$ , and the initial reaction mixtures for the cross-exchange between [Fe(C<sub>5</sub>H<sub>4</sub>CH<sub>3</sub>)] and [Co(terpy)<sub>2</sub>](PF<sub>6</sub>)<sub>3</sub> in neat acetonitrile at 25 ± 0.1°C. .... 193

Table A5.8 Kinetic summary of the cross-exchange rate constants,  $k_{23}$  and  $k_{32}$ , and the measured equilibrium constants for the forward reaction,  $K_{23}$ , between [Fe(C<sub>5</sub>H<sub>4</sub>CH<sub>3</sub>)] and [Co(terpy)<sub>2</sub>](PF<sub>6</sub>)<sub>3</sub> in neat acetonitrile at 25 ± 0.1°C. .... 194

## LIST OF FIGURES

Figure 1.1 Schematic of the basic components and operating principals of a DSSC.....	9
Figure 1.2 Relative energy diagram of a DSSC and the various electron-transfer pathways associated with solar cell operation. ....	10
Figure 1.3 Potential energy curves of the reactants and products for an outersphere electron-transfer reaction as a function of reaction coordinate. <sup>61</sup> .....	22
Figure 1.4 Plot demonstrating the relationship between the electron-transfer rate constant and the driving force for an electron-transfer reaction according to Marcus theory. Note- in the Marcus normal region $-\Delta G^o < \lambda_{et}$ where as in the Marcus inverted region $-\Delta G^o > \lambda_{et}$ . <sup>64</sup> .....	25
Figure 2.1 Basic operating components of a stopped-flow instrument. ....	37
Figure 2.2 a) Evolution and decay of a cross-exchange reaction mixture's absorbance as a function of wavelength, $\lambda$ , over a 150 nm range monitored by stopped-flow spectroscopy. b) Absorbance decay of a reactant species at a single $\lambda$ as a function of time. ....	38
Figure 2.3 a) CVs of reacting species in a cross-exchange reaction mixture used to determine the equilibrium constant for the reaction. b) Molar extinction coefficients as a function of wavelength for each reactant and product of a cross-exchange reaction mixture. ....	43
Figure 2.4 a) Plot of absorbance at a single wavelength, $\lambda$ , vs. time, corresponding to the decay of a single reactant species (red dots) and the resulting fit (black line). b) Residual plot to show the goodness of fit for the absorbance plot shown in a).....	44
Figure 2.5 a) Example of an absorbance versus time plot for a cross-exchange reaction that contains multiple processes, i.e. reactant decomposition, aside from charge transfer. b) Plot of residuals for a cross-exchange reaction that contains multiple processes aside from a single electron-transfer, which cannot be fit to simple pseudo-first order decay kinetics.	45
Figure 2.6 Example of an observed pseudo-first order rate constants, $k_{obs}$ , versus the excess reactant concentrations plot for the reactions between $[A]^+$ and $[B]$ for the homogeneous cross-exchange Reaction (2.1) above. ....	46
Figure A2.1 Olis RSM 1000 UV-Vis Rapid Scanning Spectrometer.....	53
Figure 3.1 Molecular structures of a) cobalt tris(2,2'-bipyridine), $[Co(bpy)_3]^{3+/2+}$ and b) cobalt bis(1,4,7-trithiacyclononane), $[Co(ttcn)_2]^{3+/2+}$ .....	62
Figure 3.2 a) Plot of absorbance at 650 nm vs. time, corresponding to the growth of the $[Fe(C_5H_4CH_3)_2]^+$ species (red dots) and the resulting fit (black line) for the reduction of	

[Co(bpy)<sub>3</sub>]<sup>3+</sup> (2.00 x 10<sup>-3</sup> M) by [Fe(C<sub>5</sub>H<sub>4</sub>CH<sub>3</sub>)<sub>2</sub>] (1.90 x 10<sup>-4</sup> M). b) Observed pseudo-first order rate constants, *k*<sub>obs</sub>, versus the excess reactant concentrations for the reactions between [Fe(C<sub>5</sub>H<sub>4</sub>CH<sub>3</sub>)<sub>2</sub>] and [Co(bpy)<sub>3</sub>]<sup>3+</sup> in acetonitrile with 0.1 M LiTFSI at 25 ± 0.4°C. .... 71

Figure 3.3 a) Plot of absorbance at 480 nm vs. time, corresponding to decay of the [Co(ttcn)<sub>2</sub>]<sup>3+</sup> species (red dots) and the resulting fit (black line) for the reduction of [Co(ttcn)<sub>2</sub>]<sup>3+</sup> (1.45×10<sup>-4</sup> M) by [Co(bpy)<sub>3</sub>]<sup>2+</sup> (6.25×10<sup>-3</sup> M). b) Observed pseudo-first order rate constants, *k*<sub>obs</sub>, versus the excess reactant concentrations for the reactions between [Co(bpy)<sub>3</sub>]<sup>2+</sup> and [Co(ttcn)<sub>2</sub>]<sup>3+</sup> in acetonitrile with 0.1 M LiTFSI at 25 ± 0.4°C. .... 72

Figure 3.4 a) Plots of representative *J-V* curves of DSSCs with the [Co(bpy)<sub>3</sub>]<sup>3+/2+</sup> (red) and [Co(ttcn)<sub>2</sub>]<sup>3+/2+</sup> (blue) redox shuttles for FS (solid) and BS (dotted) illumination directions. b) IPCE curves for DSSCs with the [Co(bpy)<sub>3</sub>]<sup>3+/2+</sup> (red circles) and [Co(ttcn)<sub>2</sub>]<sup>3+/2+</sup> (blue triangles) redox shuttles under FS (filled) and BS (hollow) illumination; film thickness, 7.1 μm. .... 84

Figure 3.5 Light harvesting efficiency (*η*<sub>LH</sub>) of 7.1μm thick TiO<sub>2</sub> films sensitized with the D35cpdt dye in DSSCs with the [Co(bpy)<sub>3</sub>]<sup>3+/2+</sup> (red circles) and [Co(ttcn)<sub>2</sub>]<sup>3+/2+</sup> (blue triangles) redox shuttles under FS (filled) and BS illumination (hollow). .... 85

Figure 3.6 Experiment (shape) and fit (line) results of a) IPCE(BS/FS) ratios and b) IPCEs for DSSCs employing the [Co(bpy)<sub>3</sub>]<sup>3+/2+</sup> (red circles) and [Co(ttcn)<sub>2</sub>]<sup>3+/2+</sup> (blue triangles) redox shuttles. .... 87

Figure 3.7 IPCE curves for DSSCs with 1 ALD cycle of Al<sub>2</sub>O<sub>3</sub> employing the [Co(bpy)<sub>3</sub>]<sup>3+/2+</sup> (red circles) and [Co(ttcn)<sub>2</sub>]<sup>3+/2+</sup> (blue triangles) redox shuttles under FS (filled) and BS illumination (hollow). .... 90

Figure 3.8 a) Lifetimes vs. applied voltage (symbols) and the global fit (lines) used for the IPCE ratio fits for DSSCs employing the [Co(bpy)<sub>3</sub>]<sup>3+/2+</sup> (red dots) and [Co(ttcn)<sub>2</sub>]<sup>3+/2+</sup> (blue dots) redox shuttles with (filled) and without (hollow) 1 ALD cycle Al<sub>2</sub>O<sub>3</sub> coating. b) IPCE ratio (blue triangles) and fit results (blue line) to Equation (3.19) for DSSCs with 1 ALD cycle of Al<sub>2</sub>O<sub>3</sub> coating employing the [Co(ttcn)<sub>2</sub>]<sup>3+/2+</sup> redox shuttle..... 91

Figure A3.1 <sup>1</sup>H NMR of [Co(bpy)<sub>3</sub>](TFSI)<sub>2</sub> in acetonitrile-*d*<sub>3</sub>..... 100

Figure A3.2 <sup>1</sup>H NMR of [Co(bpy)<sub>3</sub>](TFSI)<sub>3</sub> in acetonitrile-*d*<sub>3</sub>..... 100

Figure A3.3 <sup>1</sup>H NMR of [Co(ttcn)<sub>2</sub>](TFSI)<sub>2</sub> in acetonitrile-*d*<sub>3</sub>..... 101

Figure A3.4 <sup>1</sup>H NMR of [Co(ttcn)<sub>2</sub>](TFSI)<sub>3</sub> in acetonitrile-*d*<sub>3</sub>. Inset enhances the observed multiplet. .... 101

Figure A3.5 Transmittance (T%) of a DSSC with a 7.1μm thick TiO<sub>2</sub> mesoporous film sensitized with the D35cpdt dye. .... 102

Figure A3.6 Transmittance (T%) (filled) and reflectance (R%) (hollow) of an FTO glass substrate (red triangles) and a 1.2 mm high quality glass substrate (black circles). ..... 102

Figure A3.7 Transmittance (T%) (filled) and reflectance (R%) (hollow) of a photoanode substrate- FTO with TiO<sub>2</sub> ALD blocking layer (black circles) and counter electrode-platinized FTO (red triangles). Note- T% = 77-82 % at  $\lambda = 450-750$  nm for the photoanode substrate, but ca. 4-5 % units lower for the counter electrode, due mainly to the light absorption by the platinum catalyst layer. R% = 10-12 % at  $\lambda = 450-750$  nm for photoanode substrate, and ca. 5-10 % units higher for the counter electrode, due again to the platinum catalyst layer which induces an increased roughness to the electrode surface. .... 103

Figure A3.8 Transmittance (T%) of electrolyte layer between counter electrode and TiO<sub>2</sub> film for [Co(bpy)<sub>3</sub>]<sup>3+/2+</sup> (blue solid line) and [Co(ttcn)<sub>2</sub>]<sup>3+/2+</sup> (orange dashed line). Note- the electrolyte transmittances are normalized to the path length of the actual cell which is  $\sim 18 \mu\text{m}$  (Surlyn film thickness,  $25 \mu\text{m}$ , subtracted by the TiO<sub>2</sub> film thickness,  $7.1 \mu\text{m}$ ). ..... 103

Figure A3.9 Transmittance (T%) and reflectance (R%) of sample cells (sandwich cells assembled using bare 1.2 mm high quality microglass substrates filled with electrolyte) of various TiO<sub>2</sub> film thicknesses,  $d$ , (600 nm, 810 nm,  $1.50 \mu\text{m}$ ,  $1.80 \mu\text{m}$ ) at  $\lambda = 450-750$  nm. Electrolyte composition: 0.2 M Co(II), 20 mM Co(III), 0.10 M LiTFSI, 10 mM Chenodeoxycholic acid. Note- The absorption maximum of the adsorbed dye is at  $\lambda_{\text{max}} \approx 470$  nm and the transmittance decreases with increasing film thickness. T% is close to zero at  $\lambda = 450-500$  nm for film thickness  $1.80 \mu\text{m}$ , which indicates the film is thick enough to absorb all incident photons effectively in that wavelength range. A thicker film will further broaden the zero transmittance range. R% is  $\sim 10$  % and decreases slightly with increasing film thickness at  $\lambda = 400-700$  nm, indicating that the dye absorbs light strongly and suppresses the light scattering from the film effectively. .... 104

Figure A3.10 Absorbance of D35cpdt sensitized TiO<sub>2</sub> films with various thicknesses,  $d$ , (600 nm, 810 nm,  $1.50 \mu\text{m}$ ,  $1.80 \mu\text{m}$ ) calculated using Equation (2.1). ..... 104

Figure A3.11 Absorbance of sensitized films ( $A_D$ ) vs. film thickness,  $d$ , at 467nm ( $\lambda_{\text{max}}$ ) and its linear least squares fit curve:  $y = 1.004x + 0.0159$ ,  $R = 0.970$ . The error bars indicate the standard deviation from transmittance and reflectance measurements. Note- The linear relation of  $A_D$  and  $d$  indicates a homogeneous dye loading across the film. Also, The value of the slope was used to calculate the absorptivity of D35cpdt sensitized TiO<sub>2</sub> film using Equation (2.1) of the main text. .... 105

Figure A3.12 Normalized absorptivity profile of a D35cpdt sensitized TiO<sub>2</sub> film. Note- The absorptivity profile was further used for calculation of light harvesting efficiencies ( $\eta_{\text{LH}}$ ) and IPCEs. .... 105

Figure A3.13 Normalized absorbance of the D35cpdt dye in ethanol. .... 106

Figure A3.14 Absorbance of 100 times diluted electrolyte solutions containing (0.2 M Co(II), 20 mM Co(III), 0.1 M LiTFSI and 10 mM Chenodeoxycholic acid), [Co(bpy)<sub>3</sub>]<sup>3+/2+</sup> (blue solid line) and [Co(ttcn)<sub>2</sub>]<sup>3+/2+</sup> (orange dashed line). Note- the electrolyte solution is

diluted to keep the maximum absorbance below 2 (99% light is absorbed according to  $A = -\lg T$ ) for calculating the extinction coefficient and the electrolyte absorptivity,  $\alpha_e$ . ..... 106

Figure A3.15 Normalized CVs of  $[\text{Fe}(\text{C}_5\text{H}_4)_2]$  (red line),  $[\text{Fe}(\text{C}_5\text{H}_4\text{CH}_3)_2]$  (black line),  $[\text{Co}(\text{bpy})_3](\text{TFSI})_2$  (green line) and  $[\text{Co}(\text{ttn})_2](\text{TFSI})_2$  (yellow line) in acetonitrile with 0.1 M LiTFSI supporting electrolyte, using a gold disk working electrode, a platinum mesh counter electrode and a homemade  $\text{Ag}/\text{AgNO}_3$  (0.1M TBAPF<sub>6</sub> in acetonitrile) reference electrode..... 107

Figure A3.16 CV of a D35cpdt sensitized ITO nanoparticle film at a 10 mV/s scan rate, using a platinum mesh counter electrode and a homemade  $\text{Ag}/\text{AgNO}_3$  (0.1M TBAPF<sub>6</sub> in acetonitrile) reference electrode. Note- Ferrocene (Fc) was used to calibrate the reference electrode potential before and after measurements..... 107

Figure A3.17 IPCE ratios for DSSCs containing either  $[\text{Co}(\text{bpy})_3]^{3+/2+}$  (red circles) or  $[\text{Co}(\text{ttn})_2]^{3+/2+}$  (blue triangles) redox shuttles with a 7.1  $\mu\text{m}$  mesoporous  $\text{TiO}_2$  film sensitized with the D35cpdt dye. .... 108

Figure A3.18 IPCEs for DSSCs utilizing  $[\text{Co}(\text{ttn})_2]^{3+/2+}$  and 3.7 $\mu\text{m}$   $\text{TiO}_2$  mesoporous films sensitized with D35cpdt. Note- FS illumination (filled triangles) and BS illumination (hollow triangles). .... 108

Figure A3.19 Charge collection efficiencies (shape) and the corresponding fit (line) results for DSSCs employing  $[\text{Co}(\text{bpy})_3]^{3+/2+}$  (red circles) and  $[\text{Co}(\text{ttn})_2]^{3+/2+}$  (blue triangles) redox shuttles. (FS illumination (filled) and BS illumination (hollow)). Note- 3.7 $\mu\text{m}$  films were used for DSSCs with  $[\text{Co}(\text{ttn})_2]^{3+/2+}$  ( $\eta_{inj} \times \eta_{reg} \approx 1.00$ ) and 7.1 $\mu\text{m}$  films were used for DSSCs with  $[\text{Co}(\text{bpy})_3]^{3+/2+}$  ( $\eta_{inj} \times \eta_{reg} \approx 0.54$ )..... 109

Figure A3.20 IPCE (shape) and fit (line) results for DSSCs with 1 ALD cycle of  $\text{Al}_2\text{O}_3$  coating using  $[\text{Co}(\text{bpy})_3]^{3+/2+}$  (red) and  $[\text{Co}(\text{ttn})_2]^{3+/2+}$  (blue) redox shuttles paired with the D35cpdt dye on 7.1 $\mu\text{m}$  thick films. Note- FS illumination (filled) and BS illumination (hollow)..... 109

Figure A3.21 Plots of a) charge collection efficiencies,  $\eta_{inj} \times \eta_{reg} \approx 0.74$  for  $[\text{Co}(\text{bpy})_3]^{3+/2+}$  &  $\eta_{inj} \times \eta_{reg} \approx 0.72$  for  $[\text{Co}(\text{ttn})_2]^{3+/2+}$ ; b)  $\eta_{inj} \times \eta_{reg}$  determined by dividing the IPCE with LHE (taking charge collection efficiency as 100%) for DSSCs with 1 ALD cycle of  $\text{Al}_2\text{O}_3$  coating using  $[\text{Co}(\text{bpy})_3]^{3+/2+}$  (red),  $[\text{Co}(\text{ttn})_2]^{3+/2+}$  (blue) redox shuttles paired with the D35cpdt dye on 7.1 $\mu\text{m}$  thick films. Note- FS illumination (filled) and BS illumination (hollow)..... 110

Figure A3.22 a) Lifetime plots and b)  $R_{CT}$  versus chemical capacitance  $C_\mu$  from electrochemical impedance measurements for DSSCs using  $[\text{Co}(\text{bpy})_3]^{3+/2+}$  (red) and  $[\text{Co}(\text{ttn})_2]^{3+/2+}$  (blue) redox shuttles paired with the D35cpdt dye with (filled) and without (hollow) 1 ALD cycle  $\text{Al}_2\text{O}_3$  coating on 7.1  $\mu\text{m}$   $\text{TiO}_2$  films. Note- superimposed lines are lifetimes derived from open circuit voltage decay measurements..... 110

Figure 4.1 a) Molecular structure of  $[\text{Co}(\text{ptpy})_3]^{+0}$ . b) CVs of  $[\text{Co}(\text{ptpy})_3]$  in acetonitrile with 0.1 M LiTFSI supporting electrolyte as a function of scan rate using a platinum disk

working electrode, a platinum mesh counter electrode and a Ag/AgNO<sub>3</sub> (0.1 M TBAPF<sub>6</sub> acetonitrile) reference electrode..... 125

Figure 4.2 a) Plot of absorbance at 433 nm vs. time, corresponding to decay of the [Co(ppy)<sub>3</sub>] species (red dots) and the resulting fit (black line) for the oxidation of [Co(ppy)<sub>3</sub>] (5.00 x 10<sup>-5</sup> M) by [Co(bpyCl<sub>2</sub>)<sub>3</sub>]<sup>3+</sup> (5.00×10<sup>-4</sup> M). b) Observed pseudo-first order rate constants, *k*<sub>obs</sub>, versus the excess concentration of [Co(bpyCl<sub>2</sub>)<sub>3</sub>]<sup>3+</sup> for the reactions between [Co(ppy)<sub>3</sub>] and [Co(bpyCl<sub>2</sub>)<sub>3</sub>]<sup>3+</sup>. .... 127

Figure 4.3 Plots of current density versus applied potential, *J* vs. *V*, corresponding to DSSCs filled with [Co(bpy)<sub>3</sub>]<sup>3+/2+</sup> electrolyte (red line) and a tandem electrolyte containing [Co(ppy)<sub>3</sub>] and [Co(bpy)<sub>3</sub>]<sup>3+/2+</sup> (green line) under AM 1.5G illumination. .... 131

Figure A4.1 <sup>1</sup>H NMR of [Co(ppy)<sub>3</sub>] in CDCl<sub>3</sub>. .... 139

Figure A4.2 <sup>1</sup>H NMR of [Co(bpyCl<sub>2</sub>)<sub>3</sub>](PF<sub>6</sub>)<sub>2</sub> in acetonitrile-*d*<sub>3</sub>. .... 140

Figure A4.3 <sup>1</sup>H NMR of [Co(bpyCl<sub>2</sub>)<sub>3</sub>](PF<sub>6</sub>)<sub>3</sub> in acetonitrile-*d*<sub>3</sub>. .... 140

Figure A4.4 Randles-Sevcik plot of both anodic, *I*<sub>pa</sub>, (filled red diamonds) and cathodic, *I*<sub>pc</sub>, (open red diamonds) peak currents versus the square root of the scan rate, *v*<sup>1/2</sup>, for the [Co(ppy)<sub>3</sub>] scan rate dependence, Figure 4.1b. The fit (black line) to *I*<sub>pa</sub> vs *v*<sup>1/2</sup> (top plot) was used to estimate the diffusion coefficient of [Co(ppy)<sub>3</sub>]. .... 141

Figure A4.5 Normalized CVs of [Fe(C<sub>5</sub>H<sub>5</sub>)<sub>2</sub>] (Fc) (pink line), [Co(ppy)<sub>3</sub>] (green line) and [Co(bpyCl<sub>2</sub>)<sub>3</sub>](PF<sub>6</sub>)<sub>2</sub> (blue line) in acetonitrile with 0.1 M TBAPF<sub>6</sub> supporting electrolyte at a scan rate of 100 mV/s using a platinum disk working electrode, a platinum mesh counter electrode and a Ag/AgNO<sub>3</sub> (0.1 M TBAPF<sub>6</sub> acetonitrile) reference electrode.. 141

Figure A4.6 IPCE plots of DSSCs containing a [Co(bpy)<sub>3</sub>]<sup>3+/2+</sup> electrolyte (red dots) and a tandem electrolyte containing [Co(ppy)<sub>3</sub>] & [Co(bpy)<sub>3</sub>]<sup>3+/2+</sup> (green dots) both paired with the D35cpdt dye. .... 142

Figure A4.7 Light intensity, *ϕ*, dependence on short circuit photocurrent, *J*<sub>lim</sub>, in DSSCs employing a tandem electrolyte of [Co(ppy)<sub>3</sub>] & [Co(bpy)<sub>3</sub>] with the D35cpdt dye. ... 142

Figure A4.8 a) Dark *J*-*V* curves corresponding to DSSCs filled with [Co(bpy)<sub>3</sub>]<sup>3+/2+</sup> electrolyte (red line) and a tandem electrolyte containing [Co(ppy)<sub>3</sub>] & [Co(bpy)<sub>3</sub>]<sup>3+/2+</sup> (green line) both with the D35cpdt dye. b) Electron lifetimes of DSSCs containing a [Co(bpy)<sub>3</sub>]<sup>3+/2+</sup> electrolyte (red dots) and a tandem electrolyte containing [Co(ppy)<sub>3</sub>] & [Co(bpy)<sub>3</sub>]<sup>3+/2+</sup> (green dots) using open circuit voltage decay (OCVD). A dark OCVD measurement with a cell containing the tandem electrolyte is also overlaid (black dots) to compare degree of [Co(ppy)<sub>3</sub>]<sup>+</sup> recombination. .... 143

Figure A4.9 Normalized CVs of [Co(bpy)<sub>3</sub>](TFSI)<sub>2</sub> (red line) and [Co(ppy)<sub>3</sub>] (green line) in acetonitrile with 0.1 M LiTFSI supporting electrolyte at a scan rate of 100 mV/s using a platinum disk working electrode, a platinum mesh counter electrode and a Ag/AgNO<sub>3</sub> (0.1 M TBAPF<sub>6</sub> acetonitrile) reference electrode. .... 143

Figure 5.1 Single crystal representations of a)  $[\text{Co}(\text{PY}_5\text{Me}_2)(\text{CN})](\text{OTf})$  and b)  $[\text{Co}(\text{PY}_5\text{Me}_2)(\text{CN})](\text{OTf})_2$  provided by Olex2 and structurally refined by ShelXT software. Note- the solvent and counter ions are excluded for clarity in each of the crystal structures above. Depicted ellipsoids are at the 50% probability level. .... 164

Figure 5.9 Single crystal representation of the Dimer Complex provided by Olex2 and structurally refined by ShelXT software. Note- the solvent and counter ions are excluded for clarity in the crystal structure above. Depicted ellipsoids are at the 50% probability level. .... 167

Figure 5.10 Raman spectra using single crystals of a)  $[\text{Co}(\text{PY}_5\text{Me}_2)(\text{CN})](\text{OTf})$  (red line) and  $[\text{Co}(\text{PY}_5\text{Me}_2)(\text{CN})](\text{OTf})_2$  (green line) as well as b) the Dimer complex (blue line). .... 169

Figure 5.11 UV-Vis spectra of  $[\text{Co}(\text{PY}_5\text{Me}_2)(\text{CN})](\text{OTf})$  (red line) and  $[\text{Co}(\text{PY}_5\text{Me}_2)(\text{CN})](\text{OTf})_2$  (green line) measured under air free conditions in acetonitrile. Inset- enhances the d-d transition of the  $[\text{Co}(\text{PY}_5\text{Me}_2)(\text{CN})](\text{OTf})_2$  complex. .... 171

Figure 5.12 Cyclic Voltammograms (CVs) of  $[\text{Co}(\text{PY}_5\text{Me}_2)(\text{CN})](\text{OTf})$  (red line) and  $[\text{Co}(\text{PY}_5\text{Me}_2)(\text{MeCN})](\text{OTf})_2$  (dark blue dashed line) measured in acetonitrile with 0.1 M TBAPF<sub>6</sub> using a platinum disk working electrode, a platinum mesh counter electrode and a homemade Ag/AgNO<sub>3</sub> (0.1 M TBAPF<sub>6</sub> acetonitrile) reference electrode. .... 172

Figure 5.13 a) Plot of absorbance at 505 nm vs. time, corresponding to the growth of the  $[\text{Co}(\text{terpy})_2]^{2+}$  species (red dots) and the resulting single exponential fit (black line) for the reduction of  $[\text{Co}(\text{terpy})_2]^{3+}$  ( $4.0 \times 10^{-5}$  M) by  $[\text{Co}(\text{PY}_5\text{Me}_2)(\text{CN})]^+$  ( $1.2 \times 10^{-3}$  M). b) Pseudo-first order rate constants,  $k_{\text{obs}}$ , versus the excess concentration of  $[\text{Co}(\text{PY}_5\text{Me}_2)(\text{CN})]^+$  for the reactions between  $[\text{Co}(\text{PY}_5\text{Me}_2)(\text{CN})]^+$  and  $[\text{Co}(\text{terpy})_2]^{3+}$ . .... 175

Figure 5.14 a) Current density ( $J$ ) and b) log of current density ( $J$ ) versus applied potential ( $E$ ) plots for  $[\text{Co}(\text{PY}_5\text{Me}_2)(\text{CN})](\text{OTf})_2$  (green dots) and  $[\text{Co}(\text{bpy})_3](\text{PF}_6)_3$  (light blue dots) OSRSs measured using a mesoporous TiO<sub>2</sub> working electrode, a platinum mesh counter electrode and a homemade Ag/AgNO<sub>3</sub> (0.1M TBAPF<sub>6</sub>) reference electrode in an acetonitrile solution with 0.1M LiOTf. .... 178

Figure A5.1 Mass spectrum of  $[\text{Co}(\text{PY}_5\text{Me}_2)(\text{MeCN})](\text{OTf})_2$ . .... 194

Figure A5.2 Single crystal representation of the hexadentate Cobalt Cluster Complex provided by Olex2 and structurally refined by ShelXT software. Note- the protons, counterions and solvent are omitted for image clarity. .... 195

Figure A5.3 Single crystal representation of  $[\text{Co}(\text{PY}_5\text{Me}_2)(\text{F})](\text{OTf})_2$  provided by Olex2 and structurally refined by ShelXT software. Note- the counterions and solvent molecules are omitted for image clarity. .... 195

Figure A5.4 <sup>1</sup>H NMR of  $[\text{Co}(\text{PY}_5\text{Me}_2)(\text{MeCN})](\text{OTf})_2$  in acetonitrile-*d*<sub>3</sub>. .... 196

Figure A5.23 $^1\text{H}$ NMR of $[\text{Co}(\text{PY}_5\text{Me}_2)(\text{CN})](\text{OTf})$ in acetonitrile- $d_3$ . Inset shows there are no chemical shifts downfield from 25 ppm. ....	196
Figure A5.24 $^1\text{H}$ NMR of $[\text{Co}(\text{PY}_5\text{Me}_2)(\text{CN})](\text{OTf})_2$ in acetonitrile- $d_3$ . Inset shows the chemical shift and integration for the methyl groups of the $\text{PY}_5\text{Me}_2$ ligand. ....	197
Figure A5.25 $^1\text{H}$ NMR of the Dimer Complex in acetonitrile- $d_3$ . Inset is meant to demonstrate that there are no chemical shifts in the aromatic region for the $[\text{Co}(\text{PY}_5\text{Me}_2)(\text{CN})](\text{OTf})_2$ and/or free $\text{PY}_5\text{Me}_2$ ligand. ....	197
Figure A5.26 a) $^1\text{H}$ NMR indicating the stability of $[\text{Co}(\text{PY}_5\text{Me}_2)(\text{CN})](\text{OTf})$ with 0.1M $\text{TBAPF}_6$ in acetonitrile- $d_3$ after several days and b) an enhancement of the aromatic region with the free $\text{PY}_5\text{Me}_2$ ligand (purple line) overlaid on the $[\text{Co}(\text{PY}_5\text{Me}_2)(\text{CN})](\text{OTf})$ (red line) spectrum. The inset of a) indicates the chemical shifts for the formation of the Dimer Complex. The inset of b) indicates the chemical shifts associated with the TBA. ....	198
Figure A5.27 a) & b) $^1\text{H}$ NMR indicating the stability of $[\text{Co}(\text{PY}_5\text{Me}_2)(\text{CN})](\text{OTf})_2$ with 0.1M $\text{TBAPF}_6$ in acetonitrile- $d_3$ after several days. The inset of a) indicates the chemical shift for the methyl groups of the $\text{PY}_5\text{Me}_2$ ligand. The inset of b) indicates the chemical shifts associated with the TBA. Note- $[\text{Co}(\text{PY}_5\text{Me}_2)(\text{CN})](\text{OTf})_2$ is sparingly soluble in acetonitrile with 0.1M $\text{TBAPF}_6$ supporting electrolyte. ....	198
Figure A5.28 Magnetic susceptibility measurements in acetonitrile- $d_3$ using the Evans Method and following the $^1\text{H}$ chemical shift of Ferrocene, $[\text{Fe}(\text{C}_5\text{H}_5)_2]$ , after additions of the paramagnetic $[\text{Co}(\text{PY}_5\text{Me}_2)(\text{CN})](\text{OTf})$ complex. ....	199
Figure A5.29 UV-Vis spectrum of the $\text{PY}_5\text{Me}_2$ ligand, where $\text{PY}_5\text{Me}_2$ represents 2,6-bis(1,1-bis(2-pyridyl)ethyl)pyridine, in acetonitrile. ....	199
Figure A5.30 UV-Vis spectra of the $[\text{Co}(\text{terpy})_2](\text{PF}_6)_2$ (pink) and $[\text{Co}(\text{terpy})_2](\text{PF}_6)_3$ (orange) complexes, where terpy represents 2,2':6',2''-terpyridine, in acetonitrile. ....	200
Figure A5.31 Normalized CV of the Dimer Complex measured in acetonitrile with 0.1 M $\text{TBAPF}_6$ supporting electrolyte using a platinum disk working electrode, a platinum mesh counter electrode and a homemade $\text{Ag}/\text{AgNO}_3$ (0.1 M $\text{TBAPF}_6$ acetonitrile) reference electrode. ....	200
Figure A5.32 Normalized CVs of $[\text{Fe}(\text{C}_5\text{H}_5)_2]$ (black line), $[\text{Fe}(\text{C}_5\text{H}_4\text{CH}_3)_2]$ (green line) and $[\text{Co}(\text{terpy})_2](\text{PF}_6)_2$ (pink line) measured in acetonitrile with 0.1 M $\text{TBAPF}_6$ supporting electrolyte using a platinum disk working electrode, a platinum mesh counter electrode and a homemade $\text{Ag}/\text{AgNO}_3$ (0.1 M $\text{TBAPF}_6$ acetonitrile) reference electrode. ....	201
Figure A5.33 a) Plot of absorbance at 505 nm vs. time, corresponding to the growth of the $[\text{Co}(\text{terpy})_2]^{2+}$ species (red dot) and the resulting fit (black line) for the reduction of $[\text{Co}(\text{terpy})_2]^{3+}$ ( $3.0 \times 10^{-5}$ M) by $[\text{Fe}(\text{C}_5\text{H}_4\text{CH}_3)]$ ( $6.0 \times 10^{-4}$ M). b) Observed pseudo-first order rate constants, $k_{\text{obs}}$ , versus the excess concentration of $[\text{Fe}(\text{C}_5\text{H}_4\text{CH}_3)]$ for the reactions between $[\text{Fe}(\text{C}_5\text{H}_4\text{CH}_3)]$ and $[\text{Co}(\text{terpy})_2]^{3+}$ . ....	201

Figure A5.34 NMR tubes displaying [Co(PY<sub>5</sub>Me<sub>2</sub>)(CN)] degradation (precipitate) in neat acetonitrile-*d*<sub>3</sub> (right) and in acetonitrile-*d*<sub>3</sub> with 0.1 M TBAPF<sub>6</sub> supporting electrolyte (left)..... 202

Figure A5.35 Experimental three-electrode setup used to measure the recombination kinetics of [Co(PY<sub>5</sub>Me<sub>2</sub>)(CN)](OTf)<sub>2</sub> and [Co(bpy)<sub>3</sub>](PF<sub>6</sub>)<sub>3</sub>. Depicted is a mesoporous TiO<sub>2</sub> film sintered to an FTO substrate (working electrode) clamped to a cuvette cutout and exposed to 2mL of an acetonitrile containing 20mM of the oxidized redox shuttle and 0.1M LiOTf. A high surface area platinum (Pt) mesh was used as a counter electrode and a homemade Ag/AgNO<sub>3</sub> (0.1M TBAPF<sub>6</sub>) was used as a reference electrode as well. CVs were taken with a Pt wire working electrode before and after the dark recombination studies in order to check that the redox potentials of [Co(PY<sub>5</sub>Me<sub>2</sub>)(CN)](OTf)<sub>2</sub> and [Co(bpy)<sub>3</sub>](PF<sub>6</sub>)<sub>3</sub> were stable and/or side products weren't forming.<sup>16</sup> ..... 202

Figure 6.1 a) Single crystal representation of [Co(PY<sub>5</sub>Me<sub>2</sub>)(NCS)](OTf) provided by Olex2 and structurally refined by ShelXT software. Note- the counterions and solvent molecules are omitted for image clarity. b) CV of [Co(PY<sub>5</sub>Me<sub>2</sub>)(NCS)](OTf) in acetonitrile with 0.1 M TBAPF<sub>6</sub> using a platinum working electrode, a platinum mesh counter electrode and a homemade (0.1 M TBAPF<sub>6</sub> in acetonitrile) Ag/AgNO<sub>3</sub> reference electrode. .... 211

Figure 6.1 a) A detailed image of the PIA setup. b) Sample holder for full DSSC PIA studies. Note- the laser and mirror are enclosed in a housing to eliminate any extraneous light. .... 218

Figure 6.2 a) PIA of a complete DSSC containing a TiO<sub>2</sub> filmed sensitized with the D35cpdt interfaced with an inert acetonitrile electrolyte containing 0.1 M LiTFSI. b) Proposed three electrode setup for measuring PIA with fully constructed dye cells..... 219

Figure A6.1 <sup>1</sup>H NMR of [Co(PY<sub>5</sub>Me<sub>2</sub>)(NCS)](OTf) in acetonitrile-*d*<sub>3</sub>. .... 224

## LIST OF SCHEMES

Scheme 1.1 Diagram to describe outersphere electron-transfer. ....	21
Scheme A2.1 Derivation for isolating the observed pseudo-first order cross-exchange rate constant, $k_{obs}$ , under flooding conditions. <sup>23</sup> .....	49
Scheme A2.2 Derivation to fit raw absorbance in order to isolate $k_{obs}$ for cross-exchange reactions under pseudo-first order conditions. ....	50
Scheme A2.3 Derivation to verify at a given wavelength, where multiple species are absorbing, the change in only one species is being monitored in order to extract the observed pseudo-first order rate constant, $k_{obs}$ , for the cross-exchange reaction under flooding conditions. <sup>23</sup> .....	50
Scheme A2.4 Derivation describing the spectrophotometric determination of the cross-exchange equilibrium constant, $K_{12}$ . ....	52
Scheme 5.1 Splitting of the d-orbitals based on the hypothesized Jahn-Teller compression of the $[\text{Co}(\text{PY}_5\text{Me}_2)(\text{CN})]^+$ complex.....	184
Scheme 6.1 Synthetic route for creating new OSRSs using the pentacoordinated, $\text{PY}_5\text{Me}_2$ , ligand.....	210
Scheme A6.1 Mathematical theory of steady-state PIA measurements. <sup>27</sup> .....	222

## KEY TO ABBREVIATIONS

$\Delta A$	Absorbance Difference
$\Delta G^0$ or $\Delta G$	Driving Force or Free Energy of Reaction
$\Delta E$	Formal Potential Difference
$\Delta z$	Change in Charge
$\alpha_{dye}$	Dye Absorptivity
$\alpha_e$	Electrolyte Absorptivity
$\epsilon$	Static Dielectric Constant of Medium
$\epsilon_o$	Permittivity of Free Space
$\epsilon_{sol}$	Static Dielectric Constant of Solvent
$\epsilon_{TiO_2}$	Static Dielectric Constant of Anatase $TiO_2$
$\eta$	DSSC Device Efficiency
$\eta_{cc}$	Charge Collection Efficiency
$\eta_{inj}$	Injection Efficiency
$\eta_{LH}$	Light Harvesting Efficiency
$\eta_{reg}$	Regeneration Efficiency
$\lambda$	Wavelength
$\lambda_{\#\#}$	Total Reorganization Energy of a Self-Exchange Reaction
$\lambda_{D/D^+}$	Reorganization Energy of Dye Self-Exchange Reaction
$\lambda_{DR}$	Reorganization Energy of Dye and Redox Shuttle Cross-Exchange Reaction
$\lambda_{et}$	Reorganization Energy of Recombination

	Reaction
$\lambda_{in}$	Inner-sphere Reorganization Energy
$\lambda_o$	Outer-sphere Reorganization Energy
$\lambda_{o,TiO_2}$	Outer-sphere Reorganization Energy at a TiO <sub>2</sub> Interface
$\lambda_{R/R^+}$	Reorganization Energy of Redox Shuttle Self-Exchange Reaction
$\nu_n$	Vibrational Frequency Factor
$\nu$	Scan Rate
$\phi$	Light Intensity
$A$	Absorbance
$A_0$	Initial Absorbance
$A_\infty$	Equilibrium Absorbance
$A_D$	Absorbance of Sensitized Film
$a$	Radius of Reactant
AgTFSI	Silver Bis(trifluoromethane)sulfonamide
AgOTf	Silver Triflate
ALD	Atomic Layer Deposition
AM 1.5G	Air Mass Simulated 1 Sun Illumination
bpy	2,2'-bipyridine
bpyCl <sub>2</sub>	4,4'-dichloro-2,2'-bipyridine
bpyPY4	6,6'-bis(1,1-di(pyridin-2-yl)ethyl)-2,2'-bipyridine
BS	Back Side
((C <sub>8</sub> H <sub>16</sub> CH <sub>3</sub> ) <sub>2</sub> bpy)	4,4'-dinonyl-2,2'-bipyridine

cb	Conduction Band
CdTe	Cadmium Telluride
CIGS	Copper Indium Gallium Selenide
Cu	Copper
CV	Cyclic Voltammetry
<i>d</i>	Film Thickness
D35cpdt	3-{6-{4-[bis(2',4'-dibutyloxybiphenyl-4-yl)amino-]phenyl}-4,4-dihexyl-cyclopenta-[2,1-b:3,4-b']dithiophene-2-yl}-2-cyanoacrylic acid
dcbpy	4,4'-dicarboxy-2,2'-bipyridine
dmbpy	6,6'-dimethyl-2,2'-bipyridine
dmp	2,9-dimethylphenanthroline or Neocuproine
DSSC	Dye-Sensitized Solar Cell
<i>E</i>	Potential or Applied Voltage
<i>E<sup>o</sup></i>	Formal Reduction Potential
<b>E<sub>cb</sub></b>	Energy of the Conduction Band
<i>E<sub>f</sub></i>	Fermi Level or Fermi Energy
<i>E<sub>f,0</sub></i>	Fermi Level at no Bias
<i>E<sub>g</sub></i>	Band Gap
EIS	Electrochemical Impedance Spectroscopy
Eq.	Equation
<i>F</i>	Faraday's Constant
<i>f</i>	Non-linear Correction Term
Fc/Fc <sup>+</sup>	Ferrocene/Ferrocenium

Fe	Iron
<i>FF</i>	Fill Factor
FS	Front Side
FTO	Fluorine Doped Tin Oxide
<i>hν</i>	Light Excitation
<i>-hν</i>	Dye Relaxation
HOMO	Highest Occupied Molecular Orbital
HS	High Spin
HTM	Hole Transport Material
<i>I</i>	Ionic Strength
I	Current
$I_3^-/I^-$	Triiodide/Iodide
IPCE	Incident Photon to Current Efficiency
ITO	Tin Doped Indium Oxide
<i>J</i>	Current Density
J	Coupling Constant
<i>J<sub>sc</sub></i>	Short Circuit Current Density
<i>K<sub>##</sub></i>	Equilibrium Constant of Cross-Exchange Reaction
<i>K<sub>DR</sub></i>	Equilibrium Constant of Dye and Redox Shuttle Cross-Exchange Reaction
<i>k<sub>##</sub></i>	Rate Constant for Respective Self-Exchange and/or Cross-Exchange Reactions
<i>k<sub>b</sub></i>	Boltzmann's Constant
<i>k<sub>D/D+</sub></i>	Dye Self-exchange Rate Constant

$k_{DR}$	Dye and Redox Shuttle Cross-Exchange Rate Constant
$k_{et,max}$	Rate Constant at Optimal Exoergicity
$k_{obs}$	Observed Pseudo-First Order Rate Constant
$k_{R/R+}$	Redox Shuttle Self-exchange Rate Constant
$k_{rec,R+}$	Rate Constant for Recombination to the Oxidized Redox Shuttle
$k_{rec,D+}$	Rate Constant for Dye Recombination
$k_{reg}$	Regeneration Rate Constant
$L_n$	Diffusion Length of Electron
LHE	Light Harvesting Efficiency
LiOTf	Lithium Triflate
LiTFSI	Lithium Bis(trifluoromethane)sulfonamide
LS	Low Spin
LUMO	Lowest Unoccupied Molecular Orbital
MeCN	Acetonitrile
N3	Cis-bis(isothiocyanato)bis(2,2'-bipyridyl-4,4'-dicarboxylato)ruthenium(II)
N719	Di-tetrabutylammonium Cis-bis(isothiocyanato)bis(2,2'-bipyridyl-4,4'-dicarboxylato)ruthenium(II)
$n$	Number of Electrons Transferred
$N_A$	Avagadro's Number
NCS	Isothiocyanate Ligand
NHE	Normal Hydrogen Electrode
Ni	Nickel

$(^1\text{H})$ NMR	(Proton) Nuclear Magnetic Resonance
$[n_s]$	Surface Electron Concentration of $\text{TiO}_2$
$n_{sol}$	Refractive Index of Solvent
$n_{\text{TiO}_2}$	Refractive Index of Anatase $\text{TiO}_2$
OCVD	Open Circuit Voltage Decay
OSRS	Outersphere Redox Shuttle
$\text{N}(\text{CH}_3)_2$	Dimethylamine
$P$	Porosity
$P_{in}$	Input Power
PCE	Power Conversion Efficiency
PIA	Photoinduced Absorption Spectroscopy
PMT	Photomultiplier Tube
PV	Photovoltaic
ptpy	2-(p-tolyl)pyridine
$\text{PY}_5\text{Me}_2$	2,6-bis(1,1-bis(2-pyridyl)ethyl)pyridine
$q$	Charge of an Electron
$R^2$	Goodness of Fit
$R$	Total Reflectance
$R$	Gas Constant
$[R]$ or $[R^+]$	Redox Shuttle Concentration or Oxidized Redox Shuttle Concentration
$r$	Separation Distance
$R_e$	Reactant Center-to-Center Separation Distance

$R_B$	Reflectance of Unsensitized Blank Cell
$R_D$	Reflectance of Sensitized Sample Cell
$R_{FTO}$	Reflectance of FTO with TiO <sub>2</sub> Blocking Layer
$R_{Pt}$	Reflectance of Platinized FTO
RSM	Rapid Scanning Monochromator
Ru	Ruthenium
Rxn.	Reaction
SCE	Saturated Calomel Electrode
SCN <sup>-</sup>	Thiocyanate
Si	Silicon
SrSnO <sub>3</sub>	Strontium Stannate
SrTiO <sub>3</sub>	Strontium Titanate
ss	Surface States
$T$	Temperature
$T_B$	Transmittance of Unsensitized Blank Cell
$T_D$	Transmittance of Sensitized Sample Cell
$T_E$	Transmittance of Electrolyte
$T_{FTO}$	Transmittance of FTO with TiO <sub>2</sub> Blocking Layer
$T_{Pt}$	Transmittance of Platinized FTO
$t$	Time
TBA	Tetrabutylammonium
TBAPF <sub>6</sub>	Tetrabutylammonium Hexafluorophosphate

TBP	4- <i>tert</i> -butylpyridine
TFSI	Bis(trifluoromethane)sulfonamide
TiO <sub>2</sub>	Titanium Dioxide
ttn	1,4,7-Trithiacyclononane
$U_{rec,R+}$	Recombination Rate
$V$	Applied Voltage
$V_{oc}$	Open Circuit Voltage
$W_{##}$	Work Term of Cross-Exchange Reaction
$w_{##}$	Work Associated with Self-exchange and/or Cross-exchange Reactions
Y123	3-{6-{4-[bis(2',4'-dihexyloxybiphenyl-4-yl)amino-]phenyl}-4,4-dihexyl-cyclopenta-[2,1-b:3,4-b']dithiophene-2-yl}-2-cyanoacrylic acid
$Z$	Frequency Factor
Z907	Cis-bis(isothiocyanato)(2,2'-bipyridyl-4,4'-dicarboxylato)(4,4'-di-nonyl-2'-bipyridyl)ruthenium(II)
$z_i$ or $z_j$	Charges of Reacting Species

# **Chapter 1. An Introduction to Dye-Sensitized Solar Cell Research**

## **1.1 Motivation for Renewable Energy Research**

“The most unequivocally important technological problems that we as a society face today is our global energy future.”<sup>1</sup> This speaks volumes as our global energy demands have become a major source of political, social, environmental and economic unrest throughout the world today. In a 2006 publication by Lewis and Nocera, the energy race coined “The TeraWatt Challenge” was brought to a head and the demand for renewable energy become blatantly clear.<sup>2</sup> It was noted in the same article that as of the turn of the 21<sup>st</sup> century the world energy consumption was around 13.5 TW/yr and was projected to more than double to 30 TW/yr by 2050. Such staggering predictions were based on modest estimates of population growth and annual gross domestic product increases. The major source of concern relative to these numbers, however, was the source of the energy supply. In 2001, 85% of the 13.5 TW of consumed energy was supplied by fossil fuel sources, with nearly equal parts coming from coal, oil and natural gas. Although fossil fuel sources are capable of sustaining the worlds increasing energy demands, with reserves projected to last hundreds of more years, the environmental cost of relying on these energy sources could be devastating. A repercussion of burning fossil fuels is the carbon dioxide (CO<sub>2</sub>) that is released into the atmosphere. Recent studies have shown a strong correlation between accumulated CO<sub>2</sub> emissions and the earth’s surface temperatures.<sup>3</sup> In tracking global climate change related to greenhouse gas emissions such as CO<sub>2</sub>, NASA has documented a ~25 ppm increase in CO<sub>2</sub> levels and a ~0.4°C increase in temperature since 2006.<sup>4</sup> Although the demand for alternatives to fossil fuels has been addressed as a major source of concern, they still comprise nearly 85% of our energy demands according to BP’s newest

statistical review on world energy.<sup>5</sup> This is frightening, as it has been estimated that climate change due to increases in CO<sub>2</sub> concentrations are irreversible for 1,000 years even after cessation.<sup>6</sup> As our energy demands continue to grow at an alarming rate (2016- 18.5 TW/yr)<sup>5</sup>, it is our job to find a disruptive technology that utilizes clean energy to stabilize CO<sub>2</sub> emissions as a result of our economic growth.

The primary carbon free or renewable energy sources are wind, tidal, hydroelectric, geothermal, biomass, nuclear and solar.<sup>1</sup> Although a small component of each renewable energy source might be necessary to accommodate our future energy needs, solar by itself is the only viably scalable source to meet such large-scale energy demands. More sunlight strikes the earth in one hour (120,000 TW) than all of the energy consumed in a single year (18.5 TW).<sup>1,7</sup> While this is a striking number, much of the earth (~73%) is covered in water, which provides an adjusted terrestrial global solar energy power potential of ~600 TW (A value still much larger than our energy demands). Assuming photovoltaic (PV) devices became a widely adapted technology, it has been estimated that 20 TW of energy could feasibly be produced by covering only 0.16% of land with 10% efficient devices.<sup>7</sup> With such a statement in mind, the question as to why PV technology has contributed only 1.3%<sup>5</sup> to the total global power generation should be raised? Although the technology is beginning to have a noticeable impact in terms of sources of power generation growth, the cost of this technology is still a concern. Given solar energy is intermittent and diffuse compared to fossil fuels, PV technology must rely on materials and manufacturing costs to be very inexpensive to make the technology economical.<sup>2</sup>

As of 2016, over 94% of the PV market was controlled by crystalline silicon, with ~ 5% contribution from thin film technologies such as CdTe and CIGS.<sup>8</sup> Silicon possesses

an advantage over the thin film technologies listed, as it is nontoxic, earth abundant and cheap. Although silicon itself is a cheap material, the manufacturing cost to produce crystalline silicon PVs is expensive and labor intensive. Manufactured single crystalline and polycrystalline silicon devices averaging ~14-23% power conversion efficiencies (PCEs) require 99.9999% purity.<sup>9</sup> Though the cost of producing silicon PVs continues to drop, as of the mid 2000s production costs ranged from \$0.25-\$0.65 per kWh, which is roughly 5 times higher than electricity produced by fossil fuels.<sup>7,9,10</sup> From a materials scientist perspective, the root of the high cost stems from the directionality and strength of silicon's covalent bonds, which makes it difficult to cut and requires high temperatures to process.<sup>9</sup> Another intrinsic problem with silicon is the materials ability to absorb light. Thick slabs of silicon (> 100 $\mu$ m) are necessary to efficiently harvest light. The brittle nature of the thick material requires a rigid support from heavy pieces of glass that add to the cost and limit the array of applications these devices can be used for. As we look to the future, it is necessary to find more economically viable photovoltaics to circumvent the high manufacturing costs of silicon PV technology. One alternative, which has the capability of utilizing cheap, earth abundant materials with high-throughput roll-to-roll printing, is dye-sensitized solar cells (DSSCs).

The ability of DSSCs to implement cheap materials over silicon photovoltaics stems from multiple components these devices use to separate the processes of charge generation, charge separation and charge collection. Through clever design, DSSCs make use of a wide band gap semiconductor material to transport electrons. They also utilize a dye, functionalized to the surface of the semiconductor, to harvest light and separate the exciton through injection of the electron into the semiconductor, as well as a liquid

electrolyte to shuttle holes to the counter electrode while the semiconductor transports injected electrons to the anode. Silicon PVs, however, rely on a single material to absorb light, separate the resulting excitons and transport charge to their respective contacts. The benefit of using a wide band gap semiconductor ( $E_g > 3$  eV) in DSSCs ensures that no excitation or hole generation occurs in the medium. This eliminates recombination within the material, which suppresses the performance of silicon photovoltaics. Thus, low quality and inexpensive materials can be used to produce efficient DSSCs. Another significant advantage to dye cells over silicon PVs is that it is a thin film technology. The high surface area mesoporous films developed for these systems only requires a few microns ( $\sim 5$ - $15$   $\mu\text{m}$ ) of material for traditional sensitizers to absorb all incident light. This is nearly an order of magnitude less material than that needed for silicon PVs. Lastly; DSSCs are also amenable to a multitude of modifications that can improve their performance. Since the device is integrated with a semiconductor material, sensitizer and redox electrolyte, each of these three components can be tuned to conduct fundamental studies, which can pave the way for device optimization and future commercialization.

## **1.2 Historical Development of DSSCs**

Dye-sensitization is a field of study that came to fruition from early silver halide studies, where, in 1887, Moser observed sensitization of a semiconductor under sub-band gap illumination while working with silver halides coated in erythrosine.<sup>11</sup> Over 40 years later, Gurney and Mott proposed the mechanism for dye-sensitization of a crystalline semiconductor involved electron-transfer from an excited state of the sensitizer into the conduction band of the semiconductor.<sup>12</sup> In 1968, Gerischer would corroborate the proposed electron-transfer mechanism as a result of conducting electrochemical studies

that produced current under illumination of dyes such as fluorescein and rose bengale interfaced with single crystal ZnO.<sup>13</sup> Upon excitation, enhanced photocurrents were observed for solutions containing the dissolved dyes compared those that did not, a phenomenon that could be modulated by turn the incident light on and off. This account could be viewed as the earliest photoelectrochemical cell. Shortly after, Gerischer also provided motivation for the development of dissolved redox shuttles as he and Tributsch observed that photocurrent, as a result of sensitization, could be increased by the addition of a reducing agent such as hydroquinone. The documented phenomena would be coined “supersensitization”.<sup>14</sup>

Very low photocurrents were observed for these early examples of photoelectrochemical cells. The reason for this observation was a due to setup of the system. For photocurrent to be generated, these cells required the dissolved sensitizer to diffuse to the surface of the semiconductor to inject electrons. As a result, the majority of the photoexcited dyes in the bulk solution would relax back down to its ground state before injection could occur. The short lifetime of the dyes compared to the timescale of diffusion only allowed a small fraction of those dyes to inject near the surface. To alleviate this problem, dyes were functionalized with substituents that would allow them to be anchored to the surface of the semiconductor. Osa and Fujihira provided the first example of covalently linking rhodamine B to TiO<sub>2</sub> and SnO<sub>2</sub> through the use of silyl groups.<sup>15,16</sup> While this was beneficial in mitigating the constraints of diffusion and providing efficient injection yields, low photocurrents for these cells were still measured due to poor light absorption of the monolayer of dye.

Use of transition metal sensitizers became a key step in developing the dye cells we are accustomed to fabricating today. Several initial reports of dye-sensitization using transition metal complexes implemented  $[\text{Ru}(\text{bpy})_3]^{2+}$  due to its well-defined properties. A key study carried out by Sutin and Clark revealed that the photocurrent of this complex tracked with light intensity as well as the absorption profile of the sensitizer.<sup>17</sup> To eliminate the diffusion constraints of  $[\text{Ru}(\text{bpy})_3]^{2+}$ , Goodenough et. al. functionalized carboxylic acid groups to the bpy ligand in order to anchor the dye to various semiconductor surfaces ( $\text{TiO}_2$ ,  $\text{SnO}_2$  and  $\text{SrTiO}_3$ ).<sup>17</sup> Unfortunately, the  $[\text{Ru}(\text{bpy})_2(\text{dcbpy})]^{2+}$  dye yielded poor internal conversion efficiencies and consequently small energy conversion efficiencies in attempts to carry out water electrolysis. The monolayer coverage of dye still plagued light absorption of these sensitizers, which resulted in low internal conversion efficiencies, and the sluggish reduction of the dye via electron-transfer from water hampered energy conversion efficiencies. A major breakthrough in dye-sensitization came in 1985 when Grätzel and co-workers used a polycrystalline anatase  $\text{TiO}_2$  electrode sensitized with  $[\text{Ru}(\text{bpy})_2(\text{dcbpy})]^{2+}$  and the aforementioned hydroquinone “supersensitizer”. The enhanced roughness (~100 fold) of the colloidal  $\text{TiO}_2$  nanoparticles led to external quantum efficiencies of over 40% under monochromatic illumination with injection yields as large as 60%.<sup>17</sup> Building upon this work, Grätzel *et. al.* further enhanced the roughness of the nanocrystalline  $\text{TiO}_2$  film, while also modifying the regenerating molecule from hydroquinone to  $\text{I}_3^-/\text{I}^-$ . The superior regeneration coupled with the higher surface area for dye coverage brought about incident photo-to-current efficiencies (IPCEs) of 70% and a power conversion efficiency of 12% under monochromatic light. While impressive, the major drawback to these photoelectrochemical cells came from the optical properties of

the dye. The wide optical gap of  $[\text{Ru}(\text{dcbpy})_3]^{2+}$  only allowed absorption of light out to  $\sim 550$  nm.<sup>18</sup> By utilizing a trimeric ruthenium cluster developed by Scandola *et. al.*,<sup>17</sup> to enhance optical absorption of the dye, along with the development of high surface area nanoporous film (roughness factor  $\sim 1000$ ), Grätzel was able to astoundingly produce PCEs over  $\sim 7$  % under 1 Sun conditions.<sup>19</sup> A comparison of the absorption profile to the collected IPCE suggested that the external quantum yields were optimized. Long-term stability measurements of the cells over a two-month span demonstrated over 5 million turnovers without degradation, which was a clear indication of feasibility for practical applications. Follow-up work resulted in modifications of the sensitizer to the now commonly used N3 dye and N719 dye. Optimized cells sustaining over 10 % PCEs were quickly obtained for the cells employing N3 with  $\text{I}_3^-/\text{I}^-$  and the electrolyte additive 4-*tert*-butylpyridine in acetonitrile.<sup>20</sup> Termed “The Grätzel cell”, this semiconductor ( $\text{TiO}_2$ ), dye (N3, N719, Z907, etc...), redox shuttle ( $\text{I}_3^-/\text{I}^-$ ) and non-aqueous solvent system (acetonitrile) became the basis for dye cell construction, the details of which will be described in the section below. Recent progress in developing one-electron outersphere redox shuttles (OSRSs) has provided the ability to circumvent the limitations of  $\text{I}_3^-/\text{I}^-$  and has afforded the opportunity to further enhance dye cell performance en route to becoming a competitive technology to silicon PVs.

### 1.3 Operating Principals of DSSCs

The main components and operating principals of a modern DSSC are outlined in Figure 1.1. A complete solar cell is comprised of a photoanode, a liquid electrolyte and a counter electrode. The photoanode consists of a transparent conductive glass substrate, generally FTO (fluorine doped tin oxide) or ITO (tin doped indium oxide), which is

functionalized with a compact thin film atop, known as a blocking layer, of the appropriate semiconductor oxide. During solar cell operation, the role of the blocking layer is critical as it acts to prevent the phenomena of shunting.<sup>21</sup> Doctor bladed over a patterned section of the blocking layer is a high surface area mesoporous film of semiconductor nanoparticles (~15-30 nm) that chemically matches the semiconductor oxide of the blocking layer underneath. To create a robust film, nanoparticles are annealed to the FTO substrate. A wide bandgap semiconductor, typically TiO<sub>2</sub> (~3.2 eV), is chosen and acts as a scaffold for the adsorption of a sensitizer to its surface as well as a material to transport electrons to the anode. The sensitizer is the key component to the photoanode, which provides the solar cell's photovoltaic properties. An ideal sensitizer absorbs light strongly in the visible and IR regions of the electromagnetic spectrum and has the proper energetics to inject electrons into the semiconductor material that it is anchored to. A detailed explanation of the charge-transfer processes involved in a DSSC will be discussed below. The sensitizer is required to not only operate synergistically with the semiconductor, but also with the redox shuttle of the liquid electrolyte permeating the pores of the semiconductor film. The primary purpose of the redox shuttle is to complete the circuit between the photoanode and counter electrode. It acts to provide electrons to oxidize dye, a process known as regeneration, and capture electrons at the counter electrode. The counter electrode is typically comprised of another transparent conductive glass substrate (FTO) coated by a thin layer of a catalyst (Pt) to facilitate charge-transfer. Other additives such as Li<sup>+</sup> salts and pyridine derivatives i.e. 4-tert-butylpyridine can be mixed into the electrolyte and have been known to modulate the energetics of the semiconductor's conduction band and/or passivate the surface of TiO<sub>2</sub>

by blocking active reductive sites for recombination.<sup>22,23</sup> The solvent of choice for the liquid electrolyte is typically acetonitrile.

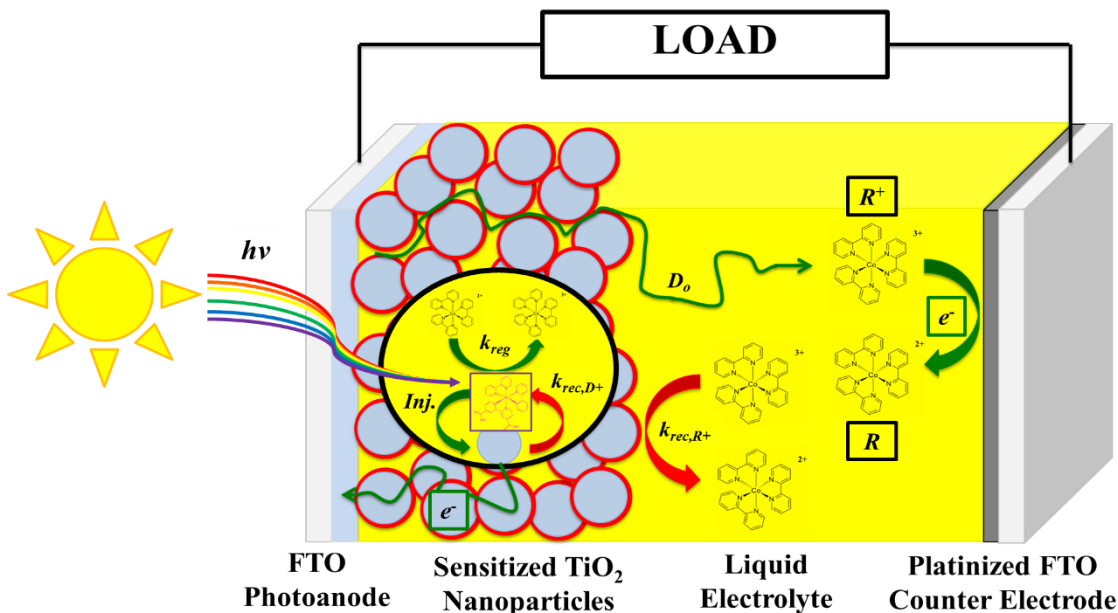


**Figure 1.1** Schematic of the basic components and operating principals of a DSSC.

The basic charge-transfer pathways involved in a DSSC are outlined in the relative energy diagram of Figure 1.2. Solar cell operation begins when light shining on the photoanode excites the sensitizer ( $h\nu$ ) anchored to the mesoporous semiconductor film. Upon excitation, the dye rapidly injects an electron into the conduction band of the semiconductor. The injected electron then diffuses through the extended states of the conduction band via a trapping and detrapping mechanism to be collected at the FTO substrate of the photoanode.<sup>24</sup> Extracted electrons at the FTO substrate act to do work on an external load before being collected at the counter electrode. Meanwhile, the oxidized dye on the semiconductor surface is regenerated ( $k_{\text{reg}}$ ) by a redox shuttle dissolved in the

liquid electrolyte. After regenerating the dye, the redox shuttle then diffuses back to the counter electrode to capture electrons that were pulled out of the system. Each of the electron-transfer pathways that were just described, Figure 1.2 (green arrows), include the positive pathways for charge separation and charge collection; however, there are a number of recombination pathways (red arrows) that limit the performance of DSSCs. The three pathways for recombination highlighted and discussed in more detail below include relaxation of the excited sensitizer ( $-h\nu$ ), back electron-transfer from the conduction band ( $cb$ ) or surface states ( $ss$ ) of the semiconductor to the oxidized dye ( $k_{cb,D^+}$  or  $k_{ss,D^+}$ ) as well as back electron-transfer from the conduction band ( $cb$ ) or surface states ( $ss$ ) of the semiconductor to the oxidized redox shuttle in solution ( $k_{cb,R^+}$  or  $k_{ss,R^+}$ ).

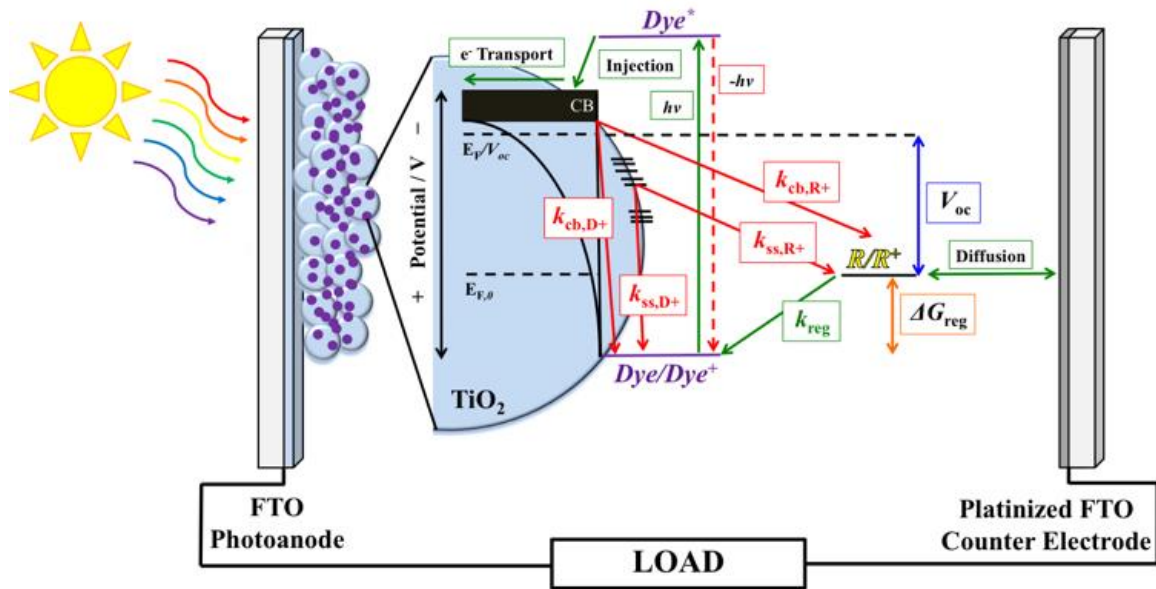


**Figure 1.2** Relative energy diagram of a DSSC and the various electron-transfer pathways associated with solar cell operation.

Of the recombination pathways described above and shown in Figure 1.2, relaxation or radiative/nonradiative recombination of the excited chromophore tends to be dismissed as the rate limiting process in determining DSSC device efficiency. The relaxation rate,  $-k_r$ , for the most common ruthenium sensitizers and/or organic dyes is on a time scale inferior to injection.<sup>23,25</sup> However, much of this is true only under short circuit conditions where the electron density, related to the Fermi level,  $E_f$ , is low within the semiconductor film, Figure 1.2. Under operating conditions or near open circuit where the electron density within the semiconductor nanoparticle is high, relaxation has been shown to be less than unity.<sup>26</sup> This can be attributed to the band edge movement of the semiconductor. As the Fermi level moves closer to the conduction band and the electron density increases, the conduction band tends to move toward more negative potentials. The band edge movement causes the density and distribution of conduction band states to move as well. This creates problems since the process of injection is highly dependent on the density and distribution of the acceptor states relative to the excited state (LUMO) of the dye. Most ruthenium and organic sensitizers have been well optimized energetically for proper injection; however, all optimizations are relative to a single material, TiO<sub>2</sub>, which is a major drawback for designing next generation solar cells. The desire to study new materials will be the focus of the future directions in Chapter 7. Other prominent examples of poor injection have resulted from modification of the chromophore. Use of more earth abundant elements such as iron (Fe) to replace ruthenium (Ru) has resulted in major injection problems stemming from fast relaxation of the excited electron into a quintet state below the conduction band of TiO<sub>2</sub>. Ligand modification is necessary to push this state

above the TiO<sub>2</sub> conduction band or new materials are need to be interfaced with these chromophores to ensure injection becomes quantitative.<sup>27</sup>

Recombination to the oxidized dye and oxidized redox shuttle are generally viewed as the primary kinetic bottlenecks in determining DSSC device efficiencies and will be a major focus of this dissertation. To alleviate dye recombination, the kinetics for regeneration must be faster than the dyes interception of electrons from the semiconductor. The branching ratio between dye recombination and dye regeneration dictates the regeneration efficiency in dye cells and is key to determining device performance. This in turn suggests that the dye and redox shuttle must work synergistically with one another to ensure efficient charge-transfer is carried out while recombination is retarded. If we consider the options for improving DSSC performance there appear to be are two primary pathways: (1) Utilizing broader absorbing dyes to increase the photocurrent ( $J_{sc}$ ) or (2) implementing more positive redox shuttles to increase the photovoltage ( $V_{oc}$ ), Equation (1.1). With the library of sensitizers that already exist today, identification of new redox shuttles will ultimately be necessary to achieve either goal.

$$\eta = \frac{J_{sc}V_{oc}FF}{P_{in}} \times 100\% \quad \text{Eq. (1.1)}$$

#### 1.4 Reliance on the I<sub>3</sub><sup>-</sup>/I<sup>-</sup> Electrolyte

Since the development of the Gratzel cell in the early 1990's, I<sub>3</sub><sup>-</sup>/I<sup>-</sup> has reigned as the champion redox shuttle for over 20 years.<sup>28-30</sup> DSSC efficiencies during this time quickly rose from a few percent to a record high 11%.<sup>30</sup> Stability measurements of these devices also suggested cell lifetimes would exceed 10 years under operational conditions.<sup>31</sup>

Although rapid success came as a result of utilizing this redox shuttle system, power conversion efficiencies (PCEs) for these DSSCs rapidly reached a glass ceiling and have remained stagnant to this day. Much of the success and limitations of the  $I_3^-/I^-$  electrolyte system stems from the sensitizers that the redox shuttle can be paired with.<sup>32,33</sup> Proper dye engineering is necessary for efficient regeneration given the shuttles complicated innersphere mechanism for charge-transfer.

Kinetic investigations as to the mechanism for regeneration using  $I_3^-/I^-$  yields an  $I^-$  bound intermediate to the oxidized sensitizer,  $[Dye^+ \cdots I^-]$ .<sup>32</sup> This innersphere mechanism for charge-transfer thus requires sensitizers with auxiliary ligands for  $I^-$  to bind to. Dyes such as N3,  $[Ru(dcbpy)_2(NCS)_2]$ , N719,  $[Ru(dcbpy)_2(NCS)_2](TBA)_2$ , and Z907,  $[Ru(dcbpy)((C_8H_{16}CH_3)_2bpy)(NCS)_2]$ , have achieved great success with  $I_3^-/I^-$  as the hole upon oxidation lies on the  $-NCS$  ligand to which  $I^-$  is able to bond to and regenerate.<sup>24</sup> DSSCs utilizing this dye-electrolyte combination sustain admirable performance ( $\sim 10\%$  PCE) due the ability of  $I_3^-/I^-$  to rapidly regenerate the oxidized sensitizer, while effectively retarding recombination to the oxidized electrolyte. As a result, large diffusion lengths of the electron ( $L_n$ ) are measured providing near unity charge collection efficiencies ( $\eta_{cc}$ ).<sup>34</sup> Efficient regeneration in these systems, however, comes at a large energy cost. The measured standard reduction potential for  $I_3^-/I^-$  is 0.35V vs. NHE, while the standard reduction potential for N3 is 1.1V vs. NHE.<sup>31</sup> This equates to  $\sim 0.75V$  of overpotential to drive the regeneration reaction. If half of this internal potential loss could be gained, it is predicted that device efficiencies could reach 15%.<sup>31</sup>

The need for such a large driving force sets an upper limit for the maximum attainable short circuit density ( $J_{sc}$ ) and open circuit voltage ( $V_{oc}$ ) based on the optical gap

of the dye and the inability to tune the potential of the redox shuttle. Since these systems have been well optimized, it is no wonder why DSSC device performances reached a plateau. Aside from intrinsic problems surrounding the energetics of the  $I_3^-/I^-$  electrolyte system, the shuttle is also corrosive and a competitive light absorber to the dye.<sup>35</sup> With so many eminent drawbacks, it has become clear that new redox shuttles are necessary to realize the full potential of DSSCs.

### 1.5 Device Integration of Outersphere Redox Shuttles

One-electron outersphere redox shuttles (OSRSs) have arisen as attractive alternatives to the  $I_3^-/I^-$  electrolyte system for two primary reasons. The first is that their mechanism for charge-transfer is much more simplistic. The math and basic concepts to describe outersphere electron-transfer reactions has already been solved using Marcus theory. The details of which will be described below and throughout the rest of this dissertation. Second, the redox potential, particularly for transition metal OSRSs, is highly tunable. By changing the ligand framework around the metal center, one can adjust the driving force for regeneration and recombination among various dye and redox shuttle pairs.<sup>36-39</sup> Use of Marcus theory and the ability to modify the redox shuttles potential provides a powerful route to conduct fundamental kinetic studies to understand charge-transfer within working DSSC devices.

Original attempts to integrate OSRSs into DSSCs led to very poor performing cells. The bottleneck to the success of these redox shuttles resulted from shunting and fast recombination from  $TiO_2$  to the oxidized redox shuttle.<sup>40,41</sup> Ferrocene/ferrocenium ( $Fc/Fc^+$ ) can be viewed as the first example of an OSRS used in DSSCs. Transient absorption studies revealed that efficient regeneration can be measured for Ferrocene when paired with the

Z907 dye, despite 0.3 eV less driving force compared to  $I_3^-/I^-$ , however, recombination to the ferrocenium is excessively fast, which minimizes the  $J_{sc}$  and  $V_{oc}$  of the cell.<sup>42,43</sup> By effectively passivating the FTO surface and any exposed  $TiO_2$  through the use of insulating siloxanes, Gregg *et. al.* was able to demonstrate that  $Fc/Fc^+$  could be used, at least to some extent, as a redox shuttle.<sup>40</sup> Atomic layer deposition (ALD) has also been used to passivate the FTO surface and block the pathway for shunting. Conformal layers of  $TiO_2$  can be deposited on FTO to create a thin film that is pinhole free. To further improve performance a thin insulating layer of aluminum oxide,  $Al_2O_3$ , can also be deposited between the mesoporous semiconductor and the sensitizer and has been shown to drastically improve the performance of DSSCs utilizing  $Fc/Fc^+$  derivatives by blocking back electron-transfer from the  $TiO_2$  film. Importantly, although cell performances were low, Hamann *et. al.* demonstrated through these Ferrocene studies that recombination tracked with driving force by modifying the potential of Ferrocene through the use of adding electron withdrawing groups to the cyclopentadiene ring.<sup>41</sup> Although never intended to be a practical redox shuttle, much has been learned as a result of integrating  $Fc/Fc^+$  into DSSC systems. Years after these original studies, Daeneke *et. al.* was able to make a 7.5% device using Ferrocene.<sup>44</sup> Modification of the sensitizer was important to the success of these cells and for emerging OSRS systems as well. Use of an organic sensitizer with a large extinction coefficient allowed cells to be made with half the thickness of films sensitized with traditional ruthenium sensitizers ( $\sim 8.3 \mu m$ ). The steric bulk of the dye was also effective at passivating the  $TiO_2$  surface to inhibit recombination. The major downfall, however, of the Ferrocene system, is the sensitivity of the Ferrocenium to oxygen. All cells employing

these redox shuttles need to be meticulously fabricated and sealed inside a glovebox, which ultimately limit its practical use as an alternative redox shuttle to  $I_3^-/\Gamma^-$ .

Other interesting transition metal OSRSs of note have incorporated copper, nickel and ruthenium. Copper redox shuttles are interesting systems that have garnered much attention as of late.<sup>45,46</sup> Although copper redox shuttles can be competitive light absorbers to the dye, the ease of fabrication make them attractive systems to conduct fundamental studies. I will refrain from going into much too detail here, as they will be discussed as a future direction in Chapter 6; however, Hattori *et. al.*'s JACS publication in 2005 is a seminal paper for copper redox shuttle research.<sup>47</sup> A striking result that came out of this paper was that under low light conditions ( $20 \text{ mW/cm}^2$ )  $[Cu(dmp)_2]^{2+/+}$  sustained a higher  $V_{oc}$  than  $I_3^-/\Gamma^-$ . This result became a catalyst to re-evaluate copper years later. To rationalize the dye cell data, Hattori attempted to use Marcus theory and the measured self-exchange rate constants for the various copper redox shuttles to understand the trend in DSSC performance, however, based on recent studies, it seems Marcus theory may not apply to these unique systems. Nickel has also been incorporated in creating interesting alternative redox shuttles. The one-electron exchange from Ni(IV/III) in the Ni bis(dicarbollide) system has demonstrate fast and quantitative regeneration at low donor concentrations, as well as slow recombination kinetics upon conformational change from cis to trans during reduction; however, the complicated synthesis of the ligand is unfavorable for practical use.<sup>48</sup> Ruthenium OSRSs have also been employed in DSSCs for their promise of efficient regeneration at low overpotentials, along with the desire to obtain large  $V_{oc}$ 's. Indeed, Zhou has demonstrated cells achieving  $V_{oc}$ 's of 0.9 V; however, due to solubility constraints cell performance was low.  $[Ru(bpy)_3]^{2+}$  has been implemented for "single component" cells

that reached nearly 5 % efficiencies under low light conditions (0.1 Suns), but diffusion limitations coupled with solubility limitations stymied performance under 1 Sun conditions. In general, as a feasible OSRS for dye cells, most ruthenium OSRSs lack stability, solubility and the ability to be a non-competitive light absorber in solution.

Among all OSRSs studied to date, cobalt polypyridyl complexes have received the most attention as a promising class of OSRSs.<sup>36,43,49-54</sup> The attractive features of these complexes aside from their tunability is their ease of fabrication, long-term stability and weak light absorption properties within the visible region. Nusbaumer *et. al.* provided the first successful example of a cobalt polypyridyl complex,  $[\text{Co}(\text{dbbip})_2]^{3+/2+}$ , that was integrated into DSSCs. The comparable recombination kinetics to the then champion  $\text{I}_3^-/\text{I}^-$  electrolyte was an exciting result, which provided devices with ~2 % efficiencies. Much of this shuttles success was attributed to the dye to which it was paired to. Switching from N3 to a neutral sensitizer (Z316) provided enhanced performances and a prime example of the proper dye engineering necessary in attempting to synergistically balance regeneration and recombination via screening of the  $\text{TiO}_2$  interface. Though recombination at the interface was still rather fast, mass transport was noted as a problem as well. Nearly a year later, Sapp *et. al.* screened over 10 different cobalt polypyridyl complexes using commercially available ligands in an effort to determine, which complexes could match comparably to  $\text{I}_3^-/\text{I}^-$  mediated DSSCs.<sup>55</sup>  $[\text{Co}(\text{DTB})_3]^{3+/2+}$  exhibited external quantum efficiencies ~80 % as high as  $\text{I}_3^-/\text{I}^-$ . The benefit of this mediator would be realized later as a result from poorer electronic coupling and longer range charge-transfer to the dye due to the steric bulk of the ligand. Unfortunately, use of this mediator brings about large mass transport problems that either needed to be overcome by a solvent or counterion modification. Diffusion of this

redox shuttle system was determined to be an order of magnitude slower than  $I_3^-/I^-$ .<sup>56</sup> The first attempt to move away from using conventional dyes such as N3 or N719 in conjunction with cobalt OSRSs was carried out by Hamann and Klahr.<sup>33</sup> Variation of the N3 sensitizer to  $[Ru(bpy)_2(dcbpy)]^{2+}$ , which sustained a potential  $\sim 0.5V$  negative of N3, combined with concentration studies indicated that the homologous set of substituted cobalt tris(bipyridine) complexes was not regeneration limited. However, even with a thin tunneling layer ( $Al_2O_3$ ) deposited between the dye and  $TiO_2$  interface, recombination to these shuttles was concluded to be fast and rate limiting. Shortly after this account, a seminal paper was put out by Feldt et al. investigating the performance of cells utilizing  $[Co(bpy)_3]^{3+/2+}$  and  $[Co(phen)_3]^{3+/2+}$  in conjunction with two organic dyes D35 and D29, which provided staggering PCEs of nearly 7%.<sup>57</sup> Under the same principles that provided Ferrocene's successful integration into dye cells, this group used a bulky organic sensitizer to passivate the  $TiO_2$  surface, as well as cut the film thickness while still achieving quantitative light harvest. Such a motif sparked a surge of novel research that ultimately led to the champion device. A record efficiency of  $\sim 13\%$  was reported 2014 for DSSCs containing  $[Co(bpy)_3]^{3+/2+}$  and a Zinc porphyrin dye SM315.<sup>49</sup> Use of such D- $\pi$ -bridge-A dyes to provide long range separation of the hole from the  $TiO_2$  surface drove the success of these systems and has become a popular motif for producing highly efficient dye cells. In an attempt to build off of the success of cobalt tris(bipyridine) similarly tunable structural designs have been made to the ligand frame work to further increase device performance, but none have succeeded in surmounting  $[Co(bpy)_3]^{3+/2+}$ . Although inferior to  $[Co(bpy)_3]^{3+/2+}$ , work done by Bach and Long provided an interesting platform for the design of new OSRSs.<sup>58</sup> Use of a pentadentate ligand,  $PY_5Me_2$ , provided the opportunity

to functionalize the sixth coordination site of the cobalt metal center with common electrolyte additives such as TBP or NMBI providing complexes of the form:  $[\text{Co}(\text{PY}_5\text{Me}_2)(\text{X})]^{3+/2+}$  (X = TBP or NMBI). Performances as high as 9% were reached when using these shuttles with the organic sensitizer MK2. In Chapter 5 we seek to build off this work through modification of the exogenous ligand in an effort to synthesize new OSRSs to regenerate IR or near-IR absorbing sensitizers.

An interesting facet to using cobalt complexes as OSRSs in dye cells is the ability to tune not only the redox potential, but the spin-state of the complex as well. Such a synthetic handle provides power over dictating the kinetics of charge-transfer within these systems. Although high efficiencies are achieved in DSSCs utilizing  $[\text{Co}(\text{bpy})_3]^{3+/2+}$ , large driving forces are still necessary for efficient solar cell operation. Nearly 0.4 eV separates the redox potential of  $[\text{Co}(\text{bpy})_3]^{3+/2+}$  and SM315 in the record device.<sup>49</sup> Feldt et. al. carried out an investigation to determine the kinetics of regeneration on a series of cobalt polypyridyl complexes and found that at least 0.39 eV of driving force was necessary to achieve regeneration efficiencies of ~90%.<sup>36</sup> This large overpotential for efficient charge-transfer constrains improvement of device PCEs, Equation (1.1). The reason these systems require such a large overpotential for regeneration results from the complexes inherently sluggish kinetics. During oxidation from Co(II) to Co(III),  $[\text{Co}(\text{bpy})_3]^{3+/2+}$  and other similar polypyridyl cobalt complexes go through a spin change from HS ( $t_{2g}^5 e_g^2$ ) to LS ( $t_{2g}^6 e_g^0$ ). This spin change results in a large reorganization or structural change of the complex, which slows down charge-transfer. The large reorganization can be viewed as detrimental to the pathway for regeneration; however, it is beneficial for slowing recombination. By cleverly modifying the ligand around the cobalt metal center a change in spin-state of the

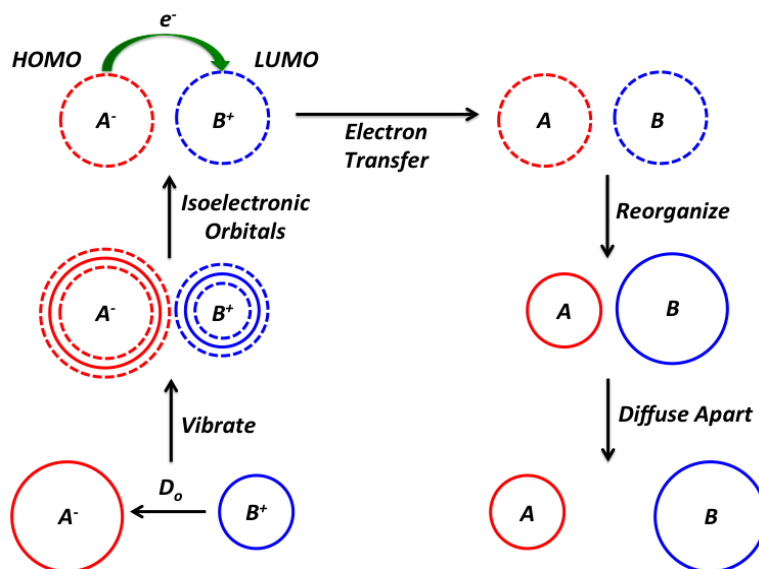
Co(II) can be realized. Forcing the complex to be LS in its reduced state, upon oxidation, is expected to produce faster electron-transfer kinetics due to the smaller change in antibonding occupancy i.e. LS Co(II) ( $t_{2g}^6 e_g^1$ ) to LS ( $t_{2g}^6 e_g^0$ ). The goal of designing new LS Co(II) is to minimize the driving force necessary for regeneration in hopes of improving device efficiencies. Balancing the kinetics of regeneration and recombination within the DSSC system is predicated on two primary components: reorganization energy and driving force. Marcus theory, as highlighted in detail below, provides predictive power to describe the kinetics of charge-transfer within the DSSC system through the use of these two parameters.

## **1.6 Modeling Recombination and Regeneration using the Principals of Marcus Theory**

The most challenging problem to overcome in DSSCs is the ability to optimize regeneration by way of a minimal overpotential ( $\leq 100$  meV) for electron-transfer, while also retarding recombination. To do so, there needs to be a quantitative handle on the charge-transfer rates associated with each of these two kinetic pathways. One of the key motivations for transitioning to OSRSs, as previously mentioned, is that Marcus theory can be applied to understand the electron-transfer within these DSSC systems.<sup>37,59,60</sup> Unlike the  $I_3^-/\Gamma$  electrolyte, which involves a complicated innersphere mechanism (i.e. a through bond or a chemical bridging interaction) for electron-transfer, the mechanism for electron-transfer is much more simplistic for OSRSs. As the name implies, OSRSs transfer charge based on an outersphere reaction, where electron-transfer relies on the close approach of the interacting molecules, which remain separate and intact during the charge-transfer event. The rate at which the electron hops from one molecule to the other is predicated on

the separation distance and electronic coupling of the two species. Scheme 1.1 describes the sequence of events before and after charge-transfer, while Figure 1.3 correlates these events as a function of free-energy change.

**Scheme 1.1** Diagram to describe outersphere electron-transfer.



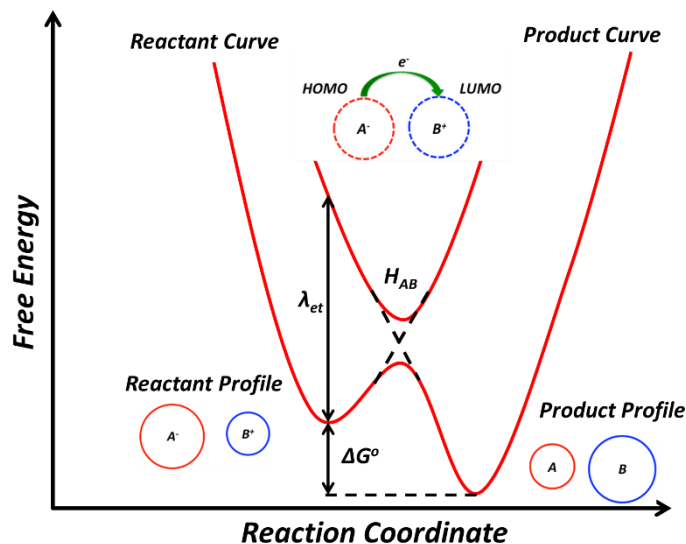


**Figure 1.3** Potential energy curves of the reactants and products for an outersphere electron-transfer reaction as a function of reaction coordinate.<sup>61</sup>

Marcus theory seeks to describe the charge-transfer event illustrated in Scheme 1.1 by assuming that the two reacting species are a set of harmonic oscillators in solution. As the reacting pair diffuses to one another, they vibrate (expand and contract) in such a way that the HOMO of the donor becomes isoelectronic with the LUMO of the acceptor, where upon electron-transfer occurs. The events leading up to and after electron-transfer requires energy for both the innersphere (i.e. bond length or bond angle changes) of the molecules to reorganize,  $\lambda_i$ , as well as the outersphere (i.e. solvent) to reorganize,  $\lambda_o$ . The sum of these energies make up the total reorganization energy for charge-transfer,  $\lambda_{et}$ :  $\lambda_{et} = \lambda_{in} + \lambda_o$ . To describe in full the kinetics associated with the charge-transfer process, Marcus theory models the coupling ( $H_{AB}$ ), total reorganization energy ( $\lambda_{et}$ ) and driving force for electron-transfer ( $\Delta G^o$ ) using modified Arrhenius theory, Equations (1.2) and (1.3).<sup>19-21</sup>

$$k_{et} = k_{et,max} e^{-(\Delta G^o + \lambda_{et})^2 / 4\lambda k_b T} \quad \text{Eq. (1.2)}$$

$$k_{et,max} = \frac{2\pi}{\hbar} H_{AB}^2 \frac{1}{(4\pi\lambda_{et}RT)^{1/2}} \quad \text{Eq. (1.3)}$$

Although Equation (1.2) is generally used to describe homogeneous electron-transfer reactions, it can also be used to describe heterogeneous charge-transfer events such as recombination in DSSCs. By determining the formal potential of the redox shuttle and/or dye, along with their respective reorganization energies, one can determine the rate constants for interfacial charge transfer at any given applied bias within the cell. The free energy,  $-ΔG^o$ , for back electron-transfer being the potential difference between the electronic states (i.e. conduction band or surface states), Figure (1.2), of the semiconductor and the formal potentials of either the redox shuttle or dye. Determination of the formal potential for either the dye or redox shuttle can be measured simply by CV measurements; the redox shuttle by solution based measurements and the dye by anchoring it directly to a conductive substrate. The more daunting task is determining the reorganization energies of these complexes, a challenge that I will focus of the ensuing chapters.

Elucidation of the dye and redox shuttle reorganization energies are very important because they not only provide information regarding recombination kinetics, but they can also offer insight as to the kinetics for regeneration. For example, if we assume Figure 1.3 above describes an electron-transfer event such as regeneration in a DSSC. Such a charge-transfer event between the two different chemically distinct species i.e. dye and redox shuttle can be described as a cross-exchange reaction.<sup>43</sup> The total reorganization energy for that reaction,  $\lambda_{DR}$ , is equal to the sum of the self-exchange reorganization energies of each individual molecule:  $\lambda_{DR} = \lambda_{D/D^+} + \lambda_{R/R^+}$ . (Note- A self-exchange reaction is an electron-transfer reaction between two chemically identical species differing only in

oxidation state. The free energy for such a reaction is equal to zero and the  $\Delta G^0$  term of Equation (1.2) drops out providing the relationship between the self-exchange rate constant and the total reorganization energy for the self-exchange reaction.) Coupling Equation (1.2) with the relationship describing the total reorganization energy for a cross-exchange reaction,  $\lambda_{DR}$ , provides the well-known Marcus cross-relation, Equation (1.4):<sup>61,65</sup>

$$k_{reg} \cong \sqrt{k_{(D/D^+)k_{(R/R^+)K_{D/R}}} \quad \text{Eq. (1.4)}$$

where the rate constant for regeneration,  $k_{reg}$ , is proportional to the self-exchange rate constants for the dye,  $k_{D/D^+}$ , and redox shuttle,  $k_{R/R^+}$ , as well as the equilibrium constant for the reaction,  $K_{DR}$ . As you can see, the Marcus cross-relation links the cross-exchange rate constant to the free energy or driving force for the reaction and the individual self-exchange rate constants of the reacting species. Therefore, knowledge of the self-exchange rate constants,  $k_{D/D^+}$  and  $k_{R/R^+}$ , and consequently the self-exchange reorganization energies of the dye and redox shuttle should provide important information regarding the rates of regeneration. Since  $k_{reg}$  is directly proportional to  $k_{R/R^+}$ , we have looked to synthesize fast-exchanging cobalt redox shuttles to exploit this relation through manipulation of the metal center's spin-state. The hope is that the faster self-exchange rate constant will provide quantitative regeneration at minimal driving forces. Motivation for fast exchange kinetics are evident as we look at its relationship between electron-transfer,  $k_{et}$ , and the driving force of the reaction,  $-\Delta G^0$ , Figure 1.4. A smaller driving force for electron-transfer tends to slow the kinetics of the reaction due to the larger induced activation energy. To enhance electron-transfer within the Marcus normal region, such as the regeneration reaction,

smaller reorganization energies and consequently larger self-exchange rate constants are necessary for the redox shuttle to increase  $k_{et}$  or  $k_{reg}$ , Figure 1.4.

It stands to reason that a delicate balance, as we will see in the coming chapters, is necessary for optimizing the reactions of regeneration and recombination. While faster self-exchanging redox shuttles tend to optimize the pathway for regeneration they also tend to be plagued by fast recombination i.e. ferrocene and ruthenium redox shuttles described above. Even when the inverted region can be reached for the recombination reactions ( $\Delta G^o = E_{cb} - E^o_{R/R+}$ ), Figure 1.4, DSSCs still tend to perform poorly as the regime for electron-transfer changes from conduction band recombination to predominately surface state recombination.<sup>59</sup> In the coming chapters we will attempt to reconcile the problems associated with recombination and regeneration through the design of new OSRSs. The desire is to provide strategies for designing next generation DSSCs that have the ability to compete with commercially available silicon PVs and up and coming Perovskite solar cells.

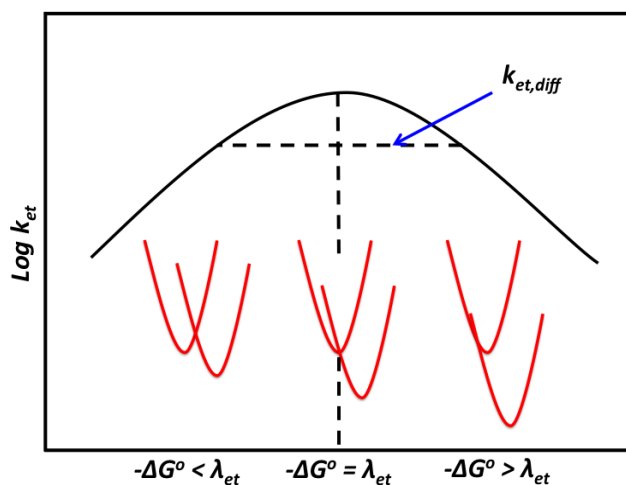


**Figure 1.4** Plot demonstrating the relationship between the electron-transfer rate constant and the driving force for an electron-transfer reaction according to Marcus theory. Note in the Marcus normal region  $-\Delta G^o < \lambda_{et}$  where as in the Marcus inverted region  $-\Delta G^o > \lambda_{et}$ .<sup>64</sup>

## 1.7 Dissertation Overview

In terms of defining the kinetics of regeneration and recombination in DSSCs, it is clear, through the use of Marcus theory, that the identity of the dye and redox shuttle's self-exchange rate constants are critical to understanding the kinetics for electron-transfer. As a result, this dissertation will discuss our results and conclusions for a variety of new cobalt OSRSs that have been subject to kinetic analysis in relation to their self-exchange rate constants and DSSC device performances upon integration. In the design of new one-electron OSRSs, a general synthetic motif that we have exploited is the design of LS Co(II) complexes in an effort to optimize the pathway for regeneration. We rationalized that the transition from LS Co(II) to LS Co(III) upon oxidation would elicit fast self-exchange kinetics that would ultimately enhance the kinetics of regeneration compared to commonly used HS Co(II) complexes used in the literature. To isolate the self-exchange rate constants of newly designed OSRSs, Chapter 2 discusses the methodology I have put together to determine these values using stopped-flow spectroscopy. Using stopped-flow and the methodology outlined in Chapter 2, Chapter 3 investigates the self-exchange kinetics of a LS Co(II) complex,  $[\text{Co}(\text{tten})_2]^{2+}$ , and the current champion redox shuttle HS Co(II) complex,  $[\text{Co}(\text{bpy})_3]^{2+}$ . Modeling of external quantum yield measurements coupled with the measured self-exchange rate constants provided insight as to the regeneration efficiencies,  $\eta_{reg}$ , and charge collection efficiencies,  $\eta_{cc}$ , related to the diffusion lengths,  $L_n$ , of electrons, in the two different systems. After concluding that DSSCs utilizing  $[\text{Co}(\text{bpy})_3]^{2+}$  and the D35cpdt dye are regeneration limited, a tandem electrolyte containing  $[\text{Co}(\text{bpy})_3]^{2+}$  and a newly designed Co(IV/III) OSRS,  $[\text{Co}(\text{ptpy})_3]^{+/0}$ , is implemented in Chapter 4 to alleviate such regeneration limitations. Before integration into the cell, the

self-exchange rate constant for  $[\text{Co}(\text{ptpy})_3]^{+/0}$  was determined and provided the first example of a self-exchange rate constant measured for a molecular Co(IV/III) OSRS at room temperature. Realizing the limitations of a tandem electrolyte in Chapter 4, we take on a new direction for improving device performance in Chapter 5 by creating a new LS Co(II) OSRS,  $[\text{Co}(\text{PY}_5\text{Me}_2)(\text{CN})]^+$ , with a much more negative redox potential than  $[\text{Co}(\text{tten})_2]^{2+}$ . A full characterization of the complex is carried out, which leads to our understanding of the complexes instability in solution. To avoid degradation in solution, we envision using the complex as a solid-state hole conductor for future DSSC applications. In closing, Chapter 6 will be devoted to discussing the future directions of DSSCs which build upon the knowledge gained from this dissertation and the exciting research being carried out in our lab today.

## **REFERENCES**

## REFERENCES

1. Lewis, N. S. Powering the Planet. *MRS Bull.* **2007**, 32 (10), 808–820.
2. Lewis, N. S.; Nocera, D. G. Powering the Planet: Chemical Challenges in Solar Energy Utilization. *Proc. Natl. Acad. Sci. U. S. A.* **2006**, 103 (43), 15729–15735.
3. Hoffert, M. I.; Caldeira, K.; Jain, A. K.; Haites, E. F.; Harvey, L. D. D.; Potter, S. D.; Schlesinger, M. E.; Schneider, S. H.; Watts, R. G.; Wigley, T. M. L.; et al. Energy Implications of Future Stabilization of Atmospheric CO<sub>2</sub> Content. *Nature* **1998**, 395 (6705), 881–884.
4. Global Climate Change: Vital Signs of the Planet, <https://climate.nasa.gov/>, (Accessed December 2017).
5. BP Statistical Review of World Energy June 2017, <https://www.bp.com/en/global/corporate/energy-economics/statistical-review-of-world-energy.html>, (accessed December 2017).
6. Solomon, S.; Plattner, G.-K.; Knutti, R.; Friedlingstein, P. Irreversible Climate Change due to Carbon Dioxide Emissions. *Proc. Natl. Acad. Sci. U. S. A.* **2009**, 106 (6), 1704–1709.
7. Lewis, N. S.; Crabtree, G.; Nozik, A. J.; Wasielewski, M. R.; Alivisatos, P. Basic Research Needs for Solar Energy Utilization. *Basic Energy Sci. Work. Sol. Energy Util.* **2005**, 276.
8. IEA: Trends 2016 in Photovoltaic Applications, <http://www.iea-pvps.org/index.php?id=3>, (accessed December 2017).
9. Tao, M. Inorganic Photovoltaic Solar Cells: Silicon and Beyond. *Electrochem. Soc. Interface* **2008**, 17 (4), 30–35.
10. Slaoui, A.; Collins, R. T. Advanced Inorganic Materials for Photovoltaics. *MRS Bull.* **2007**, 32 (3), 211–218.
11. Moser, J. Notiz Über Verstärkung Photoelektrischer Ströme Durch Optische Sensibilisierung. *Monatsh. Chem.* **1887**, 8 (1), 373.
12. Mott, N. F. On the Absorption of Light by Crystals. *Proc. Roy. Soc. London* **1938**, 167 (930), 384–391.
13. Mandal, D.; Hamann, T. W. Band Energies of Nanoparticle Semiconductor Electrodes Determined by Spectroelectrochemical Measurements of Free Electrons. *Phys. Chem. Chem. Phys.* **2015**, 17 (17), 11156–11160.

14. Tributsch, H. G. und H. Elektrochemische Untersuchungen Zur Spektralen Sensibilisierung von ZnO-Einkristallen. *Ber. Bunsenges. Phys. Chem.* **1968**, *72*, 437–445.
15. Fujihira, M.; Ohishi, N.; Osa, T. Photocell Using Covalently-Bound Dyes on Semiconductor Surfaces. *Nature* **1977**, *268* (5617), 226–228.
16. TETSUO, OSA; MASAMICHI, F. Photocell Using Covalently-Bound Dyes on Semiconductor Surfaces. *Nature* **1976**, *264*, 349–350.
17. Clark, W. D. K.; Sutin, N. Spectral Sensitization of N-Type TiO<sub>2</sub> Electrodes by Polypyridineruthenium(II) Complexes. *J. Am. Chem. Soc.* **1977**, *99* (14), 4676–4682.
18. Vlachopoulos, N.; Liska, P.; Augustynski, J.; Graetzel, M. Very Efficient Visible Light Energy Harvesting and Conversion by Spectral Sensitization of High Surface Area Polycrystalline Titanium Dioxide Films. *J. Am. Chem. Soc.* **1988**, *110* (4), 1216–1220.
19. Oregan, B.; Gratzel, M. A Low-Cost, High-Efficiency Solar-Cell Based on Dye-Sensitized Colloidal TiO<sub>2</sub> Films. *Nature* **1991**, *353* (6346), 737–740.
20. Nazeeruddin, M. K.; Kay, A.; Rodicio, I.; Humphry-Baker, R.; Müller, E.; Liska, P.; Vlachopoulos, N.; Grätzel, M. Conversion of Light to Electricity by Cis-X<sub>2</sub>Bis (2,2'-Bipyridyl-4,4'-Dicarboxylate) Ruthenium (II) Charge-Transfer Sensitizers (X = Cl<sup>-</sup>, Br<sup>-</sup>, I<sup>-</sup>, CN<sup>-</sup>, and SCN<sup>-</sup>) on Nanocrystalline TiO<sub>2</sub> Electrodes. *J. Am. Chem. Soc.* **1993**, *115* (14), 6382–6390.
21. Li, F.; Jennings, J. R.; Wang, Q. Determination of Sensitizer Regeneration Efficiency in Dye-Sensitized Solar Cells. *ACS Nano* **2013**, *7* (9), 8233–8242.
22. Yang, X.; Zhang, S.; Zhang, K.; Liu, J.; Qin, C.; Chen, H.; Islam, A.; Han, L. Coordinated Shifts of Interfacial Energy Levels: Insight into Electron Injection in Highly Efficient Dye-Sensitized Solar Cells. *Energy Environ. Sci.* **2013**, *6* (12), 3637–3645.
23. Koops, S. E.; Regan, B. C. O.; Barnes, P. R. F.; Durrant, J. R. Parameters Influencing the Efficiency of Electron Injection in Dye-Sensitized Solar Cells. *J. Am. Chem. Soc.* **2009**, *131* (13), 4808–4818.
24. Hagfeldt, A.; Boschloo, G.; Sun, L.; Kloo, L.; Pettersson, H. Dye-Sensitized Solar Cells. *Chem. Rev.* **2010**, *110* (11), 6595–6663.
25. Akın, S.; Açıkgöz, S.; Gülen, M.; Akyürek, C.; Sönmezoglu, S. Investigation of the Photoinduced Electron Injection Processes for Natural Dye-Sensitized Solar Cells: The Impact of Anchoring Groups. *RSC Adv.* **2016**, *6* (88), 85125–85134.
26. Tachibana, Y.; Haque, S. A.; Mercer, I. P.; Moser, J. E.; Klug, D. R.; Durrant, J. R. Modulation of the Rate of Electron Injection in Dye-Sensitized Nanocrystalline TiO<sub>2</sub> Films by Externally Applied Bias. *J. Phys. Chem. B* **2001**, *105* (31), 7424–7431.

27. Harlang, T. C. B.; Liu, Y.; Gordivska, O.; Fredin, L. A.; Jr, C. S. P.; Huang, P.; Chábera, P.; Kjaer, K. S.; Mateos, H.; Uhlig, J.; et al. Iron Sensitizer Converts Light to Electrons with 92% Yield. *Nat. Chem.* **2015**, *7* (11), 883–889.
28. Gratzel, M. Recent Advances in Sensitized Mesoscopic Solar Cells. *Acc. Chem. Res.* **2009**, *42* (11), 1788–1798.
29. Nazeeruddin, M. K.; Pechy, P.; Renouard, T.; Zakeeruddin, S. M.; Humphry-Baker, R.; Comte, P.; Liska, P.; Cevey, L.; Costa, E.; Shklover, V.; et al. Engineering of Efficient Panchromatic Sensitizers for Nanocrystalline TiO<sub>2</sub>-Based Solar Cells. *J. Am. Chem. Soc.* **2001**, *123* (8), 1613–1624.
30. CHIBA, Y.; ISLAM, A.; WATANABE, Y.; KOMIYA, R.; KOIDE, N.; HAN, L. Dye-Sensitized Solar Cells with Conversion Efficiency of 11.1%. *Japanese J. Appl. Physics, Part 2 Lett.* **2006**, *45* (25), 638–640.
31. Boschloo, G.; Hagfeldt, A. Characteristics of the Iodide / Triiodide Redox Mediator in Dye-Sensitized Solar Cells. *Acc. Chem. Res.* **2009**, *42* (11), 1819–1826.
32. Clifford, J. N.; Palomares, E.; Nazeeruddin, K.; Gra, M.; Durrant, J. R. Dye Dependent Regeneration Dynamics in Dye Sensitized Nanocrystalline Solar Cells : Evidence for the Formation of a Ruthenium Bipyridyl Cation / Iodide Intermediate. *J. Phys. Chem. C* **2007**, *111* (17), 6561–6567.
33. Klahr, B. M.; Hamann, T. W. Performance Enhancement and Limitations of Cobalt Bipyridyl Redox Shuttles in Dye-Sensitized Solar Cells. *J. Phys. Chem. C* **2009**, *113* (31), 14040–14045.
34. Jennings, J. R.; Liu, Y.; Wang, Q. Efficiency Limitations in Dye-Sensitized Solar Cells Caused by Inefficient Sensitizer Regeneration. *J. Phys. Chem. C* **2011**, *115* (30), 15109–15120.
35. Hamann, T. W. The End of Iodide ? Cobalt Complex Redox Shuttles in DSSCs. *Dalt. Trans.* **2012**, *41* (11), 3111–3115.
36. Feldt, S. M.; Lohse, P. W.; Kessler, F.; Nazeeruddin, M. K.; Gratzel, M.; Boschloo, G.; Hagfeldt, A. Regeneration and Recombination Kinetics in Cobalt Polypyridine Based Dye-Sensitized Solar Cells, Explained Using Marcus Theory. *Phys. Chem. Chem. Phys.* **2013**, *15* (19), 7087–7097.
37. Xie, Y.; Baillargeon, J.; Hamann, T. W. Kinetics of Regeneration and Recombination Reactions in Dye-Sensitized Solar Cells Employing Cobalt Redox Shuttles. *J. Phys. Chem. C* **2015**, *119* (50), 28155–28166.
38. Baillargeon, J.; Xie, Y.; Hamann, T. W. Bifurcation of Regeneration and Recombination in Dye-Sensitized Solar Cells via Electronic Manipulation of Tandem Cobalt Redox Shuttles. *ACS Appl. Mater. Interfaces* **2017**, *9* (39), 33544–33548.

39. Ondersma, J. W.; Hamann, T. W. Recombination and Redox Couples in Dye-Sensitized Solar Cells. *Coord. Chem. Rev.* **2013**, *257* (9–10), 1533–1543.
40. Gregg, B. A.; Pichot, F.; Ferrere, S.; Fields, C. L. Interfacial Recombination Processes in Dye-Sensitized Solar Cells and Methods To Passivate the Interfaces. *J. Phys. Chem. B* **2001**, *105* (7), 1422–1429.
41. Hamann, T. W.; Farha, O. K.; Hupp, J. T. Outer-Sphere Redox Couples as Shuttles in Dye-Sensitized Solar Cells . Performance Enhancement Based on Photoelectrode Modification via Atomic Layer Deposition. *J. Phys. Chem. C* **2008**, *112* (49), 19756–19764.
42. Cazzanti, S.; Caramori, S.; Argazzi, R.; Elliott, C. M.; Bignozzi, C. A.; Chimica, D.; Uni, V.; Borsari, V. L. Efficient Non-Corrosive Electron-Transfer Mediator Mixtures for Dye-Sensitized Solar Cells. *J. Am. Chem. Soc.* **2006**, *128* (31), 9996–9997.
43. Hamann, T. W.; Ondersma, J. W. Dye-Sensitized Solar Cell Redox Shuttles. *Energy Environ. Sci.* **2011**, *4* (2), 370.
44. Daeneke, T.; Kwon, T. H.; Holmes, A. B.; Duffy, N. W.; Bach, U.; Spiccia, L. High-Efficiency Dye-Sensitized Solar Cells with Ferrocene-Based Electrolytes. *Nat. Chem.* **2011**, *3* (3), 211–215.
45. Freitag, M.; Giordano, F.; Yang, W.; Pazoki, M.; Hao, Y.; Zietz, B.; Grätzel, M.; Hagfeldt, A.; Boschloo, G. Copper Phenanthroline as a Fast and High-Performance Redox Mediator for Dye-Sensitized Solar Cells. *J. Phys. Chem. C* **2016**, *120* (18), 9595–9603.
46. Li, J.; Yang, X.; Yu, Z.; Gurzadyan, G. G.; Cheng, M.; Zhang, F.; Cong, J.; Wang, W.; Wang, H.; Li, X.; et al. Efficient Dye-Sensitized Solar Cells with [Copper(6,6'-Dimethyl-2,2'-bipyridine)<sub>2</sub>]<sup>2+/1+</sup> Redox Shuttle. *RSC Adv.* **2017**, *7* (8), 4611–4615.
47. Hattori, S.; Wada, Y.; Yanagida, S.; Fukuzumi, S. Blue Copper Model Complexes with Distorted Tetragonal Geometry Acting as Effective Electron-Transfer Mediators in Dye-Sensitized Solar Cells. *J. Am. Chem. Soc.* **2005**, *127* (26), 9648–9654.
48. Li, T. C.; Spokoyny, A. M.; She, C.; Farha, O. K.; Mirkin, C. a; Marks, T. J.; Hupp, J. T. Ni (III)/(IV) Bis(dicarbollide) as a Fast , Noncorrosive Redox Shuttle for Dye-Sensitized Solar Cells. *J. Am. Chem. Soc.* **2010**, *132* (13), 4580–4582.
49. Mathew, S.; Yella, A.; Gao, P.; Humphry-Baker, R.; Curchod, B. F. E.; Ashari-Astani, N.; Tavernelli, I.; Rothlisberger, U.; Nazeeruddin, M. K.; Grätzel, M. Dye-Sensitized Solar Cells with 13% Efficiency Achieved through the Molecular Engineering of Porphyrin Sensitizers. *Nat. Chem.* **2014**, *6* (3), 242–247.
50. Katz, M. J.; DeVries Vermeer, M. J.; Farha, O. K.; Pellin, M. J.; Hupp, J. T. Dynamics of Back Electron Transfer in Dye-Sensitized Solar Cells Featuring 4-Tert-Butyl-

- Pyridine and Atomic-Layer-Deposited Alumina as Surface Modifiers. *J. Phys. Chem. B* **2015**, *119* (24), 7162–7169.
51. Soman, S.; Xie, Y.; Hamann, T. W. Cyclometalated Sensitizers for DSSCs Employing Cobalt Redox Shuttles. *Polyhedron* **2014**, *82*, 139–147.
  52. Yang, W.; Vlachopoulos, N.; Hao, Y.; Hagfeldt, A.; Boschloo, G. Efficient Dye Regeneration at Low Driving Force Achieved in Triphenylamine Dye LEG4 and TEMPO. *Phys. Chem. Chem. Phys.* **2015**, *17*, 15868–15875.
  53. Ahmad, S.; Bessho, T.; Kessler, F.; Baranoff, E.; Frey, J.; Yi, C.; Grätzel, M.; Nazeeruddin, M. K. A New Generation of Platinum and Iodine Free Efficient Dye-Sensitized Solar Cells. *Phys. Chem. Chem. Phys.* **2012**, *14* (30), 10631–10639.
  54. Ondersma, J. W.; Hamann, T. W. Spatially Resolved Sources of Dark Current from TiO<sub>2</sub> Nanoparticle Electrodes. *Langmuir* **2011**, *27* (21), 13361–13366.
  55. Sapp, S. A.; Elliott, C. M.; Contado, C.; Caramori, S.; Bignozzi, C. A. Substituted Polypyridine Complexes of Cobalt (II/III) as Efficient Electron-Transfer Mediators in Dye-Sensitized Solar Cells. *J. Am. Chem. Soc.* **2002**, *124* (37), 11215–11222.
  56. Nelson, J. J.; Amick, T. J.; Elliott, C. M. Mass Transport of Polypyridyl Cobalt Complexes in Dye-Sensitized Solar Cells with Mesoporous TiO<sub>2</sub> Photoanodes. *J. Phys. Chem. C* **2008**, *112* (46), 18255–18263.
  57. Feldt, S. M.; Gibson, E. A.; Gabrielsson, E.; Sun, L.; Boschloo, G.; Hagfeldt, A. Design of Organic Dyes and Cobalt Polypyridine Redox Mediators for High-Efficiency Dye-Sensitized Solar Cells. *J. Am. Chem. Soc.* **2010**, *132* (46), 16714–16724.
  58. Kashif, M. K.; Axelson, J. C.; Duffy, N. W.; Forsyth, C. M.; Chang, C. J.; Long, J. R.; Spiccia, L.; Bach, U. A New Direction in Dye-Sensitized Solar Cells Redox Mediator Development: In Situ Fine-Tuning of the Cobalt(II)/(III) Redox Potential through Lewis Base Interactions. *J. Am. Chem. Soc.* **2012**, *134* (40), 16646–16653.
  59. Ondersma, J. W.; Hamann, T. W. Measurements and Modeling of Recombination from Nanoparticle TiO<sub>2</sub> Electrodes. *J. Am. Chem. Soc.* **2011**, *133* (21), 8264–8271.
  60. Feldt, S. M.; Lohse, P. W.; Kessler, F.; Nazeeruddin, M. K.; Grätzel, M.; Boschloo, G.; Hagfeldt, A. Regeneration and Recombination Kinetics in Cobalt Polypyridine Based Dye-Sensitized Solar Cells, Explained Using Marcus Theory. *Phys. Chem. Chem. Phys.* **2013**, *15* (19), 7087–7097.
  61. Marcus, R. A.; Sutin, N. Electron Transfers in Chemistry and Biology. *Biochim. Biophys. Acta - Rev. Bioenerg.* **1985**, *811* (3), 265–322.
  62. Sutin, N. Theory of Electron Transfer Reactions: Insights and Hindsight. *Prog. Inorg. Chem.* **1983**, *30*, 441–498.

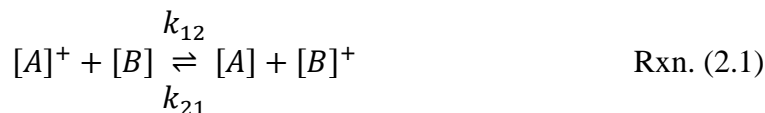
63. Chou, M.; Creutz, C.; Sutin, N. Rate Constants and Activation Parameters for Outer-Sphere Electron-Transfer Reactions and Comparisons with the Predictions of Marcus Theory. *J. Am. Chem. Soc.* **1977**, *99* (17), 5615–5623.
64. Sutin, N. Nuclear, Electronic, and Frequency Factors in Electron Transfer Reactions. *Acc. Chem. Res.* **1982**, *15* (9), 275–282.
65. Marcus, R. A. Chemical and Electrochemical Electron-Transfer Theory. *Annu. Rev. Phys. Chem.* **1964**, *15* (1), 155–196.

## Chapter 2. Stopped-Flow Spectroscopy: A Tool to Define the Self-Exchange Kinetics of One-Electron OSRSs

### 2.1 Introduction

Stopped-flow spectroscopy has been a powerful tool for extracting useful kinetic information for a variety of systems in biology and chemistry.<sup>1-14</sup> For the purposes of this research, stopped-flow has been used to understand the kinetics of electron-transfer amongst interesting one-electron OSRSs used in DSSCs. Use of this spectroscopic technique affords the opportunity to indirectly measure OSRSs self-exchange rate constants. As mentioned in Chapter 1, motivation for extracting self-exchange rate constants comes from the desire to understand the kinetics of regeneration and recombination in operating solar cells. We will apply the knowledge gained from extracting these rate constants to better understand the kinetics of regeneration using the Marcus cross-relation, Equation (1.4), while consequently shining light on the recombination reactions associated with the redox shuttles reorganization energy, Equation (1.2), in the ensuing chapters.<sup>15-17</sup>

In order to calculate the unknown self-exchange rate constant for an OSRS of interest, stopped-flow provides the link through the direct measurement of a cross-exchange rate constant. By performing a series of homogeneous cross-exchange reactions, similar to that shown in Reaction (2.1), and fitting the kinetic traces provided by stopped-flow, the cross-exchange rate constant,  $k_{12}$ , can be directly determined.



By applying the Marcus cross-relation discussed in Chapter 1, we can take the experimentally determined cross-exchange rate constant and evaluate the unknown self-exchange rate constant of newly designed one-electron OSRSs. Given the importance of these values to the analysis within this dissertation, it seems vital to discuss the operating principals of stopped-flow spectroscopy along with some basic experimental design rules in order to understand how the reported self-exchange rate constants are accurately measured.

## **2.2 Results and Discussion**

### *2.2.1 Basics of Operation*

A cartoon of the basic operating components of the stopped-flow system are outlined in Figure 2.1 and a photograph of the physical instrument with its various labeled constituents can be found in the Appendix, Figure A2.1. As depicted in Figure 2.1 below, the stopped-flow is comprised of a series of parts that rival that of a simple UV-Vis spectrometer. However, unlike a conventional UV-Vis, samples are mixed and injected into an observation cell in order to monitor the kinetic traces or absorbance changes of various reaction mixtures.

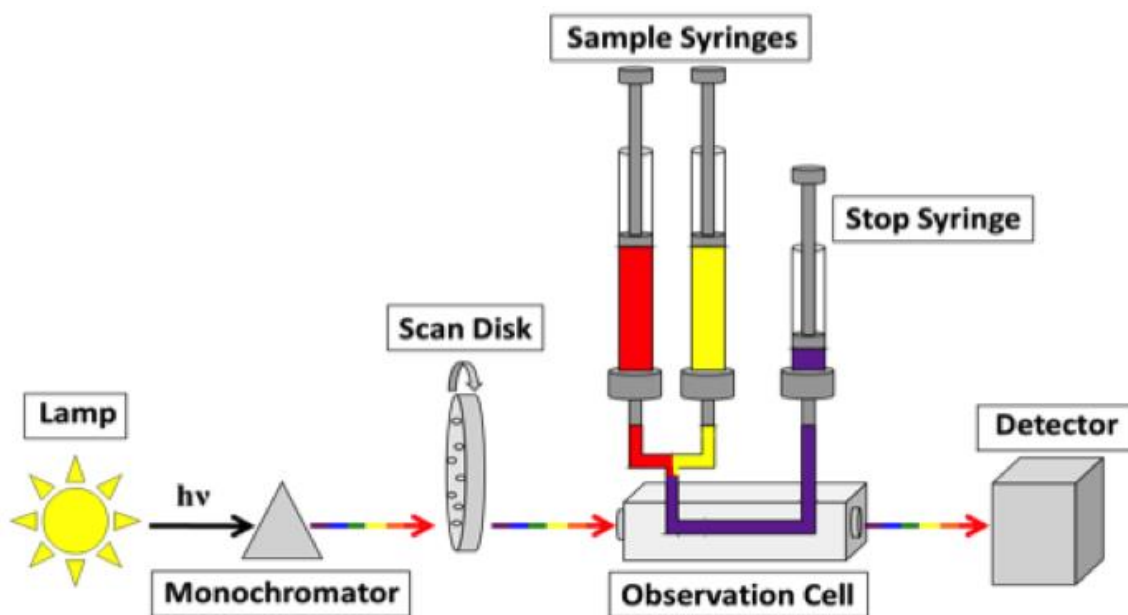


**Figure 2.1** Basic operating components of a stopped-flow instrument.

A measurement begins by mixing the reactant solutions in the sample syringes and injecting them into a 1 cm observation cell. As fresh solution enters the observation cell, it pushes the old reaction mixture out, filling a stopped-syringe. White light emitted from a xenon arc lamp is passed through a monochromator and the resulting monochromatic light is used to probe the sample mixture in the observation cell. Before the monochromatic light reaches the observation cell, however, it is chopped by a rotating scandisk. The scandisk rotates fast enough to provide millisecond resolution or 1000 scans/s for any given wavelength,  $\lambda$ , within a 225 nm range. After the monochromatic light is passed through the scandisk and observation cell the absorbance of the sample is measure directly by a photomultiplier tube (PMT) positioned directly behind the observation cell. Any scattering or reflectance is mitigated by another PMT positioned 90° from the observation cell, Figure A2.1.

An example of a collected data set is shown in Figure 2.2. As previously mentioned, the absorption profile of the reactant mixture is provided over a range of wavelengths, Figure 2.2a, to which a single wavelength can be chosen to fit for kinetic information, Figure 2.2b. Data collection begins when the reaction mixture flows into the observation cell and fills the stopped-syringe ( $t = 0$  s). The decay traces provided are fit from time zero till the sample reaches equilibrium. Conveniently, when studying cross-reactions with fast electron-transfer, the stopped-flow instrument provides what is called pre-trigger data. Pre-trigger data is the absorbance of your sample before time zero i.e. before the stopped-syringe becomes filled, Figure 2.2b. In the limit of fast electron-transfer, time zero can be adjusted accordingly to accommodate such conditions and to provide more accurate fits to the data sets.

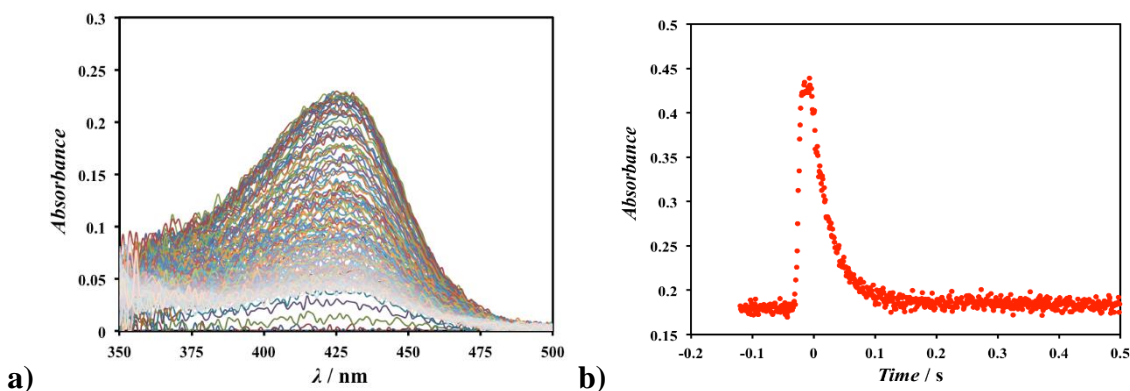


**Figure 2.2** a) Evolution and decay of a cross-exchange reaction mixture's absorbance as a function of wavelength,  $\lambda$ , over a 150 nm range monitored by stopped-flow spectroscopy. b) Absorbance decay of a reactant species at a single  $\lambda$  as a function of time.

### 2.2.2 Experimental Design Principals

To determine the self-exchange kinetics of an OSRS, the measurement requires the design of multiple cross-exchange reactions between two different redox shuttles, as shown in Reaction (2.1). In designing a proper set of cross-exchange reactions, a few important

points should be considered. For example, if we look at Reaction (2.1) above and are interested in identifying the self-exchange rate constant of complex  $[B]^{+/0}$  it is advantageous to cross  $[B]^{+/0}$  with another complex that has well-defined kinetics. Well-defined kinetics means that the self-exchange rate constant for molecule  $[A]^{+/0}$  has previously been measured and its mechanism for electron-transfer is also a one-electron outersphere reaction. Use of another OSRS will solidify that the observed kinetic traces are simply a result of charge-transfer and not some other chemical reaction occurring in solution. In an ideal case, if each reactant and product formed in solution can be chemically isolated before running stopped-flow, simple steady-state  $^1\text{H}$  NMR studies can be conducted to confirm that the reaction is well-behaved upon mixing the two OSRSs; for example  $[A]^+$  and  $[B]$  of Reaction (2.1). A well-behaved reaction observed by  $^1\text{H}$  NMR should only show the chemical shifts of  $[A]$ ,  $[A]^+$ ,  $[B]$  and  $[B]^+$ , since the Reaction (2.1) reaches equilibrium.

Aside from crossing  $[B]$  with a well-characterized complex, another important design rule for measuring cross-exchange reactions is to impart what is called flooding conditions or pseudo-first order reaction conditions. This is critical to an easier analysis of the observed kinetic traces. Referring back to Figure 2.1, the reacting solutions are pushed through an observation cell, while the kinetics of the reaction is being monitored. As the mixture fills and sets in the observation cell there lies the possibility of a concentration gradient within the observation chamber. This can pose a problem if second order kinetics is applied to the system. Given the half-life for second order chemical kinetics is concentration dependent, more rigorous mathematical corrections are needed to account for such a phenomenon.<sup>18,19</sup> If, however, pseudo-first order reaction conditions are applied

to the system, the potential concentration gradient doesn't become an issue, as the half-life for first order kinetics is concentration independent. Such an approach leads to a much more straightforward analysis of the observed cross-exchange rate constants,  $k_{obs}$ , for the various reactions. Scheme A2.1 of the Appendix provides mathematical support for observing simple first order kinetics while imparting pseudo-first order reaction conditions where  $[A]^+$  and  $[A]$  are in at least ten times excess to  $[B]$  and  $[B]^+$ .<sup>3</sup> Assuming the reaction reaches equilibrium, for reasons that will be discussed below, the integrated first order rate law and resulting observed pseudo-first order rate constant,  $k_{obs}$ , can be expressed by Equations (2.1) and (2.2), respectively.

$$[B]_t = [B]_e + ([B]_0 - [B]_e)exp^{-k_{obs}t} \quad \text{Eq. (2.1)}$$

$$k_{obs} = k_{12}[A]_t^+ + k_{21}[A]_t \quad \text{Eq. (2.2)}$$

Although Equation (2.2) describes a change in concentration is necessary to extract the  $k_{obs}$  for Reaction (2.1), Scheme A2.2 of the Appendix mathematically indicates that raw absorbance plots, Figure 2.2b, can be directly fit. In order to determine the forward cross-exchange rate constant,  $k_{12}$ , for Reaction (2.1) above, the excess concentration of  $[A]^+$  need only be varied in order to linearly change  $k_{obs}$  for the various cross-exchange reactions. By plotting the observed rate constants,  $k_{obs}$ , versus the excess concentration of  $[A]^+$ , the forward cross-exchange rate constant,  $k_{12}$ , can be extracted from the slope of the linear regression.

With the understanding that another well-characterized OSRS should be paired with the OSRS you are interested in studying, along with the fact that flooding conditions

need to be upheld while conducting the cross-exchange measurements; the stage is set to cleverly choose a well-defined OSRS, such as  $[A]^{+/0}$  of Reaction (2.1), to carry out your cross-exchange studies. Some simple measurements such as CV and UV-Vis can be taken before attempting stopped-flow to provide predictability as to how fast you can expect a reaction to take place and whether or not the reaction will provide enough of an absorption change for the stopped-flow to detect.

In regards to the speed of electron-transfer, this is dictated by the self-exchange rate constants of each molecule  $[A]$  and  $[B]$ , as well as the driving force or free energy difference for the reaction according to the Marcus cross-exchange Equation (2.3) below. The concentrations of each molecule will also affect the rate of charge-transfer, but more importantly concentration changes will dictate absorption changes, which is how we track the kinetics of the reaction. Choice of a slow self-exchanging molecule in place of  $[A]^{+/0}$  will ultimately reduce the cross-exchange rate constant and speed of the reaction with molecule  $[B]^{+/0}$ , since the two rate constants are proportional to one another:<sup>15,20</sup>

$$k_{12} \cong \sqrt{k_{(A/A^+)}k_{(B/B^+)}}K_{12} \quad \text{Eq. (2.3)}$$

Similarly, by minimizing the free energy,  $\Delta G$ , of Reaction (2.1) one can also expect slower electron-transfer as it relates to the equilibrium constant,  $K_{12}$ , of the reaction through Equation (2.4).

$$-nF\Delta E = -RT\ln K_{12} \quad \text{Eq. (2.4)}$$

Both the left and right side of Equation (2.4) are expressions for  $\Delta G$ , which implies knowledge of the formal potential difference,  $\Delta E$ , between complex  $[A]^{+/0}$  and complex  $[B]^{+/0}$  will provide insight as to magnitude of the cross-exchange rate constant. The smaller formal potential difference between the two complexes will result in a smaller  $K_{12}$  and slower electron-transfer. By minimizing the value of  $K_{12}$  you can ensure that the reaction will reach equilibrium as has been solved for in Scheme A2.1 of the Appendix. To measure the formal potential,  $E^\circ$ , of the reacting species  $[A]^+$  and  $[B]$ , simple cyclic voltammograms (CVs) of each complex can be measured, Figure 2.3a.

In regards to measuring observable absorption changes, it is useful to carry out simple UV-Vis measurements to determine the molar extinction coefficients of each species formed in solution, Figure 2.3b. This provides predictive power to estimate the expected absorption profile before and after the reaction has reached equilibrium. The difference spectrum should provide the relative change in absorption based on the final concentrations calculated from the measured equilibrium constant. Steady-state spectrophotometric titrations can also be carried out to verify the expected absorption profiles, as well as provide a supporting route in determining the equilibrium constant,  $K_{12}$ , for the reaction, see Scheme A2.4 of the Appendix. Although it is obvious in Figure 2.3b to monitor the changing absorbance of  $[B]$  around 650 nm, since it has the highest extinction coefficient in a region of the visible spectrum that no other species absorbs light, it isn't necessary to choose a wavelength that only one species primarily absorbs. Given flooding conditions are imparted, it is approximated that the concentration changes for those species in high excess i.e.  $[A]^+$  and  $[A]$  of Reaction (2.1), will remain nearly unchanged during and after the reaction has reached equilibrium. This assumption dictates

that at any given wavelength the absorption change can be fit as a function of a single absorbing species, Scheme A2.3, in order to extract  $k_{obs}$  for the reaction.

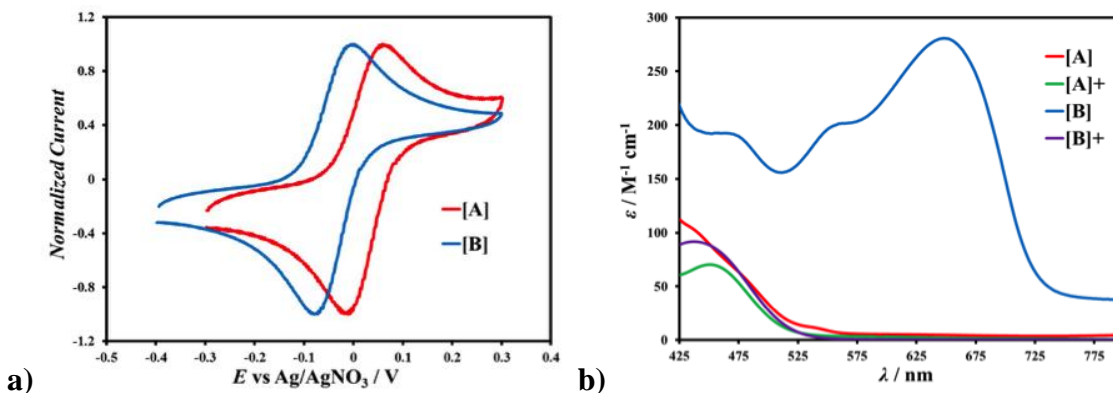


**Figure 2.3** a) CVs of reacting species in a cross-exchange reaction mixture used to determine the equilibrium constant for the reaction. b) Molar extinction coefficients as a function of wavelength for each reactant and product of a cross-exchange reaction mixture.

### 2.2.3 Data Analysis and Fitting

After designing the proper cross-exchange reaction and collecting the kinetic traces necessary to determine the cross-exchange rate constant,  $k_{12}$ , proper data fitting is imperative. As mentioned above, Equation (2.1) can be used to directly fit the raw absorbance plots extracted from the various kinetic studies. Figure 2.4a provides an example of a fit plot to the measured raw absorbance, while Figure 2.4b depicts the goodness of fit from the resulting residuals. Based on the minimal error and even distribution of the residuals from the beginning until the end of the measurement, Figure 2.4b suggests that the data set was fit properly. I would like to make this explicit and make note that residual plots are key to an accurate data analysis. These plots can be very informative and in the case of Figure 2.5b, they can provide clear evidence as a poor fit to the data. As we examine Figure 2.5b, it appears at longer times the data set fits well,

however, at shorter times ( $t < 2$  s) it is clear another process is occurring. Indeed, this residual plot was taken from measurements on a redox shuttle that will be discussed in Chapter 5 where the supporting electrolyte of the system was facilitating the decomposition of the OSRS in solution. It is speculated that at shorter times the curve is representative of electron-transfer, while at longer times the trailing curve is indicative of a slow decomposition.

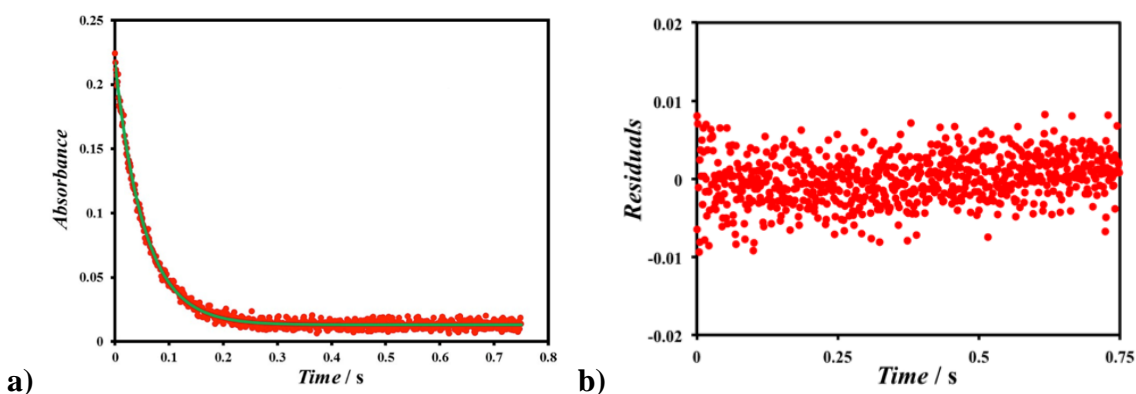


**Figure 2.4** a) Plot of absorbance at a single wavelength,  $\lambda$ , vs. time, corresponding to the decay of a single reactant species (red dots) and the resulting fit (black line). b) Residual plot to show the goodness of fit for the absorbance plot shown in a).

Aside from observing non-uniform residuals upon fitting the kinetic traces, another obvious indication that decomposition or side reactions might be occurring comes from the observation that the equilibrium absorbance of the system is never reached. If we refer to Figure 2.5a this point becomes clear. The equilibrium absorbance of the system rests around 0.33 and still appears to be decaying before fresh solution is pushed into the observation cell. After pushing the old solution out and allowing the fresh solution to react, it appears that the mixture slowly approaches the equilibrium absorbance of the old solution, but still remains  $\sim 0.01$  above while linearly decaying over longer time intervals. A well-

behaved system such as the one shown in Figure 2.2b does not show this phenomenon. Once the newly injected solution reaches equilibrium, the absorbance is matched with the old solution that was originally pushed out of the observation cell.

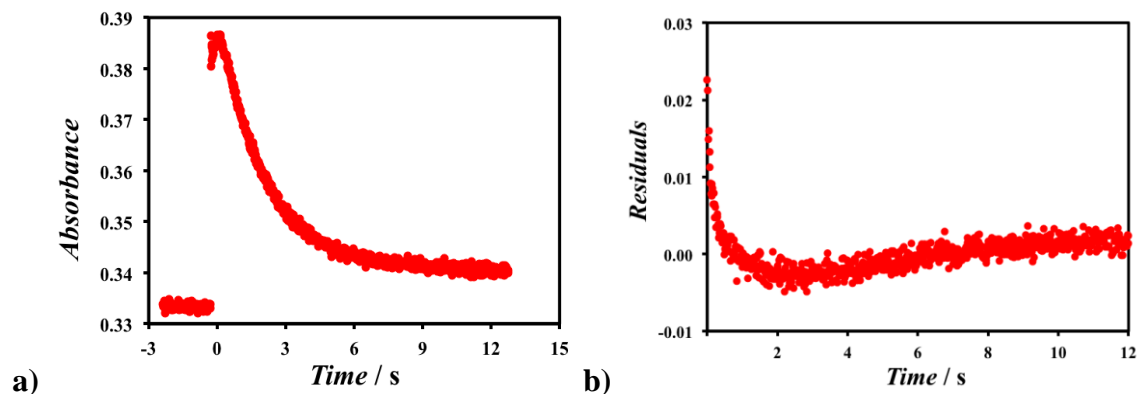


**Figure 2.5** a) Example of an absorbance versus time plot for a cross-exchange reaction that contains multiple processes, i.e. reactant decomposition, aside from charge transfer. b) Plot of residuals for a cross-exchange reaction that contains multiple processes aside from a single electron-transfer, which cannot be fit to simple pseudo-first order decay kinetics.

After identifying well behaved cross-exchange kinetics and correctly fitting the collected data at varying concentrations of  $[A]^+$ , Reaction (2.1), the measured observed pseudo-first order rate constants,  $k_{obs}$ , need to be plotted as a function of the excess concentration of  $[A]^+$  to determine the forward cross-exchange rate constant,  $k_{12}$ . Figure 2.6 provides an example of such a plot. The error associated with determining  $k_{obs}$  is represented in Figure 2.6 as the standard deviation of at least seven independent trials at a given concentration. The error associated with each reactant concentration is typically not represented since it is so minimal. Equation (2.2) above indicates that the slope of Figure 2.6 will provide the forward cross-exchange rate constant,  $k_{12}$ , while the y-intercept will provide the information necessary to isolate the reverse cross-exchange rate constant,  $k_{21}$ .

After determining both values, the equilibrium constant,  $K_{12}$ , can also be determined using Equation (2.5).

$$K_{12} = k_{12}/k_{21} \quad \text{Eq. (2.5)}$$

To substantiate the measured  $k_{12}$  and  $k_{21}$  values, the calculated  $K_{12}$  can be compared to the values obtained from CV measurements and/or spectrophotometric titrations.

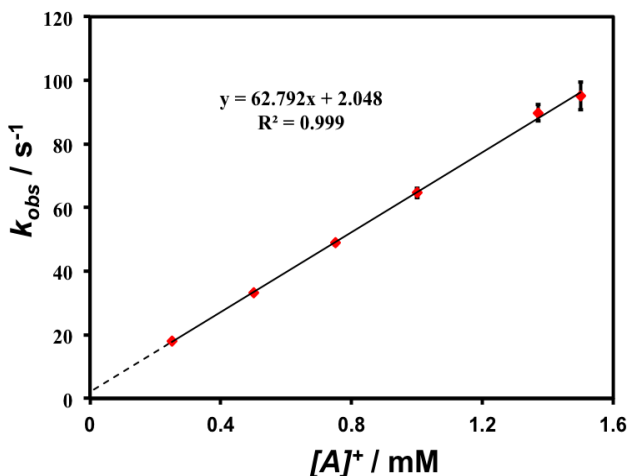


**Figure 2.6** Example of an observed pseudo-first order rate constants,  $k_{\text{obs}}$ , versus the excess reactant concentrations plot for the reactions between  $[A]^+$  and  $[B]$  for the homogeneous cross-exchange Reaction (2.1) above.

After determining  $k_{12}$  from Figure 2.6, calculation of the unknown self-exchange rate constant,  $k_{B/B^+}$ , for complex  $[B]^{+/0}$  becomes simple through the application of the Marcus cross-relation, Equation (2.3) above. Typically, the equilibrium value,  $K_{12}$ , used in the final calculation is the one measured from CV measurements, since it produces the least amount of error. By plugging in the measured cross-exchange rate constant,  $k_{12}$ , the known self-exchange rate constant,  $k_{A/A^+}$ , of complex  $[A]^{+/0}$  and the measured equilibrium constant

for the reaction,  $K_{12}$ , only a single variable left, which is the unknown self-exchange rate constant,  $k_{B/B^+}$ , of complex  $[B]^{+/0}$ .

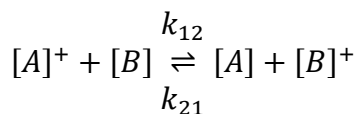
### 2.3 Conclusion

This chapter was designed to provide critical insight as to the methodology of stopped-flow spectroscopy. Stopped-flow has provided the basis for extracting useful kinetic information on a number of OSRSs that our group has used in numerous dye cell studies.<sup>21,22</sup> By determining the self-exchange rate constants of such OSRSs, it has been our goal to apply these values in a manner that is informative to the processes of regeneration and recombination, the likes of which will be discussed in the ensuing chapters. Although the next few chapters will also walk through the process of determining the unknown self-exchange rate constants of OSRSs using stopped-flow, this chapter was designed to go deeper into how and why the outlined experimental conditions were imposed, with mathematical support in the Appendix. Proper experimental design has taken years to perfect; however, with the knowledge laid out above, one can be assured that following the outlined experimental protocol will provide meaningful results for future OSRSs they are interested in studying.

## **APPENDIX**

## APPENDIX

**Scheme A2.1** Derivation for isolating the observed pseudo-first order cross-exchange rate constant,  $k_{obs}$ , under flooding conditions.<sup>23</sup>



Experimental Design:  $[A]^+ \gg [B]$  &  $[A] \gg [B]^+$

$$[A]_0^+ + [B]_0 + [A]_0 + [B]_0^+ = [A]_t^+ + [B]_t + [A]_t + [B]_t^+ = [A]_e^+ + [B]_e + [A]_e + [B]_e^+$$

$$\frac{[A]_e[B]_e^+}{[A]_e^+[B]_e} = K_{12} = \frac{k_{12}}{k_{21}}$$

$$\text{Normalized Rate} = -\frac{d[A]^+}{dt} = -\frac{[B]}{dt} = \frac{[A]}{dt} = \frac{[B]^+}{dt}$$

$$-\frac{d[B]_t}{dt} = k_{12}[A]_t^+[B]_t - k_{21}[A]_t[B]_t^+ = k'_{12}[B]_t - k'_{21}[B]_t^+$$

$$k'_{12} = k_{12}[A]_t^+$$

$$k'_{21} = k_{21}[A]_t$$

$$[B]_t^+ = [A]_e^+ + [B]_e + [A]_e + [B]_e^+ - [A]_t^+ - [B]_t - [A]_t$$

$$-\frac{d[B]_t}{dt} = k_{12}[A]_t^+[B]_t - k_{21}[A]_t([A]_e^+ + [B]_e + [A]_e + [B]_e^+ - [A]_t^+ - [B]_t - [A]_t)$$

$$-\frac{d[B]_t}{dt} = k_{12}[A]_t^+[B]_t - k_{21}([A]_t[A]_e^+ + [A]_t[B]_e + [A]_t[A]_e + [A]_t[B]_e^+ - [A]_t[A]_t^+ - [A]_t[B]_t - [A]_t[A]_t)$$

$$\text{Assumptions: } [A]_t^+ = [A]_e^+ \text{ \& } [A]_t = [A]_t \text{ \& } [A]_e[B]_e^+ = \frac{k_{12}}{k_{21}}[A]_e^+[B]_e$$

$$-\frac{d[B]_t}{dt} = k_{12}([A]_t^+[B]_t - [A]_e^+[B]_e) + k_{21}([A]_t[B]_t - [A]_t[B]_e)$$

$$\text{Simplification: } k_{obs} = k'_{12} + k'_{21} = k_{12}[A]_t^+ + k_{21}[A]_t$$

$$-\frac{d[B]_t}{dt} = k_{obs}([B]_t - [B]_e)$$

$$\int_{[B]_0}^{[B]_t} \frac{d[B]_t}{([B]_t - [B]_e)} = -k_{obs} \int_{t_0}^t dt$$

$$[B]_t = [B]_e + ([B]_0 - [B]_e) \exp^{-k_{obs}t}$$

**Scheme A2.2** Derivation to fit raw absorbance in order to isolate  $k_{obs}$  for cross-exchange reactions under pseudo-first order conditions.

$$\ln \left[ \frac{([B]_t - [B]_e)}{([B]_0 - [B]_e)} \right] = -k_{obs}t$$

$$([B]_t - [B]_e) = ([B]_0 - [B]_e) \exp^{-k_{obs}t}$$

$$[B]_t = [B]_e + ([B]_0 - [B]_e) \exp^{-k_{obs}t}$$

$$\text{Beer's Law: } A_B = \varepsilon_B l [B]$$

$$\frac{A_{B_t}}{\varepsilon_B l} = \frac{A_{B_e}}{\varepsilon_B l} + \frac{(A_{B_0} - A_{B_e}) \exp^{-k_{obs}t}}{\varepsilon_B l}$$

$$A_{B_t} = A_{B_e} + (A_{B_0} - A_{B_e}) \exp^{-k_{obs}t}$$

Raw Absorbance Fitting Equation used in Regression Wizard Software

$$y = A + (B - A) \exp^{-kx}$$

$$y = A_{B_t}$$

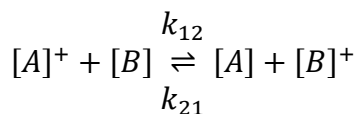
$$A = A_{B_e}$$

$$B = A_{B_0}$$

$$k = k_{obs}$$

$$x = t \text{ (Time in seconds)}$$

**Scheme A2.3** Derivation to verify at a given wavelength, where multiple species are absorbing, the change in only one species is being monitored in order to extract the observed pseudo-first order rate constant,  $k_{obs}$ , for the cross-exchange reaction under flooding conditions.<sup>23</sup>



Experimental Design:  $[A]^+ \gg [B]$  &  $[A] \gg [B]^+$

$$[A]_0^+ + [B]_0 + [A]_0 + [B]_0^+ = [A]_t^+ + [B]_t + [A]_t + [B]_t^+ = [A]_e^+ + [B]_e + [A]_e + [B]_e^+$$

$$\frac{[A]_e[B]_e^+}{[A]_e^+[B]_e} = K_{12} = \frac{k_{12}}{k_{21}}$$

$$\text{Normalized Rate} = -\frac{d[A]^+}{dt} = -\frac{[B]}{dt} = \frac{[A]}{dt} = \frac{[B]^+}{dt}$$

$$-\frac{d[B]_t}{dt} = k_{12}[A]_t^+[B]_t - k_{21}[A]_t[B]_t^+ = k'_{12}[B]_t - k'_{21}[B]_t^+$$

$$k'_{12} = k_{12}[A]_t^+$$

$$k'_{21} = k_{21}[A]_t$$

$$\ln \left[ \frac{[B]_t - [B]_e}{[B]_0 - [B]_e} \right] = -k_{obs}t$$

\*Note- Want to prove that we can monitor a  $\lambda$ , which many species absorb and still be able to back out  $k_{obs}$  with respect to fitting for a single absorbing species [B] at that  $\lambda$ .

$$\text{Functional Form: } \ln \left[ \frac{y_t - y_e}{y_0 - y_e} \right] = -k_{obs}t$$

\*Note-  $y_i$  is a proportionality constant between species  $i$  and its contribution to the absorbance.

$$y_0 = y_{A^+}[A]_0^+ + y_B[B]_0 + y_A[A]_0 + y_{B^+}[B]_0^+$$

$$[A]_0 = [A]_e^+ + [B]_e + [A]_e + [B]_e^+ - [A]_0^+ - [B]_0 - [B]_0^+$$

$$[A]_0 = ([A]_e^+ - [A]_0^+) + ([B]_e - [B]_0) + ([B]_e^+ - [B]_0^+) + [A]_e$$

$$\text{*Note- } [B]_0^+ = 0$$

$$[B]_e - [B]_0 = [A]_e^+ - [A]_0^+$$

$$[B]_e^+ - [B]_0^+ = [B]_0 - [B]_e$$

$$[A]_e = K_{12} \frac{[A]_e^+[B]_e}{[B]_e^+} = K_{12} \frac{[A]_e^+[B]_e}{([A]_0^+ - [A]_e^+)}$$

$$y_0 = y_{A^+}[A]_0^+ + y_B[B]_0 + y_A \left[ ([B]_e - [B]_0) + ([B]_e - [B]_0) + ([B]_e^+ - [B]_0^+) + K_{12} \frac{[A]_e^+[B]_e}{[B]_e^+} \right] + y_{B^+}[B]_0^+$$

$$y_t = y_{A^+}[A]_t^+ + y_B[B]_t + y_A[A]_t + y_{B^+}[B]_t^+$$

$$[A]_t = [A]_e^+ + [B]_e + [A]_e + [B]_e^+ - [A]_t^+ - [B]_t - [B]_t^+$$

$$[A]_t = ([A]_e^+ - [A]_t^+) + ([B]_e - [B]_t) + ([B]_e^+ - [B]_t^+) + [A]_e$$

$$[B]_e - [B]_t = [A]_e^+ - [A]_t^+$$

$$[B]_e^+ - [B]_t^+ = [B]_t - [B]_e$$

$$y_t = y_{A^+}[A]_t^+ + y_B[B]_t + y_A \left[ ([B]_e - [B]_t) + ([B]_e - [B]_t) + ([B]_e^+ - [B]_t^+) + K_{12} \frac{[A]_e^+[B]_e}{[B]_e^+} \right] + y_{B^+}[B]_t^+$$

$$y_e = y_{A^+}[A]_e^+ + y_B[B]_e + y_A[A]_e + y_{B^+}[B]_e^+$$

$$y_e = y_{A^+}[A]_e^+ + y_B[B]_e + y_A \left( K_{12} \frac{[A]_e^+[B]_e}{[B]_e^+} \right) + y_{B^+}[B]_e^+$$

$$\ln \left[ \frac{(y_{A^+}[A]_t^+ + y_B[B]_t + y_A \left[ ([B]_e^+ - [B]_t^+) + K_{12} \frac{[A]_e^+[B]_e}{[B]_e^+} \right] + y_{B^+}[B]_t^+) - (y_{A^+}[A]_e^+ + y_B[B]_e + y_A \left( K_{12} \frac{[A]_e^+[B]_e}{[B]_e^+} \right) + y_{B^+}[B]_e^+)}{(y_{A^+}[A]_0^+ + y_B[B]_0 + y_A \left[ ([B]_e^+ - [B]_0^+) + K_{12} \frac{[A]_e^+[B]_e}{[B]_e^+} \right] + y_{B^+}[B]_0^+) - (y_{A^+}[A]_e^+ + y_B[B]_e + y_A \left( K_{12} \frac{[A]_e^+[B]_e}{[B]_e^+} \right) + y_{B^+}[B]_e^+)} \right] = -k_{obs}t$$

$$\ln \left[ \frac{y_{A^+}([A]_t^+ - [A]_e^+) + y_B([B]_t - [B]_e) + y_A([B]_e^+ - [B]_t^+) + y_{B^+}([B]_t^+ - [B]_e^+)}{y_{A^+}([A]_0^+ - [A]_e^+) + y_B([B]_0 - [B]_e) + y_A([B]_e^+ - [B]_0^+) + y_{B^+}([B]_0^+ - [B]_e^+)} \right] = -k_{obs}t$$

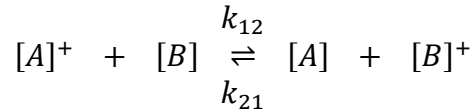
\*Note- Substitutions are shown above.

$$\ln \left[ \frac{y_{A^+}([B]_t - [B]_e) + y_B([B]_t - [B]_e) + y_A([B]_e - [B]_t) + y_{B^+}([B]_e - [B]_t)}{y_{A^+}([B]_0 - [B]_e) + y_B([B]_0 - [B]_e) + y_A([B]_e - [B]_0) + y_{B^+}([B]_e - [B]_t)} \right] = -k_{obs}t$$

$$\ln \left[ \frac{(y_{A^+} + y_B - y_A - y_{B^+})([B]_t - [B]_e)}{(y_{A^+} + y_B - y_A - y_{B^+})([B]_0 - [B]_e)} \right] = -k_{obs}t$$

$$\ln \left[ \frac{([B]_t - [B]_e)}{([B]_0 - [B]_e)} \right] = -k_{obs}t$$

**Scheme A2.4** Derivation describing the spectrophotometric determination of the cross-exchange equilibrium constant,  $K_{12}$ .



I:	$[A]_0^+$	$[B]_0$	$[A]_0$	$0$
C:	$-x$	$-x$	$+x$	$+x$
E:	$[A]_0^+ - x$	$[B]_0 - x$	$[A]_0 + x$	$x$

Equilibrium Absorbance

Beer's Law:  $A_e = \epsilon l [C]_e$

$$A_e = \epsilon_{A^+} l [A]_e^+ + \epsilon_B l [B]_e + \epsilon_A l [A]_e + \epsilon_{B^+} l [B]_e^+$$

Note: Path Length (l) = 1 cm

$$A_e = [\epsilon_{A^+}([A]_0^+ - x)] + [\epsilon_B([B]_0 - x)] + [\epsilon_A([A]_0 + x)] + (\epsilon_{B^+}x)$$

$$x = \frac{A_e - (\epsilon_{A^+}[A]_0^+ + \epsilon_B[B]_0 + \epsilon_A[A]_0)}{\epsilon_A + \epsilon_{B^+} - \epsilon_{A^+} - \epsilon_B}$$

$$\frac{[A]_e[B]_e^+}{[A]_e^+[B]_e} = K_{12} = \frac{([A]_0 + x)(x)}{([A]_0^+ - x)([B]_0 - x)}$$

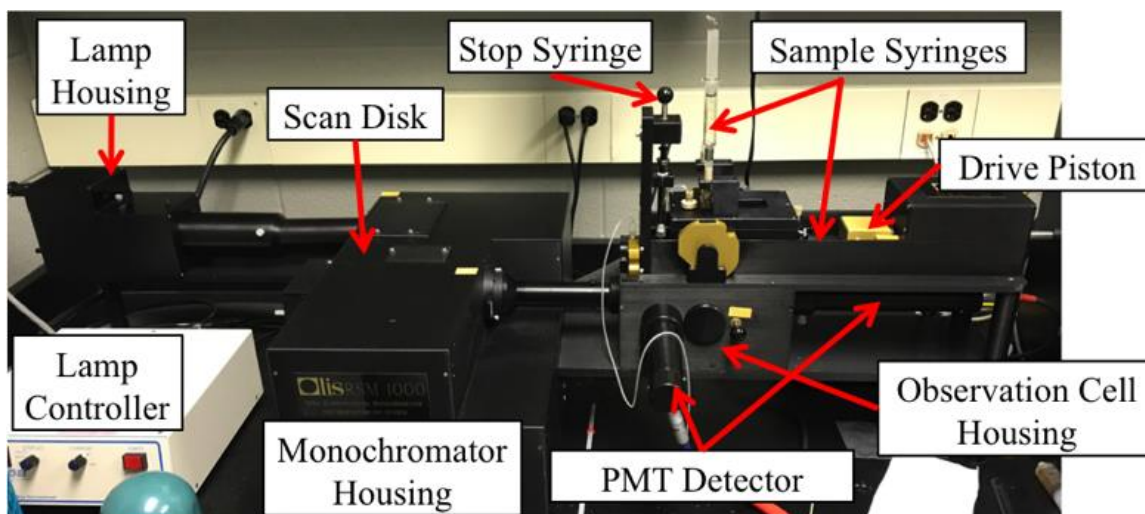


**Figure A2.1** Olis RSM 1000 UV-Vis Rapid Scanning Spectrometer.

## **REFERENCES**

## REFERENCES

1. Wherland, S. Non-Aqueous, Outer-Sphere Electron Transfer Kinetics of Transition Metal Complexes. *Coord. Chem. Rev.* **1993**, *123* (1–2), 169–199.
2. Chaka, G.; Kandegedara, A.; Heeg, M. J.; Rorabacher, D. B. Comparative Study of Donor Atom Effects on the Thermodynamic and Electron-Transfer Kinetic Properties of copper(II/I) Complexes with Sexadentate Macrocyclic Ligands. [CuII/I([18]aneS4N2)] and [CuII/I([18]aneS4O2)]. *Dalt. Trans.* **2007**, *6* (4), 449–458.
3. Xie, B.; Wilson, L. J.; Stanbury, D. M. Cross-Electron-Transfer Reactions of the [CuII/I(bite)]<sup>2+/+</sup> Redox Couple. *Inorg. Chem.* **2001**, *40* (14), 3606–3614.
4. Dunn, B. C.; Ochrymowycz, L. A.; Rorabacher, D. B. Electron-Transfer Kinetics of the Copper(II/I) Complex with 1,4,8,11-Tetrathiacyclotetradecane in Acetonitrile. *Inorg. Chem.* **1995**, *34* (7), 1954–1956.
5. Hattori, S.; Wada, Y.; Yanagida, S.; Fukuzumi, S. Blue Copper Model Complexes with Distorted Tetragonal Geometry Acting as Effective Electron-Transfer Mediators in Dye-Sensitized Solar Cells. *J. Am. Chem. Soc.* **2005**, *127* (26), 9648–9654.
6. Symes, M. D.; Surendranath, Y.; Lutterman, D. A.; Nocera, D. G. Bidirectional and Unidirectional PCET in a Molecular Model of a Cobalt-Based Oxygen-Evolving Catalyst. *J. Am. Chem. Soc.* **2011**, *133* (14), 5174–5177.
7. Fukuzumi, S.; Miyamoto, K.; Suenobu, T.; Van Caemelbecke, E.; Kadish, K. M. Electron Transfer Mechanism of Organocobalt Porphyrins. Site of Electron Transfer, Migration of Organic Groups, and Cobalt-Carbon Bond Energies in Different Oxidation States. *J. Am. Chem. Soc.* **1998**, *120* (12), 2880–2889.
8. Surendranath, Y.; Lutterman, D. A.; Liu, Y.; Nocera, D. G. Nucleation, Growth and Repair of a Cobalt-Based Oxygen Evolving Catalyst. *J. Am. Chem. Soc.* **2012**, *134* (14), 6326–6336.
9. Chou, M.; Creutz, C.; Sutin, N. Rate Constants and Activation Parameters for Outer-Sphere Electron-Transfer Reactions and Comparisons with the Predictions of Marcus Theory. *J. Am. Chem. Soc.* **1977**, *99* (17), 5615–5623.
10. Young, R. C.; Keene, F. R.; Meyer, T. J. Measurement of Rates of Electron Transfer between Ru(bpy)<sub>3</sub><sup>2+</sup> and Fe(phen)<sub>3</sub><sup>2+</sup> and between Ru(phen)<sub>3</sub><sup>3+</sup> and Ru(bpy)<sub>3</sub><sup>2+</sup> by Differential Excitation Flash Photolysis. *J. Am. Chem. Soc.* **1977**, *99* (8), 2468–2473.
11. Groves, J. T.; Lee, J.; Marla, S. S. Detection and Characterization of an Oxomanganese (V) Porphyrin Complex by Rapid-Mixing Stopped-Flow Spectrophotometry. *J. Am. Chem. Soc.* **1997**, *119* (27), 6269–6273.

12. Landry, A. P.; Ballou, D. P.; Banerjee, R. H<sub>2</sub>S Oxidation by Nanodisc-Embedded Human Sulfide Quinone Oxidoreductase. *J. Biol. Chem.* **2017**, *292* (28), 11641–11649.
13. Parker, B. F.; Zhang, Z.; Leggett, C. J.; Arnold, J.; Rao, L. Kinetics of Complexation of V(V), U(VI), and Fe(III) with Glutaroimide-Dioxime: Studies by Stopped-Flow and Conventional Absorption Spectroscopy. *Dalt. Trans.* **2017**, *46* (33), 11084–11096.
14. Eisenhart, T. T.; Howland, W. C.; Dempsey, J. L. Proton-Coupled Electron Transfer Reactions with Photometric Bases Reveal Free Energy Relationships for Proton Transfer. *J. Phys. Chem. B* **2016**, *120* (32), 7896–7905.
15. Marcus, R. A.; Sutin, N. Electron Transfers in Chemistry and Biology. *Biochim. Biophys. Acta - Rev. Bioenerg.* **1985**, *811* (3), 265–322.
16. Sutin, N. Nuclear, Electronic, and Frequency Factors in Electron Transfer Reactions. *Acc. Chem. Res.* **1982**, *15* (9), 275–282.
17. Sutin, N. Theory of Electron Transfer Reactions: Insights and Hindsight. *Prog. Inorg. Chem.* **1983**, *30*, 441–498.
18. Meagher, N. E.; Rorabacher, D. B. Mathematical Treatment for Very Rapid Second-Order Reversible Kinetics As Measured by Stopped-Flow Spectrophotometry with Corrections for the Cell Concentration Gradient. *J. Phys. Chem.* **1994**, *98* (48), 12590–12593.
19. Dunn, B. C.; Meagher, N. E.; Rorabacher, D. B. Resolution of Stopped-Flow Kinetic Data for Second-Order Reactions with Rate Constants up to 10<sup>8</sup> M<sup>-1</sup> S<sup>-1</sup> Involving Large Concentration Gradients. Experimental Comparison Using Three Independent Approaches. *J. Phys. Chem.* **1996**, *100* (42), 16925–16933.
20. Marcus, R. A. Chemical and Electrochemical Electron-Transfer Theory. *Annu. Rev. Phys. Chem.* **1964**, *15* (1), 155–196.
21. Xie, Y.; Baillargeon, J.; Hamann, T. W. Kinetics of Regeneration and Recombination Reactions in Dye-Sensitized Solar Cells Employing Cobalt Redox Shuttles. *J. Phys. Chem. C* **2015**, *119* (50), 28155–28166.
22. Baillargeon, J.; Xie, Y.; Hamann, T. W. Bifurcation of Regeneration and Recombination in Dye-Sensitized Solar Cells via Electronic Manipulation of Tandem Cobalt Redox Shuttles. *ACS Appl. Mater. Interfaces* **2017**, *9* (39), 33544–33548.
23. Espenson, J. H. CHEMICAL KINETICS AND REACTION Second Edition.

## Chapter 3. Kinetics of Regeneration and Recombination in DSSCs using Cobalt OSRSs

*\*I would like to acknowledge Yuling Xie for her contribution to this chapter. Yuling collected all optical and solar cell measurements and modeled the collected IPCEs.*

### 3.1 Abstract

The key to achieving high efficiency DSSCs is the realization of a redox shuttle that exhibits quantitative dye regeneration at a minimal driving force. Since the electron diffusion length,  $L_n$ , of the system is controlled by recombination to the redox shuttle; an optimal redox couple must balance the kinetics of these two key electron-transfer reactions. Therefore, in this chapter we seek out how to balance these electron-transfer pathways by investigating dye regeneration efficiencies,  $\eta_{reg}$ , and electron diffusion lengths,  $L_n$ , of DSSCs employing two different cobalt redox shuttles: cobalt tris-bipyridine,  $[\text{Co}(\text{bpy})_3]^{3+/2+}$  and cobalt bis-trithiacyclononane,  $[\text{Co}(\text{ttcn})_2]^{3+/2+}$  with the same molecular sensitizer, D35cpdt. The values of  $\eta_{reg}$  and  $L_n$  were experimentally determined by coupling optical measurements with front and back incident photon to current efficiency (IPCE) measurements. The regeneration of the D35cpdt dye was found to be quantitative with  $[\text{Co}(\text{ttcn})_2]^{3+/2+}$ ; however, dye regeneration with the current champion redox shuttle  $[\text{Co}(\text{bpy})_3]^{3+/2+}$  is sub-optimal despite a larger driving force for the reaction. Although regeneration was determined to be quantitative for cells utilizing  $[\text{Co}(\text{ttcn})_2]^{3+/2+}$ , a shorter electron diffusion length, due to faster recombination, was measured for DSSCs employing  $[\text{Co}(\text{ttcn})_2]^{3+/2+}$  compared to  $[\text{Co}(\text{bpy})_3]^{3+/2+}$ . The origin of the measured regeneration and recombination rates were associated with the self-exchange rate constants of the two redox shuttles. Differing only by a single anti-bonding electron in their reduced states, the self-

exchange rate constant for  $[\text{Co}(\text{ttn})_2]^{3+/2+}$  was determined to be four orders of magnitude larger than  $[\text{Co}(\text{bpy})_3]^{3+/2+}$  according to stopped-flow spectroscopy measurements. Application of Marcus theory allowed the difference in self-exchange rate constants to quantitatively account for the differences in regeneration efficiencies and electron diffusion lengths of the two redox shuttles. To further improve DSSC performance, atomic layer deposition (ALD) was used to add a single layer of alumina onto the  $\text{TiO}_2$  film prior to dye loading. Interestingly, the resulting improvement stemmed from different causes. The alumina layer was found to reduce recombination to the redox shuttle and thereby increase  $L_n$  for  $[\text{Co}(\text{ttn})_2]^{3+/2+}$ , whereas improved dye regeneration efficiency was observed for the  $[\text{Co}(\text{bpy})_3]^{3+/2+}$  redox shuttle through the reduction of recombination to the oxidized dye. These findings clearly demonstrate the fine balance between the regeneration and recombination reactions when outersphere redox shuttles are employed in DSSCs. What seems promising from these studies is that isolation of the efficiency-limiting reactions allows us to design strategies to overcome such barriers, which will be discussed herein and the focus of the ensuing chapters.

### **3.2 Introduction**

DSSCs have garnered substantial interest since the seminal report in 1991 by O'Regan and Grätzel that demonstrated that these devices are capable of producing high solar power conversion efficiencies with potentially inexpensive materials.<sup>1</sup> The vast majority of subsequent research on DSSCs, as mentioned in Chapter 1, has utilized the  $\text{I}_3^-/\text{I}^-$  redox shuttle since it long produced the highest efficiencies with a variety of sensitizers and photoanode materials. The good performance of these cells is a consequence of slow recombination kinetics, which allows for excellent charge collection even with a thick

(~14-16  $\mu\text{m}$ ) high surface area photoanode. Despite the advantages of  $\text{I}_3^-/\text{I}^-$ , it suffers from several well-known drawbacks. Most importantly, in terms of device efficiency, is the large energy penalty required to achieve efficient dye regeneration. In addition, the mechanism for charge-transfer is complicated and the inability to systematically tune the properties of  $\text{I}_3^-/\text{I}^-$  make it impossible for general design principles to be established in order to create a superior redox shuttle. One-electron OSRSs are attractive alternatives to  $\text{I}_3^-/\text{I}^-$  because their properties are tunable and they are capable of being utilized for broader systematic investigations.<sup>2-6</sup>

The most promising OSRSs examined to date are based on cobalt complexes. Early fundamental studies by Klahr *et al.*, using a series of cobalt polypyridyl complexes, provided one of the first examples of an OSRS outperforming the  $\text{I}_3^-/\text{I}^-$  electrolyte.<sup>2</sup> Despite ~0.5 eV of extra driving force for regeneration compared to the N3 dye ( $-\Delta G_{reg} \approx 0.7$  eV), the cobalt redox shuttles demonstrated higher IPCEs than  $\text{I}_3^-/\text{I}^-$  when paired with the ruthenizer,  $[\text{Ru}(\text{dcbpy})_2(\text{bpy})]^{2+}$ . This study provided evidence that the chemical structure of the molecular sensitizer played a more critical role than the driving force in dictating efficient regeneration using the  $\text{I}_3^-/\text{I}^-$  electrolyte. Growing interest in cobalt OSRSs rapidly expanded following a report in 2010 by Feldt *et al.*, which indicated a DSSC power conversion efficiency (PCE) of 6.7% under one sun illumination using the cobalt tris-bipyridine,  $[\text{Co}(\text{bpy})_3]^{3+/2+}$ , redox shuttle in combination with an organic dye, D35.<sup>7</sup> This redox shuttle quickly became attractive for its use in DSSCs due to its ease of fabrication using commercial ligands, its nonvolatile and noncorrosive nature, as well as its minimal competitive light absorption. Follow up work on optimizing the sensitizer and electrolyte

has since allowed  $[\text{Co}(\text{bpy})_3]^{3+/2+}$  to produce the highest reported PCE for a DSSC of ~13%.<sup>8,9</sup>

The use of cobalt transition metal complexes provides a motif to tune its redox potential through modification of the ligand framework. This unique ability can provide a detailed understanding of the structure-function relationship of these systems and is expected to lead to even further cell optimization. Since the cobalt complexes of interest are one-electron OSRSs their behavior should be interpretable by Marcus theory. Work by Feldt *et al.* has proven that this assumption is true as they studied the regeneration and recombination kinetics in DSSCs using a series cobalt tris-bipyridine and cobalt bis-phenanthroline redox couples.<sup>10</sup> We would argue, however, that their interpreted results in terms of Marcus theory are misleading. Interestingly, in the manuscript the authors showed a plot of the regeneration half times vs. driving force plateauing at a driving force of ~0.6 eV with value of  $\sim 10^5 \text{ s}^{-1}$  to which they interpreted as an indication of reaching the Marcus inverted region.<sup>10</sup> There are many explanations for such rates to plateau,<sup>11</sup> however, with the most likely reason being a diffusion limited reaction. Indeed, diffusion limited regeneration was demonstrated in a related study by Daeneke *et al.* using a series of ferrocene derivatives, however with an apparent diffusion limited rate constant about an order of magnitude larger than that observed for the cobalt complexes.<sup>6</sup> Cobalt polypyridyl complexes are known to have very slow diffusion coefficients in mesoporous  $\text{TiO}_2$ ,<sup>12</sup> which may account for this discrepancy. While, as the authors noted, the maximum rate constant observed is slower than expected for a diffusion limited reaction, it is orders of magnitude lower than expected for a maximum rate constant ( $-\Delta G^0 = \lambda$ ).<sup>13,14</sup> In addition, the combination of the driving force corresponding to the maximum regeneration rate with

dark current and lifetime measurements of recombination indicate a reorganization energy of only 0.6 eV for these cobalt complexes, which was taken as evidence that both regeneration and recombination reactions occur in the inverted region. This is in disagreement with known low self-exchange rate constants of such cobalt(II) complexes due to large inner-sphere reorganization energy,<sup>15</sup> all previous ground state bimolecular solution measurements of electron transfer,<sup>14</sup> measurements of electron-transfer rate constants at ideal ZnO single electrodes,<sup>16</sup> and modeling of recombination in DSSCs.<sup>3</sup> Since the regeneration and recombination reactions (in addition to light absorption and diffusion coefficient) dictate the performance of any redox shuttle in a DSSC, it is crucial to fully understand such electron-transfer behavior in a framework that would allow predictive power to further enhance DSSC performance. Therefore, it seems urgent to provide a correct interpretation for the electron-transfer pathways within the DSSC system using OSRSs and the Marcus framework.

In addition to driving force, the Marcus model also indicates a strong dependence on reorganization energy for electron-transfer. Until now, there have been no reports on the reorganization energy dependence on regeneration, nor any steady-state measurements of regeneration with cobalt-based redox shuttles. Therefore, in this chapter, we will seek to compare the self-exchange rate constants and reorganization energies of two cobalt OSRS,  $[\text{Co}(\text{bpy})_3]^{3+/2+}$  and cobalt bis(trithiacyclononane),  $[\text{Co}(\text{ttn})_2]^{3+/2+}$ , Figure 3.1, to the dye regeneration efficiency, electron diffusion length and consequently the photovoltaic performance.<sup>17</sup>

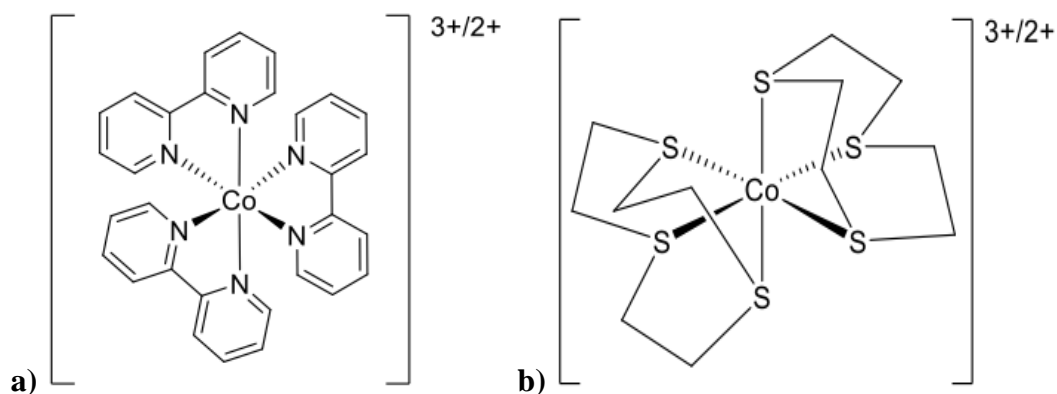


**Figure 3.1** Molecular structures of **a**) cobalt tris(2,2'-bipyridine),  $[\text{Co}(\text{bpy})_3]^{3+/2+}$  and **b**) cobalt bis(1,4,7-trithiacyclononane),  $[\text{Co}(\text{ttcn})_2]^{3+/2+}$ .

Stopped-flow spectroscopy will be used to isolate the self-exchange rate constants for both cobalt OSRSs. The measured self-exchange rate constants will be coupled with modeled IPCE data to help form a comprehensive picture of the effect of reorganization energy and driving force for the two key reactions involving a redox shuttle (regeneration and recombination) on the overall performance of DSSCs employing such one-electron OSRSs. All results and predictions based on the kinetics of regeneration and recombination are interpreted using the Marcus formalism for electron-transfer. The conclusions derived from these results are in stark contrast to previous reports. Finally, to help further improve the DSSC performance using these redox shuttles, I will discuss the effect of adding a thin insulating layer of aluminum oxide onto the  $\text{TiO}_2$  films before dye loading. Interestingly, the observed improvement arises from two separately distinct causes.

### 3.3 Experimental

#### 3.3.1 Materials

All reagents were obtained from commercial suppliers (Alfa Aesar or Sigma Aldrich) and used as received unless otherwise stated. Solvents used in the synthesis of

both redox shuttles were of reagent grade. Acetonitrile (anhydrous, Sigma Aldrich) and lithium bis(trifluoromethane)sulfonamide (99.95% trace metals basis, Sigma Aldrich), LiTFSI, used to carry out all kinetics studies and solar cell measurements were stored in a glovebox (MBRAUN Labmaster SP) under an inert and moisture free atmosphere. The D35cpdt (95%, Dyenamo) dye and chenodeoxycholic acid (Solaronix) were stored outside the glovebox and used as received.

### 3.3.2 Synthesis of Cobalt OSRS

The synthesis of  $[\text{Co}(\text{bpy})_3]^{3+/2+}$  and  $[\text{Co}(\text{ttcn})_2]^{3+/2+}$  were carried out by a previously reported procedure.<sup>17</sup> Briefly,  $[\text{Co}(\text{bpy})_3](\text{TFSI})_2$  was prepared by dissolving cobalt chloride hexahydrate,  $\text{CoCl}_2 \cdot 6\text{H}_2\text{O}$ , (1 eq.) into a methanolic solution. To a separate solution of methanol 2,2'-bipyridine, bpy, (3.1 eq.) was dissolved then charged to the stirring methanolic solution of  $\text{CoCl}_2 \cdot 6\text{H}_2\text{O}$ , which turned immediately from purple to dark yellow. The solution was allowed to stir ~2 hours before it was concentrated and precipitated using an excess of LiTFSI. The crude product was subsequently recrystallized in a minimal amount of acetonitrile and precipitated using diethyl ether yielding the pure paramagnetic product. Oxidation of  $[\text{Co}(\text{bpy})_3](\text{TFSI})_2$  was carried out by dissolving the complex (1 eq.) in a minimal amount of acetonitrile and adding (~1.2 eq.) AgTFSI dissolved in acetonitrile. After addition, the reaction mixture was stirred for ~1 hour before being syringe filtered and precipitated with diethyl ether to yield the pure  $[\text{Co}(\text{bpy})_3](\text{TFSI})_3$  product. <sup>1</sup>H NMR (500 MHz, acetonitrile-*d*<sub>3</sub>) δ 8.69 (dd, *J* = 8.1, 1.4 Hz, 6H), 8.49 (td, *J* = 7.9, 1.3 Hz, 6H), 7.74 (ddd, *J* = 7.5, 5.9, 1.5 Hz, 6H), 7.27 (dd, *J* = 6.0, 1.2 Hz, 6H).

Similarly,  $[\text{Co}(\text{ttcn})_2]^{3+/2+}$  was synthesized by dissolving cobalt tetrafluoroborate hexahydrate,  $\text{Co}(\text{BF}_4)_2 \cdot 6\text{H}_2\text{O}$ , (1 eq.) into an ethanolic solution. To a separate solution of ethanol 1,4,7-trithiacyclononane, ttcn, (2.1 eq.) was dissolved then charged to the stirring ethanolic solution of  $\text{Co}(\text{BF}_4)_2 \cdot 6\text{H}_2\text{O}$ . The reaction mixture was allowed to stir for ~2 hours before the ethanol was rotovapped off and the  $[\text{Co}(\text{ttcn})_2](\text{BF}_4)_2$  product was redissolved in water. Dissolution of the pure  $[\text{Co}(\text{ttcn})_2](\text{TFSI})_2$  product resulted upon addition of excess LiTFSI to the  $[\text{Co}(\text{ttcn})_2](\text{BF}_4)_2$  dissolved in water. Oxidation of  $[\text{Co}(\text{ttcn})_2](\text{TFSI})_2$  was carried out following the same procedure as  $[\text{Co}(\text{bpy})_3](\text{TFSI})_2$  described above. Note- $^1\text{H}$  NMR spectra of each paramagnetic and diamagnetic cobalt complex synthesized can be found in the Appendix, Figures A3.1-A3.4.

### 3.3.3 Cross-Exchange Kinetics

Stopped-flow spectroscopy was used to perform all experimental kinetic studies. Samples were measured using an Olis RSM 1000 DeSa rapid-scanning spectrophotometer with dual-beam UV-Vis recording to the Olis SpectralWorks software. The instrument contained a quartz cell with a 1 cm path length. Scans were taken once every millisecond with 1 nm resolution. The 150 W Xenon arc lamp was controlled using an LPS-220B Lamp Power Supply and held to within 80-83 W during each measurement. The temperature was also held constant at  $25 \pm 0.4^\circ\text{C}$  using a Forma Scientific Model 2006 bath and circulator. All  $[\text{Co}(\text{bpy})_3](\text{TFSI})_{3/2}$ ,  $[\text{Co}(\text{ttcn})_2](\text{TFSI})_{3/2}$  and 1,1'-dimethylferrocene,  $[\text{Fe}(\text{C}_5\text{H}_4\text{CH}_3)_2]$ , solutions were prepared using dry acetonitrile. The ionic strengths were adjusted to 0.1 M using LiTFSI.

Pseudo-first order conditions were implemented, which maintained at least a 10-fold excess of a single reactant and product species. The  $[\text{Co}(\text{bpy})_3](\text{TFSI})_3$  and

[Co(bpy)<sub>3</sub>](TFSI)<sub>2</sub> concentrations were held in excess while the [Co(bpy)<sub>3</sub>](TFSI)<sub>3</sub> concentration was varied during the reaction with [Fe(C<sub>5</sub>H<sub>4</sub>CH<sub>3</sub>)<sub>2</sub>]. The spectral changes were monitored at 650 nm, following the growing absorbance of the ferrocenium, [Fe(C<sub>5</sub>H<sub>4</sub>CH<sub>3</sub>)<sub>2</sub>]<sup>+</sup>, species. Absorbance measurements of the [Co(bpy)<sub>3</sub>](TFSI)<sub>2</sub> and [Co(ttcn)<sub>2</sub>]<sup>3+</sup> reactions were monitored at 480 nm, following the decay of the [Co(ttcn)<sub>2</sub>]<sup>3+</sup> species. The [Co(bpy)<sub>3</sub>](TFSI)<sub>2</sub> and [Co(bpy)<sub>3</sub>](TFSI)<sub>3</sub> concentrations for these reactions were held in excess while the [Co(bpy)<sub>3</sub>](TFSI)<sub>2</sub> concentration was varied. Scientific Data Analysis Software provided fits for the observed pseudo-first order rate constants,  $k_{obs}$ , using a nonlinear least-squares regression. Seven independent trials were averaged to provide the measured  $k_{obs}$  values. Absorbance plots for each pseudo-first order reaction were fit using:  $A = A_{\infty} + (A_0 - A_{\infty})e^{-k_{obs}t}$ . The second-order rate constants were calculated from the slopes of the  $k_{obs}$  versus excess concentration of [Co(bpy)<sub>3</sub>]<sup>3+</sup> or [Co(bpy)<sub>3</sub>]<sup>2+</sup> plots, which had goodness of fits:  $R^2 > 0.992$ . The error associated with the measured  $k_{obs}$  values were taken to be the standard deviation of the seven independent trials measured at a single concentration. The minimal error in concentration was propagated based on prepared stock solutions of each reaction mixture. Uniform mixing by the stopped-flow instrument was assumed for each independent trial.

### 3.3.4 Solar Cell Preparation

TiO<sub>2</sub> electrodes were prepared on FTO glass substrates (TEC 15, Hartford). The glass substrates were cleaned in an ultrasonic bath using (in order) soap water, deionized water, isopropyl alcohol and acetone. The glass substrates were then coated with a blocking layer of TiO<sub>2</sub> via ALD at 225°C using 1000 cycles of titanium isopropoxide (99.999% trace metals basis, Sigma-Aldrich) and water with reactant exposure times of 0.3 s and 0.015 s,

respectively. Nitrogen was allowed to purge the system for 5 s between exposures. All ALD depositions were done using a Savannah 200 instrument (Cambridge Nanotech Inc).<sup>18</sup> A highly transparent TiO<sub>2</sub> mesoporous film was prepared by doctor blading a paste of ~10-15 nm TiO<sub>2</sub> nanoparticles (Ti-Nanoxide HT/SP, Solaronix) onto the TiO<sub>2</sub> coated FTO-glass substrate. The TiO<sub>2</sub> layer was allowed to relax for 20 min at room temperature and 20 minutes at 80°C. The electrodes were then annealed by heating in air to 325°C for 5 min, 375°C for 5 min, 450°C for 5 min and 500°C for 15 min. For some electrodes, aluminum oxide, Al<sub>2</sub>O<sub>3</sub>, was deposited immediately following removal of the films from the oven. ALD was used to deposit the aluminum oxide layer via trimethylaluminum (TMA, Aldrich) and water as precursors. Al<sub>2</sub>O<sub>3</sub> was grown at 250°C using reactant exposure times of 10 s for both precursors and nitrogen purge times of 10 s between exposures.<sup>2</sup> The resulting electrodes were annealed again in air to 500°C for 30 min. The film thicknesses, *d*, were measured using a Dektak3 Surface Profiler. Two film thicknesses (7.2 μm and 3.7 μm) were prepared and used in DSSCs described herein. The electrodes were allowed to cool to a temperature of 80°C before being immersed in a D35cpdt dye solution consisting of 0.2 mM D35cpdt and 5 mM chenodeoxycholic acid in ethanol. After immersion the anodes were left to soak overnight in the dark. After 20-24 hours, the electrodes were rinsed with acetonitrile. To seal each cell, a ~25 μm thick Surlyn frame (Solaronix) was sandwiched between the TiO<sub>2</sub> nanoparticle electrode and the platinized FTO counter electrode, by applying light pressure at ~150°C. Electrolytes consisting of 0.2 M Co(II), 20 mM Co(III), 0.1 M LiTFSI and 10 mM Chenodeoxycholic acid in acetonitrile were introduced by capillary force through the two pre-drilled holes on the platinum counter electrode. The cells were subsequently sealed using a microglass coverslip and Surlyn film.

Note- the holes drilled on the counter electrode were positioned apart from the cell active area to avoid unwanted light loss from the sealing glass when light was illuminated from the counter electrode side.

### *3.3.5 Solar Cell Measurements*

Photoelectrochemical measurements were performed with a potentiostat (Autolab PGSTAT 126N) interfaced with a Xenon Arc Lamp. An AM 1.5 solar filter was used to simulate sunlight at  $100 \text{ mW cm}^{-2}$ . The light intensity was calibrated with a certified reference cell system (Oriol® Reference Solar Cell & Meter). An additional 400 nm long-pass filter was used to prevent direct excitation of the  $\text{TiO}_2$  in all light measurements. A black mask with an aperture area ( $0.4 \times 0.4 \text{ cm}^2$ ) was applied on top of the cell. Open circuit voltage decay (OCVD) measurements were performed by turning on the light until the voltage stabilized, followed by switching the light off and recording the decay of the voltage. Electrochemical impedance spectroscopy, EIS, measurements were performed in the dark using an FRA2 integrated with the PGSTAT 126N. The impedance spectra were recorded at applied voltages from -0.3 to -0.6 V, stepped in 25 mV increments, with a 10 mV alternating potential superimposed on the direct bias. Each impedance measurement consisted of frequency sweeps from  $5 \times 10^{-2}$  to  $1 \times 10^5$  Hz in equally spaced logarithmic steps. All IPCE measurements were made using monochromatic light at 10 nm intervals between 400 nm and 750 nm in the absence of bias light i.e. short circuit conditions. To obtain monochromatic light a monochromator (Horiba Jobin Yvon MicroHR) was interfaced to the 450 W Xenon arc light source. Both the entrance and exit slit widths were set to 0.75 mm to meet an 8 nm line width, which provided good resolution IPCEs. The photon flux of the light incident on the samples was measured with a laser power meter

(Nova II Ophir). The cells were illuminated from either the TiO<sub>2</sub> photoanode side (Front side- FS) or the Pt counter electrode side (Back side- BS).

### 3.3.6 Preparation of Sample Cells for Optical Measurements

Quantitative *in situ* measurements of the transmittance for complete DSSCs is difficult because most of the light from 400 nm to 600 nm is absorbed by the sensitized TiO<sub>2</sub> films used in the assembled cells, see Figure A3.5 of the Appendix. Therefore, additional TiO<sub>2</sub> films of various thicknesses (600 nm, 810 nm, 1.50 μm and 1.80 μm) were prepared by diluting the Solaronix HT/SP TiO<sub>2</sub> paste with α-terpineol and organic binders. Further, to avoid light leakage<sup>19</sup> from the side of the substrate and minimize substrate light absorption, high-quality microglass (VWR Micro Slides, 1.2mm thick) substrates were used instead of FTO glass substrates, Figure A3.6. The TiO<sub>2</sub> (HT/SP) film was deposited on the glass substrate using the same method as the TiO<sub>2</sub> nanoparticle electrodes described above. The resulting glass substrates with TiO<sub>2</sub> films were then sensitized using the same dye solution composition and soaking conditions described above. The glass substrates with sensitized TiO<sub>2</sub> films were then sandwiched with another 1.2 mm thick high quality microglass substrate using a 25 μm Surlyn film frame in the same manner as the solar cell assembly procedure previously described. Electrolyte was induced through pre-drilled holes of the glass slide. Four sample sandwich cells of each thickness (600 nm, 810 nm, 1.50 μm and 1.80 μm) with each electrolyte ([Co(bpy)<sub>3</sub>]<sup>3+/2+</sup> and [Co(ttcn)<sub>2</sub>]<sup>3+/2+</sup>) were assembled. A total of 48 cells were made for the 12 conditions. Nonsensitized blank control cells were also made in parallel with sensitized sample cells.

### 3.3.7 Optical Measurements

Optical transmittance and reflectance measurements were performed using a Perkin-Elmer Lambda 35 UV-vis spectrometer with a Labsphere integrating sphere. Measurements of both sample cells and blank cells were taken. The absorbance of dye-sensitized TiO<sub>2</sub> films ( $A_D$ ) of various film thicknesses were calculated through the following Equation (2.1) which was adapted from thin film absorbance measurements:<sup>20</sup>

$$A_D = -\log \left( \frac{T_B \times T_D}{T_B^2 - (R_D - R_B) T_D^2} \right) = \frac{-\alpha_{dye} \times d}{\ln 10} \quad \text{Eq. (3.1)}$$

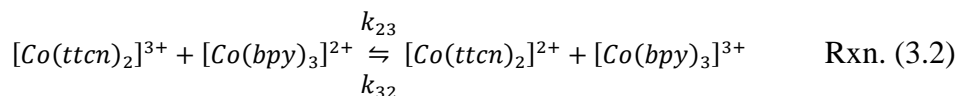
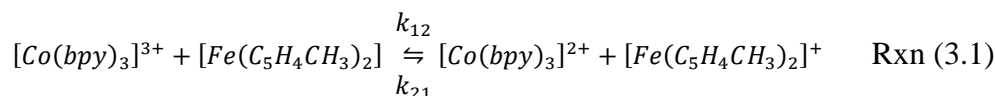
here  $T_B$  and  $R_B$  are the transmittance and reflectance of the nonsensitized blank cells, while  $T_D$  and  $R_D$  are the transmittance and reflectance of the sensitized sample cells. Equation (2.1) only applies when competitive absorption from the electrolyte is minimal compared to absorption from the sensitized film. Because there is negligible absorption from the TiO<sub>2</sub> film and glass substrate in the visible region of the light spectrum, the blank sample cell can be simplified to an integrated substrate without any solid-liquid interface. Thus, the sensitized sample can be considered as the addition of a single strongly absorbing thin film layer to the blank. In this way, the measured absorbance of the dyed film can be simplified to a two-layer thin film model, which takes into account the overall reflectance, and scattered light of the complicated sandwiched sample cell system.<sup>21</sup> The sensitized film absorbance was used to make a plot of  $A_D$  vs.  $d$ . A straight line was fit to the plot of  $A_D$  vs.  $d$  and the absorptivity of the sensitized film was determined from the slope, see Figures A3.7-A3.14 of the Appendix which led to the fit plot of Figure A3.11. This procedure

assumes dye loading is homogeneous throughout the TiO<sub>2</sub> film. A porosity,  $P = 0.7$ , was used to account for light absorption by the electrolyte filled in the pores.

### 3.4 Results and Discussion

#### 3.4.1 Determining the self-exchange kinetics of $[Co(bpy)_3]^{3+/2+}$ and $[Co(ttcn)_2]^{3+/2+}$

The second order forward cross-exchange rate constants,  $k_{12}$  and  $k_{23}$ , as well as the reverse cross-exchange rate constants,  $k_{21}$  and  $k_{32}$ , for the following two reactions were determined using stopped-flow spectroscopy:



1,1'-dimethylferrocene,  $[Fe(C_4H_4CH_3)_2]$ , was chosen for the cross-exchange reaction with  $[Co(bpy)_3]^{3+/2+}$  due to its well defined self-exchange rate constant and known outersphere one-electron transfer mechanism.<sup>22,23</sup> The small potential difference between  $[Co(bpy)_3]^{3+/2+}$  and  $[Fe(C_4H_4CH_3)_2]^{+/0}$ , Figure A3.15, was also favorable for slowing down the electron exchange between the two redox shuttles on a time scale that could be observable by stopped-flow. The decision to cross  $[Co(ttcn)_2]^{3+}$  with  $[Co(bpy)_3]^{2+}$  was made for similar arguments. Figure 3.2a shows a plot of the absorbance at 650 nm vs. time, which corresponds to the growth of the ferrocenium,  $[Fe(C_4H_4CH_3)_2]^+$ , species due to the oxidation of  $[Fe(C_4H_4CH_3)_2]$  by  $[Co(bpy)_3]^{3+}$ , while Figure 3.3a shows a plot of the absorbance at 480 nm vs. time, which corresponds to the decay of the  $[Co(ttcn)_2]^{3+}$  species due to its reduction by  $[Co(bpy)_3]^{2+}$ . In both Reactions (3.1) and (3.2), the  $[Co(bpy)_3]^{3+/2+}$

species were held in excess. The resulting observed pseudo-first order rate constants,  $k_{obs}$ , for Reactions (3.1) and (3.2) were expressed by:

$$k_{obs} = k_{12}[Co(bpy)_3]^{3+} + k_{21}[Co(bpy)_3]^{2+} \quad \text{Eq. (3.2)}$$

$$k_{obs} = k_{23}[Co(bpy)_3]^{2+} + k_{32}[Co(bpy)_3]^{3+} \quad \text{Eq. (3.3)}$$

A straight-line fit to the  $k_{obs}$  values versus the concentration of excess reactant material, Figures 3.2b and 3.3b, provided the forward and reverse cross-exchange rate constants from the slopes and y-intercepts, respectively. The reaction mixtures and observed pseudo-first order rate constants for both electron-transfer reactions can be found in the Appendix Tables A3.1 and A3.2.

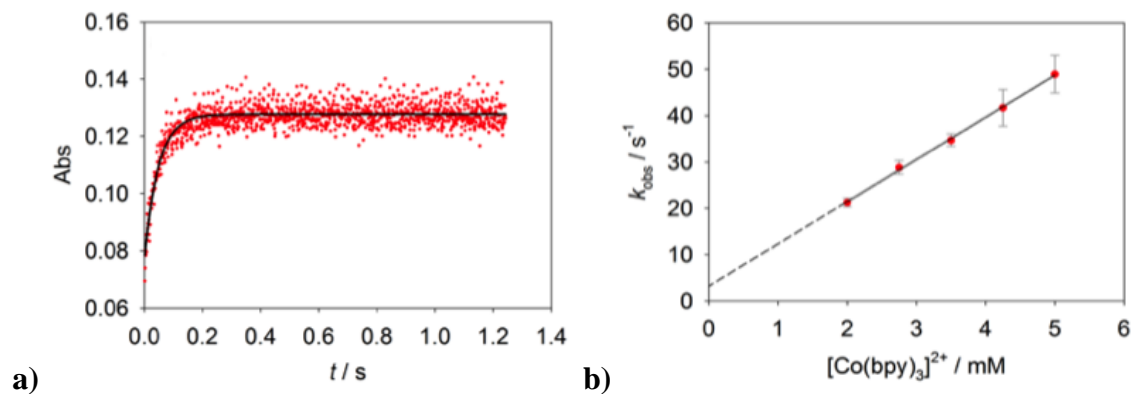


**Figure 3.2 a)** Plot of absorbance at 650 nm vs. time, corresponding to the growth of the  $[Fe(C_5H_4CH_3)_2]^+$  species (red dots) and the resulting fit (black line) for the reduction of  $[Co(bpy)_3]^{3+}$  ( $2.00 \times 10^{-3}$  M) by  $[Fe(C_5H_4CH_3)_2]$  ( $1.90 \times 10^{-4}$  M). **b)** Observed pseudo-first order rate constants,  $k_{obs}$ , versus the excess reactant concentrations for the reactions between  $[Fe(C_5H_4CH_3)_2]$  and  $[Co(bpy)_3]^{3+}$  in acetonitrile with 0.1 M LiTFSI at  $25 \pm 0.4^\circ C$ .

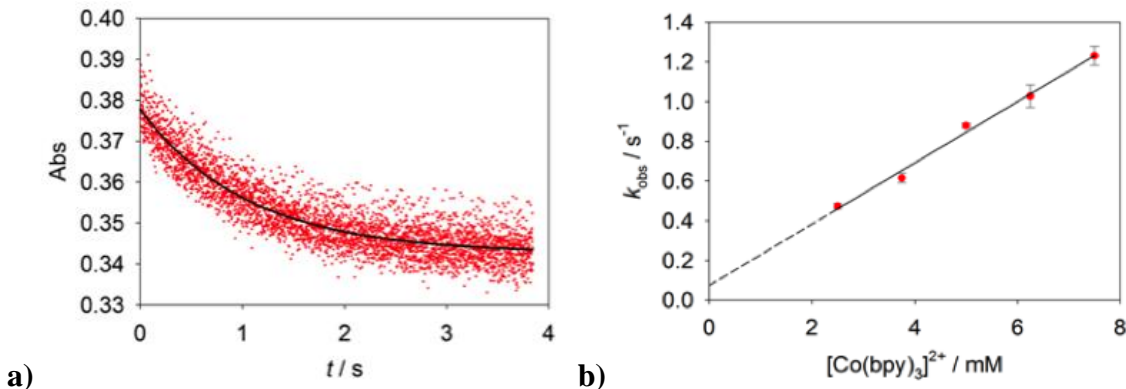


**Figure 3.3** **a)** Plot of absorbance at 480 nm vs. time, corresponding to decay of the  $[\text{Co}(\text{ttcn})_2]^{3+}$  species (red dots) and the resulting fit (black line) for the reduction of  $[\text{Co}(\text{ttcn})_2]^{3+}$  ( $1.45 \times 10^{-4} \text{ M}$ ) by  $[\text{Co}(\text{bpy})_3]^{2+}$  ( $6.25 \times 10^{-3} \text{ M}$ ). **b)** Observed pseudo-first order rate constants,  $k_{\text{obs}}$ , versus the excess reactant concentrations for the reactions between  $[\text{Co}(\text{bpy})_3]^{2+}$  and  $[\text{Co}(\text{ttcn})_2]^{3+}$  in acetonitrile with 0.1 M LiTFSI at  $25 \pm 0.4^\circ\text{C}$ .

the Marcus cross-relation, Equation (3.4), was used to calculate the self-exchange rate constant,  $k_{22}$ , for  $[\text{Co}(\text{bpy})_3]^{3+/2+}$  using the experimentally determined cross-exchange rate constant,  $k_{12}$ , for Reaction (3.1) and the previously determined self-exchange rate constant,  $k_{11}$ , for  $[\text{Fe}(\text{C}_5\text{H}_4\text{CH}_3)_2]^{+0}$ .<sup>13,24</sup> This experimentally determined  $k_{22}$  value for  $[\text{Co}(\text{bpy})_3]^{3+/2+}$  was then used to find the self-exchange rate constant,  $k_{33}$ , for  $[\text{Co}(\text{ttcn})_2]^{3+/2+}$  by again applying Equation (3.4) and the measured cross-exchange rate constant,  $k_{23}$ , measured for Reaction (3.2).

$$k_{12} = \sqrt{k_{11}k_{22}K_{12}f_{12}W_{12}} \quad \text{Eq. (3.4)}$$

According to Equation (3.4), the cross-exchange rate constant is a function of the corresponding self-exchange rate constants,  $k_{11}$  and  $k_{22}$ , of the donor and acceptor species, the equilibrium constant,  $K_{12}$ , for the forward electron-transfer reaction, a non-linear

correction term,  $f_{12}$ , and an electrostatic work term,  $W_{12}$ , related to bringing the reactants into contact.

The work associated with bringing the precursor complexes a separation distance,  $r$ , for electron transfer to occur was calculated using Equations (3.5) and (3.6).<sup>16,25</sup>

$$W_{12} = \exp[-(w_{12} + w_{21} - w_{11} - w_{22})/2RT] \quad \text{Eq. (3.5)}$$

$$w_{ij}(r) = \frac{z_i z_j q^2 N_A}{4\pi\epsilon_0 \epsilon r(1+\beta r)} \quad \text{Eq. (3.6)}$$

Equation (3.6) was used to determine the work associated with the forward cross-exchange reaction,  $w_{12}$ , the reverse cross-exchange,  $w_{21}$ , and the self-exchanges of both reactants,  $w_{11}$  and  $w_{22}$ , for Reactions (3.1) and (3.2), respectively. In the equation above,  $z_i$  and  $z_j$  are the charges of the reacting ions,  $q$  is the charge on an electron,  $N_A$  is Avogadro's constant,  $\epsilon_0$  is the permittivity of free space,  $\epsilon$  is the static dielectric of the medium,  $\beta = (2q^2 N_A I / 1000 \epsilon_0 \epsilon k_B T)^{1/2}$ ,  $I$  is the ionic strength of the solution and  $k_B$  is Boltzmann's constant. It is assumed in these calculations that the work is primarily Coulombic, the reactants are spherical, and the separation distance,  $r$ , is simply the center-to-center distance when the reactants come into contact. The work term calculated for each redox couple was determined to be 1.8 and 1.1 for Reactions (3.1) and (3.2), respectively. However, in both cases the calculated work is a crude approximation as the Debye-Huckel model is not expected to provide rigorously accurate results at high ionic strengths such as those used in these measurements (0.1 M supporting electrolyte).

The non-linear correction terms  $f_{12}$  and  $f_{23}$  for both reactions were calculated using Equation (3.7), assuming a frequency factor,  $Z = 10^{11} \text{ M}^{-1} \text{ s}^{-1}$ .<sup>5,13,24,26</sup> In this calculation

work is also considered and is calculated using Equation (3.6). In the case of Reaction (3.1),  $w_{12}$  and  $w_{21}$ , represent the work associated with the forward and reverse cross-exchange reactions, while  $w_{11}$  and  $w_{22}$  represent the work associated with each self-exchange reaction, as mentioned above.

$$\ln f_{12} = \frac{1}{4} \frac{\left( \ln K_{12} + \frac{w_{12} - w_{21}}{k_B T} \right)^2}{\ln \left( \frac{k_{11} k_{22}}{Z^2} \right) + \left( \frac{w_{11} + w_{22}}{k_B T} \right)} \quad \text{Eq. (3.7)}$$

The equilibrium constant for the cross-exchange reactions can be determined according to:

$$-nF\Delta E = -RT \ln K_{12} \quad \text{Eq. (3.8)}$$

where  $n$  is the number of electrons transferred ( $n = 1$ ),  $F$  is Faraday's constant,  $\Delta E$  is the formal potential difference between the oxidant and reductant in solution,  $R$  is the gas constant and  $T$  is the temperature. Cyclic voltammetry (CV) measurements, shown in Figure A3.15, indicate formal potentials,  $E^o$ , of -0.114 V, -0.051 V and 0.003 V vs. Ferrocene (Fc) for  $[\text{Fe}(\text{C}_5\text{H}_4\text{CH}_3)_2]^{+/0}$ ,  $[\text{Co}(\text{bpy})_3]^{3+/2+}$  and  $[\text{Co}(\text{ttn})_2]^{3+/2+}$ , respectively. The calculated equilibrium constants using Equation (3.8) for Reactions (3.1) and (3.2) provided values of  $11.6 \pm 2.3$  and  $8.2 \pm 1.2$  and are displayed in the Appendix, Tables A3.3 and A3.4. From detailed balance, the equilibrium constants can also be determined from the cross-exchange rate constants for the forward and reverse reactions:

$$K_{12} = k_{12}/k_{21} \quad \text{Eq. (3.9)}$$

This approach produced equilibrium constants of  $5.7 \pm 1.2$  and  $3.1 \pm 1.7$ . The good agreement between the equilibrium constants determined from thermodynamic (CVs) and kinetics measurements substantiate the measured cross-exchange rate constants.

The self-exchange rate constant,  $k_{11}$ , for  $[\text{Fe}(\text{C}_5\text{H}_4\text{CH}_3)_2]$  has been previously reported to be  $(8.3 \pm 0.8) \times 10^6 \text{ M}^{-1}\text{s}^{-1}$ , using NMR analysis.<sup>22</sup> Taking this value for  $k_{11}$ , the self-exchange rate constant,  $k_{22}$ , for  $[\text{Co}(\text{bpy})_3]^{3+/2+}$  was calculated to be  $0.27 \pm 0.06 \text{ M}^{-1}\text{s}^{-1}$ , which is in excellent agreement with the literature value  $0.645 \text{ M}^{-1}\text{s}^{-1}$  measured under similar conditions.<sup>23,27</sup> The calculated self-exchange rate constant for  $[\text{Co}(\text{bpy})_3]^{3+/2+}$  was then used to determine a value of  $(9.1 \pm 0.7) \times 10^3 \text{ M}^{-1}\text{s}^{-1}$  for the  $[\text{Co}(\text{ttn})_2]^{3+/2+}$  self-exchange rate constant,  $k_{33}$ . A summary of the self-exchange rate constants can be found in Table 3.1. It should be noted that the self-exchange value determined for  $[\text{Co}(\text{ttn})_2]^{3+/2+}$  is slightly lower than those reported in aqueous media. Previous studies in aqueous solvent provided values of  $1.3 \times 10^4 \text{ M}^{-1}\text{s}^{-1}$  using stopped-flow spectroscopy and  $1.3 \times 10^5 \text{ M}^{-1}\text{s}^{-1}$  using  $^{59}\text{Co}$  NMR spectroscopy.<sup>28,29</sup> A possible explanation for this variability would involve the difference in solvent dielectric and the work associated with forming the precursor complexes. The higher dielectric of water requires less work to bring the ions together for electron transfer, which results in an enhanced coupling, a higher pre-exponential value for the electron transfer rate and a faster electron transfer rate constant.

**Table 3.1** Summary of self-exchange rate constants,  $k_{11}$ ,  $k_{22}$ , and  $k_{33}$ , and the corresponding reduction potentials,  $E^\circ$ , for  $[\text{Fe}(\text{C}_5\text{H}_4\text{CH}_3)_2]^{+/0}$ ,  $[\text{Co}(\text{bpy})_3]^{3+/2+}$  and  $[\text{Co}(\text{ttn})_2]^{3+/2+}$  in acetonitrile with 0.1 M LiTFSI at  $25 \pm 0.4^\circ\text{C}$ .

$x$	Redox Couple	$E^\circ$ (mV vs. Fc)	$k_{xx}$ ( $\text{M}^{-1}\text{s}^{-1}$ )
1	$[\text{Fe}(\text{C}_5\text{H}_4\text{CH}_3)_2]^{+/0}$	$-114 \pm 5$	$(8.3 \pm 0.8) \times 10^6$
2	$[\text{Co}(\text{bpy})_3]^{3+/2+}$	$-51 \pm 2$	$0.27 \pm 0.06$
3	$[\text{Co}(\text{ttn})_2]^{3+/2+}$	$3 \pm 3$	$(9.1 \pm 0.7) \times 10^3$

Determination of the self-exchange rate constants for  $[\text{Co}(\text{bpy})_3]^{3+/2+}$  and  $[\text{Co}(\text{ttn})_2]^{3+/2+}$  provides predictive power in estimating the effects on regeneration efficiencies and the magnitude of recombination upon implementing these redox shuttles into dye cells. Discussed in detail below is how to interpret these two pathways (regeneration and recombination) using the principals of Marcus theory. Given the minimal potential difference between the two redox shuttles, the anticipated increase in regeneration efficiency will primarily result from the large difference in self-exchange rate constants when taking the ratio of the cross-exchange reactions. Although enhanced regeneration is expected for the faster exchanging  $[\text{Co}(\text{ttn})_2]^{3+/2+}$  complex, the degree of recombination can be amplified as well, which is reflected in the overall diffusion length of the electron in these cells. By modeling experiment i.e. external quantum yield measurements (IPCE) and comparing to theory, we can further confirm the rate limiting pathways that dictate the DSSC performance.

### 3.4.2 Understanding Regeneration using Marcus Theory

The regeneration efficiency of DSSCs is dictated by the branching ratio of dye regeneration and dye recombination as given by:

$$\eta_{reg} \cong \frac{[R]k_{reg}}{[R]k_{reg} + [n_s]k_{rec,D^+}} \quad \text{Eq. (3.10)}$$

Here  $[R]$  is the concentration of the reduced form of the redox shuttle,  $[n_s]$  is the surface electron concentration of  $\text{TiO}_2$ ,  $k_{reg}$  is the dye regeneration rate constant and  $k_{rec,D^+}$  is the rate constant for dye recombination at the  $\text{TiO}_2$  interface.<sup>30</sup> To simplify Equation (3.10) such that we elucidate the observed effect of regeneration by only changing the redox shuttle for a given dye we must: (1) Keep the concentrations of the electrolytes the same, thus  $[R]$  is constant and (2) Assume, as a first order approximation, that  $[n_s]$  is constant for the two redox shuttles at short circuit under low light intensity, i.e. the conditions of the IPCE measurements. Under these circumstances, regeneration then becomes dictated by the regeneration rate constant, which can be described using the modified Marcus cross-relation mentioned in Chapter 1, Equation (1.4).<sup>31</sup> Here, however, we refer to  $k_{R/R^+}$  as  $k_{22}$  and  $k_{33}$  which are the self-exchange rate constants for  $[\text{Co}(\text{bpy})_3]^{3+/2+}$  and  $[\text{Co}(\text{tcn})_2]^{3+/2+}$ , respectively. The self-exchange rate constants for dyes,  $k_{D/D^+}$ , attached to the  $\text{TiO}_2$  surface are ill-defined, however they are independent of the redox shuttle and therefore cancels out when taking the ratio of the regeneration rate constants. The non-linear correction term,  $f$ , and work term,  $W$ , will also fall out of the equation as they are expected to be about the same for the two redox couples which have the same charge and a similar size. Therefore, the relative rates of regeneration can be determined by taking the ratio of the redox shuttle's self-exchange rate constants and equilibrium constants:

$$\frac{k_{reg,tcn} = \sqrt{k_{33}K_{D/tcn}}}{k_{reg,bpy} = \sqrt{k_{22}K_{D/bpy}}} \quad \text{Eq. (3.11)}$$

where  $K_{D/ttcn}$  and  $K_{D/bpy}$  are the equilibrium constants for the dye ( $D$ ) regeneration reactions with  $[\text{Co}(\text{ttcn})_2]^{3+/2+}$  and  $[\text{Co}(\text{bpy})_3]^{3+/2+}$ , respectively. The equilibrium constants were determined from the potential difference of the dye and redox shuttles according to Equation (3.8). For this study an organic dye, D35cpdt, was chosen based on its well-documented energetics, favorable optical properties, see Figure A3.12, and commercial availability. The ground state potential of D35cpdt adsorbed onto a nanoparticle ITO film was determined to be 1.08 V vs. NHE by CV, see Figure A3.16 of the Appendix, and is in good agreement with the previously reported literature value.<sup>32</sup> Based on the measured potentials for each redox shuttle and the ground state potential of the adsorbed dye, the driving forces for regeneration were calculated to be 0.506 eV and 0.452 eV for  $[\text{Co}(\text{bpy})_3]^{3+/2+}$  and  $[\text{Co}(\text{ttcn})_2]^{3+/2+}$ . Based on differences in self-exchange rate constants and the calculated equilibrium constants, the regeneration rate constant using  $[\text{Co}(\text{ttcn})_2]^{2+}$  is expected to be 57 times larger than  $[\text{Co}(\text{bpy})_3]^{2+}$ , despite only a 54 mV smaller driving force. In section 2.4.5 below, the regeneration efficiency for  $[\text{Co}(\text{bpy})_3]^{2+}$  will be directly measured, which will allow us to compare the enhanced regeneration rate predicted by Marcus theory to the experimentally determined regeneration efficiency for  $[\text{Co}(\text{ttcn})_2]^{2+}$ .

### 3.4.3 Understanding Recombination using Marcus Theory

The charge collection efficiency,  $\eta_{cc}$ , is a function of diffusion length,  $L_n$ , and thus the electron lifetime,  $\tau_n$ . The electron lifetime can be expressed as the ratio of surface electron concentration of  $\text{TiO}_2$  (at a given potential),  $[n_s]$ , to the rate at which they are being lost, i.e. the rate of recombination,  $U_{rec,R+}$ . Under the assumption that the rate of recombination is dominated by electron-transfer from the conduction band to the oxidized

form of the redox shuttle, Co(III) or  $[R^+]$ , it can be described by the second order rate equation:

$$U_{rec,R^+} = [R^+][n_s]k_{rec,R^+} \quad \text{Eq. (3.12)}$$

where  $k_{rec,R^+}$  is the recombination rate constant for electron-transfer. The rate constant can be described by Marcus theory using the following equation:<sup>16</sup>

$$k_{rec,R^+} = k_{et,max} e^{-(\Delta G^0 + \lambda_{et})^2 / 4\lambda k_b T} \quad \text{Eq. (3.13)}$$

where  $-\Delta G^0$  is the driving force of the electron transfer and  $\lambda_{et}$  is the reorganization energy associated with the electron transfer. The prefactor,  $k_{et,max}$ , is the rate constant at optimal exoergicity, obtained when  $-\Delta G^0 = \lambda_{et}$ , and has been shown to have a value of  $10^{-17} - 10^{-16} \text{ cm}^4 \text{ s}^{-1}$ . In addition,  $k_{et,max}$  has a weak dependence on the reorganization energy ( $k_{et,max} \propto \lambda_{et}^{-1/2}$ ). The driving force is the difference between the conduction band energy,  $\mathbf{E}_{cb}$ , and the formal potential of the redox shuttle. Ondersma et al. used variable temperature spectroelectrochemistry to measure  $\mathbf{E}_{cb}$  for  $\text{TiO}_2$  in a comparable electrolyte ( $\text{Li}^+$  in acetonitrile) and determined a value of approximately  $-0.8 \text{ V}$  vs  $\text{Ag}/\text{AgCl}$ .<sup>3</sup> Thus, the driving force of recombination to  $[\text{Co}(\text{bpy})_3]^{3+}$  and  $[\text{Co}(\text{ttcn})_2]^{3+}$  is  $-1.106 \text{ eV}$  and  $-1.165 \text{ eV}$ , respectively.

The reorganization energy for the recombination reaction can be derived from results of the self-exchange rate constants,  $k_{22}$  and  $k_{33}$ , described above. The total

reorganization energies,  $\lambda_{22}$  or  $\lambda_{33}$ , for the  $[\text{Co}(\text{bpy})_3]^{3+/2+}$  and  $[\text{Co}(\text{tcn})_2]^{3+/2+}$  self-exchange reactions can be calculated using the relationship shown in Equation (3.14).<sup>33</sup>

$$k_{22} = \nu_n e^{-\lambda_{22}/4k_bT} \quad \text{Eq. (3.14)}$$

where  $\nu_n$  is the frequency factor.<sup>31</sup> The value for the vibrational frequency term can range from  $10^{11} - 10^{13} \text{ s}^{-1}$  depending on the changes attributed to the outersphere (solvent) or innersphere (bond length changes) reaction coordinate during electron-transfer.<sup>15,16,33</sup> A value of  $10^{13} \text{ s}^{-1}$  was used as the frequency factor,  $\nu_n$ , for both  $[\text{Co}(\text{bpy})_3]^{3+/2+}$  and  $[\text{Co}(\text{tcn})_2]^{3+/2+}$  due to the larger innersphere contribution to the total reorganization energy, *vide infra*.<sup>16</sup> The total reorganization energies,  $\lambda_{22}$  or  $\lambda_{33}$ , are the sum of both the outersphere,  $\lambda_o$ , and innersphere reorganization energies,  $\lambda_i$ . The outersphere self-exchange reorganization energy can be obtained from the dielectric continuum theory, Equation (3.15),<sup>31</sup>

$$\lambda_o = \frac{(\Delta z q)^2}{4\pi\epsilon_o} \left( \frac{1}{a} - \frac{1}{R_e} \right) \left( \frac{1}{n_{\text{sol}}^2} - \frac{1}{\epsilon_{\text{sol}}^2} \right) \quad \text{Eq. (3.15)}$$

where  $\Delta z$  is the change in charge of the cobalt complex after electron transfer,  $q$  is the charge of an electron,  $\epsilon_o$  is the permittivity of free space,  $\epsilon_{\text{sol}}$  is the static dielectric of acetonitrile (36)<sup>34</sup>,  $n_{\text{sol}}$  is the refractive index of acetonitrile (1.3442)<sup>35</sup>,  $a$  is the radius of the reactant, and  $R_e$  is the reactant center-to-center separation distance ( $R_e = 2a$ ). The radii of  $[\text{Co}(\text{bpy})_3]^{3+/2+}$  and  $[\text{Co}(\text{tcn})_2]^{3+/2+}$  were taken to be 6.5 Å and 5 Å, respectively.<sup>16</sup> Using the total reorganization energy calculated from Equation (3.14), and the outersphere

reorganization energy calculated from Equation (3.15), the innersphere reorganization energy was also determined for each complex via subtraction. Results of all reorganization energies are displayed in Table 3.2.

For the recombination reaction, the innersphere reorganization energy should be half of the value derived from the homogeneous self-exchange reaction because half as many molecules participate in each electron-transfer. The outersphere reorganization energy for the acceptor is again calculated using the dielectric continuum theory, but revised to include the refractive index of anatase TiO<sub>2</sub> ( $n_{\text{TiO}_2} = 2.54$ )<sup>35</sup> and the static dielectric of anatase TiO<sub>2</sub> ( $\epsilon_{\text{TiO}_2} = 114$ ).<sup>36,37</sup>

$$\lambda_{o,\text{TiO}_2} = \frac{(\Delta zq)^2}{8\pi\epsilon_0} \left[ \frac{1}{a} \left( \frac{1}{n_{\text{sol}}^2} - \frac{1}{\epsilon_{\text{sol}}} \right) - \frac{1}{2R_e} \left( \frac{1}{n_{\text{sol}}^2} \left( \frac{n_{\text{TiO}_2}^2 - n_{\text{sol}}^2}{n_{\text{TiO}_2}^2 + n_{\text{sol}}^2} \right) - \frac{1}{\epsilon_{\text{sol}}} \left( \frac{\epsilon_{\text{TiO}_2} - \epsilon_{\text{sol}}}{\epsilon_{\text{TiO}_2} + \epsilon_{\text{sol}}} \right) \right) \right] \quad \text{Eq. (3.16)}$$

Thus, the total reorganization energy associated with recombination at the TiO<sub>2</sub> interface becomes:  $\lambda_{et} = \lambda_{o,\text{TiO}_2} + \lambda_i/2$ . It is evident from the calculated values, Table 3.2, that the reorganization energy of [Co(bpy)<sub>3</sub>]<sup>3+/2+</sup> is dominated by a large innersphere reorganization energy as expected.<sup>15</sup>

Substituting the values of  $k_{et,max}$ ,  $-\Delta G^0$ , and  $\lambda_{et}$  determined for [Co(bpy)<sub>3</sub>]<sup>3+/2+</sup> and [Co(ttcn)<sub>2</sub>]<sup>3+/2+</sup> into Equation (3.13), allows the rate constants for recombination from the TiO<sub>2</sub> conduction band to be calculated. Since the concentration of the oxidized redox shuttles were kept constant, and assuming the surface electron concentration is nominally identical at the same electrode potentials, the relative electron lifetimes of the two redox shuttles can be determined.

**Table 3.2** Summary of the reorganization energies determined for the  $[\text{Co}(\text{bpy})_3]^{3+/2+}$  and  $[\text{Co}(\text{ttcn})_2]^{3+/2+}$  redox shuttles, and the parameters used for calculation of  $k_{rec,R+}$ .

Parameter	$[\text{Co}(\text{bpy})_3]^{3+/2+}$	$[\text{Co}(\text{ttcn})_2]^{3+/2+}$
$\lambda_o$ (eV)	0.583	0.757
$\lambda_{in}$ (eV)	2.63	1.38
$\lambda_{22}$ or $\lambda_{33}$ (eV)	3.21	2.14
$\lambda_{o,\text{TiO}_2}$ (eV)	0.369	0.543
$\lambda_{et}$ (eV)	1.68	1.23
$-\Delta G^0$ (eV)	1.11	1.17
$k_{et,max}$ ( $\text{cm}^4\text{s}^{-1}$ )	$5.50 \times 10^{-17}$	$6.42 \times 10^{-17}$
$k_{rec,R+}$ ( $\text{cm}^4\text{s}^{-1}$ )	$8.15 \times 10^{-18}$	$6.18 \times 10^{-17}$

This further allows comparisons of the expected electron diffusion lengths by Equation (3.17), since the electron diffusion coefficient,  $D_n$ , is independent of the identity of the redox shuttle.

$$L_n = \sqrt{D_n \tau_n} \quad \text{Eq. (3.17)}$$

The rate constant for recombination to  $[\text{Co}(\text{ttcn})_2]^{3+}$  is  $\sim 7.6$  times larger than for  $[\text{Co}(\text{bpy})_3]^{3+}$ , corresponding to a  $\sim 7.6$  times lower electron lifetime for  $[\text{Co}(\text{ttcn})_2]^{3+}$  compared to  $[\text{Co}(\text{bpy})_3]^{3+}$ . Therefore, the electron diffusion length with  $[\text{Co}(\text{bpy})_3]^{3+/2+}$  is estimated to be  $\sim 2.8$  times longer than that of  $[\text{Co}(\text{ttcn})_2]^{3+/2+}$ . It should be noted once again that recombination from trap states was ignored in this analysis. Recombination from the conduction band for both redox shuttles is well within the Marcus normal region. Under such conditions, recombination from conduction band electrons should dominate

contributions from trap states.<sup>3</sup> Based on these predicted values, we will compare to the measured diffusion lengths extracted from the modeled IPCE measurements below.

#### 3.4.4 Measurements and Modeling of Regeneration

Figure 3.4a shows plots of typical current density ( $J$ ) vs. applied voltage ( $V$ ) curves for DSSCs employing the  $[\text{Co}(\text{bpy})_3]^{3+/2+}$  and  $[\text{Co}(\text{ttn})_2]^{3+/2+}$  redox shuttles under simulated 1 sun illumination from both the front side (FS) (solid line) and back side (BS) (dashed line) directions. FS refers to the  $\text{TiO}_2$  substrate, while BS refers to the counter electrode / electrolyte side. The average short circuit photocurrent density ( $J_{sc}$ ), open circuit photovoltage ( $V_{oc}$ ) and fill factors ( $FF$ ) derived from the  $J$ - $V$  curves of 12 cells are given in Table 3.3. Under FS illumination, the  $J_{sc}$ 's,  $V_{oc}$ 's and  $FF$ 's of the  $[\text{Co}(\text{bpy})_3]^{3+/2+}$  cells were comparable to the  $[\text{Co}(\text{ttn})_2]^{3+/2+}$  cells. However, the overall performance for cells under BS illumination were much worse, with a significant difference between DSSCs employing the two different redox shuttles. While the BS  $J_{sc}$  decreased by  $\sim 70\%$  compared to FS illumination for  $[\text{Co}(\text{bpy})_3]^{3+/2+}$  cells, the  $J_{sc}$  for the  $[\text{Co}(\text{ttn})_2]^{3+/2+}$  cells decreased by  $\sim 90\%$ . The reduced photocurrent under BS illumination is likely due to lower charge collection efficiencies resulting from electron diffusion lengths shorter than the film thickness.<sup>38</sup> Figure 3.5b shows the average IPCE derived from eight cells containing the two different electrolytes under FS and BS illumination, with error bars representing the standard deviation. The integrated IPCEs produce  $J_{sc}$  values that agree with the measured  $J_{sc}$ 's, indicating that each IPCE contains the information relevant to the observed  $J$ - $V$  behavior.

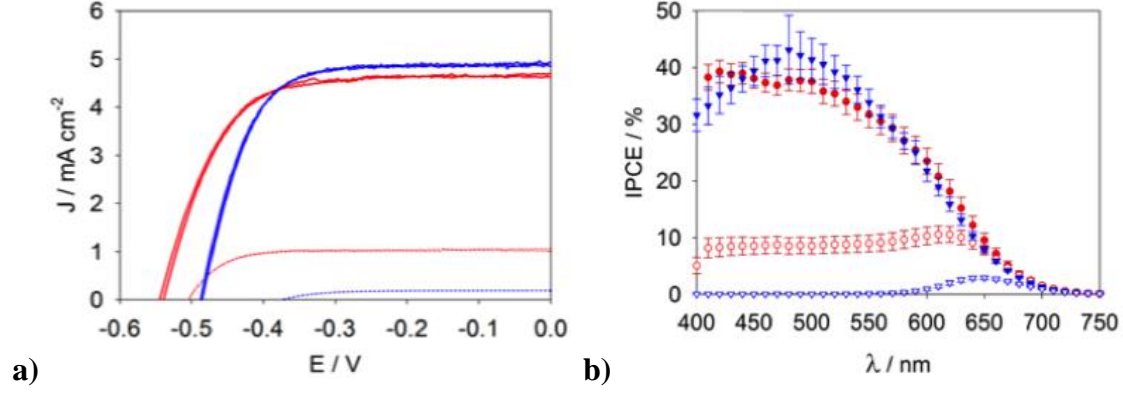


**Figure 3.4 a)** Plots of representative  $J$ - $V$  curves of DSSCs with the  $[\text{Co}(\text{bpy})_3]^{3+/2+}$  (red) and  $[\text{Co}(\text{ttcn})_2]^{3+/2+}$  (blue) redox shuttles for FS (solid) and BS (dotted) illumination directions. **b)** IPCE curves for DSSCs with the  $[\text{Co}(\text{bpy})_3]^{3+/2+}$  (red circles) and  $[\text{Co}(\text{ttcn})_2]^{3+/2+}$  (blue triangles) redox shuttles under FS (filled) and BS (hollow) illumination; film thickness,  $7.1 \mu\text{m}$ .

**Table 3.3** Average  $J$ - $V$  characteristics of twelve DSSCs under simulated 1 sun AM 1.5G illumination ( $100 \text{ mW cm}^{-2}$ ).

Redox shuttle	$[\text{Co}(\text{bpy})_3]^{3+/2+}$		$[\text{Co}(\text{ttcn})_2]^{3+/2+}$	
	FS	BS	FS	BS
$\eta$ (%)	$1.64 \pm 0.10$	$0.45 \pm 0.14$	$1.55 \pm 0.17$	$0.05 \pm 0.00$
$J_{\text{sc}}$ ( $\text{mA cm}^{-2}$ )	$4.64 \pm 0.41$	$1.19 \pm 0.55$	$4.62 \pm 0.59$	$0.22 \pm 0.23$
$V_{\text{oc}}$ (V)	$0.53 \pm 0.01$	$0.50 \pm 0.01$	$0.48 \pm 0.05$	$0.48 \pm 0.02$
$FF$	$0.66 \pm 0.04$	$0.76 \pm 0.04$	$0.69 \pm 0.05$	$0.66 \pm 0.02$

The measured IPCE can be described as the product of the light harvesting efficiency,  $\eta_{LH}$ , the electron injection efficiency,  $\eta_{inj}$ , the dye regeneration efficiency,  $\eta_{reg}$ , and the charge collection efficiency  $\eta_{cc}$ :

$$IPCE(\lambda) = \eta_{LH}(\lambda)\eta_{cc}(\lambda)\eta_{inj}(\lambda)\eta_{reg}(\lambda) \quad \text{Eq. (3.18)}$$

Figure 3.5 shows the light harvesting efficiency for both FS and BS illumination directions, determined from the photogeneration profiles described in the supporting information of our original publication.<sup>21</sup> The cells absorb strongly up to 600 nm; however, the  $\eta_{LH}$  for the BS illumination is slightly attenuated by the platinized counter electrode and liquid electrolyte between the counter electrode and TiO<sub>2</sub> film. Aside from the minor attenuated light harvest at  $\lambda < 600$  nm, there appears to be no obvious difference between FS and BS illumination for at  $\lambda > 600$  nm, which suggests that the observed differences in light harvesting efficiency cannot explain the differences in IPCEs for the different illumination directions. In addition to illumination direction, the light harvesting efficiencies are essentially the same for both redox shuttles as shown in Figure 3.5 and thus cannot account for the observed difference in their IPCE curves either.

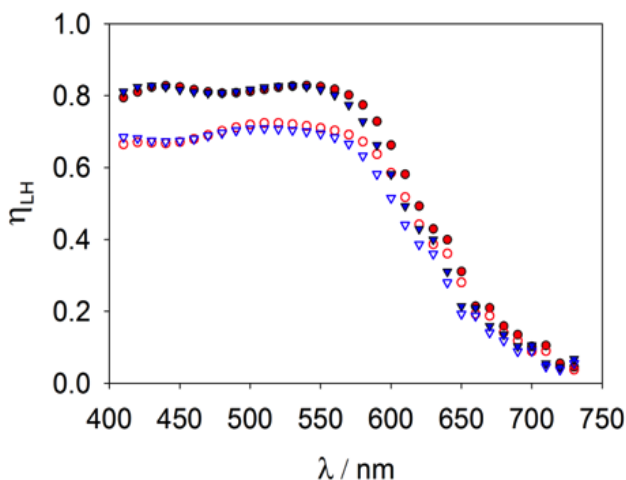


**Figure 3.5** Light harvesting efficiency ( $\eta_{LH}$ ) of 7.1  $\mu\text{m}$  thick TiO<sub>2</sub> films sensitized with the D35cpdt dye in DSSCs with the [Co(bpy)<sub>3</sub>]<sup>3+/2+</sup> (red circles) and [Co(ttcn)<sub>2</sub>]<sup>3+/2+</sup> (blue triangles) redox shuttles under FS (filled) and BS illumination (hollow).

Assuming that  $\eta_{inj}$  and  $\eta_{reg}$  are position independent, they cancel out by taking the BS/FS ratio of the IPCEs, leaving a ratio for the product of charge collection efficiency  $\eta_{cc}$ ,

and light harvesting efficiency,  $\eta_{LH}$ . The optical parameters that determine the light harvesting efficiency ratio were measured independently and the results are shown in Figure 3.5. If the light harvesting is normalized, the IPCE ratio simply becomes the ratio of the charge collection efficiencies, which is a function of the electron diffusion length,  $L_n$ , and film thickness,  $d$ . The film thickness was determined independently via profilometry. Isolation of  $L_n$  can be achieved from fitting the ratio of the IPCE spectra from the BS and FS illumination using Equation (3.19):<sup>39-41</sup>

$$\frac{IPCE(BS)}{IPCE(FS)} = \frac{T_{pt}T_e \left[ -(L_n(\alpha_{dye} + \alpha_e) + 1)e^{2d/L_n} + 2L_n(\alpha_{dye} + \alpha_e)e^{d((\alpha_{dye} + \alpha_e) + (1/L_n))} - L_n(\alpha_{dye} + \alpha_e) + 1 \right]}{(L_n(\alpha_{dye} + \alpha_e) - 1)e^{d((\alpha_{dye} + \alpha_e) + (2/L_n))} + (L_n(\alpha_{dye} + \alpha_e) + 1)e^{d(\alpha_{dye} + \alpha_e)} - 2L_n(\alpha_{dye} + \alpha_e)e^{d/L_n}} \quad \text{Eq. (3.19)}$$

Plots of  $T_{Pt}$ ,  $T_e$ ,  $\alpha_{dye}$  and  $\alpha_e$  are provided in the Appendix. IPCE(BS)/IPCE(FS) spectra were fit with  $L_n$  as the only free-fitting parameter using a nonlinear least-squares method. The IPCE(BS) values for the cells containing  $[\text{Co}(\text{ttn})_2]^{3+/2+}$  with a 7.1  $\mu\text{m}$   $\text{TiO}_2$  film were too low to acquire a meaningful fit from the IPCE ratio. Therefore, additional sets of cells were prepared with a  $\text{TiO}_2$  thickness of 3.7  $\mu\text{m}$ , which exhibited larger IPCE(BS), see Figure A3.18 of the Appendix. Figure 3.6 shows the BS/FS IPCE ratios for DSSCs employing  $[\text{Co}(\text{bpy})_3]^{3+/2+}$  (7.1  $\mu\text{m}$  thick  $\text{TiO}_2$ ) and  $[\text{Co}(\text{ttn})_2]^{3+/2+}$  (3.7  $\mu\text{m}$  thick  $\text{TiO}_2$ ) redox shuttles, as well as the results from fitting to Equation (3.19). From these fits, the electron diffusion length was determined to be  $\sim 3.3$   $\mu\text{m}$  for  $[\text{Co}(\text{bpy})_3]^{3+/2+}$  and  $\sim 1.3$   $\mu\text{m}$  for  $[\text{Co}(\text{ttn})_2]^{3+/2+}$ . The electron diffusion length for  $[\text{Co}(\text{bpy})_3]^{3+/2+}$  agrees well with a recently reported literature value of 2.8  $\mu\text{m}$ .<sup>32</sup> The results of the diffusion lengths derived from analysis of the IPCE measurements are in excellent agreement with the values estimated using Marcus theory applied to heterogeneous electron-transfer. Diffusion lengths estimated using

Marcus theory predicted cells employing  $[\text{Co}(\text{bpy})_3]^{3+/2+}$  to sustain  $\sim 2.8$  times longer diffusion lengths compared to  $[\text{Co}(\text{ttn})_2]^{3+/2+}$ , which was experimentally determined to be  $\sim 2.5$  times longer by IPCE measurements. Further support of the measured diffusion lengths came from lifetime measurements of  $[\text{Co}(\text{bpy})_3]^{3+/2+}$  and  $[\text{Co}(\text{ttn})_2]^{3+/2+}$  using the methods of OCVD and EIS. The measured lifetime for  $[\text{Co}(\text{bpy})_3]^{3+/2+}$ , normalized to a constant potential/capacitance, was determined to be  $\sim 4$  times longer than that of  $[\text{Co}(\text{ttn})_2]^{3+/2+}$ , see Figure 3.8a below and Figure A3.22 of the Appendix. This equates to a  $\sim 2$  times longer diffusion length for  $[\text{Co}(\text{bpy})_3]^{3+/2+}$  compared to  $[\text{Co}(\text{ttn})_2]^{3+/2+}$ , which also provides reasonable agreement between theory and measurements.

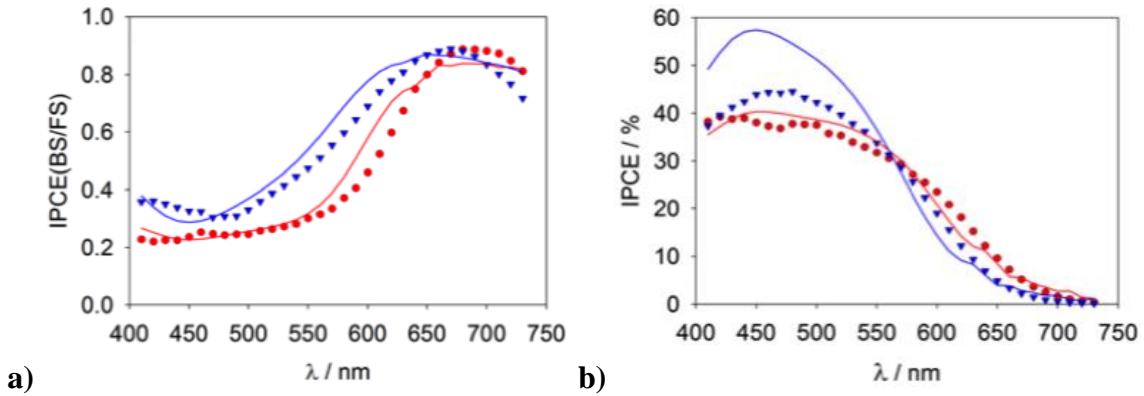


**Figure 3.6** Experiment (shape) and fit (line) results of **a)** IPCE(BS/FS) ratios and **b)** IPCEs for DSSCs employing the  $[\text{Co}(\text{bpy})_3]^{3+/2+}$  (red circles) and  $[\text{Co}(\text{ttn})_2]^{3+/2+}$  (blue triangles) redox shuttles.

Once the value of  $L_n$  is known, the IPCE, either FS or BS, can be fit to extract values for  $\eta_{inj} \times \eta_{reg}$ . For example, the IPCE(FS) is given by Equation (3.20):

$$IPCE(FS) = \frac{(1-R)L_n\eta_{inj}\eta_{reg}\alpha_{dye}e^{-d(\alpha_{dye}+\alpha_e)}(L_n(\alpha_{dye}+\alpha_e)-1)e^{d((\alpha_{dye}+\alpha_e)+(2/L_n))} + (L_n(\alpha_{dye}+\alpha_e)+1)e^{d(\alpha_{dye}+\alpha_e)} - 2L_n(\alpha_{dye}+\alpha_e)e^{d/L_n}}{[L_n^2(\alpha_{dye}+\alpha_e)^2](e^{2d/L_n+1})} \quad \text{Eq. (3.20)}$$

with only the product of  $\eta_{inj}$  and  $\eta_{reg}$  as a single fitting parameter. Using this approach, the product  $\eta_{inj} \times \eta_{reg}$  was  $\sim 0.54$  for  $[\text{Co}(\text{bpy})_3]^{3+/2+}$  and  $\sim 1$  for  $[\text{Co}(\text{ttcn})_2]^{3+/2+}$ . Since the same sensitizer and electrolyte, except for identity of redox shuttle, is used in both systems, the electron injection efficiency is taken to be identical. Therefore, the difference in  $\eta_{inj} \times \eta_{reg}$  for the two redox shuttles can be attributed to only differences in dye regeneration efficiencies. Thus, the regeneration efficiency,  $\eta_{reg}$ , for  $[\text{Co}(\text{bpy})_3]^{3+/2+}$  is  $\sim 0.54$ , whereas  $\eta_{reg}$  for  $[\text{Co}(\text{ttcn})_2]^{3+/2+}$  is  $\sim 1$ . Comparing the experimentally determined regeneration efficiencies to those predicted by Marcus theory, the  $\sim 57$  times larger regeneration rate constant for  $[\text{Co}(\text{ttcn})_2]^{3+/2+}$  compared to  $[\text{Co}(\text{bpy})_3]^{3+/2+}$  results in an increased regeneration efficiency from 0.54 to 0.99, once again, in excellent agreement with our results.

It should be noted that our measured  $\eta_{reg}$  is in stark contrast with the literature. A prior report using  $[\text{Co}(\text{bpy})_3]^{3+/2+}$  paired with the very similar D35 dye, found that a driving force of only 0.39 eV was necessary to produce a regeneration efficiency of 91 %, which is higher than observed here.<sup>42</sup> However, the regeneration efficiency in that work was determined with transient absorption (TA) measurements on sensitized photoanodes in contact with electrolyte solutions instead of complete devices. The importance of using complete devices to make accurate measurements of regeneration has been addressed by Barnes and coworkers.<sup>43</sup> Jennings and Li, *et al.* also characterized dye regeneration and dye recombination kinetics for the iodide/triiodide redox shuttle in complete DSSCs by TA, IPCE and impedance spectroscopy measurements over a range of background light intensities at open circuit. They found that the regeneration efficiency measured from an

incomplete cell system is an overestimation.<sup>44,45</sup> Thus, the differences between our reported regeneration efficiencies and prior reports of this system can be attributed to the different measurement conditions.

#### 3.4.5 *Effect of an Alumina Layer*

The deposition of insulating blocking layers on the TiO<sub>2</sub> surface has been demonstrated to be an effective means of reducing the rate of back electron-transfer to the oxidized redox shuttle in order to increase the electron diffusion length and overall efficiency of DSSCs employing outersphere redox shuttles.<sup>2,18,46</sup> We note that a blocking layer on the TiO<sub>2</sub> surface should likewise slow the rate of recombination to the oxidized dye. Since the regeneration efficiency is determined by the kinetic competition of dye reduction by the reduced form of the redox shuttle and electrons in TiO<sub>2</sub>, slowing down back electron-transfer from TiO<sub>2</sub> should also improve the regeneration efficiency. Thus, the addition of a blocking layer should improve the performance of [Co(ttcn)<sub>2</sub>]<sup>3+/2+</sup> and [Co(bpy)<sub>3</sub>]<sup>3+/2+</sup>, however for different reasons. In order to test these ideas, we applied one ALD cycle of alumina onto the TiO<sub>2</sub> substrate prior to dye loading. Figure 3.7 shows the FS and BS IPCEs for DSSCs employing the [Co(bpy)<sub>3</sub>]<sup>3+/2+</sup> (7.1 μm thick TiO<sub>2</sub>) and [Co(ttcn)<sub>2</sub>]<sup>3+/2+</sup> (7.1 μm thick TiO<sub>2</sub>) redox shuttles with the addition of 1 ALD cycle of aluminum oxide, Al<sub>2</sub>O<sub>3</sub>.

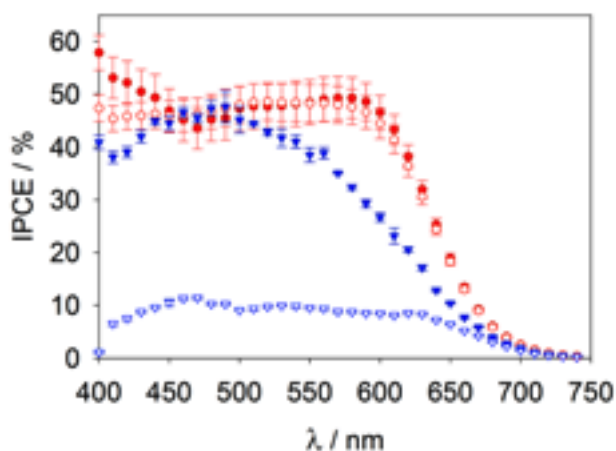


**Figure 3.7** IPCE curves for DSSCs with 1 ALD cycle of Al<sub>2</sub>O<sub>3</sub> employing the [Co(bpy)<sub>3</sub>]<sup>3+/2+</sup> (red circles) and [Co(ttcn)<sub>2</sub>]<sup>3+/2+</sup> (blue triangles) redox shuttles under FS (filled) and BS illumination (hollow).

The FS and BS IPCE's for [Co(bpy)<sub>3</sub>]<sup>3+/2+</sup> are nominally identical, which indicates that  $L_n > d$  and a good fit for a value of  $L_n$  is not feasible. In this case, assuming that the  $\eta_{cc}$  is unity, the product of  $\eta_{inj} \times \eta_{reg}$  can be extracted simply by dividing the IPCE by the  $\eta_{LH}$ . This results in a value of  $\sim 0.7$  for  $\eta_{inj} \times \eta_{reg}$ . (see Figure A3.21 of the Appendix) As described above, the diffusion length is equal to the square root of the product of the electron diffusion coefficient,  $D_n$ , and the electron lifetime,  $\tau_n$ , according to Equation (3.17). Since  $D_n$  is independent of the alumina layer or redox shuttle, the diffusion length can be determined by comparing ratios of the square root of electron lifetimes. Figure 3.8a shows electron lifetimes plotted as a function of cell voltage which were determined from open circuit photovoltage decay measurements.<sup>47</sup> Electrochemical impedance spectroscopy measurements were also performed which produced similar values of  $\tau_n$ , and verified that the conduction band and electron concentration was constant through comparisons of the capacitance as shown previously, see Figure A3.22.<sup>46</sup> Through a global fit of the lifetimes

with a fixed slope, the electron lifetime was found increased by a factor of  $8.6 \pm 1.1$ , which indicates an increase in  $L_n$  by  $\sqrt{8.6}$  to  $\sim 9.53 \mu\text{m}$  for  $[\text{Co}(\text{bpy})_3]^{3+/2+}$  with an alumina layer compared to unmodified electrodes. This result is consistent with  $L_n > d$  as suggested above. Use of this estimated  $L_n$  value allowed for the fitting of IPCE's which produced a value of  $\sim 0.7$  for  $\eta_{inj} \times \eta_{reg}$ . A similar procedure was applied to DSSCs containing the  $[\text{Co}(\text{ttn})_2]^{3+/2+}$  redox shuttle. In this case, since the electron lifetime increases by a factor of  $8.6 \pm 1.1$ , it results in an increase of  $L_n$  by  $\sqrt{8.6}$  to  $\sim 3.8 \mu\text{m}$ . The FS and BS IPCEs are sufficiently different with the  $[\text{Co}(\text{ttn})_2]^{3+/2+}$  redox shuttle, however, to allow for an accurate fit of the IPCE ratio. This fit produced a value of  $\sim 2.5 \mu\text{m}$  for  $[\text{Co}(\text{ttn})_2]^{3+/2+}$ . Fitting the IPCEs with this value of  $L_n$  produced a value of  $\sim 0.7$  for  $\eta_{inj} \times \eta_{reg}$ . A summary of all fit values for above DSSCs conditions are given in Table 3.

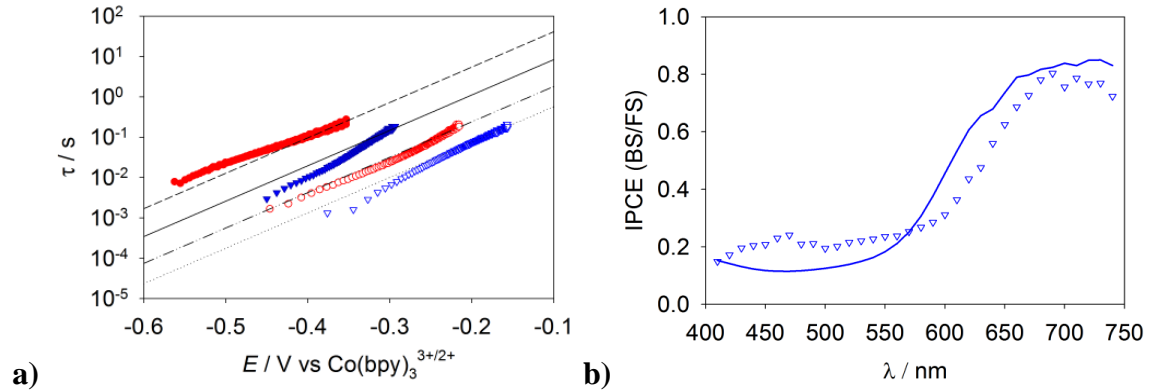


**Figure 3.8 a)** Lifetimes vs. applied voltage (symbols) and the global fit (lines) used for the IPCE ratio fits for DSSCs employing the  $[\text{Co}(\text{bpy})_3]^{3+/2+}$  (red dots) and  $[\text{Co}(\text{ttn})_2]^{3+/2+}$  (blue dots) redox shuttles with (filled) and without (hollow) 1 ALD cycle  $\text{Al}_2\text{O}_3$  coating. **b)** IPCE ratio (blue triangles) and fit results (blue line) to Equation (3.19) for DSSCs with 1 ALD cycle of  $\text{Al}_2\text{O}_3$  coating employing the  $[\text{Co}(\text{ttn})_2]^{3+/2+}$  redox shuttle.

**Table 3.4** Fit values of  $L_n$  and  $\eta_{inj} \times \eta_{reg}$  for DSSCs employing  $[\text{Co}(\text{bpy})_3]^{3+/2+}$  and  $[\text{Co}(\text{ttn})_2]^{3+/2+}$  redox shuttles with and without 1 ALD cycle of  $\text{Al}_2\text{O}_3$  as a blocking layer. Also shown is the driving force for regeneration,  $-\Delta G_{reg}^0$ , for each of the two redox shuttles.

Redox Shuttle	ALD Cycles	$L_n / \mu\text{m}$	$\eta_{inj} \times \eta_{reg}$	$-\Delta G_{reg}^0$ (eV)
$[\text{Co}(\text{bpy})_3]^{3+/2+}$	0	$3.25 \pm 0.16$	$0.54 \pm 0.03$	0.506
	1	9.53*	$0.74 \pm 0.04$	
$[\text{Co}(\text{ttn})_2]^{3+/2+}$	0	$1.30 \pm 0.05$	$1.00 \pm 0.05$	0.452
	1	$2.45 \pm 0.04$	$0.72 \pm 0.01$	

As mentioned above, addition of the alumina blocking layer was shown to reduce the rate of recombination to the oxidized redox shuttle by a factor of  $8.6 \pm 1.1$ , as it presents essentially a tunneling barrier layer for electrons to transfer from  $\text{TiO}_2$  to solution. Since the alumina layer is also between the  $\text{TiO}_2$  and dye, it should also slow recombination to the oxidized dye by a comparable amount. The addition of a barrier layer should not affect the rate of dye regeneration, however. Therefore, assuming the rate constant of recombination to the oxidized dye is reduced by a factor of  $8.6 \pm 1.1$  upon the addition of an alumina layer, and a constant rate of regeneration, the regeneration efficiency for  $[\text{Co}(\text{bpy})_3]^{3+/2+}$  would increase from 0.54 to 0.91. The product of  $\eta_{inj} \times \eta_{reg}$  for DSSCs with an alumina layer and the  $[\text{Co}(\text{bpy})_3]^{3+/2+}$  redox shuttle was found to be  $\sim 0.7$ , however. These results suggest that the injection efficiency is diminished.

Since regeneration with  $[\text{Co}(\text{ttn})_2]^{3+/2+}$  is quantitative on the unmodified electrodes, slowing down recombination to the oxidized dye with the addition of an alumina blocking layer cannot increase the regeneration efficiency. We note that it is also not reasonable to expect the alumina layer to decrease the regeneration efficiency, since the dye contacting the solution and redox shuttle are unaltered. Because the  $\text{Al}_2\text{O}_3$  blocking layer is between

the TiO<sub>2</sub> nanoparticle and the dye, however, it should reduce the rate of charge injection as it weakens the electronic coupling between the dye and TiO<sub>2</sub> surface.<sup>48,49</sup> Therefore, the decrease in  $\eta_{inj} \times \eta_{reg}$  to  $\sim 0.7$  for DSSCs with an alumina layer and the [Co(ttcn)<sub>2</sub>]<sup>3+/2+</sup> redox shuttle is attributed to a decrease in injection efficiency. This assignment is consistent for both redox shuttles, which should both produce quantitative regeneration (with an alumina layer), however, D35cpdt only injects through the alumina barrier layer with an efficiency of  $\sim 70\%$ .

If we further investigate the injection limitations of the D35cpdt dye, we can make comparisons based on the structurally similar D35 dye. The excited state lifetime of the D35 dye co-absorbed with chenodeoxycholic acid on TiO<sub>2</sub> and ZrO<sub>2</sub> surfaces from time resolved fluorescence measurements are reported to be  $\tau_{TiO_2} \sim 0.15$  ns and  $\tau_{ZrO_2} \sim 1.42$  ns. Since the conduction band of ZrO<sub>2</sub> is too high for electron injection by the excited dye, the injection efficiency can be determined via  $\eta_{inj} \approx 1 - \tau_{TiO_2} / \tau_{ZrO_2}$  which produces  $\sim 90\%$  injection efficiency.<sup>50</sup> Because D35 and D35cpdt dyes have the same donor and anchoring groups, they have similar LUMO levels ( $E_{LUMO}(D35) = -1.21$  V vs. NHE<sup>51</sup> and  $E_{LUMO}(D35cpdt) = -1.17$  V vs. NHE<sup>52</sup>) situated on the cyanoacetic acid unit that binds to the TiO<sub>2</sub> surface. The similar driving forces and electronic couplings between the two dyes should result in negligible differences in rates of electron injection with the two dyes. Therefore, assuming the electron injection rate is also slowed down by a factor of  $8.6 \pm 1.1$  upon the addition of an alumina barrier layer, with a constant rate of competitive decay processes, the injection yield would decrease from 90% to 51%. Relatively small differences in cell preparation can affect the band edge positions and therefore rate of injection, which can account for quantitative injection found here compared to the 90 %

injection efficiency reported previously.<sup>50</sup> In addition, the tunneling barrier height of injection should be somewhat smaller than for recombination since the electrons are higher in energy, which should result in a smaller attenuation of injection compared to recombination with the addition of the alumina layer. Some combination of these factors can readily account for the differences in injection efficiency from 100–70% found here, compared to the 90–51% predicted from literature values. In any case, the quantitative injection for D35cpdt on a bare TiO<sub>2</sub> electrode and the 30% reduction in injection efficiency with an alumina barrier layer reported herein is in good general agreement with previous literature results. Finally, it should be noted that the large effect of decreasing the injection efficiency with an Al<sub>2</sub>O<sub>3</sub> blocking layer found here differs from previous reports using inorganic Ru-based dyes, since the latter exhibits longer excited state lifetimes of ~20 ns.<sup>40,53</sup>

### 3.5 Conclusion

Cross-exchange measurements were performed for two redox shuttles, [Co(bpy)<sub>3</sub>]<sup>3+/2+</sup> and [Co(ttcn)<sub>2</sub>]<sup>3+/2+</sup>, to determine their respective self-exchange rate constants and reorganization energies associated with electron-transfer. The self-exchange rate constant of [Co(ttcn)<sub>2</sub>]<sup>3+/2+</sup> was measured to be ~10<sup>4</sup> larger than [Co(bpy)<sub>3</sub>]<sup>3+/2+</sup>. The origin of the fast exchange kinetics can be attributed to the fact that [Co(ttcn)<sub>2</sub>]<sup>2+</sup> is low spin d<sup>7</sup> whereas [Co(bpy)<sub>3</sub>]<sup>2+</sup> is high spin d<sup>7</sup>. Upon oxidation, both complexes become low spin d<sup>6</sup>. As a consequence, charge-transfer changes the electron occupancy of the antibonding e<sub>g</sub> orbitals for both cobalt complexes (assuming approximately O<sub>h</sub> symmetry), which produces a rather large change in innersphere reorganization energy associated with metal-ligand bond lengths. Indeed, previously determined EXAFS measurements reported Co-N bond length

changes of  $\sim 0.19$  Å upon reduction of related complexes to  $[\text{Co}(\text{bpy})_3]^{3+}$  such as  $[\text{Co}(\text{phen})_3]^{3+}$ .<sup>15</sup> The reduction of  $[\text{Co}(\text{ttn})_2]^{3+}$  is expected to have a smaller effect on bond length change since the occupation of the  $e_g$  orbitals changes by a single electron compared to the two electron loss for  $[\text{Co}(\text{bpy})_3]^{3+}$  or  $[\text{Co}(\text{phen})_3]^{3+}$ . This is consistent with the faster self-exchange rate constant and lower innersphere reorganization energy determined herein. The faster self-exchange rate constant of  $[\text{Co}(\text{ttn})_2]^{3+/2+}$  induces more efficient dye regeneration, corroborating the predictions made by the Marcus cross-relation. For both redox shuttles, the reorganization energies were determined to be much larger ( $>1$  eV) than the driving force for regeneration. The larger reorganization energy of  $[\text{Co}(\text{bpy})_3]^{3+/2+}$  compared to  $[\text{Co}(\text{ttn})_2]^{3+/2+}$  is consistent with slower recombination and longer diffusion lengths. It was observed that the addition of insulating alumina layer between  $\text{TiO}_2$  and the dye was able to improve the electron diffusion length as well as dye regeneration efficiency. However, use of the D35cpdt dye resulted in diminished injection efficiencies when adding the alumina layer. To circumvent such a problem, it is necessary to utilize a dye with a longer excited state lifetime.

All reported results are consistent with regeneration and recombination reactions in the Marcus normal region for both cobalt redox shuttles. This is obviously a very important point in considering design rules for alternative redox shuttles. The key to significantly improving the device efficiency is to minimize the energy required to drive the key forward reactions (injection and regeneration), without compromising the electron diffusion length by increasing recombination. Our results point to two potential pathways to further improve the efficiency of DSSCs with OSRSs. The first is to further hinder recombination to fast redox shuttles such as  $[\text{Co}(\text{ttn})_2]^{3+/2+}$  (or Ferrocene) which are capable of quantitative dye

regeneration with minimal driving force, but are limited by short electron diffusion lengths. The alternative is to utilize a redox shuttle such as  $[\text{Co}(\text{bpy})_3]^{3+/2+}$  with a sufficient electron diffusion length to allow quantitative carrier collection, but is limited by inefficient regeneration. Chapter 4 will further exploit this alternative by using the properties of  $[\text{Co}(\text{bpy})_3]^{3+/2+}$  and attempting to circumvent the inefficient regeneration through the use of a tandem electrolyte containing a fast self-exchanging cobalt (IV/III) complex  $[\text{Co}(\text{ptpy})_3]^{+/0}$ . As demonstrated in this chapter, both of the aforementioned strategies can be effectively utilized through modification of the photoanode with a tunneling barrier layer, as it can increase both the dye regeneration efficiency and collection efficiency by slowing recombination to the dye and redox shuttle, respectively. For this to be really effective, however, an energetically matched dye must be identified with a sufficient excited state lifetime to efficiently inject through the barrier layer. Alternatively, as these reactions are in the Marcus normal region, it should be possible to concomitantly increase regeneration and charge collection with a fast exchanging redox shuttle by moving the redox potential more negative. The expectation being that minimization of driving force between the conduction band and the redox shuttle will drastically slow recombination. Our efforts to synthesize such a redox shuttle will be discussed in Chapter 5. For this strategy to be effective, the redox shuttle would also have to be matched to a near-IR absorbing dye with a more negative ground state potential. It is our belief that such a multi-component optimization could lead to DSSCs, which exhibit efficiencies competitive to Perovskite and other third generation PVs.

## **APPENDIX**

## APPENDIX

**Table A3.1** Observed pseudo-first order rate constants,  $k_{\text{obs}}$ , and the initial reaction mixtures for the cross-exchange between  $[\text{Co}(\text{bpy})_3]^{3+}$  and  $[\text{Fe}(\text{C}_5\text{H}_4\text{CH}_3)_2]$ , see Reaction (3.1) of the main text.

$[\text{Fe}(\text{C}_5\text{H}_4\text{CH}_3)_2] / (\text{M})$	$[\text{Co}(\text{bpy})_3]^{3+} / (\text{M})$	$[\text{Co}(\text{bpy})_3]^{2+} / (\text{M})$	$k_{\text{obs}} / (\text{s}^{-1})$
$1.90 \times 10^{-4}$	$2.00 \times 10^{-3}$	$2.00 \times 10^{-3}$	$21.2 \pm 0.9$
	$2.75 \times 10^{-3}$		$28.8 \pm 1.5$
	$3.50 \times 10^{-3}$		$34.7 \pm 1.3$
	$4.25 \times 10^{-3}$		$41.7 \pm 3.9$
	$5.00 \times 10^{-3}$		$49.0 \pm 4.0$

**Table A3.2** Observed pseudo-first order rate constants,  $k_{\text{obs}}$ , and the initial reaction mixtures for the cross-exchange between  $[\text{Co}(\text{ttn})_2]^{3+}$  and  $[\text{Co}(\text{bpy})_3]^{2+}$ , see Reaction (3.2) of the main text.

$[\text{Co}(\text{ttn})_2]^{3+} / (\text{M})$	$[\text{Co}(\text{bpy})_3]^{2+} / (\text{M})$	$[\text{Co}(\text{bpy})_3]^{2+} / (\text{M})$	$k_{\text{obs}} / (\text{s}^{-1})$
$1.45 \times 10^{-4}$	$2.50 \times 10^{-3}$	$1.50 \times 10^{-3}$	$0.47 \pm 0.01$
	$3.75 \times 10^{-3}$		$0.62 \pm 0.02$
	$5.00 \times 10^{-3}$		$0.88 \pm 0.01$
	$6.25 \times 10^{-3}$		$1.0 \pm 0.06$
	$7.50 \times 10^{-3}$		$1.2 \pm 0.05$

**Table A3.3** Kinetic summary of the cross-exchange rate constants,  $k_{12}$  and  $k_{21}$ , measured equilibrium constants for the forward reaction,  $K_{12}$ , the nonlinear correction term,  $f_{12}$ , and work term,  $W_{12}$ , associated with bringing precursor complexes together for Reaction (3.1) between  $[\text{Fe}(\text{C}_5\text{H}_4\text{CH}_3)_2]$  and  $[\text{Co}(\text{bpy})_3]^{3+}$  in acetonitrile with 0.1 M LiTFSI at  $25 \pm 0.4^\circ\text{C}$ .

<b>Kinetic Parameter</b>	<b>Reaction (3.1) cross-exchange values</b>
$K_{12}$ (Nernst)	$11.6 \pm 2.3$
$K_{12}$ ( $k_{12} / k_{21}$ )	$5.7 \pm 1.2$
$k_{12} / (\text{M}^{-1}\text{s}^{-1})$	$(9.1 \pm 0.2) \times 10^3$
$k_{21} / (\text{M}^{-1}\text{s}^{-1})$	$(1.6 \pm 0.3) \times 10^3$
$f_{12}$	0.99
$W_{12}$	1.8

**Table A3.4** Kinetic summary of the cross-exchange rate constants,  $k_{23}$  and  $k_{32}$ , measured equilibrium constants for the forward reaction,  $K_{23}$ , the nonlinear correction term,  $f_{23}$ , and work term,  $W_{23}$ , associated with bringing precursor complexes together for Reaction (3.2) between  $[\text{Co}(\text{bpy})_3]^{2+}$  and  $[\text{Co}(\text{ttcn})_2]^{3+}$  in acetonitrile with 0.1 M LiTFSI at  $25 \pm 0.4^\circ\text{C}$ .

<b>Kinetic Parameter</b>	<b>Reaction (3.2) cross-exchange values</b>
$K_{23}$ (Nernst)	$8.2 \pm 1.2$
$K_{23}$ ( $k_{23} / k_{32}$ )	$3.1 \pm 1.7$
$k_{23} / (\text{M}^{-1}\text{s}^{-1})$	$(1.5 \pm 0.1) \times 10^2$
$k_{32} / (\text{M}^{-1}\text{s}^{-1})$	$49.5 \pm 27.6$
$f_{23}$	0.97
$W_{23}$	1.1

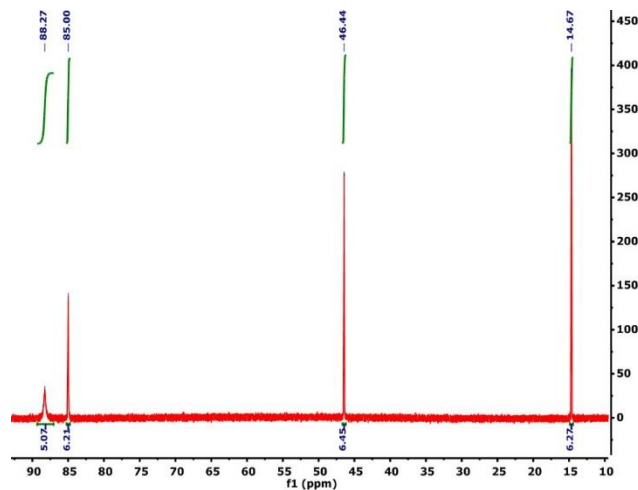


**Figure A3.1**  $^1\text{H}$  NMR of  $[\text{Co}(\text{bpy})_3](\text{TFSI})_2$  in  $\text{acetonitrile-}d_3$ .

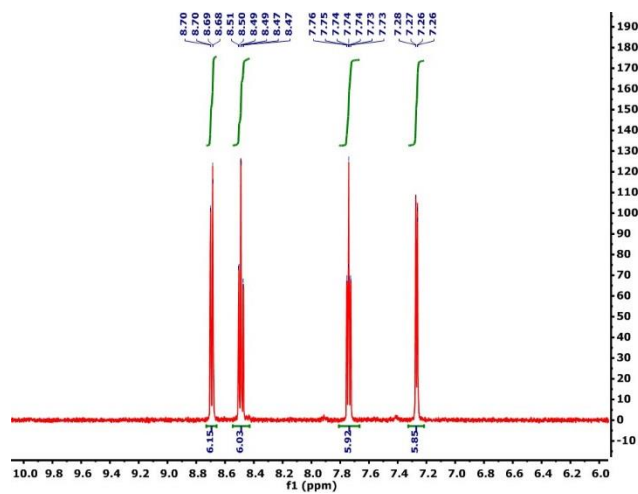


**Figure A3.2**  $^1\text{H}$  NMR of  $[\text{Co}(\text{bpy})_3](\text{TFSI})_3$  in  $\text{acetonitrile-}d_3$ .

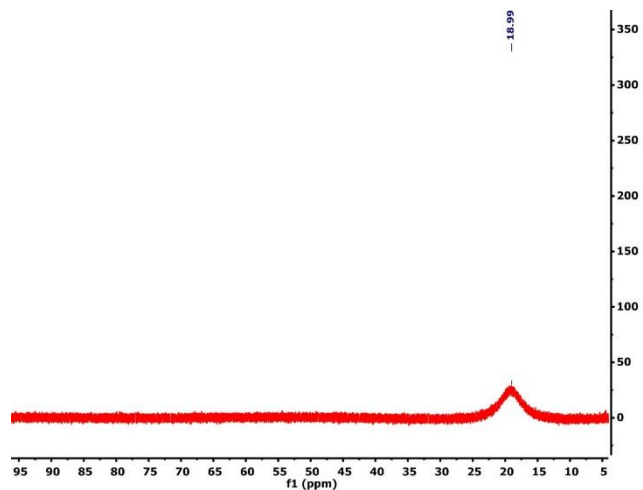


**Figure A3.3**  $^1\text{H}$  NMR of  $[\text{Co}(\text{ttcn})_2](\text{TFSI})_2$  in acetonitrile- $d_3$ .

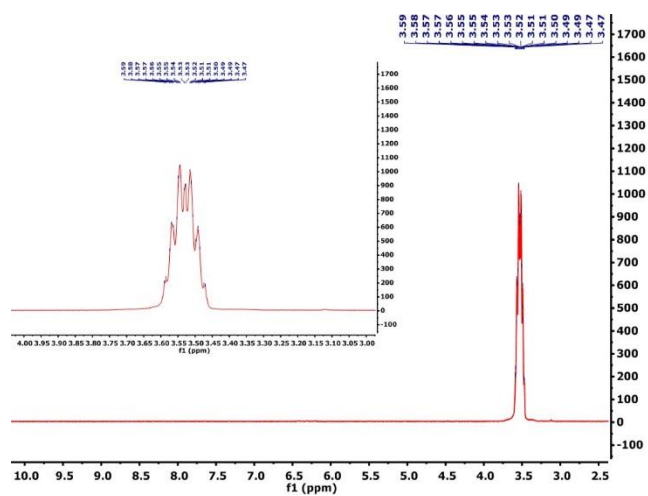


**Figure A3.4**  $^1\text{H}$  NMR of  $[\text{Co}(\text{ttcn})_2](\text{TFSI})_3$  in acetonitrile- $d_3$ . Inset enhances the observed multiplet.

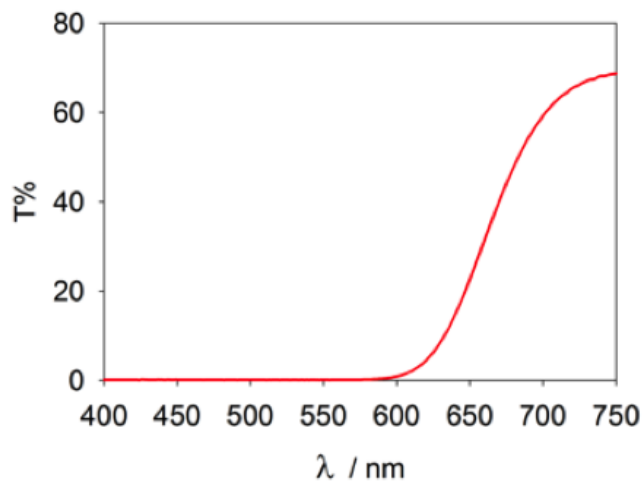


**Figure A3.5** Transmittance (T%) of a DSSC with a 7.1 $\mu$ m thick TiO<sub>2</sub> mesoporous film sensitized with the D35cpdt dye.

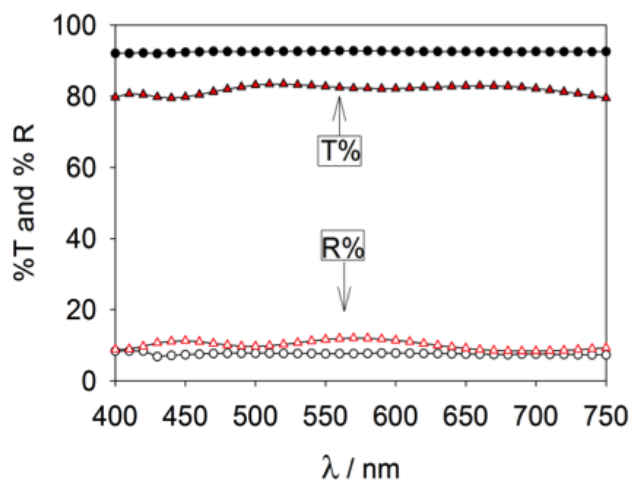


**Figure A3.6** Transmittance (T%) (filled) and reflectance (R%) (hollow) of an FTO glass substrate (red triangles) and a 1.2 mm high quality glass substrate (black circles).

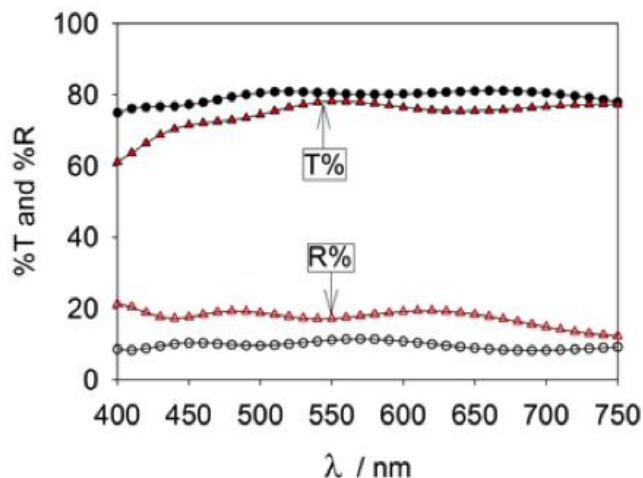


**Figure A3.7** Transmittance (T%) (filled) and reflectance (R%) (hollow) of a photoanode substrate- FTO with TiO<sub>2</sub> ALD blocking layer (black circles) and counter electrode-platinized FTO (red triangles). Note- T% = 77-82 % at  $\lambda = 450-750$  nm for the photoanode substrate, but ca. 4-5 % units lower for the counter electrode, due mainly to the light absorption by the platinum catalyst layer. R% = 10-12 % at  $\lambda = 450-750$  nm for photoanode substrate, and ca. 5-10 % units higher for the counter electrode, due again to the platinum catalyst layer which induces an increased roughness to the electrode surface.

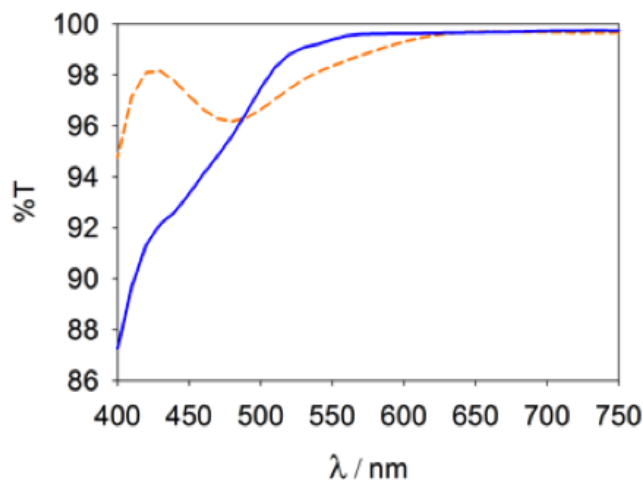


**Figure A3.8** Transmittance (T%) of electrolyte layer between counter electrode and TiO<sub>2</sub> film for [Co(bpy)<sub>3</sub>]<sup>3+/2+</sup> (blue solid line) and [Co(ttcn)<sub>2</sub>]<sup>3+/2+</sup> (orange dashed line). Note- the electrolyte transmittances are normalized to the path length of the actual cell which is ~18  $\mu\text{m}$  (Surlyn film thickness, 25  $\mu\text{m}$ , subtracted by the TiO<sub>2</sub> film thickness, 7.1  $\mu\text{m}$ ).

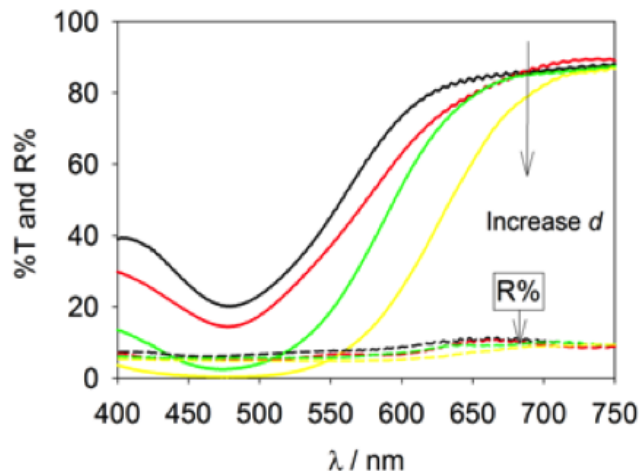


**Figure A3.9** Transmittance (T%) and reflectance (R%) of sample cells (sandwich cells assembled using bare 1.2 mm high quality microglass substrates filled with electrolyte) of various TiO<sub>2</sub> film thicknesses,  $d$ , (600 nm, 810 nm, 1.50  $\mu$ m, 1.80  $\mu$ m) at  $\lambda = 450$ -750 nm. Electrolyte composition: 0.2 M Co(II), 20 mM Co(III), 0.10 M LiTFSI, 10 mM Chenodeoxycholic acid. Note- The absorption maximum of the adsorbed dye is at  $\lambda_{\text{max}} \approx 470$  nm and the transmittance decreases with increasing film thickness. T% is close to zero at  $\lambda = 450$ -500 nm for film thickness 1.80  $\mu$ m, which indicates the film is thick enough to absorb all incident photons effectively in that wavelength range. A thicker film will further broaden the zero transmittance range. R% is  $\sim 10$  % and decreases slightly with increasing film thickness at  $\lambda = 400$ -700 nm, indicating that the dye absorbs light strongly and suppresses the light scattering from the film effectively.

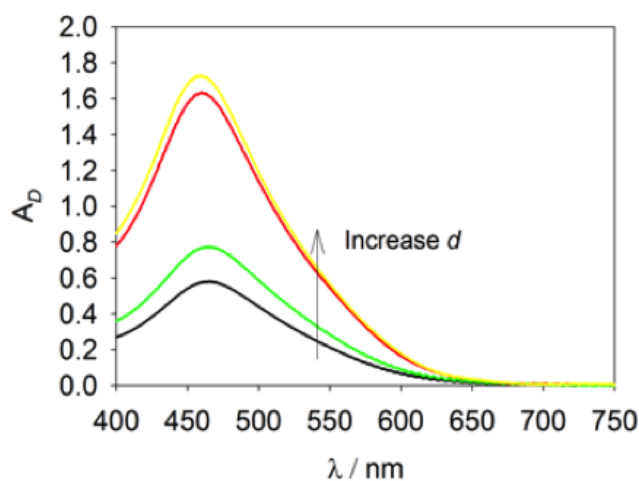


**Figure A3.10** Absorbance of D35cpdt sensitized TiO<sub>2</sub> films with various thicknesses,  $d$ , (600 nm, 810 nm, 1.50  $\mu$ m, 1.80  $\mu$ m) calculated using Equation (2.1).

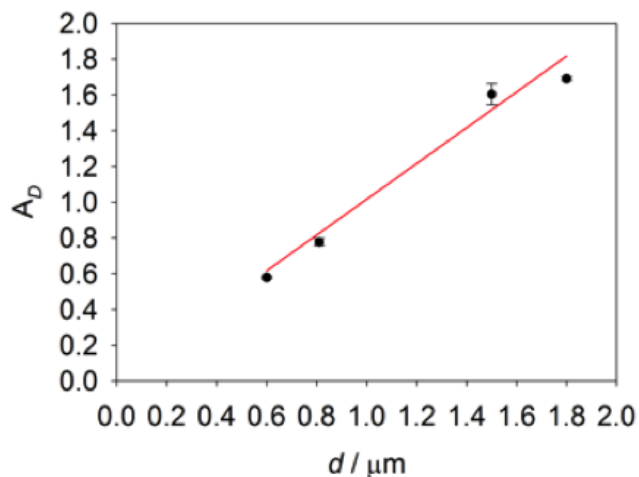


**Figure A3.11** Absorbance of sensitized films ( $A_D$ ) vs. film thickness,  $d$ , at 467nm ( $\lambda_{\text{max}}$ ) and its linear least squares fit curve:  $y = 1.004x + 0.0159$ ,  $R = 0.970$ . The error bars indicate the standard deviation from transmittance and reflectance measurements. Note- The linear relation of  $A_D$  and  $d$  indicates a homogeneous dye loading across the film. Also, The value of the slope was used to calculate the absorptivity of D35cpdt sensitized  $\text{TiO}_2$  film using Equation (2.1) of the main text.

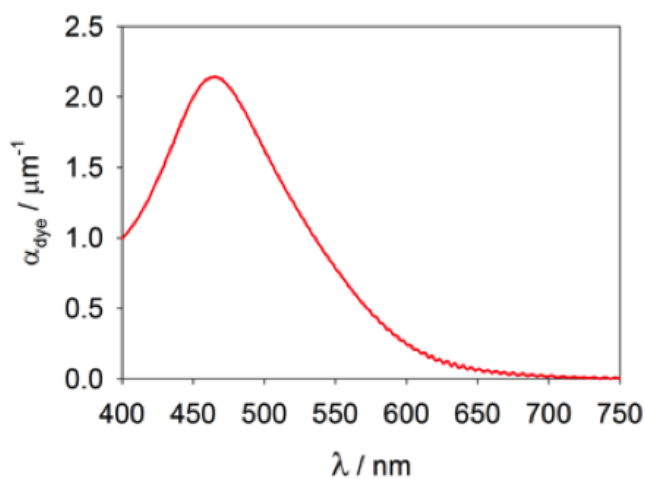


**Figure A3.12** Normalized absorptivity profile of a D35cpdt sensitized  $\text{TiO}_2$  film. Note- The absorptivity profile was further used for calculation of light harvesting efficiencies ( $\eta_{\text{LH}}$ ) and IPCEs.

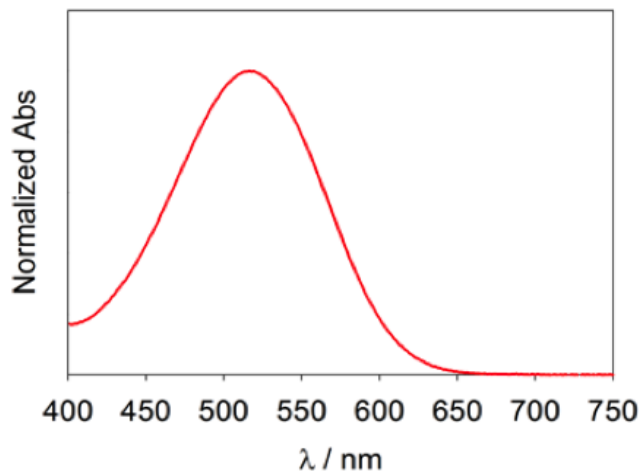


**Figure A3.13** Normalized absorbance of the D35cpdt dye in ethanol.

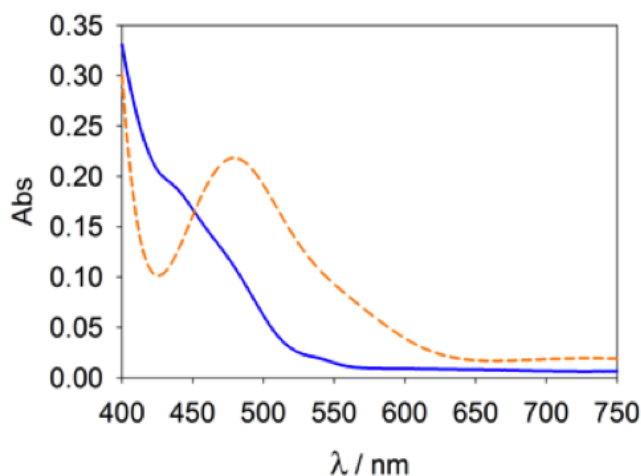


**Figure A3.14** Absorbance of 100 times diluted electrolyte solutions containing (0.2 M Co(II), 20 mM Co(III), 0.1 M LiTFSI and 10 mM Chenodeoxycholic acid),  $[\text{Co}(\text{bpy})_3]^{3+/2+}$  (blue solid line) and  $[\text{Co}(\text{ttcn})_2]^{3+/2+}$  (orange dashed line). Note- the electrolyte solution is diluted to keep the maximum absorbance below 2 (99% light is absorbed according to  $A = -\lg T$ ) for calculating the extinction coefficient and the electrolyte absorptivity,  $\alpha_e$ .

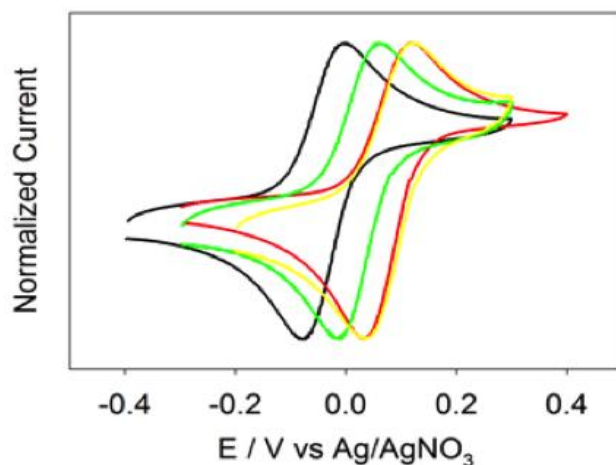


**Figure A3.15** Normalized CVs of [Fe(C<sub>5</sub>H<sub>4</sub>)<sub>2</sub>] (red line), [Fe(C<sub>5</sub>H<sub>4</sub>CH<sub>3</sub>)<sub>2</sub>] (black line), [Co(bpy)<sub>3</sub>](TFSI)<sub>2</sub> (green line) and [Co(ttcn)<sub>2</sub>](TFSI)<sub>2</sub> (yellow line) in acetonitrile with 0.1 M LiTFSI supporting electrolyte, using a gold disk working electrode, a platinum mesh counter electrode and a homemade Ag/AgNO<sub>3</sub> (0.1M TBAPF<sub>6</sub> in acetonitrile) reference electrode.

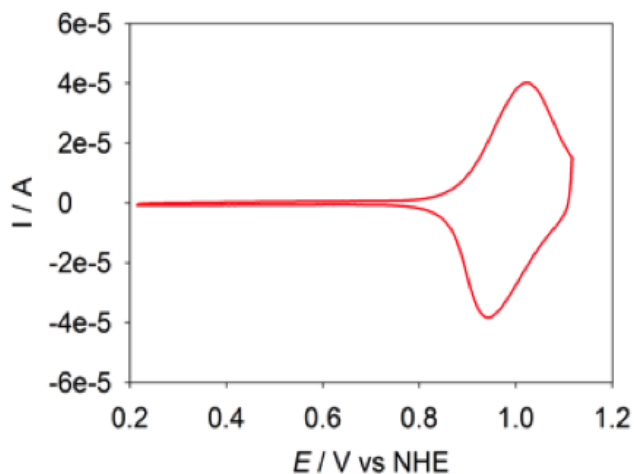


**Figure A3.16** CV of a D35cpdt sensitized ITO nanoparticle film at a 10 mV/s scan rate, using a platinum mesh counter electrode and a homemade Ag/AgNO<sub>3</sub> (0.1M TBAPF<sub>6</sub> in acetonitrile) reference electrode. Note- Ferrocene (Fc) was used to calibrate the reference electrode potential before and after measurements.

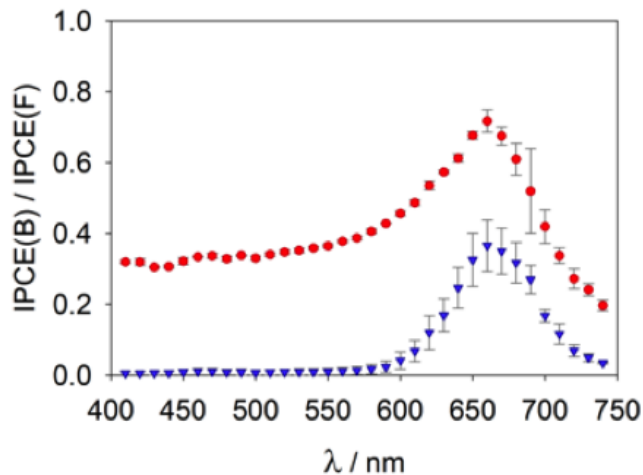


**Figure A3.17** IPCE ratios for DSSCs containing either  $[\text{Co}(\text{bpy})_3]^{3+/2+}$  (red circles) or  $[\text{Co}(\text{ttcn})_2]^{3+/2+}$  (blue triangles) redox shuttles with a  $7.1 \mu\text{m}$  mesoporous  $\text{TiO}_2$  film sensitized with the D35cpdt dye.

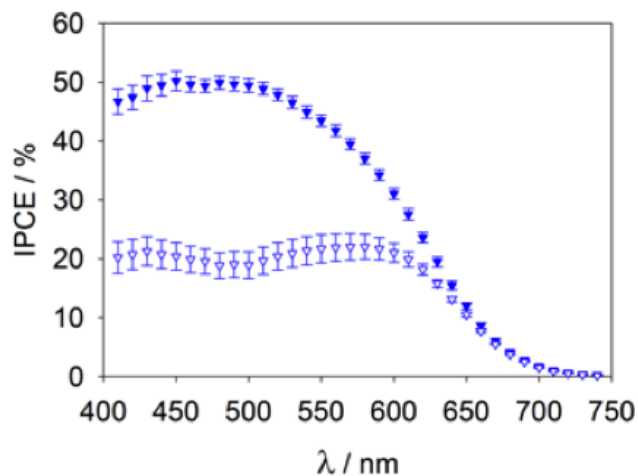


**Figure A3.18** IPCEs for DSSCs utilizing  $[\text{Co}(\text{ttcn})_2]^{3+/2+}$  and  $3.7 \mu\text{m}$   $\text{TiO}_2$  mesoporous films sensitized with D35cpdt. Note- FS illumination (filled triangles) and BS illumination (hollow triangles).

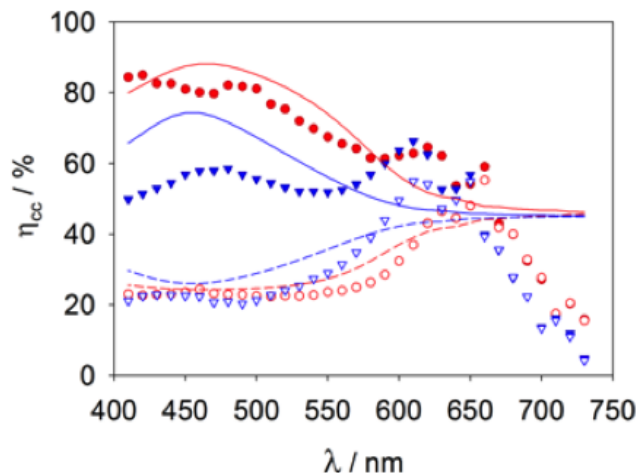


**Figure A3.19** Charge collection efficiencies (shape) and the corresponding fit (line) results for DSSCs employing  $[\text{Co}(\text{bpy})_3]^{3+/2+}$  (red circles) and  $[\text{Co}(\text{ttcn})_2]^{3+/2+}$  (blue triangles) redox shuttles. (FS illumination (filled) and BS illumination (hollow)). Note-  $3.7\mu\text{m}$  films were used for DSSCs with  $[\text{Co}(\text{ttcn})_2]^{3+/2+}$  ( $\eta_{inj} \times \eta_{reg} \approx 1.00$ ) and  $7.1\mu\text{m}$  films were used for DSSCs with  $[\text{Co}(\text{bpy})_3]^{3+/2+}$  ( $\eta_{inj} \times \eta_{reg} \approx 0.54$ ).

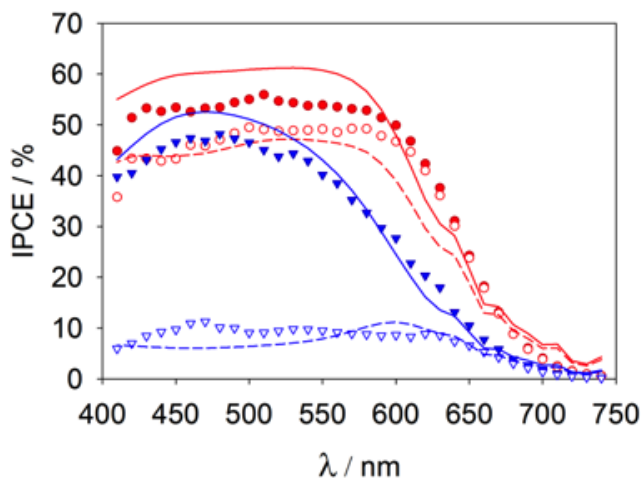


**Figure A3.20** IPCE (shape) and fit (line) results for DSSCs with 1 ALD cycle of  $\text{Al}_2\text{O}_3$  coating using  $[\text{Co}(\text{bpy})_3]^{3+/2+}$  (red) and  $[\text{Co}(\text{ttcn})_2]^{3+/2+}$  (blue) redox shuttles paired with the D35cpdt dye on  $7.1\mu\text{m}$  thick films. Note- FS illumination (filled) and BS illumination (hollow).

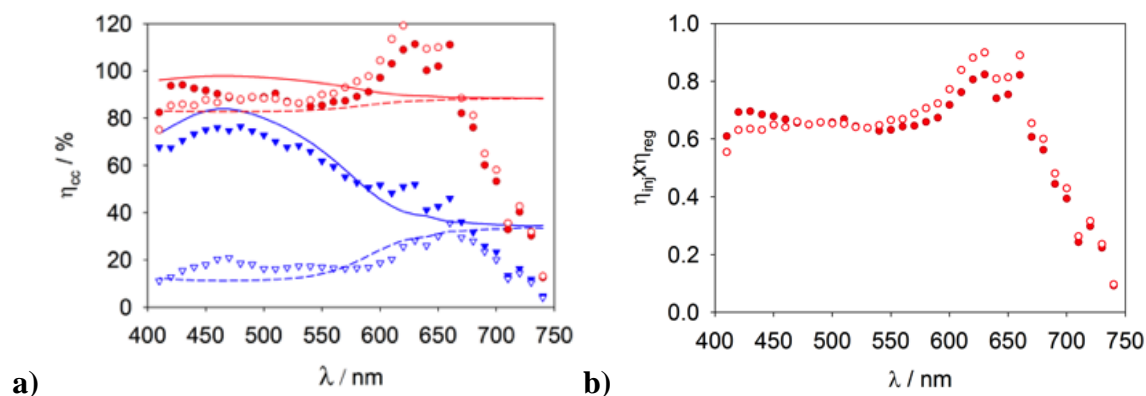


**Figure A3.21** Plots of **a)** charge collection efficiencies,  $\eta_{inj} \times \eta_{reg} \approx 0.74$  for  $[\text{Co}(\text{bpy})_3]^{3+/2+}$  &  $\eta_{inj} \times \eta_{reg} \approx 0.72$  for  $[\text{Co}(\text{ttcn})_2]^{3+/2+}$ ; **b)**  $\eta_{inj} \times \eta_{reg}$  determined by dividing the IPCE with LHE (taking charge collection efficiency as 100%) for DSSCs with 1 ALD cycle of  $\text{Al}_2\text{O}_3$  coating using  $[\text{Co}(\text{bpy})_3]^{3+/2+}$  (red),  $[\text{Co}(\text{ttcn})_2]^{3+/2+}$  (blue) redox shuttles paired with the D35cpdt dye on  $7.1\mu\text{m}$  thick films. Note- FS illumination (filled) and BS illumination (hollow).

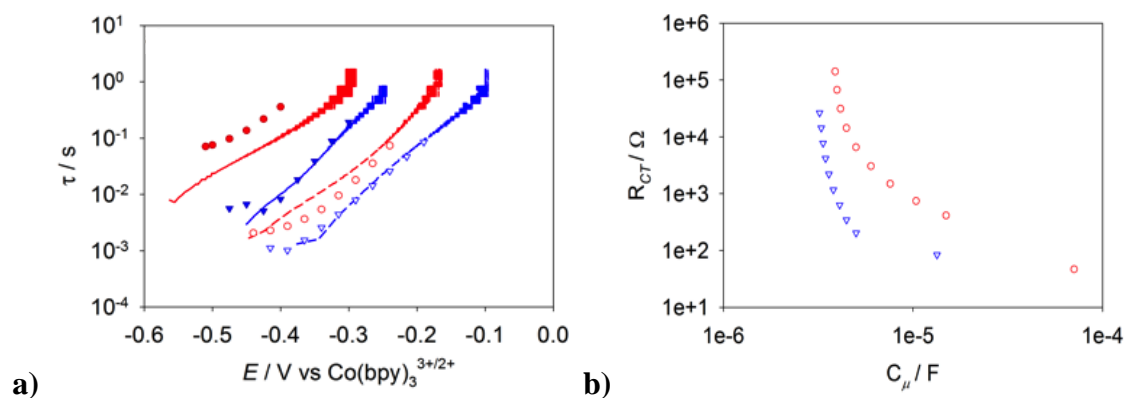


**Figure A3.22** **a)** Lifetime plots and **b)**  $R_{CT}$  versus chemical capacitance  $C_\mu$  from electrochemical impedance measurements for DSSCs using  $[\text{Co}(\text{bpy})_3]^{3+/2+}$  (red) and  $[\text{Co}(\text{ttcn})_2]^{3+/2+}$  (blue) redox shuttles paired with the D35cpdt dye with (filled) and without (hollow) 1 ALD cycle  $\text{Al}_2\text{O}_3$  coating on  $7.1\mu\text{m}$   $\text{TiO}_2$  films. Note- superimposed lines are lifetimes derived from open circuit voltage decay measurements.

## REFERENCES

## REFERENCES

1. Oregan, B.; Gratzel, M. A Low-Cost, High-Efficiency Solar-Cell Based on Dye-Sensitized Colloidal TiO<sub>2</sub> Films. *Nature* **1991**, *353* (6346), 737–740.
2. Klahr, B. M.; Hamann, T. W. Performance Enhancement and Limitations of Cobalt Bipyridyl Redox Shuttles in Dye-Sensitized Solar Cells. *J. Phys. Chem. C* **2009**, *113* (31), 14040–14045.
3. Ondersma, J. W.; Hamann, T. W. Measurements and Modeling of Recombination from Nanoparticle TiO<sub>2</sub> Electrodes. *J. Am. Chem. Soc.* **2011**, *133* (21), 8264–8271.
4. Li, T. C.; Spokoyny, A. M.; She, C.; Farha, O. K.; Mirkin, C. a; Marks, T. J.; Hupp, J. T. Ni (III)/(IV) Bis(dicarbollide) as a Fast , Noncorrosive Redox Shuttle for Dye-Sensitized Solar Cells. *J. Am. Chem. Soc.* **2010**, *132* (13), 4580–4582.
5. Hattori, S.; Wada, Y.; Yanagida, S.; Fukuzumi, S. Blue Copper Model Complexes with Distorted Tetragonal Geometry Acting as Effective Electron-Transfer Mediators in Dye-Sensitized Solar Cells. *J. Am. Chem. Soc.* **2005**, *127* (26), 9648–9654.
6. Daeneke, T.; Mozer, A. J.; Uemura, Y.; Makuta, S.; Fekete, M.; Tachibana, Y.; Koumura, N.; Bach, U.; Spiccia, L. Dye Regeneration Kinetics in Dye-Sensitized Solar Cells. *J. Am. Chem. Soc.* **2012**, *134* (41), 16925–16928.
7. Feldt, S. M.; Gibson, E. A.; Gabrielsson, E.; Sun, L.; Boschloo, G.; Hagfeldt, A. Design of Organic Dyes and Cobalt Polypyridine Redox Mediators for High-Efficiency Dye-Sensitized Solar Cells. *J. Am. Chem. Soc.* **2010**, *132* (46), 16714–16724.
8. Mathew, S.; Yella, A.; Gao, P.; Humphry-Baker, R.; Curchod, B. F. E.; Ashari-Astani, N.; Tavernelli, I.; Rothlisberger, U.; Nazeeruddin, M. K.; Grätzel, M. Dye-Sensitized Solar Cells with 13% Efficiency Achieved through the Molecular Engineering of Porphyrin Sensitizers. *Nat. Chem.* **2014**, *6* (3), 242–247.
9. Yella, A.; Lee, H.-W.; Tsao, H. N.; Yi, C.; Chandiran, A. K.; Nazeeruddin, M. K.; Diau, E. W.-G.; Yeh, C.-Y.; Zakeeruddin, S. M.; Grätzel, M. Porphyrin-Sensitized Solar Cells with Cobalt (II/III)-Based Redox Electrolyte Exceed 12 Percent Efficiency. *Science* **2011**, *334* (6056), 629–634.
10. Feldt, S. M.; Lohse, P. W.; Kessler, F.; Nazeeruddin, M. K.; Gratzel, M.; Boschloo, G.; Hagfeldt, A. Regeneration and Recombination Kinetics in Cobalt Polypyridine Based Dye-Sensitized Solar Cells, Explained Using Marcus Theory. *Phys. Chem. Chem. Phys.* **2013**, *15* (19), 7087–7097.
11. Marcus, R. A.; Sides, P. Marcus, R. A.; Siders, P. in “Mechanistic Aspects of Inorganic Reactions”; Rorabacher, D. B., Endicott, J. F., Eds.; American Chemical Society: Washington, D.C., 1982; ACS Symp. Ser. No. 198, Chapter 10, p235. In *Mechanistic*

- Aspects of Inorganic Reactions*; Rorabacher, D. B., Endicott, J. F., Eds.; American Chemical Society: Washington, D. C., 1982; p 235.
12. Nelson, J. J.; Amick, T. J.; Elliott, C. M. Mass Transport of Polypyridyl Cobalt Complexes in Dye-Sensitized Solar Cells with Mesoporous TiO<sub>2</sub> Photoanodes. *J. Phys. Chem. C* **2008**, *112* (46), 18255–18263.
  13. Marcus, R. A.; Amos, A. Electron Transfers in Chemistry and Biology and Norman Sutin B. *Biochim. Biophys. Acta* **1985**, *811*, 265–322.
  14. Brunschwig, B. S.; Creutz, C.; Sutin, N. Optical Transitions of Symmetrical Mixed-Valence Systems in the Class II-III Transition Regime. *Chem. Soc. Rev.* **2002**, *31* (3), 168–184.
  15. Brunschwig, B. S.; Creutz, C.; Macartney, D. H.; Sham, T.-K.; Sutin, N. The Role of Inner-Sphere Configuration Changes in Electron-Exchange Reactions of Metal Complexes. *Faraday Discuss. Chem. Soc.* **1982**, *74* (2), 113.
  16. Hamann, T. W.; Gstrein, F.; Brunschwig, B. S.; Lewis, N. S. Measurement of the Dependence of Interfacial Charge-Transfer Rate Constants on the Reorganization Energy of Redox Species at N-ZnO/H<sub>2</sub>O Interfaces. *J. Am. Chem. Soc.* **2005**, *127* (40), 13949–13954.
  17. Xie, Y.; Hamann, T. W. Fast Low-Spin Cobalt Complex Redox Shuttles for Dye-Sensitized Solar Cells. *J. Phys. Chem. Lett.* **2013**, *4* (2), 328–332.
  18. Soman, S.; Xie, Y.; Hamann, T. W. Cyclometalated Sensitizers for DSSCs Employing Cobalt Redox Shuttles. *Polyhedron* **2014**, *82*, 139–147.
  19. Tachibana, Y.; Hara, K.; Sayama, K.; Arakawa, H. Quantitative Analysis of Light-Harvesting Efficiency and Electron-Transfer Yield in Ruthenium-Dye-Sensitized Nanocrystalline TiO<sub>2</sub> Solar Cells. *Chem. Mater.* **2002**, *14* (7), 2527–2535.
  20. Klahr, B. M.; Martinson, A. B. F.; Hamann, T. W. Photoelectrochemical Investigation of Ultrathin Film Iron Oxide Solar Cells Prepared by Atomic Layer Deposition. *Langmuir* **2011**, *27* (1), 461–468.
  21. Xie, Y.; Baillargeon, J.; Hamann, T. W. Kinetics of Regeneration and Recombination Reactions in Dye-Sensitized Solar Cells Employing Cobalt Redox Shuttles. *J. Phys. Chem. C* **2015**, *119* (50), 28155–28166.
  22. Held, R. P.; Luksha, E.; Denessen, H. J. M.; Alfenaar, M.; Singla, S. J. P.; Neruia, P.; Cole, R. H.; Kuchitsu, K.; Katrfky, a R.; Rutherford, D.; et al. Electron Exchange between Ferrocene and Ferrocenium Ion. Effects of Solvent and of Ring Substitution on the Rate. *J. Phys. Chem.* **1980**, *84* (23), 3094–3099.

23. Dunn, B. C.; Ochrymowycz, L. A.; Rorabacher, D. B. Electron-Transfer Kinetics of the Copper(II/I) Complex with 1,4,8,11-Tetrathiacyclotetradecane in Acetonitrile. *Inorg. Chem.* **1995**, *34* (7), 1954–1956.
24. Marcus, R. A. Chemical and Electrochemical Electron-Transfer Theory. *Annu. Rev. Phys. Chem.* **1964**, *15* (1), 155–196.
25. Sutin, N. Nuclear, Electronic, and Frequency Factors in Electron Transfer Reactions. *Acc. Chem. Res.* **1982**, *15* (9), 275–282.
26. Xie, B.; Wilson, L. J.; Stanbury, D. M. Cross-Electron-Transfer Reactions of the [CuII/I(bite)]<sup>2+/+</sup> Redox Couple. *Inorg. Chem.* **2001**, *40* (14), 3606–3614.
27. Chaka, G.; Kandegedara, A.; Heeg, M. J.; Rorabacher, D. B. Comparative Study of Donor Atom Effects on the Thermodynamic and Electron-Transfer Kinetic Properties of copper(II/I) Complexes with Sexadentate Macrocyclic Ligands. [CuII/I([18]aneS4N2)] and [CuII/I([18]aneS4O2)]. *Dalton Trans.* **2007**, *6* (4), 449–458.
28. Koppers, H. J.; Neves, A.; Pomp, C.; Ventur, D.; Wieghardt, K.; Nuber, B.; Weiss, J. Electron-Transfer Barriers in cobalt(III) and cobalt(II) Bis Complexes of 1,4,7-Triazacyclononane(tacn) and 1,4,7-Trithiacyclononane (Ttcn). Crystal Structures of [CoII(tacn)<sub>2</sub>]<sub>2</sub>·2H<sub>2</sub>O and of [CoIII(ttcn)<sub>2</sub>](ClO<sub>4</sub>)<sub>3</sub>. *Inorg. Chem.* **1986**, *25* (14), 2400–2408.
29. Chandrasekhar, S. .; McAuley, A. Syntheses, Structure, and Reactivity of Cobalt and Nickel Complexes of 1,4,7-Trithiacyclodecane: Self-Exchange Rates for Co(S<sub>6</sub>)<sup>2+ / 3+</sup> Couples from <sup>59</sup>Co NMR Spectroscopy. *Inorg. Chem.* **1992**, *31* (3), 480–487.
30. Hamann, T. W.; Ondersma, J. W. Dye-Sensitized Solar Cell Redox Shuttles. *Energy Environ. Sci.* **2011**, *4* (2), 370.
31. Marcus, R. A.; Sutin, N. Electron Transfers in Chemistry and Biology. *Biochim. Biophys. Acta - Rev. Bioenerg.* **1985**, *811* (3), 265–322.
32. Yang, W.; Vlachopoulos, N.; Hao, Y.; Hagfeldt, A.; Boschloo, G. Efficient Dye Regeneration at Low Driving Force Achieved in Triphenylamine Dye LEG4 and TEMPO Redox Mediator Based Dye-Sensitized Solar Cells. *Phys. Chem. Chem. Phys.* **2015**, *17*, 15868–15875.
33. Royea, W. J.; Hamann, T. W.; Brunschwig, B. S.; Lewis, N. S. A Comparison between Interfacial Electron-Transfer Rate Constants at Metallic and Graphite Electrodes. *J. Phys. Chem. B* **2006**, *110* (39), 19433–19442.
34. Blomgren, G. E. Physical and Chemical Properties of Non-Aqueous Solutions. In *Non-aqueous Electrochemistry*; Aurbach, D., Ed.; Marcel Dekker: New York, NY, 1999; pp 53–79.

35. *CRC Handbook of Chemistry and Physics, 81st Ed*, 81st ed.; Lide, D. R., Ed.; CRC Press: Boca Raton, FL, 2001.
36. Enright, B.; Fitzmaurice, D. Spectroscopic Determination of Electron and Hole Effective Masses in a Nanocrystalline Semiconductor Film. *J. Phys. Chem.* **1996**, *100* (3), 1027–1035.
37. Rothenberger, G.; Fitzmaurice, D.; Gratzel, M. Spectroscopy of Conduction Band Electrons in Transparent Metal Oxide Semiconductor Films: Optical Determination of the Flatband Potential of Colloidal Titanium Dioxide Films. *J. Phys. Chem.* **1992**, *96* (14), 5983–5986.
38. Peter, L. Characterization and Modeling of Dye-Sensitized Solar Cells. *J. Phys. Chem. C* **2007**, *6*, 555–565.
39. Halme, J.; Boschloo, G.; Hagfeldt, A.; Lund, P. Spectral Characteristics of Light Harvesting, Electron Injection, and Steady-State Charge Collection in Pressed TiO<sub>2</sub> Dye Solar Cells. *J. Phys. Chem. C* **2008**, *112* (14), 5623–5637.
40. Barnes, P. R. F.; Anderson, A. Y.; Koops, S. E.; Durrant, J. R.; O'Regan, B. C. Electron Injection Efficiency and Diffusion Length in Dye-Sensitized Solar Cells Derived from Incident Photon Conversion Efficiency Measurements. *J. Phys. Chem. C* **2009**, *113* (3), 1126–1136.
41. Barnes, P. R. F.; Liu, L.; Li, X.; Anderson, A. Y.; Kisserwan, H.; Ghaddar, T. H.; Durrant, J. R.; Regan, B. C. O. Re-Evaluation of Recombination Losses in Dye-Sensitized Cells: The Failure of Dynamic Relaxation Methods to Nanoporous Photoelectrodes. *Nano Lett.* **2009**, *9* (10), 3532–3538.
42. Feldt, S. M.; Wang, G.; Boschloo, G.; Hagfeldt, A. Effects of Driving Forces for Recombination and Regeneration on the Photovoltaic Performance of Dye-Sensitized Solar Cells Using Cobalt Polypyridine Redox Couples. *J. Phys. Chem. C* **2011**, *115* (43), 21500–21507.
43. Barnes, P. R. F.; Anderson, A. Y.; Durrant, J. R.; O'Regan, B. C. Simulation and Measurement of Complete Dye Sensitized Solar Cells: Including the Influence of Trapping, Electrolyte, Oxidised Dyes and Light Intensity on Steady State and Transient Device Behaviour. *Phys. Chem. Chem. Phys.* **2011**, *13* (13), 5798–5816.
44. Jennings, J. R.; Liu, Y.; Wang, Q. Efficiency Limitations in Dye-Sensitized Solar Cells Caused by Inefficient Sensitizer Regeneration. *J. Phys. Chem. C* **2011**, *115* (30), 15109–15120.
45. Li, F.; Jennings, J. R.; Wang, Q. Determination of Sensitizer Regeneration Efficiency in Dye-Sensitized Solar Cells. *ACS Nano* **2013**, *7* (9), 8233–8242.

46. Ondersma, J. W.; Hamann, T. W. Impedance Investigation of Dye-Sensitized Solar Cells Employing Outer-Sphere Redox Shuttles. *J. Phys. Chem. C* **2010**, *114* (1), 638–645.
47. Zaban, A.; Greenshtein, M.; Bisquert, J. Determination of the Electron Lifetime in Nanocrystalline Dye Solar Cells by Open-Circuit Voltage Decay Measurements. *Chemphyschem* **2003**, *4* (8), 859–864.
48. Makinen K Hakkinen, H, V. H. Atomic Layer Deposition of Aluminum Oxide on TiO<sub>2</sub> and Its Impact on N3 Dye Adsorption from First Principles. *J. Phys. Chem. C* **2011**, *115* (18), 9259.
49. Palomares, E.; Clifford, J. N.; Haque, S. a; Lutz, T.; Durrant, J. R. Control of Charge Recombination Dynamics in Dye Sensitized Solar Cells by the Use of Conformally Deposited Metal Oxide Blocking Layers Control of Charge Recombination Dynamics in Dye Sensitized Solar Cells by the Use of Conformally Deposited Metal Oxide B. *J. Am. Chem. Soc.* **2003**, *125* (11), 475–482.
50. Dryza, V.; Bieske, E. J. Does the Triphenylamine-Based D35 Dye Sensitizer Form Aggregates on Metal-Oxide Surfaces? *J. Photochem. Photobiol. A Chem.* **2015**, *302*, 35–41.
51. Ellis, H.; Eriksson, S. K.; Feldt, S. M.; Gabrielsson, E.; Lohse, P. W.; Lindblad, R.; Sun, L. Linker Unit Modification of Triphenylamine-Based Organic Dyes for. *J. Phys. Chem. C* **2013**, *117* (41), 21029–21036.
52. Gabrielsson, E.; Ellis, H.; Feldt, S.; Tian, H.; Boschloo, G.; Hagfeldt, A.; Sun, L. Convergent/divergent Synthesis of a Linker-Varied Series of Dyes for Dye-Sensitized Solar Cells Based on the D35 Donor. *Adv. Energy Mater.* **2013**, *3* (12), 1647–1656.
53. Koops, S. E.; O'Regan, B. C.; Barnes, P. R. F.; Durrant, J. R. Parameters Influencing the Efficiency of Electron Injection in Dye-Sensitized Solar Cells. *J. Am. Chem. Soc.* **2009**, *131* (13), 4808–4818.

## Chapter 4. Bifurcation of Regeneration and Recombination in DSSCs via Electronic Manipulation of Tandem Cobalt Redox Shuttles

*\*Proud to announce this manuscript was published in a special edition of Applied Materials and Interfaces in honor of Joe Hupp's Birthday. Happy Birthday Joe!*

### 4.1 Abstract

A cobalt(IV/III) redox shuttle, cobalt tris(2-(p-tolyl)pyridine),  $[\text{Co}(\text{ptpy})_3]^{+/0}$ , was synthesized and investigated for use in DSSCs. An incredibly fast self-exchange rate constant of  $(9.2 \pm 3.9) \times 10^8 \text{ M}^{-1}\text{s}^{-1}$  was determined for  $[\text{Co}(\text{ptpy})_3]^{+/0}$ , making it an ideal candidate for dye regeneration. To avoid fast recombination and solubility limitations, a tandem electrolyte containing  $[\text{Co}(\text{ptpy})_3]$  and cobalt tris(2,2'-bipyridine),  $[\text{Co}(\text{bpy})_3]^{3+/2+}$ , was utilized. An improved short circuit current density was achieved for DSSCs employing the tandem electrolyte, compared to electrolytes containing only  $[\text{Co}(\text{bpy})_3]^{3+/2+}$ . The results are consistent with superior dye regeneration based on predictions made using Marcus Theory.

### 4.2 Introduction

After several decades of reliance on  $\text{I}_3^-/\text{I}^-$ , cobalt OSRSs have arisen as the most promising class of redox shuttle for DSSCs.<sup>1,2</sup> Much of the success in transitioning DSSCs to OSRSs, including cobalt complexes, results from pioneering research of Hupp and co-workers on the elucidation of key electron-transfer reactions and development of novel DSSC components.<sup>3-7</sup> Impressively, Grätzel and coworkers built upon this knowledge and pushed the power conversion efficiency of DSSCs to 13% through the use of a  $[\text{Co}(\text{bpy})_3]^{3+/2+}$  in combination with a Zn-porphyrin sensitizer SM315.<sup>8</sup> The success of  $[\text{Co}(\text{bpy})_3]^{3+/2+}$  can be attributed to sufficiently slow recombination kinetics from  $\text{TiO}_2$  to

allow for excellent charge collection efficiency,  $\eta_{cc}$ . The slow recombination results from a large innersphere reorganization energy as the LS Co(III) gets reduced to a HS Co(II).<sup>9,10</sup> Although retarding recombination is advantageous for creating relatively efficient DSSCs, the large reorganization energy barrier also inhibits dye regeneration and prevents realization of DSSCs with efficiencies approaching state-of-the-art silicon or perovskite photovoltaics. For example, in Chapter 3 we demonstrated that even with a 0.5 eV driving force, the regeneration efficiency,  $\eta_{reg}$ , of the D35cpdt dye with  $[\text{Co}(\text{bpy})_3]^{2+}$  is only ~54%.<sup>11</sup>

One significant advantage of using outersphere coordination complexes such as  $[\text{Co}(\text{bpy})_3]^{3+/2+}$  as redox shuttles, instead of  $\text{I}_3^-/\text{I}^-$ , is their tunability. Introduction of electron donating or withdrawing groups to modulate the redox potential has been shown to affect the driving force and thus rates of dye regeneration and recombination.<sup>2,3,12</sup> We also previously showed that use of  $[\text{Co}(\text{ttn})_2]^{3+/2+}$ , where the trithiacyclononane ligand produces a LS Co(II) complex, offers an alternative synthetic route to manipulate the kinetics of recombination and regeneration.<sup>11</sup> Indeed, the electron-transfer self-exchange rate constant,  $k_{se}$ , for  $[\text{Co}(\text{ttn})_2]^{3+/2+}$  is more than four orders of magnitude faster than  $[\text{Co}(\text{bpy})_3]^{3+/2+}$ . This difference in  $k_{se}$  can be understood by comparing changes in electron occupancy of the anti-bonding  $e_g$  orbitals (assuming  $O_h$  symmetry); oxidation of  $[\text{Co}(\text{bpy})_3]^{2+}$  removes two electrons from the anti-bonding orbitals whereas oxidation of  $[\text{Co}(\text{ttn})_2]^{2+}$  removes only one. As a result, there is a lower innersphere reorganization for  $[\text{Co}(\text{ttn})_2]^{3+/2+}$ , compared to  $[\text{Co}(\text{bpy})_3]^{3+/2+}$ . The faster  $k_{se}$  results in 57 times faster regeneration kinetics, and quantitative regeneration efficiency,  $\eta_{reg}$ , when pairing these redox shuttles with the organic dye D35cpdt, despite only a ~54 meV lower driving force.

Unfortunately, the faster self-exchange kinetics also resulted in faster recombination and no net improvement in performance.

The Marcus cross-relation suggests that in order to efficiently regenerate a dye with a minimal driving force (ca. 100 meV), a  $k_{se}$  even faster than  $[\text{Co}(\text{ttcn})_2]^{3+/2+}$  is required. We reasoned that a cobalt(IV/III) redox couple, which would have no change in the occupancy of antibonding d-orbitals during the self-exchange reaction, should exhibit very fast kinetics, analogous to the isoelectronic ruthenium(III/II) redox couples. There have been very limited kinetic studies on cobalt(IV/III) couples, however. Low temperature ESR line broadening measurements (243 K) on a model compound of coenzyme B12,  $[(\text{DH})_2\text{Co}^{\text{III}}(\text{Me})(\text{py})]$  (DH = the anion of dimethylglyoxime, Me = methyl, py = pyridine), resulted in a  $k_{se}$  of  $8.4 \times 10^8 \text{ M}^{-1}\text{s}^{-1}$ .<sup>13</sup> NMR line broadening measurements of a  $\text{Co}_4\text{O}_4$  cubane model compound of the Co-Pi water oxidation catalyst produced  $k_{se}$ 's of  $(1.3 \pm 0.24) \times 10^4 - (3 \pm 0.21) \times 10^5 \text{ M}^{-1}\text{s}^{-1}$  (values are pH dependent).<sup>14</sup> Although the cubane is an example of a cobalt(IV/III) exchange, the charge is delocalized and may not be representative of cobalt(IV/III) molecular complexes. In this work, we investigate the cross-exchange kinetics of cobalt tris(2-(p-tolyl)pyridine),  $[\text{Co}(\text{ptpy})_3]^{+0}$ , using stopped-flow spectroscopy which allowed determination of the  $k_{se}$  at room temperature and explored its use in DSSCs.

## 4.3 Experimental

### 4.3.1 Materials

All materials were purchased from commercial suppliers and used as received. However, tetrahydrofuran (Fisher Chemical, Optima), used in the  $[\text{Co}(\text{ptpy})_3]$  synthesis, was distilled over sodium/benzophenone and stored in a glovebox (MBRAUN Labmaster

SP) prior to use. Acetonitrile (Fisher Chemical Certified ACS,  $\geq 99.5\%$ ), used in all electrochemistry, stopped-flow and solar cell measurements, was purified on an activated alumina column before being stored in a glovebox. Tetrabutylammonium hexafluorophosphate, TBAPF<sub>6</sub>, (Sigma-Aldrich, 98%) was recrystallized from ethanol/diethyl ether and dried under vacuum. Both supporting electrolytes, TBAPF<sub>6</sub> and lithium bis(trifluoromethane)sulfonamide, LiTFSI, were stored in a glovebox as well under moisture free conditions prior to use.

#### 4.3.2 Synthesis of OSRSs

The synthesis of the [Co(bpy)<sub>3</sub>](TFSI)<sub>2</sub> and [Co(bpy)<sub>3</sub>](TFSI)<sub>3</sub> OSRSs were prepared as described in Chapter 3. The [Co(bpyCl<sub>2</sub>)<sub>3</sub>](PF<sub>6</sub>)<sub>2</sub> complex was prepared using a previously published procedure.<sup>15</sup> However, oxidation to [Co(bpyCl<sub>2</sub>)<sub>3</sub>](PF<sub>6</sub>)<sub>3</sub> was carried out using 1.2 equivalents of NOPF<sub>6</sub> in a minimal amount (~5 mL) of acetonitrile. The reaction mixture was allowed to stir for 30 minutes before being concentrated, precipitated with diethyl ether, vacuum filtered and washed with methanol, water and diethyl ether. The synthesis and purification of the [Co(pty)<sub>3</sub>] complex was carried out using a modified procedure from the literature.<sup>16</sup> Such changes included purchasing the 2-Mesitylmagnesium bromide Grignard reagent (Sigma-Aldrich) prior to use rather than making it in-situ, as well as replacing the original ligand 2-phenylpyridine with 2-(p-tolyl)pyridine. All cobalt complexes: [Co(bpyCl<sub>2</sub>)<sub>3</sub>](PF<sub>6</sub>)<sub>2</sub>, [Co(bpyCl<sub>2</sub>)<sub>3</sub>](PF<sub>6</sub>)<sub>3</sub> and [Co(pty)<sub>3</sub>] were characterized using elemental analysis, Table A4.1. [Co(pty)<sub>3</sub>] was further characterized using <sup>1</sup>H NMR, Figure A4.1. <sup>1</sup>H NMR (500 MHz, Chloroform-d)  $\delta$  7.79 (dt, J = 8.2, 1.1 Hz, 3H), 7.58 (ddd, J = 8.1, 7.3, 1.6 Hz, 3H), 7.53 (d, J = 7.8 Hz, 3H), 7.18 (ddd, J = 5.6, 1.7, 0.8 Hz, 3H), 6.77 (ddd, J = 7.1, 5.6, 1.3 Hz, 3H), 6.74 – 6.68 (m,

3H), 6.33 (d,  $J = 1.6$  Hz, 3H), 2.08 (s, 9H). Note- The  $^1\text{H}$  NMR of the paramagnetic and diamagnetic,  $[\text{Co}(\text{bpyCl}_2)_3]^{2+}$  and  $[\text{Co}(\text{bpyCl}_2)_3]^{3+}$  complexes, can be found in the Appendix Figures A4.2-A4.3.

#### 4.3.3 Electrochemistry

CV measurements were performed with an Autolab PGSTAT 126N potentiostat using a platinum disk working electrode, platinum mesh counter electrode and  $\text{Ag}/\text{AgNO}_3$  (0.1 M  $\text{TBAPF}_6$  acetonitrile) reference electrode. The error associated with each redox shuttle's formal potential,  $E^\circ$ , is based on the standard deviation of the formal potentials measured over three separate days. Reference conversion to NHE was done assuming the potential of Ferrocene (Fc) in acetonitrile is 0.40 V vs. SCE.<sup>17</sup> The active area of the platinum disk electrode was determined to be 0.024  $\text{cm}^2$  based on capacitance measurements using CV.

#### 4.3.4 Cross-Exchange Kinetics

All stopped-flow measurements were performed using a similar methodology to that previously described in Chapter 2. Briefly, samples were measured using an Olis RSM 1000 DeSa rapid-scanning spectrophotometer with dual-beam UV-Vis recording to Olis SpectralWorks software. The instrument contained a quartz cell with a 1 cm path length. Scans were taken once every millisecond with 1 nm resolution. The 150 W Xenon arc lamp was controlled using an LPS-220B Lamp Power Supply and held to within 79-80 W during each measurement. The temperature was also held constant at  $25 \pm 0.1^\circ\text{C}$  using a NESLAB RTE-140 chiller/circulator. All  $[\text{Co}(\text{ptpy})_3]$  and  $[\text{Co}(\text{bpyCl}_2)_3](\text{PF}_6)_{3/2}$  solutions were prepared using dry acetonitrile. The ionic strengths were adjusted to 0.1 M using  $\text{TBAPF}_6$ .

Pseudo-first order conditions were implemented, which maintained at least a 10-fold excess of a single reactant and product species. Both of the  $[\text{Co}(\text{bpyCl}_2)_3](\text{PF}_6)_3$  and  $[\text{Co}(\text{bpyCl}_2)_3](\text{PF}_6)_2$  concentrations for these measurements were held in excess while the  $[\text{Co}(\text{bpyCl}_2)_3](\text{PF}_6)_3$  concentration was varied for the reactions with  $[\text{Co}(\text{ptpy})_3]$ . The spectral changes were monitored at 433 nm, following the decaying absorbance of the  $[\text{Co}(\text{ptpy})_3]$  species. Scientific Data Analysis Software provided fits for the observed pseudo-first order rate constants,  $k_{\text{obs}}$ , using a nonlinear least-squares regression. Seven independent trials were averaged to provide the measured  $k_{\text{obs}}$  values. Absorbance plots for each pseudo-first order reaction were fit using:  $A = A_{\infty} + (A_0 - A_{\infty})e^{-k_{\text{obs}}t}$ . The second-order rate constants were calculated from the slope of the  $k_{\text{obs}}$  vs. the excess concentration of  $[\text{Co}(\text{bpyCl}_2)_3](\text{PF}_6)_3$ , which had a goodness of fit,  $R^2 > 0.999$ . The error associated with measured  $k_{\text{obs}}$  values were taken to be the standard deviation of seven independent trials at a given concentration. The minimal error in concentration was propagated based on prepared stock solutions of each reaction mixture. Uniform mixing by the stopped-flow instrument was assumed for each independent trial.

#### 4.3.5 Solar Cell Fabrication and Characterization

Solar cell fabrication and characterization was performed in the same manner as described in Chapter 2. Briefly, FTO glass substrates (TEC 15, Hartford),  $12 \Omega \text{ cm}^{-2}$ , were used to prepare the  $\text{TiO}_2$  photoanodes. The glass substrates were cleaned in an ultrasonic bath using (in order) soap water, deionized water, isopropyl alcohol and acetone. ALD was used to provide a blocking layer of  $\text{TiO}_2$ . A Savannah 200 instrument (Cambridge Nanotech Inc) deposited 1000 cycles of titanium isopropoxide (99.999% trace metals basis, Sigma-Aldrich) at  $225^\circ\text{C}$  and water using reactant exposure times of 0.3 s and 0.015 s,

respectively. Between each exposure, nitrogen was purged for 5 s. A transparent TiO<sub>2</sub> nanoparticle layer was prepared by doctor blading a paste of 15-20 nm TiO<sub>2</sub> nanoparticles (Ti-Nanoxide T/SP, Solaronix) on the TiO<sub>2</sub> coated FTO-glass substrate. The doctor bladed TiO<sub>2</sub> film was allowed to relax for 10 min at room temperature and 10 minutes at 100°C. The electrodes were then annealed by heating in air to 325°C for 5 min, 375°C for 5 min, 450°C for 5 min and 500°C for 15 min. The electrodes were allowed to cool to a temperature of 80°C before being immersed in a D35cpdt dye solution consisting of 0.2 mM D35cpdt (Dyename, 95%) and 5 mM chenodeoxycholic acid (Solaronix) in ethanol, and left to soak overnight in the dark. After 20-24 hours, the electrodes were rinsed with acetonitrile. A ~25 µm thick Surlyn frame (Solaronix) was sandwiched between the TiO<sub>2</sub> nanoparticle electrode and a platinized FTO electrode. Light pressure was applied at ~100°C to seal the cell. Electrolyte was introduced by capillary force through two pre-drilled holes on the platinum counter electrode, which were subsequently sealed with a microglass coverslip (VWR) and Surlyn film. Eight cells were prepared in total using two different electrolytes. The compositions of each electrolyte were as follows: (1) 0.2 M [Co(bpy)<sub>3</sub>](TFSI)<sub>2</sub>, 20 mM [Co(bpy)<sub>3</sub>](TFSI)<sub>3</sub>, and 0.1 M LiTFSI (Sigma-Aldrich, 99.95% trace metal basis) in acetonitrile. (2) 0.2 M [Co(bpy)<sub>3</sub>](TFSI)<sub>2</sub>, 20 mM [Co(bpy)<sub>3</sub>](TFSI)<sub>3</sub>, 0.61 mM [Co(pty)<sub>3</sub>] and 0.1 M LiTFSI in acetonitrile. Throughout this chapter electrolyte (1) will be referred to as the [Co(bpy)<sub>3</sub>]<sup>3+/2+</sup> electrolyte, while electrolyte (2) will be referred to as the tandem electrolyte.

Photoelectrochemical measurements were performed with a potentiostat (Autolab PGSTAT 126N) interfaced with a Xenon Arc Lamp. An AM 1.5 solar filter was used to simulate sunlight at 100 mW cm<sup>-2</sup> and the light intensity was calibrated with a certified

reference cell system (Oriel® Reference Solar Cell & Meter). An additional 400 nm longpass filter was used to prevent direct excitation of the TiO<sub>2</sub> in all light measurements. A black mask with an aperture area (0.4 × 0.4 cm<sup>2</sup>) was applied on top of the cell. A set of neutral density filters (Thorlabs NEK01S) was used to conduct light intensity dependence measurements. OCVD measurements were performed in two different ways. Both were measured galvanostatically; however, in order to determine the degree of recombination to the [Co(pty)<sub>3</sub>]<sup>+</sup> complex, OCVD measurements for the tandem cells were measured under light and dark conditions. Light OCVD measurements were conducted as described in Chapter 3. Dark OCVD measurements were taken by applying the DSSCs open circuit potential for twenty seconds then measuring the cells voltage as it decayed back to solution potential.

IPCE measurements, performed under monochromatic light, were completed using a monochromator (Horiba Jobin Yvon MicroHR) attached to the 450 W Xenon arc light source. Both entrance and exit slit width were set to 0.75 mm to meet an 8 nm line width for good resolution. The photon flux of the light incident on the samples was measured with a laser power meter (Nova II Ophir). IPCE measurements were made at 10 nm intervals between 400 nm and 750 nm at short circuit in the absence of bias light.

## 4.4 Results and Discussion

### 4.4.1 Electrochemical Properties of [Co(pty)<sub>3</sub>]

[Co(pty)<sub>3</sub>]<sup>+0</sup>, Figure 4.1a, was synthesized via a modified literature procedure, as described in the experimental section above. CVs of [Co(pty)<sub>3</sub>] as a function of scan rate are displayed in Figure 4.1b. Variation of the scan rate from 25 to 2500 mV s<sup>-1</sup> resulted in a constant peak separation of 78 mV and a formal potential,  $E^\circ$ , of 0.779 V vs. NHE. The

ratio of the anodic and cathodic peak currents,  $I_{pa}/I_{pc}$ , was  $\sim 1.1$ , and the peak currents were proportional to the square root of the scan rate,  $v^{1/2}$ , Figure A4.4 of the Appendix, indicating  $[\text{Co}(\text{ptpy})_3]^{+/0}$  is reversible.<sup>18</sup> A linear fit of  $I_{pa}$  vs  $v^{1/2}$ , Figure A4.4, produced a diffusion coefficient of  $1.5 \times 10^{-5} \text{ cm}^2 \text{ s}^{-1}$  for  $[\text{Co}(\text{ptpy})_3]$  by application of the Randles-Sevcik equation.<sup>18</sup>

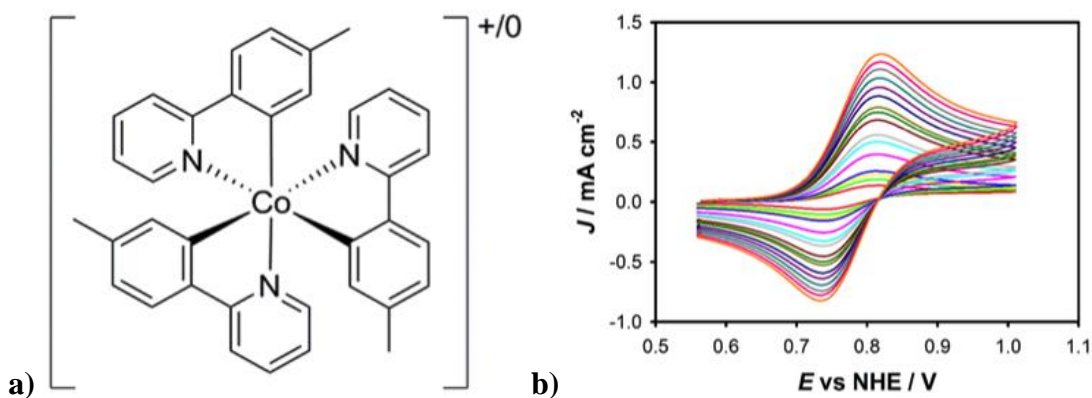
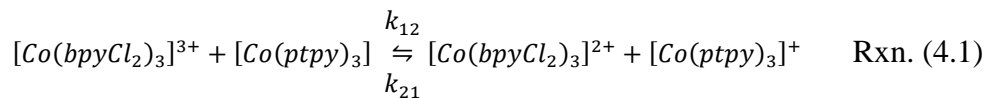


**Figure 4.1** a) Molecular structure of  $[\text{Co}(\text{ptpy})_3]^{+/0}$ . b) CVs of  $[\text{Co}(\text{ptpy})_3]$  in acetonitrile with 0.1 M LiTFSI supporting electrolyte as a function of scan rate using a platinum disk working electrode, a platinum mesh counter electrode and a Ag/AgNO<sub>3</sub> (0.1 M TBAPF<sub>6</sub> acetonitrile) reference electrode.

#### 4.4.2 Self-Exchange Kinetics of $[\text{Co}(\text{ptpy})_3]^{+/0}$ via Stopped-Flow Spectroscopy

Stopped-flow spectroscopy was used to determine the homogeneous self-exchange rate constant for  $[\text{Co}(\text{ptpy})_3]^{+/0}$ . A cross-exchange reaction between cobalt tris(4,4'-dichloro-2,2'-bipyridine),  $[\text{Co}(\text{bpyCl}_2)_3]^{3+}$ , and  $[\text{Co}(\text{ptpy})_3]$  was performed, which provided the second order forward and reverse cross-exchange rate constants,  $k_{12}$  and  $k_{21}$ , for Reaction (4.1):



Selection of  $[Co(bpyCl_2)_3]^{3+}$  for the cross-exchange with  $[Co(ppy)_3]$  was based on  $[Co(bpy)_3]^{3+/2+}$  known outersphere one electron transfer mechanism and slow electron-transfer kinetics.<sup>11,19</sup> The small potential difference between  $[Co(bpyCl_2)_3]^{3+/2+}$  and  $[Co(ppy)_3]^{+/0}$ , Figure A4.5, was also favorable for slowing down the electron exchange between the two redox shuttles on a time scale that could be observable by stopped-flow. Figure 4.2a shows a plot of the absorbance at 433 nm vs. time, which corresponds to the decay of the  $[Co(ppy)_3]$  species due to its oxidation by  $[Co(bpyCl_2)_3]^{3+}$ . In all reactions the  $[Co(bpyCl_2)_3]^{3+/2+}$  species were held in excess of  $[Co(ppy)_3]$ , which allowed the observed rate constants,  $k_{obs}$ , to be expressed by:<sup>20</sup>

$$k_{obs} = k_{12}[Co(bpyCl_2)_3]^{3+} + k_{21}[Co(bpyCl_2)_3]^{2+} \quad \text{Eq. (4.1)}$$

Figure 4.2b shows a straight line fit of the  $k_{obs}$  values plotted as a function of the excess concentration of  $[Co(bpyCl_2)_3]^{3+}$ , which produced values for the forward,  $k_{12}$ , and reverse,  $k_{21}$ , cross-exchange rate constants from the slope and y-intercept, respectively. The initial concentrations for the  $[Co(bpyCl_2)_3]^{3+/2+}$  and  $[Co(ppy)_3]$  reaction mixtures, as well as the observed pseudo-first order rate constants for these electron-transfer reactions can be found in the Appendix Table A4.2.

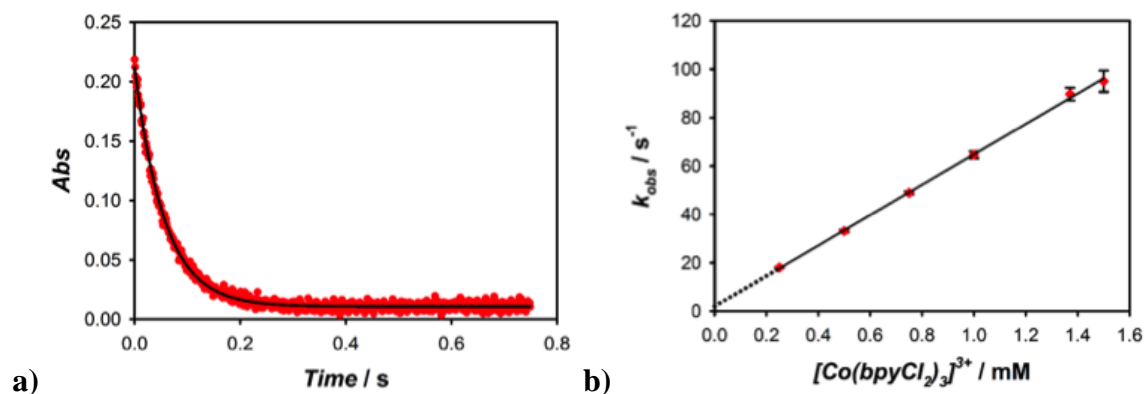


**Figure 4.2** a) Plot of absorbance at 433 nm vs. time, corresponding to decay of the  $[Co(ptypy)_3]$  species (red dots) and the resulting fit (black line) for the oxidation of  $[Co(ptypy)_3]$  ( $5.00 \times 10^{-5}$  M) by  $[Co(bpyCl_2)_3]^{3+}$  ( $5.00 \times 10^{-4}$  M). b) Observed pseudo-first order rate constants,  $k_{obs}$ , versus the excess concentration of  $[Co(bpyCl_2)_3]^{3+}$  for the reactions between  $[Co(ptypy)_3]$  and  $[Co(bpyCl_2)_3]^{3+}$ .

Using the experimentally determined cross-exchange rate constant,  $k_{12}$ , for Reaction (4.1), the Marcus cross-relation, Equation (4.2), was used to calculate the self-exchange rate constant,  $k_{11}$ , for  $[Co(ptypy)_3]^{+0,21,22}$

$$k_{12} = \sqrt{k_{11}k_{22}K_{12}f_{12}W_{12}} \quad \text{Eq. (4.2)}$$

where  $k_{22}$  is the self-exchange rate constant of  $[Co(bpyCl_2)_3]^{3+/2+}$ ,  $K_{12}$  is the equilibrium constant for the electron-transfer reaction,  $f_{12}$  is a non-linear correction term, and  $W_{12}$  is the electrostatic work term. The calculations for determining  $f_{12}$  and  $W_{12}$  terms were previously described Chapter 3. From those calculations a value of 0.92 was determined for  $f_{12}$  and 2.2 for  $W_{12}$ , Table A4.3 of the Appendix. The equilibrium constant for the electron-transfer reaction can be determined based on the free-energy difference of reaction, described by Equation (4.3):

$$-nF\Delta E = -RT\ln K_{12} \quad \text{Eq. (4.3)}$$

where  $n$  is the number of electrons transferred ( $n = 1$ ),  $F$  is Faraday's constant,  $\Delta E$  is the formal potential difference between the oxidant and reductant in solution,  $R$  is the gas constant and  $T$  is the temperature. CVs summarized in Table A4.4 of the Appendix indicate a 32 mV formal potential difference between  $[\text{Co}(\text{ptpy})_3]^{+/0}$  and  $[\text{Co}(\text{bpyCl}_2)_3]^{3+/2+}$ . The calculated equilibrium constant,  $K_{12}$ , for Reaction (4.1) is therefore  $3.5 \pm 1.3$ . From detailed balance, the equilibrium constant can also be determined from the cross-exchange rate constants for the forward and reverse reactions according to:

$$K_{12} = k_{12}/k_{21} \quad \text{Eq. (4.4)}$$

This approach produced an equilibrium constant of  $7.7 \pm 3.7$ . The agreement between the equilibrium constants determined from thermodynamic (CVs) and kinetic measurements substantiates the measured cross-exchange rate constants. The self-exchange rate constant,  $k_{22}$ , for  $[\text{Co}(\text{bpyCl}_2)_3]^{3+/2+}$  was taken to be equal to the value determined for  $[\text{Co}(\text{bpy})_3]^{3+/2+}$  measured under similar conditions, which is  $0.27 \pm 0.06 \text{ M}^{-1}\text{s}^{-1}$ .<sup>11</sup> Using these values, the self-exchange rate constant for  $[\text{Co}(\text{ptpy})_3]^{+/0}$  was calculated to be  $(9.2 \pm 3.9) \times 10^8 \text{ M}^{-1}\text{s}^{-1}$ . This very fast self-exchange rate constant is the same order of magnitude as the previously mentioned cobalt (IV/III) molecular complex,  $[(\text{DH})_2\text{Co}^{\text{III}}(\text{Me})(\text{py})]$ , measured using ESR as well as ruthenium tris(2,2'-bipyridine),  $[\text{Ru}(\text{bpy})_3]^{3+/2+}$ , ( $k_{se} = 4.2 \times 10^8 \text{ M}^{-1}\text{s}^{-1}$ ) measured by flash photolysis.<sup>13,23</sup> The fast-exchange kinetics of both  $[\text{Co}(\text{ptpy})_3]^{+/0}$  and  $[\text{Ru}(\text{bpy})_3]^{3+/2+}$  can be explained based on the isoelectronic structure of the two complexes.

In their reduced states, both complexes are low spin  $d^6$ , which consequently results in loss of electron occupancy in a bonding  $t_{2g}$  orbital (assuming  $O_h$  symmetry).

#### 4.4.3 Determination of $[\text{Co}(\text{ptpy})_3]^{+/0}$ Reorganization Energy

The fast self-exchange rate constant for  $[\text{Co}(\text{ptpy})_3]^{+/0}$  suggests minimal innersphere reorganization energy and thus the total reorganization energy is dominated by the outersphere (solvent) contribution,  $\lambda_o$ . The total reorganization energy,  $\lambda_{11}$ , for the  $[\text{Co}(\text{ptpy})_3]^{+/0}$  self-exchange reaction can be derived from the corresponding rate constant according to:

$$k_{11} = \nu_n e^{-\lambda_{11}/4k_bT} \quad \text{Eq. (4.5)}$$

where  $\nu_n$  is the frequency factor, which is taken to be  $10^{11} \text{ s}^{-1}$  due to the minimal inner-sphere reorganization energy, *vide infra*.<sup>22,24,25</sup> Equation (4.5) produces a value of 0.48 eV for  $\lambda_{11}$ . The outersphere self-exchange reorganization energy can be calculated from dielectric continuum theory using:

$$\lambda_o = \frac{(\Delta z q)^2}{4\pi\epsilon_o} \left( \frac{1}{a} - \frac{1}{R_e} \right) \left( \frac{1}{n_{sol}^2} - \frac{1}{\epsilon_{sol}^2} \right) \quad \text{Eq. (4.6)}$$

where  $\Delta z$  is the change in charge of the cobalt complex after electron transfer,  $q$  is the charge of an electron,  $\epsilon_o$  is the permittivity of free space,  $\epsilon_{sol}$  is the static dielectric of acetonitrile (36),<sup>26</sup>  $n_{sol}$  is the refractive index of acetonitrile (1.3442),<sup>27</sup>  $a$  is the radius of the reactant, and  $R_e$  is the reactant center-to-center separation distance ( $R_e = 2a$ ).<sup>22</sup> Given the structural similarity to  $[\text{Co}(\text{bpy})_3]$ , the radii of  $[\text{Co}(\text{ptpy})_3]^{+/0}$  was taken to be 6.5 Å.<sup>28</sup>

The outersphere reorganization energy was calculated to be 0.58 eV, in reasonable agreement with the value from the self-exchange, confirming negligible innersphere reorganization.

#### 4.4.4 [Co(ppy)<sub>3</sub>] Application in DSSCs

The very low reorganization energy should make [Co(ppy)<sub>3</sub>] an excellent dye-regenerator in DSSCs. Practical use of [Co(ppy)<sub>3</sub>] as a redox shuttle, however, is limited by poor solubility and the fact that the oxidized form is a good acceptor (fast recombination) and not very stable. These hurdles can be overcome, however, by employing [Co(ppy)<sub>3</sub>] in a tandem electrolyte with [Co(bpy)<sub>3</sub>]<sup>3+/2+</sup>. In this solution, any [Co(ppy)<sub>3</sub>]<sup>+</sup> formed would quickly be reduced by [Co(bpy)<sub>3</sub>]<sup>2+</sup>. Figure 4.3 depicts current density (*J*) versus applied voltage (*V*) curves for DSSCs employing a [Co(bpy)<sub>3</sub>]<sup>3+/2+</sup> electrolyte and a tandem electrolyte of [Co(ppy)<sub>3</sub>] and [Co(bpy)<sub>3</sub>]<sup>3+/2+</sup> under simulated 1 sun illumination. The average short circuit photocurrent densities, *J*<sub>sc</sub>, open circuit photovoltages, *V*<sub>oc</sub>, and fill factors, *FF*, derived from the *J*-*V* curves of four cells are given in Table A4.5. The *V*<sub>oc</sub> for both electrolyte compositions changed minimally, although it should be noted that the *V*<sub>oc</sub> of the [Co(bpy)<sub>3</sub>]<sup>3+/2+</sup> cells are smaller than literature reports for optimized devices, which utilize 4-*tert*-butylpyridine as an additive in the electrolyte.<sup>1,29</sup> For this study 4-*tert*-butylpyridine was omitted for the simplicity of understanding only the effect of adding [Co(ppy)<sub>3</sub>] to the [Co(bpy)<sub>3</sub>]<sup>3+/2+</sup> electrolyte. The major difference in performance, however, was due to an increased *J*<sub>sc</sub> for cells employing the tandem electrolyte.

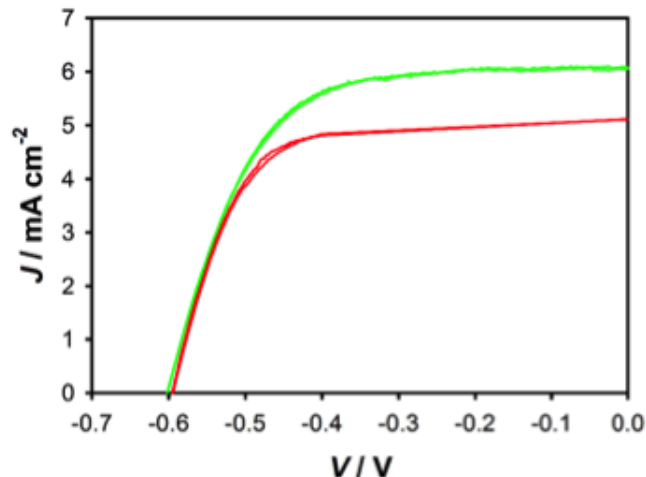


**Figure 4.3** Plots of current density versus applied potential,  $J$  vs.  $V$ , corresponding to DSSCs filled with  $[\text{Co}(\text{bpy})_3]^{3+/2+}$  electrolyte (red line) and a tandem electrolyte containing  $[\text{Co}(\text{ptpy})_3]$  and  $[\text{Co}(\text{bpy})_3]^{3+/2+}$  (green line) under AM 1.5G illumination.

Figure A4.6 shows the average IPCEs derived from the four cells containing the two different electrolytes, with error bars representing the standard deviation. Although measured under low light conditions, the IPCE values exhibit the same trends under 1 sun illumination. Validation of this statement comes from integration of each IPCE, which produced nearly the same  $J_{sc}$  value to that measured at 1 sun illumination, and a light intensity dependence study, Figure A4.7, which indicated a linear relationship from low light to 1 sun intensity. This suggests that the information from the IPCE measurements is relevant to the  $J$ - $V$  behavior. As previously discussed in Chapter 3, the IPCE can be described as the product of the light harvesting efficiency,  $\eta_{LH}$ , electron injection efficiency,  $\eta_{inj}$ , charge collection efficiency,  $\eta_{cc}$ , and the dye regeneration efficiency,  $\eta_{reg}$ :

$$IPCE(\lambda) = \eta_{LH}(\lambda)\eta_{cc}(\lambda)\eta_{inj}(\lambda)\eta_{reg}(\lambda) \quad \text{Eq. (4.7)}$$

When comparing the IPCE data of the tandem electrolyte to the  $[\text{Co}(\text{bpy})_3]^{3+/2+}$  electrolyte, the light harvesting efficiencies,  $\eta_{LH}$ , and injection efficiencies,  $\eta_{inj}$ , are expected to be the same for both cells since the two parameters are a function of the dye and in both cell configurations the D35cpdt dye was used. Figure A4.8b demonstrates that both electrolytes have nominally identical electron lifetimes, which leads to the conclusion that the charge collection is equal in both cells as well. Therefore, the increased IPCE of the tandem electrolyte appears to result strictly from improved dye regeneration efficiency,  $\eta_{reg}$ .

The dye regeneration efficiency can be described as the branching ratio between the rate of dye regeneration and dye recombination. The regeneration efficiency for the tandem electrolyte can be expressed by:

$$\eta_{reg} \cong \frac{[\text{Co}(\text{ptpy})_3]k_{reg,ptpy} + [\text{Co}(\text{bpy})_3]^{2+}k_{reg,bpy}}{[\text{Co}(\text{ptpy})_3]k_{reg,ptpy} + [\text{Co}(\text{bpy})_3]^{2+}k_{reg,bpy} + [n_s]k_{rec,D+}} \quad \text{Eq. (4.8)}$$

where  $[\text{Co}(\text{ptpy})_3]$  and  $[\text{Co}(\text{bpy})_3]^{2+}$  are the concentrations of the reduced forms of the redox shuttles,  $[n_s]$  is the surface electron concentration of  $\text{TiO}_2$ ,  $k_{reg,ptpy}$  and  $k_{reg,bpy}$  are the dye regeneration rate constants for each redox couple and  $k_{rec,D+}$  is the rate constant for recombination of electrons in the  $\text{TiO}_2$  to the oxidized dye, respectively.<sup>30</sup> The rate constants for dye regeneration can be approximated using the Marcus cross-relation, Equation (4.2). Although the self-exchange rate constants for the D35cpdt dye and other related dyes attached to the  $\text{TiO}_2$  surface are ill-defined, it is independent of the redox shuttle and therefore cancels out when taking the ratio of rate constants. The correction term,  $f$ , and work term,  $W$ , are also expected to be nearly the same and will cancel out for the two redox couples which have a similar size and charge. Therefore, the relative dye

regeneration rate constants can be determined by taking the ratio of the redox shuttle self-exchange rate constants and equilibrium constants:

$$\frac{k_{reg,ptpy} = \sqrt{k_{(ptpy/ptpy^+)} K_{D/ttcn}}}{k_{reg,bpy} = \sqrt{k_{(bpy^{2+}/bpy^{3+})} K_{D/bpy}} \quad \text{Eq. (4.9)}$$

where  $K_{D/ptpy}$  and  $K_{D/bpy}$  are the equilibrium constants for the dye ( $D$ ) regeneration reactions with  $[\text{Co}(ptpy)_3]$  and  $[\text{Co}(bpy)_3]^{2+}$ , respectively. The equilibrium constants are determined from the potential difference of the dye and redox shuttles according to Equation (4.3). The ground state potential of the D35cpdt dye adsorbed on the nanoparticle film was previously determined by CV to be 1.08 V vs. NHE.<sup>11</sup> Using this value, the resulting driving forces for regeneration was determined to be 0.503 eV and 0.301 eV for  $[\text{Co}(bpy)_3]^{3+/2+}$  and  $[\text{Co}(ptpy)_3]^{+/0}$ . Based on differences in the self-exchange rate constants and equilibrium constants, the regeneration rate constant with  $[\text{Co}(ptpy)_3]$  is expected to be 1143 times larger than  $[\text{Co}(bpy)_3]^{2+}$ . However, due to the low solubility of  $[\text{Co}(ptpy)_3]$ , the product  $k_{reg,ptpy}[\text{Co}(ptpy)_3]$  is only 3.5 times larger than  $k_{reg,bpy}[\text{Co}(bpy)_3]^{2+}$ . Assuming that  $[n_s]$  is essentially constant at short circuit under low light intensity, i.e. the conditions of the IPCE measurements, for the two electrolytes, this additional regeneration pathway should increase the regeneration efficiency from 0.54 to 0.84. This should result in an increase in the maximum IPCE from 47.5% to 77.5%, however the measured IPCE only increases to 53.5%. The difference between the calculated and measured increase in IPCE from the addition of  $[\text{Co}(ptpy)_3]$  to the electrolyte is attributed to regeneration being diffusion controlled, see Figure 1.4,  $k_{et,diff}$ . Daeneke et al. demonstrated that diffusion-limited kinetics

were present for a set of Ferrocene derivatives paired with a set of organic sensitizers when the driving force,  $-\Delta G$ , for regeneration was  $\geq 0.3$  eV.<sup>31</sup> Given the self-exchange rate constant for  $[\text{Co}(\text{ptpy})_3]$  is  $\sim 10^2$  faster than Ferrocene, the driving force is expected to be even smaller than 0.3 eV in order to reach diffusion limited regeneration, which is well within the measured driving force between  $[\text{Co}(\text{ptpy})_3]^{+/0}$  and D35cpdt.<sup>32</sup>

#### 4.5 Conclusion

In summary, the kinetics of a cobalt (IV/III) complex has been analyzed for its use as a redox shuttle in DSSCs. Cyclic voltammetry indicates  $[\text{Co}(\text{ptpy})_3]$  produces fast electron transfer kinetics based on the minimal peak separation at scan rates up to 2500  $\text{mV s}^{-1}$ , while stopped-flow spectroscopy provided the first example of a self-exchange rate constant measured at room temperature for a molecular cobalt (IV/III) complex. The extremely fast  $[\text{Co}(\text{ptpy})_3]$  kinetics rival self-exchange rate constants measured for isoelectronic ruthenium (III/II) complexes. The origin of the fast electron-transfer kinetics are attributed to a no net change in antibonding occupancy of  $[\text{Co}(\text{ptpy})_3]$  upon oxidation, which results in a negligible innersphere reorganization energy of the complex. We reasoned that the fast electron-transfer kinetics would result in improved dye regeneration assuming the electron-transfer could be modeled as a Marcus cross-exchange reaction. A tandem electrolyte containing both  $[\text{Co}(\text{ptpy})_3]$  and  $[\text{Co}(\text{bpy})_3]^{3+/2+}$  was compared side-by-side to DSSCs containing only  $[\text{Co}(\text{bpy})_3]^{3+/2+}$  in conjunction with the D35cpdt dye. The tandem electrolyte provides a route around solubility limitations and fast recombination to  $[\text{Co}(\text{ptpy})_3]^+$ . The performance of the regeneration limited  $[\text{Co}(\text{bpy})_3]^{3+/2+}$  cells were enhanced by the addition of  $[\text{Co}(\text{ptpy})_3]$  based on the improved  $J_{sc}$ ; however, diffusion

limited regeneration was observed, which didn't allow us to realize the full potential of the [Co(ppy)<sub>3</sub>] redox shuttle.

Although use of a tandem electrolyte has demonstrated enhanced DSSC performance as a result of pairing a slow exchanging redox shuttle, [Co(bpy)<sub>3</sub>]<sup>3+/2+</sup>, with a fast exchanging shuttle, [Co(ppy)<sub>3</sub>], it seems impractical that this route will provide highly efficient cells that are competitive with silicon or Perovskite PVs. Other groups have utilized the same strategy and meagerly improved performances of well-optimized devices.<sup>33,34</sup> A major issue with this route is the  $V_{oc}$  limitations set by the [Co(bpy)<sub>3</sub>]<sup>3+/2+</sup>. The ~0.5 eV energy loss as a result of having [Co(bpy)<sub>3</sub>]<sup>3+/2+</sup> in solution hampers the ability to achieve  $V_{oc}$ 's > 1 V. Small improvements in the current density and possibly the voltage will fail to push ~10% dye cells to 20%. For this reason, our group has looked at another route to enhance performance. Our thoughts, as mentioned in the conclusions of Chapter 3, are to synthesize new redox shuttles with more negative redox potentials than [Co(bpy)<sub>3</sub>]<sup>3+/2+</sup> in an effort to regenerate broader absorbing dyes. By minimizing the driving force between the conduction band and the redox shuttle, we hope to be able to mitigate recombination to fast self-exchanging redox shuttles, while also being able to quantitatively regenerate sensitizers at minimal driving forces. Although we may lose in  $V_{oc}$  it should be interesting to see how much is gained in terms of  $J_{sc}$ . Prior modeling has provided precedent for this route and indicates the ability to achieve 20% devices.<sup>35</sup> Our efforts to synthesize such a redox shuttle with fast exchange kinetics and an intrinsically negative redox potential will be describe in Chapter 5, along with our intentions on how to successfully integrate it into future DSSC systems.

## **APPENDIX**

## APPENDIX

**Table A4.1** Elemental analysis results.

Compound	Calculated (%)			Found (%)		
	C	H	N	C	H	N
[Co(bpyCl <sub>2</sub> ) <sub>3</sub> ](PF <sub>6</sub> ) <sub>2</sub> C <sub>30</sub> H <sub>18</sub> N <sub>6</sub> CoCl <sub>6</sub> P <sub>2</sub> F <sub>12</sub>	35.2	1.8	8.2	34.8	1.6	8.1
[Co(bpyCl <sub>2</sub> ) <sub>3</sub> ](PF <sub>6</sub> ) <sub>3</sub> C <sub>30</sub> H <sub>18</sub> N <sub>6</sub> CoCl <sub>6</sub> P <sub>3</sub> F <sub>18</sub>	30.8	1.6	7.2	30.1	1.2	7.2
[Co(ptpy) <sub>3</sub> ] C <sub>36</sub> H <sub>30</sub> N <sub>3</sub> Co	76.7	5.4	7.5	75.2	5.2	7.2

**Table A4.2** Observed pseudo-first order rate constants,  $k_{obs}$ , and the initial reaction mixtures for the cross-exchange between [Co(ptpy)<sub>3</sub>] and [Co(bpyCl<sub>2</sub>)<sub>3</sub>](PF<sub>6</sub>)<sub>3</sub>.

[Co(ptpy) <sub>3</sub> ] / (M)	[Co(bpyCl <sub>2</sub> ) <sub>3</sub> ] <sup>3+</sup> / (M)	[Co(bpyCl <sub>2</sub> ) <sub>3</sub> ] <sup>2+</sup> / (M)	$k_{obs}$ / (s <sup>-1</sup> )
5.00 x 10 <sup>-5</sup>	5.00 x 10 <sup>-4</sup>	5.00 x 10 <sup>-4</sup>	18.1 ± 0.2
	1.00 x 10 <sup>-3</sup>		33.1 ± 0.5
	1.50 x 10 <sup>-3</sup>		48.9 ± 0.7
	2.00 x 10 <sup>-3</sup>		64.6 ± 1.5
	2.74 x 10 <sup>-3</sup>		89.7 ± 2.6
	3.00 x 10 <sup>-3</sup>		95.0 ± 4.4

**Table A4.3** Kinetic summary of the cross-exchange rate constants,  $k_{12}$  and  $k_{21}$ , measured equilibrium constants for the forward reaction,  $K_{12}$ , the nonlinear correction term,  $f_{12}$ , and work term,  $W_{12}$ , associated with bringing precursor complexes together for Reaction (4.1) between  $[\text{Co}(\text{bpyCl}_2)_3](\text{PF}_6)_3$  and  $[\text{Co}(\text{ptpy})_3]$  in acetonitrile with 0.1 M TBAPF<sub>6</sub> at  $25 \pm 0.1^\circ\text{C}$ .

Kinetic Parameter	Cross-exchange values
$K_{12}$ (Nernst)	$3.5 \pm 1.3$
$K_{12}$ ( $k_{12} / k_{21}$ )	$7.7 \pm 3.7$
$k_{12} / (\text{M}^{-1}\text{s}^{-1})$	$(6.3 \pm 0.1) \times 10^4$
$k_{21} / (\text{M}^{-1}\text{s}^{-1})$	$(8.2 \pm 3.9) \times 10^3$
$f_{12}$	0.92
$W_{12}$	2.2

**Table A4.4** Formal reduction potentials,  $E^\circ$ , of all cobalt complexes used in the stopped-flow and DSSC studies. Ferrocene (Fc),  $[\text{Fe}(\text{C}_5\text{H}_5)_2]^{+/0}$ , is also included as a point of reference in converting from Ag/AgNO<sub>3</sub> to NHE. All formal potentials were measured using in acetonitrile with 0.1 M TBAPF<sub>6</sub> or 0.1 M LiTFSI supporting electrolyte with a platinum working electrode, a platinum mesh counter electrode and a Ag/AgNO<sub>3</sub> reference electrode (0.1 M TBAPF<sub>6</sub> acetonitrile).

Redox Couple	$E^\circ$ (mV vs Ag/AgNO <sub>3</sub> )
$[\text{Co}(\text{ptpy})_3]^{+/0}$	$231 \pm 9$
$[\text{Co}(\text{bpyCl}_2)_3]^{3+/2+}$	$263 \pm 2$
$[\text{Co}(\text{bpy})_3]^{3+/2+}$	$29 \pm 10$
$[\text{Fe}(\text{C}_5\text{H}_5)_2]^{+/0}$	$86 \pm 10$

**Table A4.5** Average  $J$ - $V$  Characteristics of four DSSCs containing a  $[\text{Co}(\text{bpy})_3]^{3+/2+}$  electrolyte and four cells with a tandem electrolyte of  $[\text{Co}(\text{ptpy})_3]$  and  $[\text{Co}(\text{bpy})_3]^{3+/2+}$ , both paired with the D35cpdt dye, and measured under 1 sun simulated AM 1.5G illumination ( $100 \text{ mW cm}^{-2}$ ).

Electrolyte	$[\text{Co}(\text{bpy})_3]^{3+/2+}$	Tandem
$\eta$ (%)	$1.99 \pm 0.11$	$2.37 \pm 0.07$
$J_{sc}$ ( $\text{mA cm}^{-2}$ )	$4.88 \pm 0.17$	$5.74 \pm 0.24$
$V_{oc}$ (V)	$0.58 \pm 0.01$	$0.60 \pm 0.01$
$ff$	$0.70 \pm 0.04$	$0.68 \pm 0.04$

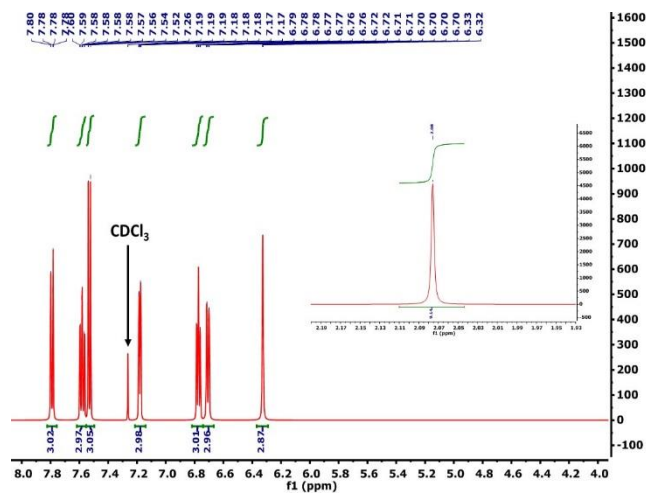


**Figure A4.1**  $^1\text{H}$  NMR of  $[\text{Co}(\text{ptpy})_3]$  in  $\text{CDCl}_3$ .

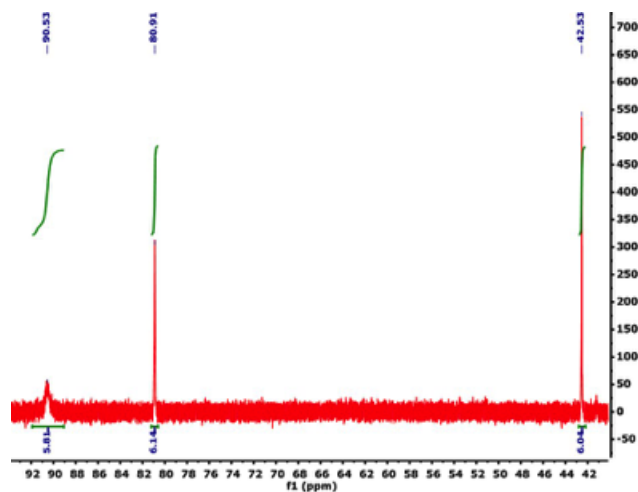


**Figure A4.2**  $^1\text{H}$  NMR of  $[\text{Co}(\text{bpyCl}_2)_3](\text{PF}_6)_2$  in  $\text{acetonitrile-}d_3$ .

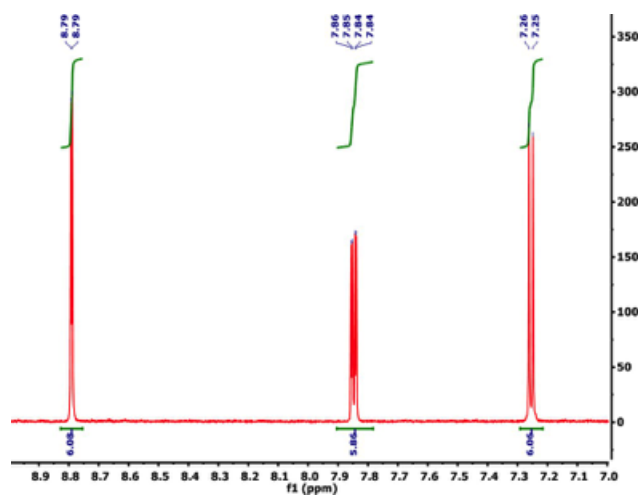


**Figure A4.3**  $^1\text{H}$  NMR of  $[\text{Co}(\text{bpyCl}_2)_3](\text{PF}_6)_3$  in  $\text{acetonitrile-}d_3$ .

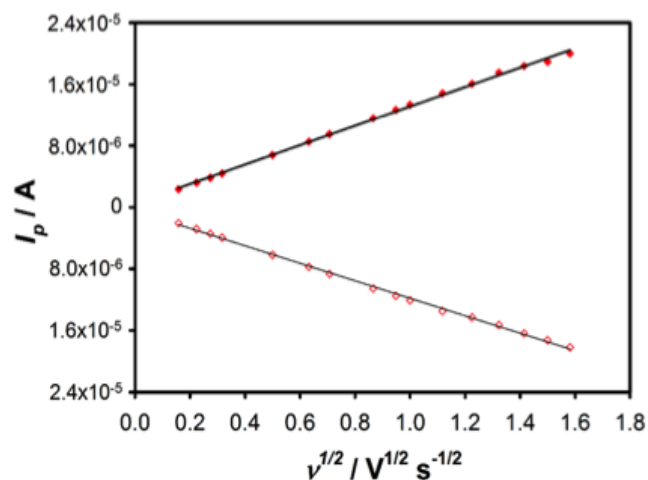


**Figure A4.4** Randles-Sevcik plot of both anodic,  $I_{pa}$ , (filled red diamonds) and cathodic,  $I_{pc}$ , (open red diamonds) peak currents versus the square root of the scan rate,  $v^{1/2}$ , for the  $[\text{Co}(\text{ptpy})_3]$  scan rate dependence, Figure 4.1b. The fit (black line) to  $I_{pa}$  vs  $v^{1/2}$  (top plot) was used to estimate the diffusion coefficient of  $[\text{Co}(\text{ptpy})_3]$ .

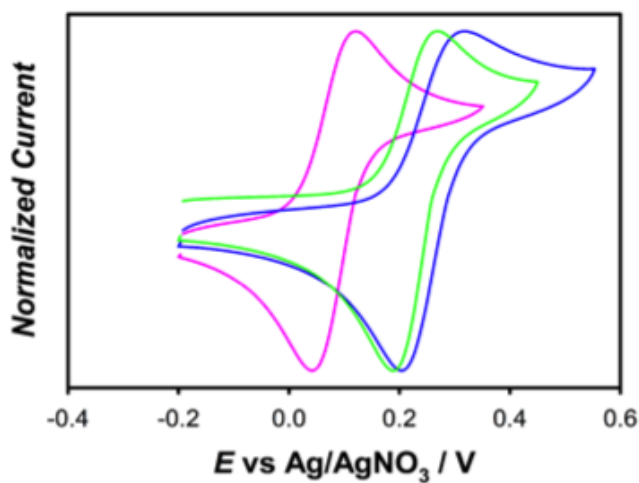


**Figure A4.5** Normalized CVs of  $[\text{Fe}(\text{C}_5\text{H}_5)_2]$  (Fc) (pink line),  $[\text{Co}(\text{ptpy})_3]$  (green line) and  $[\text{Co}(\text{bpyCl}_2)_3](\text{PF}_6)_2$  (blue line) in acetonitrile with 0.1 M TBAPF<sub>6</sub> supporting electrolyte at a scan rate of 100 mV/s using a platinum disk working electrode, a platinum mesh counter electrode and a Ag/AgNO<sub>3</sub> (0.1 M TBAPF<sub>6</sub> acetonitrile) reference electrode.

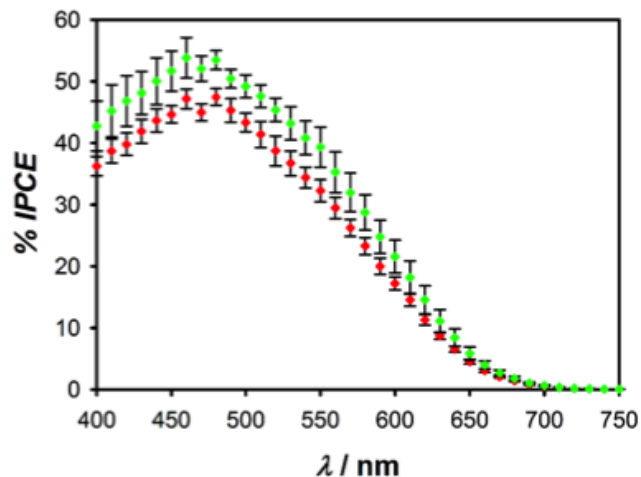


**Figure A4.6** IPCE plots of DSSCs containing a  $[\text{Co}(\text{bpy})_3]^{3+/2+}$  electrolyte (red dots) and a tandem electrolyte containing  $[\text{Co}(\text{ptpy})_3]$  &  $[\text{Co}(\text{bpy})_3]^{3+/2+}$  (green dots) both paired with the D35cpdt dye.

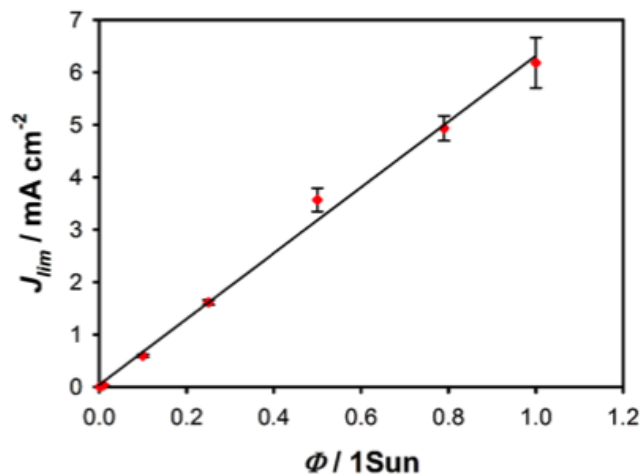


**Figure A4.7** Light intensity,  $\phi$ , dependence on short circuit photocurrent,  $J_{lim}$ , in DSSCs employing a tandem electrolyte of  $[\text{Co}(\text{ptpy})_3]$  &  $[\text{Co}(\text{bpy})_3]$  with the D35cpdt dye.

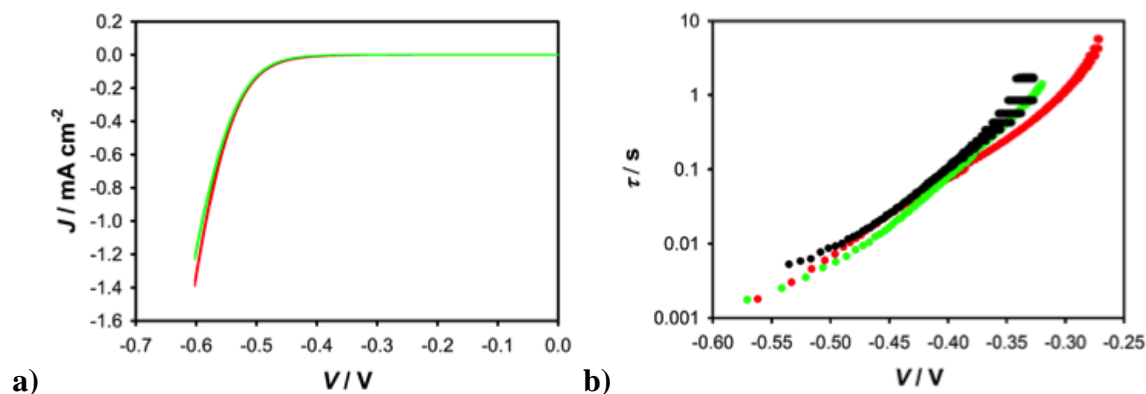


**Figure A4.8** a) Dark  $J$ - $V$  curves corresponding to DSSCs filled with  $[\text{Co}(\text{bpy})_3]^{3+/2+}$  electrolyte (red line) and a tandem electrolyte containing  $[\text{Co}(\text{ppy})_3]$  &  $[\text{Co}(\text{bpy})_3]^{3+/2+}$  (green line) both with the D35cpdt dye. b) Electron lifetimes of DSSCs containing a  $[\text{Co}(\text{bpy})_3]^{3+/2+}$  electrolyte (red dots) and a tandem electrolyte containing  $[\text{Co}(\text{ppy})_3]$  &  $[\text{Co}(\text{bpy})_3]^{3+/2+}$  (green dots) using open circuit voltage decay (OCVD). A dark OCVD measurement with a cell containing the tandem electrolyte is also overlaid (black dots) to compare degree of  $[\text{Co}(\text{ppy})_3]^+$  recombination.

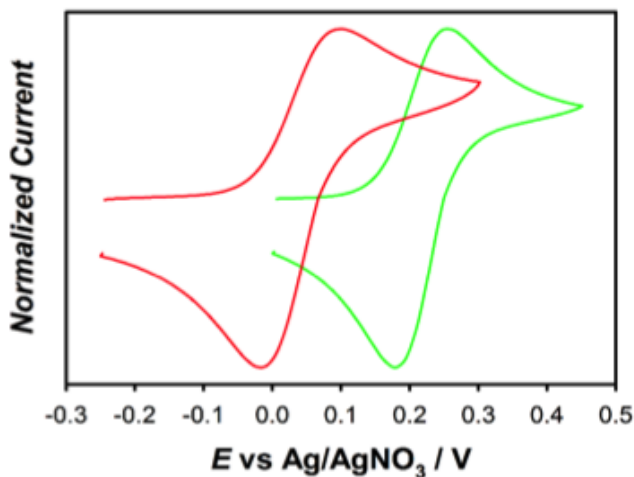


**Figure A4.9** Normalized CVs of  $[\text{Co}(\text{bpy})_3](\text{TFSI})_2$  (red line) and  $[\text{Co}(\text{ppy})_3]$  (green line) in acetonitrile with 0.1 M LiTFSI supporting electrolyte at a scan rate of 100 mV/s using a platinum disk working electrode, a platinum mesh counter electrode and a Ag/AgNO<sub>3</sub> (0.1 M TBAPF<sub>6</sub> acetonitrile) reference electrode.

## **REFERENCES**

## REFERENCES

1. Feldt, S. M.; Gibson, E. A.; Gabrielsson, E.; Sun, L.; Boschloo, G.; Hagfeldt, A. Design of Organic Dyes and Cobalt Polypyridine Redox Mediators for High-Efficiency Dye-Sensitized Solar Cells. *J. Am. Chem. Soc.* **2010**, *132* (46), 16714–16724.
2. Klahr, B. M.; Hamann, T. W. Performance Enhancement and Limitations of Cobalt Bipyridyl Redox Shuttles in Dye-Sensitized Solar Cells. *J. Phys. Chem. C* **2009**, *113* (31), 14040–14045.
3. DeVries, M. J.; Pellin, M. J.; Hupp, J. T. Dye-Sensitized Solar Cells: Driving-Force Effects on Electron Recombination Dynamics with Cobalt-Based Shuttles. *Langmuir* **2010**, *26* (11), 9082–9087.
4. Hamann, T. W.; Farha, O. K.; Hupp, J. T. Outer-Sphere Redox Couples as Shuttles in Dye-Sensitized Solar Cells . Performance Enhancement Based on Photoelectrode Modification via Atomic Layer Deposition. *J. Phys. Chem. C* **2008**, *112* (49), 19756–19764.
5. Hoffeditz, W. L.; Katz, M. J.; Deria, P.; Cutsail, G. E.; Pellin, M. J.; Farha, O. K.; Hupp, J. T. One Electron Changes Everything. A Multispecies Copper Redox Shuttle for Dye-Sensitized Solar Cells. *J. Phys. Chem. C* **2016**, *120* (7), 3731–3740.
6. Katz, M. J.; Vermeer, M. J. D.; Farha, O. K.; Pellin, M. J.; Hupp, J. T. Effects of Adsorbed Pyridine Derivatives and Ultrathin Atomic-Layer- Deposited Alumina Coatings on the Conduction Band-Edge Energy of TiO<sub>2</sub> and on Redox-Shuttle-Derived Dark Currents. *Langmuir* **2013**, *29* (2), 806–814.
7. Katz, M. J.; DeVries Vermeer, M. J.; Farha, O. K.; Pellin, M. J.; Hupp, J. T. Dynamics of Back Electron Transfer in Dye-Sensitized Solar Cells Featuring 4-Tert-Butyl-Pyridine and Atomic-Layer-Deposited Alumina as Surface Modifiers. *J. Phys. Chem. B* **2015**, *119* (24), 7162–7169.
8. Mathew, S.; Yella, A.; Gao, P.; Humphry-Baker, R.; Curchod, B. F. E.; Ashari-Astani, N.; Tavernelli, I.; Rothlisberger, U.; Nazeeruddin, M. K.; Grätzel, M. Dye-Sensitized Solar Cells with 13% Efficiency Achieved through the Molecular Engineering of Porphyrin Sensitizers. *Nat. Chem.* **2014**, *6* (3), 242–247.
9. Nakade, S.; Makimoto, Y.; Kubo, W.; Kitamura, T.; Wada, Y.; Yanagida, S. Roles of Electrolytes on Charge Recombination in Dye-Sensitized TiO<sub>2</sub> Solar Cells (2): The Case of Solar Cells Using Cobalt Complex Redox Couples. *J. Phys. Chem. B* **2005**, *109* (8), 3488–3493.
10. Ondersma, J. W.; Hamann, T. W. Measurements and Modeling of Recombination from Nanoparticle TiO<sub>2</sub> Electrodes. *J. Am. Chem. Soc.* **2011**, *133* (21), 8264–8271.

11. Xie, Y.; Baillargeon, J.; Hamann, T. W. Kinetics of Regeneration and Recombination Reactions in Dye-Sensitized Solar Cells Employing Cobalt Redox Shuttles. *J. Phys. Chem. C* **2015**, *119* (50), 28155–28166.
12. Feldt, S. M.; Lohse, P. W.; Kessler, F.; Nazeeruddin, M. K.; Gratzel, M.; Boschloo, G.; Hagfeldt, A. Regeneration and Recombination Kinetics in Cobalt Polypyridine Based Dye-Sensitized Solar Cells, Explained Using Marcus Theory. *Phys. Chem. Chem. Phys.* **2013**, *15* (19), 7087–7097.
13. Ohkubo, K.; Fukuzumi, S. Electron-Transfer Oxidation of Coenzyme B12 Model Compounds and Facile Cleavage of the cobalt(IV)-Carbon Bond via Charge-Transfer Complexes with Bases. A Negative Temperature Dependence of the Rates. *J. Phys. Chem. A* **2005**, *109* (6), 1105–1113.
14. Symes, M. D.; Surendranath, Y.; Lutterman, D. A.; Nocera, D. G. Bidirectional and Unidirectional PCET in a Molecular Model of a Cobalt-Based Oxygen-Evolving Catalyst. *J. Am. Chem. Soc.* **2011**, *133* (14), 5174–5177.
15. Ahmad, S.; Bessho, T.; Kessler, F.; Baranoff, E.; Frey, J.; Yi, C.; Grätzel, M.; Nazeeruddin, M. K. A New Generation of Platinum and Iodine Free Efficient Dye-Sensitized Solar Cells. *Phys. Chem. Chem. Phys.* **2012**, *14* (30), 10631–10639.
16. Ren, X. F.; Alleyne, B. D.; Djurovich, P. I.; Adachi, C.; Tsyba, I.; Bau, R.; Thompson, M. E. Organometallic Complexes as Hole-Transporting Materials in Organic Light-Emitting Diodes. *Inorg. Chem.* **2004**, *43* (5), 1697–1707.
17. Connelly, N. G.; Geiger, W. E. Chemical Redox Agents for Organometallic Chemistry. *Chem. Rev.* **1996**, *96* (2), 877–910.
18. Bard, A. J.; Faulkner, L. R. *Electrochemical Methods: Fundamentals and Applications*, 2nd ed.; Wiley and Sons Inc., 2000.
19. Dunn, B. C.; Ochrymowycz, L. A.; Rorabacher, D. B. Electron-Transfer Kinetics of the Copper(II/I) Complex with 1,4,8,11-Tetrathiacyclotetradecane in Acetonitrile. *Inorg. Chem.* **1995**, *34* (7), 1954–1956.
20. Xie, B.; Wilson, L. J.; Stanbury, D. M. Cross-Electron-Transfer Reactions of the [CuII/I(bite)]<sup>2+/+</sup> Redox Couple. *Inorg. Chem.* **2001**, *40* (14), 3606–3614.
21. Chou, M.; Creutz, C.; Sutin, N. Rate Constants and Activation Parameters for Outer-Sphere Electron-Transfer Reactions and Comparisons with the Predictions of Marcus Theory. *J. Am. Chem. Soc.* **1977**, *99* (17), 5615–5623.
22. Marcus, R. A.; Sutin, N. Electron Transfers in Chemistry and Biology. *Biochim. Biophys. Acta - Rev. Bioenerg.* **1985**, *811* (3), 265–322.

23. Young, R. C.; Keene, F. R.; Meyer, T. J. Measurement of Rates of Electron Transfer between Ru(bpy)<sub>3</sub><sup>2+</sup> and Fe(phen)<sub>3</sub><sup>2+</sup> and between Ru(phen)<sub>3</sub><sup>3+</sup> and Ru(bpy)<sub>3</sub><sup>2+</sup> by Differential Excitation Flash Photolysis. *J. Am. Chem. Soc.* **1977**, *99* (8), 2468–2473.
24. Sutin, N. Nuclear, Electronic, and Frequency Factors in Electron Transfer Reactions. *Acc. Chem. Res.* **1982**, *15* (9), 275–282.
25. Sutin, N. Theory of Electron Transfer Reactions: Insights and Hintsights. *Prog. Inorg. Chem.* **1983**, *30*, 441–498.
26. Blomgren, G. E. *Nonaqueous Electrochemistry*; Aurbach, D., Ed.; Marcel Dekker: New York, 1999.
27. Lide, D. R. CRC Handbook of Chemistry and Physics. 3485.
28. Hamann, T. W.; Gstrein, F.; Brunschwig, B. S.; Lewis, N. S. Measurement of the Dependence of Interfacial Charge-Transfer Rate Constants on the Reorganization Energy of Redox Species at N-ZnO/H<sub>2</sub>O Interfaces. *J. Am. Chem. Soc.* **2005**, *127* (40), 13949–13954.
29. Haque, S. A.; Palomares, E.; Cho, B. M.; Green, A. N. M.; Hirata, N.; Klug, D. R.; Durrant, J. R. Charge Separation versus Recombination in Dye-Sensitized Nanocrystalline Solar Cells: The Minimization of Kinetic Redundancy. *J. Am. Chem. Soc.* **2005**, *127* (10), 3456–3462.
30. Hamann, T. W.; Ondersma, J. W. Dye-Sensitized Solar Cell Redox Shuttles. *Energy Environ. Sci.* **2011**, *4* (2), 370.
31. Daeneke, T.; Mozer, A. J.; Uemura, Y.; Makuta, S.; Fekete, M.; Tachibana, Y.; Koumura, N.; Bach, U.; Spiccia, L. Dye Regeneration Kinetics in Dye-Sensitized Solar Cells. *J. Am. Chem. Soc.* **2012**, *134* (41), 16925–16928.
32. Edward Shih Yang, Man-Sheung Chan, and A. C. W. Electron Exchange between Ferrocene and Ferrocenium Ion. Effects of Solvent and of Ring Substitution on the Rate. *J. Phys. Chem.* **1980**, *84* (23), 3094–3099.
33. Hao, Y.; Yang, W.; Zhang, L.; Jiang, R.; Mijangos, E.; Saygili, Y.; Hammarstro, L.; Hagfeldt, A.; Boschloo, G. A Small Electron Donor in Cobalt Complex Electrolyte Significantly Improves Efficiency in Dye-Sensitized Solar Cells. *Nat. Commun.* **2016**, *7*, 1–8.
34. Yang, W.; Vlachopoulos, N.; Hao, Y.; Hagfeldt, A.; Boschloo, G. Efficient Dye Regeneration at Low Driving Force Achieved in Triphenylamine Dye LEG4 and TEMPO. *Phys. Chem. Chem. Phys.* **2015**, *17*, 15868–15875.
35. Ondersma, J. W.; Hamann, T. W. Recombination and Redox Couples in Dye-Sensitized Solar Cells. *Coord. Chem. Rev.* **2013**, *257* (9–10), 1533–1543.

## Chapter 5. Spin-Doctoring Cobalt Redox Shuttles

*\*I would like to acknowledge Yuling Xie and Austin Raithel for their contributions to this chapter. Yuling began this project and provided a solid foundation to start from. Austin assisted in the synthesis and characterization of each cobalt complex.*

### 5.1 Abstract

A new low spin (LS) cobalt(II) outersphere redox shuttle (OSRS)  $[\text{Co}(\text{PY}_5\text{Me}_2)(\text{CN})]^+$ , where  $\text{PY}_5\text{Me}_2$  represents the pentadentate ligand 2,6-bis(1,1-bis(2-pyridyl)ethyl)pyridine, has been synthesized and fully characterized for its potential application in dye-sensitized solar cells (DSSCs). Introduction of the strong field  $\text{CN}^-$  ligand into the open axial coordination site forced the cobalt(II) complex,  $[\text{Co}(\text{PY}_5\text{Me}_2)(\text{CN})]^+$ , to become LS based upon the complex's magnetic susceptibility ( $1.91 \pm 0.02 \mu_B$ ), determined by the Evans Method. Interestingly, dimerization and subsequent cobalt hexacyanide cluster formation of the  $[\text{Co}(\text{PY}_5\text{Me}_2)(\text{CN})]^+$  monomer was observed upon long-term solvent exposure or addition of a supporting electrolyte for electrochemical characterization. Although long-term stability of the  $[\text{Co}(\text{PY}_5\text{Me}_2)(\text{CN})]^+$  complex made it difficult to fabricate liquid electrolytes for DSSC applications, short-term stability in neat solvent afforded the opportunity to isolate the self-exchange kinetics of  $[\text{Co}(\text{PY}_5\text{Me}_2)(\text{CN})]^{2+/+}$  via stopped-flow spectroscopy. Use of Marcus theory provided a smaller than expected self-exchange rate constant of  $20 \pm 5.5 \text{ M}^{-1}\text{s}^{-1}$  for  $[\text{Co}(\text{PY}_5\text{Me}_2)(\text{CN})]^{2+/+}$ , which we attribute to a Jahn-Teller effect observed from the collected monomer crystallographic data. When compared side-by-side to cobalt tris(2,2'-bipyridine),  $[\text{Co}(\text{bpy})_3]^{3+}$ , DSSCs employing  $[\text{Co}(\text{PY}_5\text{Me}_2)(\text{CN})]^{2+}$  are expected to achieve superior charge collection, which result from a smaller rate constant,  $k_{et}$ , for recombination

based upon simple dark  $J-E$  measurements of the two redox shuttles. Given the negative redox potential (0.254 V vs. NHE) of  $[\text{Co}(\text{PY}_5\text{Me}_2)(\text{CN})]^{2+/+}$  and the slow recombination kinetics,  $[\text{Co}(\text{PY}_5\text{Me}_2)(\text{CN})]^{2+/+}$  becomes an attractive OSRS to regenerate near IR absorbing sensitizers in solid state DSSC devices.

## 5.2 Introduction

To date, the best performing DSSC has employed the OSRS cobalt tris(2,2'-bipyridine),  $[\text{Co}(\text{bpy})_3]^{3+/2+}$  (bpy = 2,2'-bipyridine) paired with a Zn-porphyrin sensitizer SM315 to produce a record PCE of over 13 %.<sup>1</sup> Although, DSSCs employing  $[\text{Co}(\text{bpy})_3]^{3+/2+}$  have produced the highest efficiencies, the performance of these devices are still suboptimal and can be attributed to the spin change associated with the oxidation of the cobalt metal center. We have recently shown that the large inner-sphere reorganization energy associated with the loss of two anti-bonding electrons upon oxidation of high spin (HS)  $[\text{Co}(\text{bpy})_3]^{2+}$  to low spin (LS)  $[\text{Co}(\text{bpy})_3]^{3+}$  results in inefficient dye regeneration of the organic dye D35cpdt.<sup>2,3</sup> Furthermore, our group and others have shown improved PCEs in DSSCs containing tandem electrolytes of a fast exchanging redox shuttle mixed with  $[\text{Co}(\text{bpy})_3]^{3+/2+}$  providing even more evidence that regeneration is suboptimal with electrolytes containing only  $[\text{Co}(\text{bpy})_3]^{3+/2+}$ .<sup>2,4,5</sup> Assuming regeneration can be modeled as a simple cross-exchange reaction between the dye and redox shuttle, Marcus Theory would suggest that redox shuttles with faster self-exchange kinetics should provide faster regeneration kinetics.<sup>6</sup> This in fact is true and has been demonstrated in our lab, see Chapter 3, through the use of a LS cobalt(II) OSRS  $[\text{Co}(\text{ttcn})_2]^{3+/2+}$ , where ttcn represents 1,4,7-trithiacyclononane.<sup>3</sup> Through external quantum yield measurements, it was determined that regeneration was nearly quantitative using  $[\text{Co}(\text{ttcn})_2]^{3+/2+}$  compared

to  $[\text{Co}(\text{bpy})_3]^{3+/2+}$ , despite only a  $\sim 60$  mV smaller driving force to regenerate the sensitizer D35cpdt. Unfortunately, DSSCs employing  $[\text{Co}(\text{ttcn})_2]^{3+/2+}$  suffered from faster recombination compared to  $[\text{Co}(\text{bpy})_3]^{3+/2+}$  which diminished the charge collection efficiency. In principle, the charge collection can be improved by reducing the driving force, and thus the rate of recombination, without sacrificing advantageous regeneration kinetics. However, as the ligand framework of ttcn is comprised of  $\text{sp}^3$  carbons, there are no synthetic handles to tune the redox potential i.e. adding substituents onto the carbons or increasing the number of carbon atoms on the ring system.<sup>7-9</sup> We are unaware of any alternative LS cobalt(II) OSRS to  $[\text{Co}(\text{ttcn})_2]^{3+/2+}$ , which is why we describe efforts made to exploit alternative ligand systems and seek to develop a new family of promising LS cobalt redox shuttles for DSSCs. Ideally, synthesis of new LS cobalt OSRSs would require more negative redox potentials than the commonly used cobalt polypyridyl complexes in order minimize the driving force for interfacial charge transfer i.e. slower recombination kinetics, while consequently maximizing the charge collection. With such negative redox potentials and fast exchange kinetics, efficient dye regeneration is expected at small overpotentials for sensitizers with smaller optical gaps. This in turn will provide a viable route for integrating new near IR absorbing sensitizers into DSSC devices.

Motivation for designing a new family of OSRSs has come from the groups of Bach and Long where a pentadentate ligand 2,6-bis(1,1-bis(2-pyridyl)ethyl)pyridine,  $\text{PY}_5\text{Me}_2$ , was coordinated to a cobalt center to provide the parent complex,  $[\text{Co}(\text{PY}_5\text{Me}_2)(\text{MeCN})]^{3+/2+}$ , amenable to functionalization.<sup>10-13</sup> It is expected that the variation of electron donating or withdrawing ligands in the axial site of these coordination complexes will provide a high degree of tunability with regards to formal potential and the

spin-state of the cobalt metal center. Analogous studies done by Stack et al. has already demonstrated such tunability on a series of ferrous complexes with a structurally similar ligand, 2,6-bis-(bis-2-pyridyl)methoxymethane)pyridine (PY5).<sup>14</sup> In spanning the spectrochemical series via coordination of various axial ligands (Cl<sup>-</sup>, N<sub>3</sub>, MeOH, CN<sup>-</sup>, etc...), each Fe(II) complex was highly susceptible to changes in spin-state and redox potential. Functionalization of the axial cobalt ligand via displacement of a weakly coordinated acetonitrile (MeCN) has already been done using common DSSC electrolyte additives such as 4-*tert*-butylpyridine (tBP) and *N*-methylbenzimidazole (NMBI), however, use of such pyridine derivatives failed to significantly modulate the energetics of the resulting OSRSs or the spin-state of the cobalt metal center.<sup>13</sup> To build on Stack and Bach's previous studies, we envisioned using a strong field ligand such as cyanide, CN<sup>-</sup>, to obtain the desired results. Stack demonstrated that, as a strong donor and anionic ligand, cyanide can push the redox potential more negative than most ligands in the spectrochemical series. In addition, the strong field ligand induced a LS Fe(II). With this study in mind, we reasoned that introduction of the CN<sup>-</sup> ligand to the sixth coordination site of the [Co(PY<sub>5</sub>Me<sub>2</sub>)(MeCN)]<sup>2+</sup> complex would likewise result in a rare example of a LS Co(II) complex with a potential more negative of [Co(ttcn)<sub>2</sub>]<sup>3+/2+</sup> and thus a promising new class of OSRSs.

In this chapter, we have prepared and fully characterized the cobalt complexes, [Co(PY<sub>5</sub>Me<sub>2</sub>)(CN)]<sup>2+/-</sup>. Through the use of Evans method studies, it was determined that coordination of a cyanide ligand to the parent [Co(PY<sub>5</sub>Me<sub>2</sub>)(MeCN)]<sup>2+</sup> forced the Co(II), [Co(PY<sub>5</sub>Me<sub>2</sub>)(CN)]<sup>+</sup>, to become LS. Interestingly, addition of cyanide to [Co(PY<sub>5</sub>Me<sub>2</sub>)(MeCN)]<sup>2+</sup> resulted in unexpected side reactions that were highly dependent

on the reaction conditions imparted. Depending on the equivalents of cyanide, temperature and overall reaction time, dimerization and subsequent precipitation of a cobalt hexacyanide cluster complex were observed. The dimer complex was isolated and characterized; however, due to solubility issues, the cluster complex was only analyzed by X-ray crystallography. The instability of the pure  $[\text{Co}(\text{PY}_5\text{Me}_2)(\text{CN})]^+$  complex was identified by  $^1\text{H}$  NMR and electrochemistry studies. In neat acetonitrile, the complex remains stable for kinetic measurements using stopped-flow spectroscopy; however, dimerization results almost instantaneously upon addition of a supporting electrolyte. Although stability appears to be an issue in liquid electrolytes, the short-term stability in neat solvent makes  $[\text{Co}(\text{PY}_5\text{Me}_2)(\text{CN})]^{2+/+}$  an ideal candidate as a solid state hole conductor for DSSCs.

## 5.3 Experimental

### 5.3.1 Materials

All reagents were obtained from commercial suppliers (Oakwood Chemical, Sigma Aldrich, Alfa Aesar or Strem Chemicals) and used as received unless otherwise stated. Solvents used in the synthesis, characterization and kinetics studies of all cobalt complexes were dried prior to being stored in a glovebox (MBRAUN Labmaster SP). Tetrahydrofuran (Fisher Chemical, Optima) and diethyl ether (Anhydrous, ACS Reagent,  $\geq 99.0\%$ ) were distilled over sodium/benzophenone. Methanol was dried by reacting magnesium turnings and iodine, then distilling under nitrogen and storing over  $3\text{\AA}$  molecular sieves. Acetonitrile (Fisher Chemical Certified ACS,  $\geq 99.5\%$ ) and dichloromethane (Macron Fine Chemicals AR ACS) were purified by being passed through an activated alumina column. The supporting electrolytes, tetrabutylammonium hexafluorophosphate (Sigma-Aldrich,

98%), TBAPF<sub>6</sub>, and lithium triflate (Sigma-Aldrich, 99.995% trace metals basis), LiOTf, were stored in a glovebox under moisture free conditions prior to use. However, before storing in the glovebox, TBAPF<sub>6</sub> was recrystallized from ethanol/diethyl ether and dried under vacuum.

### 5.3.2 Instrumentation

CHN analysis was conducted at Michigan State University. UV-Vis spectra were measured with a Perkin-Elmer Lambda 35 UV-Vis spectrometer using 1 cm path length quartz cuvettes. High resolution mass spectra (HRMS) were obtained at the Michigan State University Mass Spectrometry Service Center using a Waters GCT Premier instrument run on electron ionization (EI) direct probe or a Waters QTOF Ultima instrument run on electrospray ionization (ESI+). Raman spectroscopy was collected using a Renishaw inVia Raman microscope employing a RL532C100 laser source. <sup>1</sup>H NMR spectra were measured at room temperature (25 °C) on an Agilent DirectDrive2 500 MHz spectrometer and referenced to residual solvent signals. All coupling constants are apparent J values measured at the indicated field strengths in Hertz (s = singlet, d = doublet, t = triplet, q = quartet, dd = doublet of doublets, ddd = doublet of doublet of doublets, td = triplet of doublets, m = multiplet). Cyclic voltammetry (CV) measurements were performed with a μAutolabIII/FRA2 potentiostat using a platinum disk working electrode, platinum mesh counter electrode and a homemade Ag/AgNO<sub>3</sub> (0.1 M TBAPF<sub>6</sub> acetonitrile) reference electrode. Ferrocene was used as an internal reference. The error associated with each redox shuttle's formal potential,  $E^\circ$ , is based on the standard deviation of the formal potentials measured over three separate days. Reference conversion to NHE was done assuming the potential of Ferrocene in acetonitrile is 0.40 V vs SCE.<sup>15</sup> Dark *J-E*

measurements were obtained for both  $[\text{Co}(\text{PY}_5\text{Me}_2)(\text{CN})]^{2+}$  and  $[\text{Co}(\text{bpy})_3]^{3+}$  in acetonitrile with 0.1M lithium triflate, LiOTf, using a three-electrode setup interfaced with the  $\mu$ Autolab mentioned above. The three electrode setup contained a mesoporous thin film of  $\text{TiO}_2$  nanoparticles attached to an FTO substrate (fabrication described below) which acted as a working electrode, a homemade Ag/AgNO<sub>3</sub> reference (described above) along with a high surface area platinum mesh counter electrode. Figure A5.17, gives a pictorial illustration of the setup.<sup>16</sup>

### 5.3.3 X-Ray Crystallography Methodology

Crystals were mounted on a nylon loop with paratone oil on a Bruker APEX-II CCD diffractometer. The crystal was kept at  $T = 173(2)$  K during data collection. Using Olex2 (Dolomanov et al., 2009), the structure was solved with the ShelXS (Sheldrick, 2008) structure solution program, using the Direct Methods solution method. The model was refined with version 2014/6 of XL (Sheldrick, 2008) using Least Squares minimization. All non-hydrogen atoms were refined anisotropically. Hydrogen atom positions were calculated geometrically and refined using the riding model. There are two independent molecules in the asymmetric unit of the  $[\text{Co}(\text{PY}_5\text{Me}_2)(\text{CN})](\text{OTf})$  crystals. Structure and refinement data are summarized in Tables A5.2 and A5.3 for  $[\text{Co}(\text{PY}_5\text{Me}_2)(\text{CN})](\text{OTf})$ ,  $[\text{Co}(\text{PY}_5\text{Me}_2)(\text{CN})](\text{OTf})_2$ , the Dimer Complex, the Cluster Complex and  $[\text{Co}(\text{PY}_5\text{Me}_2)(\text{F})](\text{OTf})_2$ . The structures of the Cluster Complex and  $[\text{Co}(\text{PY}_5\text{Me}_2)(\text{F})](\text{OTf})_2$  can be found in the Appendix, Figures A5.21-A5.3.

### 5.3.4 Synthesis of Parent Cobalt $[\text{Co}(\text{PY}_5\text{Me}_2)(\text{MeCN})](\text{OTf})_2$ Complex

Unless otherwise noted, all synthesis procedures were performed under inert N<sub>2</sub> atmosphere using schlenk line or standard glovebox techniques. The ligand PY<sub>5</sub>Me<sub>2</sub> (2,6-

bis(1,1-bis(2-pyridyl)ethyl)pyridine) was synthesized according to a procedure previously reported in the literature.<sup>17</sup> The synthesized ligand was characterized by <sup>1</sup>H NMR and the resulting chemical shifts were matched to the literature report: <sup>1</sup>H NMR (500 MHz, acetonitrile-*d*<sub>3</sub>) δ 8.45 (ddd, *J* = 4.8, 1.9, 1.0 Hz, 4H), 7.61 (t, *J* = 7.9 Hz, 1H), 7.52 (ddd, *J* = 8.1, 7.5, 1.9 Hz, 4H), 7.14 (ddd, *J* = 7.4, 4.8, 1.1 Hz, 4H), 7.04 (d, *J* = 7.9 Hz, 2H), 6.91 (dt, *J* = 8.1, 1.0 Hz, 4H), 2.13 (s, 6H). The [Co(PY<sub>5</sub>Me<sub>2</sub>)(MeCN)](OTf)<sub>2</sub> complex (MeCN represents acetonitrile) was synthesized using a modified literature procedure.<sup>10</sup> First, [Co(PY<sub>5</sub>Me<sub>2</sub>)(I)]I was prepared, but only allowed to stir overnight (~12 hours) before being collected. Finally, metathesis of [Co(PY<sub>5</sub>Me<sub>2</sub>)(I)]I to yield [Co(PY<sub>5</sub>Me<sub>2</sub>)(MeCN)](OTf)<sub>2</sub> was done using thallium(I) triflate (TlOTf) and allowed to stir overnight (~12 hours). Characterization of the parent [Co(PY<sub>5</sub>Me<sub>2</sub>)(MeCN)](OTf)<sub>2</sub> complex was carried out by way of elemental analysis, Table A5.1, mass spectrometry, and electrochemistry i.e. cyclic voltammetry (see Figure 5.5 below). During the mass spec measurements (M<sup>+</sup>), it was observed that each of the parent complexes lost their –MeCN ligand, Figure A5.1. This resulted in intense peaks for Co(PY<sub>5</sub>Me<sub>2</sub>)<sup>2+</sup> and Co(PY<sub>5</sub>Me<sub>2</sub>)(OTf)<sup>+</sup> at 251.07 and 651.09. Elemental analysis: found (calcd) for C<sub>33</sub>H<sub>28</sub>CoF<sub>6</sub>N<sub>6</sub>O<sub>6</sub>S<sub>2</sub>: C, 45.33(47.09); H, 3.03(3.35); N, 8.56(9.99).

### 5.3.5 [Co(PY<sub>5</sub>Me<sub>2</sub>)(CN)](OTf) Synthesis

In a glovebox, [Co(PY<sub>5</sub>Me<sub>2</sub>)(MeCN)](OTf)<sub>2</sub> (0.178 mmol, 149.9 mg) was dissolved in (~5 mL) methanol and a separate methanolic solution (~3 mL) of KCN (0.264 mmol, 17.2 mg) was made before being pulled out and placed in an ice bath to cool. After allowing the mixtures to equilibrate to the temperature of the ice bath, the KCN solution was slowly charged to the stirring solution of [Co(PY<sub>5</sub>Me<sub>2</sub>)(MeCN)](OTf)<sub>2</sub>, which

immediately turned from bright yellow/orange to a dark reddish/brown. To avoid the accumulation of side-products the reaction mixture was only allowed to stir for one minute before being precipitated with dry diethyl ether. Dissolution of the crude  $[\text{Co}(\text{PY}_5\text{Me}_2)(\text{CN})](\text{OTf})$  yielded a brown powder. The supernatant was decanted in the glovebox and the pure product was obtained after recrystallizing in dichloromethane and washing with diethyl ether (yield: 65.4%). (Note- insoluble particulate in dichloromethane was syringe filtered before being crashed with diethyl ether.) Crystals suitable for single crystal X-ray diffraction analysis were obtained by slow vapor diffusion of ether into a concentrated acetonitrile solution of  $[\text{Co}(\text{PY}_5\text{Me}_2)(\text{CN})](\text{OTf})$  at room temperature. Mass spectrometry, elemental analysis and  $^1\text{H}$  NMR were also used to characterize the  $[\text{Co}(\text{PY}_5\text{Me}_2)(\text{CN})](\text{OTf})$  complex, see Appendix. An intense peak for  $[\text{Co}(\text{PY}_5\text{Me}_2)(\text{CN})]^+$  at 528.2 was observed in the mass spectra ( $\text{M}^+$ ), along with peaks for complexes that lost their exogenous CN ligand ( $[\text{Co}(\text{PY}_5\text{Me}_2)]^{2+}$  at 251 and  $[\text{Co}(\text{PY}_5\text{Me}_2)(\text{OTf})]^+$  at 651.1). Interestingly, even with pure material peaks for the oxidized complex were also observed ( $[\text{Co}(\text{PY}_5\text{Me}_2)(\text{CN})]^{2+}$  at 264.1 and  $[\text{Co}(\text{PY}_5\text{Me}_2)(\text{CN})](\text{OTf})^+$  at 677.1). Elemental analysis: found (calcd) for  $\text{C}_{31}\text{H}_{25}\text{CoF}_3\text{N}_6\text{O}_3\text{S}$ : C, 54.47(54.95); H, 3.71(3.72); N, 11.90(12.40).

#### 5.3.6 $[\text{Co}(\text{PY}_5\text{Me}_2)(\text{CN})](\text{OTf})_2$ Synthesis

$[\text{Co}(\text{PY}_5\text{Me}_2)(\text{CN})](\text{OTf})$  (0.133 mmol, 89.9 mg) was dissolved in a small amount (~5 mL) of acetonitrile. A second acetonitrile solution (~5 mL) of silver triflate,  $\text{AgOTf}$ , (0.132 mmol, 34.0 mg) was made and slowly added to the first. Fine gray silver particulate formed immediately after  $\text{AgOTf}$  addition and the reaction mixture turned from a dark reddish/brown to a light orange solution. The mixture was allowed to stir for 2 hours before

the silver particulate was syringe filtered and the crude product was crashed with diethyl ether. The supernatant was decanted and the pure light orange product (yield: 52.8%) was isolated by washing with dichloromethane and ether. Crystals suitable for single crystal X-ray diffraction analysis were obtained by slow vapor diffusion of ether into a concentrated acetonitrile solution of  $[\text{Co}(\text{PY}_5\text{Me}_2)(\text{CN})](\text{OTf})_2$  at room temperature. Mass spectroscopy, elemental analysis and  $^1\text{H}$  NMR were also used to characterize the  $[\text{Co}(\text{PY}_5\text{Me}_2)(\text{CN})](\text{OTf})_2$  complex. Intense peaks for  $[\text{Co}(\text{PY}_5\text{Me}_2)(\text{CN})]^{2+}$  at 264.1 and  $[\text{Co}(\text{PY}_5\text{Me}_2)(\text{CN})](\text{OTf})^+$  at 677.1 were observed by mass spectrometry ( $\text{M}^+$ ). However, it appeared even with pure material the mass spec also showed peaks for the reduced complex:  $[\text{Co}(\text{PY}_5\text{Me}_2)]^{2+}$  at 251,  $[\text{Co}(\text{PY}_5\text{Me}_2)(\text{OTf})]^+$  at 651.1 and  $[\text{Co}(\text{PY}_5\text{Me}_2)(\text{CN})]^+$  at 528.1.  $^1\text{H}$  NMR (500 MHz, acetonitrile- $d_3$ )  $\delta$  9.91 (dd,  $J = 6.2, 1.4$  Hz, 4H), 8.40 (dd,  $J = 8.7, 7.3$  Hz, 1H), 8.31 (d,  $J = 8.0$  Hz, 2H), 8.11 (ddd,  $J = 8.6, 7.3, 1.3$  Hz, 4H), 8.04 (dd,  $J = 8.2, 1.7$  Hz, 4H), 7.71 (ddd,  $J = 7.6, 6.2, 1.7$  Hz, 4H), 2.81 (s, 6H). Elemental analysis: Found (Calcd) for  $\text{C}_{32}\text{H}_{25}\text{CoF}_6\text{N}_6\text{O}_6\text{S}_2$ : C, 45.67(46.50); H, 3.17(3.05); N, 9.59(10.17).

### 5.3.7 Synthesis of Cross-Exchange Redox Shuttles

OSRSs used in the stopped-flow studies were either purchased from commercial suppliers or synthesized from previous literature reports. Synthesis of the  $[\text{Co}(\text{terpy})_2]^{3+/2+}$  complexes, where terpy represents 2,2':6',2''-terpyridine, was carried out using a modified literature procedure.<sup>18</sup> Briefly, the appropriate stoichiometric ratio (~2.1 equivalents) of the terpy (Alfa Aesar, 97%) ligand was reacted with (1 equivalent) cobalt dichloride hexahydrate ( $\text{CoCl}_2 \cdot 6\text{H}_2\text{O}$ ) in methanol. The reaction was brought to reflux and stirred in air for ~2 hours. Upon cooling, the reaction mixture was concentrated and an excess of  $\text{TBAPF}_6$  (~6-8 equivalents) dissolved in methanol was added. A brownish/orange solid

precipitated out of solution after sonication. The pure product was vacuum filtered and washed with copious amounts of methanol and diethyl ether before being collected and dried. The isolated paramagnetic  $[\text{Co}(\text{terpy})_2](\text{PF}_6)_2$  species was characterized by  $^1\text{H}$  NMR containing chemical shifts up to ca. 100 ppm. Oxidation of the  $[\text{Co}(\text{terpy})_2](\text{PF}_6)_2$  complex was carried out using 1.1 equivalents of nitrosonium hexafluorophosphate (Strem Chemicals, min. 97%),  $\text{NOPF}_6$ , dissolved in a minimal amount of acetonitrile. The reaction was stirred in air overnight (~12 hrs.) to ensure the reaction reached completion. Isolation of the crude  $[\text{Co}(\text{terpy})_2](\text{PF}_6)_3$  product was carried out via precipitation from acetonitrile using diethyl ether. The solid was vacuum filtered and washed with dichloromethane, methanol and diethyl ether. Recrystallization in acetonitrile yielded the pure  $[\text{Co}(\text{terpy})_2](\text{PF}_6)_3$  product confirmed via  $^1\text{H}$  NMR.  $^1\text{H}$  NMR (500 MHz, acetonitrile- $d_3$ )  $\delta$  9.16 – 9.08 (m, 2H), 9.02 (d,  $J = 8.1$  Hz, 4H), 8.61 (d,  $J = 7.8$  Hz, 4H), 8.25 (t,  $J = 7.8$  Hz, 4H), 7.44 (t,  $J = 6.8$  Hz, 4H), 7.25 (d,  $J = 5.8$  Hz, 4H). 1,1'-dimethylferrocene (Sigma Aldrich, 95%),  $[\text{Fe}(\text{C}_5\text{H}_5\text{CH}_3)_2]$ , was used as received. Oxidation of  $[\text{Fe}(\text{C}_5\text{H}_5\text{CH}_3)_2]$  to obtain the ferrocenium salt,  $[\text{Fe}(\text{C}_5\text{H}_5\text{CH}_3)_2](\text{BF}_4)$ , was carried out using a procedure reported in the literature.<sup>15</sup>

### 5.3.7 Cross-Exchange Kinetics

Stopped-flow measurements were performed using a similar methodology to that previously reported.<sup>2,3</sup> Briefly, samples were measured using an Olis RSM 1000 DeSa rapid-scanning spectrophotometer with dual-beam UV-Vis recording to Olis SpectralWorks software. The instrument contained a quartz cell with a 1 cm path length. Scans were taken once every millisecond with 1 nm resolution. The 150 W Xenon arc lamp was controlled using an LPS-220B Lamp Power Supply and held to within 79-81 W

during each measurement. The temperature was also held constant at  $25 \pm 0.1^\circ\text{C}$  using a NESLAB RTE-140 chiller/circulator. Two cross-exchange reactions were measured and described in detail below. All  $[\text{Co}(\text{PY}_5\text{Me}_2)(\text{CN})](\text{OTf})$ ,  $[\text{Co}(\text{terpy})_2](\text{PF}_6)_3$  and  $[\text{Fe}(\text{C}_5\text{H}_5\text{CH}_3)_2]^{+/0}$  solutions were prepared neat using dry acetonitrile.

Pseudo-first order conditions were implemented in both cross-exchange reactions, which maintained at least a 10-fold excess of a single reactant species. In the case of the cross-reaction between  $[\text{Fe}(\text{C}_5\text{H}_5\text{CH}_3)_2]$  and  $[\text{Co}(\text{terpy})_2](\text{PF}_6)_3$ , however, a 10-fold excess of both a single reactant and product species was maintained since the reaction was expected to reach equilibrium. The concentrations of  $[\text{Co}(\text{PY}_5\text{Me}_2)(\text{CN})](\text{OTf})$  were varied and held in excess for the reactions with  $[\text{Co}(\text{terpy})_2](\text{PF}_6)_3$ , however, both the concentrations of  $[\text{Fe}(\text{C}_5\text{H}_5\text{CH}_3)_2]$  and  $[\text{Fe}(\text{C}_5\text{H}_5\text{CH}_3)_2](\text{BF}_4)$  were held in excess while the  $[\text{Fe}(\text{C}_5\text{H}_5\text{CH}_3)_2]$  concentration was varied for the reactions with  $[\text{Co}(\text{terpy})_2](\text{PF}_6)_3$ . In both cross-exchange reactions the spectral changes were monitored at 505 nm, following the growing absorbance of the  $[\text{Co}(\text{terpy})_2]^{2+}$  species. Scientific Data Analysis Software provided fits for the pseudo-first order rate constants,  $k_{\text{obs}}$ , using a nonlinear least-squares regression. Seven independent trials were averaged to provide the measured  $k_{\text{obs}}$  values. Absorbance plots for each pseudo-first order reaction were fit using:  $A = A_\infty + (A_0 - A_\infty)e^{-k_{\text{obs}}t}$ . The second-order rate constants were calculated from the slope of the  $k_{\text{obs}}$  versus the excess concentration of either  $[\text{Co}(\text{PY}_5\text{Me}_2)(\text{CN})](\text{OTf})$  or  $[\text{Fe}(\text{C}_5\text{H}_5\text{CH}_3)_2]$  and each had a goodness of fit,  $R^2 > 0.996$ . The error associated with measured  $k_{\text{obs}}$  values were taken to be the standard deviation of the seven independent trials. The negligible error in concentration was propagated based on prepared stock solutions of each reaction mixture.

It was assumed that uniform mixing led to minimal deviation in the reactants initial concentrations.

### 5.3.9 Semiconductor Anode Fabrication

High surface area thin films of titanium dioxide ( $\text{TiO}_2$ ) on fluorine-doped tin oxide (FTO) glass substrates (TEC 15, Hartford),  $12 \Omega \text{ cm}^{-2}$ , were made to conduct recombination studies to the oxidized redox shuttles:  $[\text{Co}(\text{PY}_5\text{Me}_2)(\text{CN})]^{2+}$  and  $[\text{Co}(\text{bpy})_3]^{3+}$ . The glass substrates were cleaned in an ultrasonic bath using (in order) soap water, deionized water, acetone and isopropyl alcohol. To burn off any organic residue the substrates were then baked at  $400^\circ\text{C}$  for 30 minutes. After cooling, a blocking layer was deposited on the FTO substrates by way of atomic layer deposition (ALD). A Savannah 200 instrument (Cambridge Nanotech Inc) deposited 1000 cycles of titanium isopropoxide (99.999% trace metals basis, Sigma-Aldrich) at  $225^\circ\text{C}$  and water using reactant exposure times of 0.3 s and 0.015 s, respectively. Between each exposure, nitrogen was purged for 5 s. After ALD, a transparent thin film ( $\sim 5\text{-}6 \mu\text{m}$ ) of  $\sim 30 \text{ nm}$   $\text{TiO}_2$  nanoparticles was prepared by doctor blading a commercial paste (DSL 30NR-D, DYESOL) on the FTO glass substrates coated with the  $\text{TiO}_2$  blocking layer. The doctor bladed films were allowed to relax for 10 minutes at room temperature on benchtop, then for another 15 minutes in the oven at  $100^\circ\text{C}$ . The electrodes were annealed by heating in air to  $325^\circ\text{C}$  for 5 minutes,  $375^\circ\text{C}$  for 5 minutes,  $450^\circ\text{C}$  for 5 minutes and  $500^\circ\text{C}$  for 15 minutes. A post  $\text{TiCl}_4$  treatment was completed after cooling the sintered  $\text{TiO}_2$  anodes to  $\sim 70^\circ\text{C}$ . The post  $\text{TiCl}_4$  treatment was carried out using  $\sim 40\text{mL}$  of a  $40\text{mM}$  stock solution of  $\text{TiCl}_4$  dissolved in Milli-Q water. The solution was heated to  $70^\circ\text{C}$  for 10 minutes in an oven before the  $\text{TiO}_2$  sintered films were immersed for 30 minutes. After 30 minutes, the films were rinsed with Milli-Q water

and baked again at 500°C for another 30 minutes. Upon cooling, electrical contact was made using copper wire leads coated in silver epoxy. Before deposition of the epoxy on the FTO substrates, part of the blocking layer was manually scraped off. As the epoxy dried gently on a hotplate, the TiO<sub>2</sub> films were covered to protect against any organic residue from diffusing into the mesopores.

## 5.4 Results

### 5.4.1 Synthesis

Synthesis of the parent [Co(PY<sub>5</sub>Me<sub>2</sub>)(MeCN)](OTf)<sub>2</sub> was carried out with ease following a modified literature procedure.<sup>10</sup> Coordination of the neutral PY<sub>5</sub>Me<sub>2</sub> ligand to the acidic cobalt metal center yielded a stable halide product, [Co(PY<sub>5</sub>Me<sub>2</sub>)I]I, using the proper metal salt and the robust solvato complex, [Co(PY<sub>5</sub>Me<sub>2</sub>)(MeCN)](OTf)<sub>2</sub>, upon metathesis in a coordinating solvent such as acetonitrile. In principal, synthesis of the [Co(PY<sub>5</sub>Me<sub>2</sub>)(CN)](OTf) complex from the parent [Co(PY<sub>5</sub>Me<sub>2</sub>)(MeCN)](OTf)<sub>2</sub> should be facile and clean via the addition of a cyanide source. Interestingly, however, the cyanide ligand was observed to be much more labile than anticipated. Careful control over the reaction conditions was necessary in order to mitigate dimerization and/or subsequent cluster formation of a cobalt hexacyanide complex.

Isolation of the pure [Co(PY<sub>5</sub>Me<sub>2</sub>)(CN)](OTf) complex was obtained by ensuring the reaction between [Co(PY<sub>5</sub>Me<sub>2</sub>)(MeCN)](OTf)<sub>2</sub> and CN<sup>-</sup> was carried out using a slight excess (~1.2 – 1.5 eq.) of CN<sup>-</sup>, at low temperature (ice bath), under an inert atmosphere and in a non-competitive solvent such as methanol. By visual inspection the reaction was deemed complete within seconds as the solution changed from yellow to a dark reddish/brown upon cyanide addition. Single crystals were obtained via slow vapor

diffusion of ether into a concentrated acetonitrile solution of  $[\text{Co}(\text{PY}_5\text{Me}_2)(\text{CN})](\text{OTf})$  at room temperature, Figure 5.1a.  $^1\text{H}$  NMR of the pure paramagnetic  $[\text{Co}(\text{PY}_5\text{Me}_2)(\text{CN})](\text{OTf})$  indicated rather upfield chemical shifts that ranged from 4ppm to 20ppm, Figure A5.5, similar to that measured in our lab for  $[\text{Co}(\text{ttn})_2]$  (single broad peak at  $\sim 19$  ppm in acetonitrile- $d_3$ ), which would suggest a LS Co(II) complex. Oxidation of  $[\text{Co}(\text{PY}_5\text{Me}_2)(\text{CN})](\text{OTf})$  to produce the stable Co(III) product,  $[\text{Co}(\text{PY}_5\text{Me}_2)(\text{CN})](\text{OTf})_2$ , was obtained using silver triflate,  $\text{AgOTf}$ , in an acetonitrile solution. The short-term stability of  $[\text{Co}(\text{PY}_5\text{Me}_2)(\text{CN})](\text{OTf})$  in neat acetonitrile coupled with the rapid reaction upon addition of  $\text{Ag}^+$  yielded a clean  $[\text{Co}(\text{PY}_5\text{Me}_2)(\text{CN})](\text{OTf})_2$  product via  $^1\text{H}$  NMR, Figure A5.6. As expected, long-term stability is maintained for  $[\text{Co}(\text{PY}_5\text{Me}_2)(\text{CN})](\text{OTf})_2$  in neat solution as well as upon the addition of a supporting electrolyte, Figure A5.9. Single crystals suitable for X-Ray crystallography were again obtained via slow vapor diffusion of ether into a concentrated acetonitrile solution of  $[\text{Co}(\text{PY}_5\text{Me}_2)(\text{CN})](\text{OTf})_2$  at room temperature, Figure 5.1b. A full characterization of the structure, spin-state, optical and kinetic properties of both  $[\text{Co}(\text{PY}_5\text{Me}_2)(\text{CN})]^{2+/+}$  complexes were carried out and described in detail below.

Dimerization was observed when the reaction conditions were modified such that only one or less equivalents ( $\leq 1$  eq.) of  $\text{CN}^-$  are added to the  $[\text{Co}(\text{PY}_5\text{Me}_2)(\text{MeCN})](\text{OTf})_2$  reaction mixture. Even at low temperature (ice bath) and under an inert atmosphere, the predominant product that was obtained was a dimer complex. Single crystals were readily grown by slow vapor diffusion of diethyl ether into a concentrated acetonitrile solution containing the dimer. Structural information and vibrational properties were measured from single crystals of the dimer complex. Due to the lability of the complex upon solvation

and/or supporting electrolyte addition, Figures A5.7 and A5.13, solution measurements were avoided.

Interestingly, aside from the dimer complex a second side product was observed. This came in the form of an insoluble precipitate that would crash out if the dimer solution or a  $[\text{Co}(\text{PY}_5\text{Me}_2)(\text{CN})](\text{OTf})$  solution was allowed to set for extended periods of time. The insoluble product was also readily obtained during the synthesis of the  $[\text{Co}(\text{PY}_5\text{Me}_2)(\text{CN})](\text{OTf})$  complex if the reaction mixture was carried out at room temperature or allowed to stir for several minutes in a cold bath under conditions where excess cyanide ( $> 1.5$  eq.) was present. The thermodynamically stable species was determined to be a cluster complex whose structure can be found in Figure A5.2 of the Appendix. Single crystals were difficult to isolate as the cluster complex was only soluble in DMSO; however, tiny single crystals were obtained from an attempt to grow  $[\text{Co}(\text{PY}_5\text{Me}_2)(\text{CN})](\text{OTf})$  crystals over the course of several days.

#### 5.4.2 X-Ray Crystallography

The crystal structures of  $[\text{Co}(\text{PY}_5\text{Me}_2)(\text{CN})](\text{OTf})$  and  $[\text{Co}(\text{PY}_5\text{Me}_2)(\text{CN})](\text{OTf})_2$  are depicted in Figure 5.1. Refinement data for both complexes, as well as the Dimer Complex discussed below, are summarized in the Appendix, Table A5.2. The atom labeling is kept consistent for the  $[\text{Co}(\text{PY}_5\text{Me}_2)(\text{CN})](\text{OTf})$  and  $[\text{Co}(\text{PY}_5\text{Me}_2)(\text{CN})](\text{OTf})_2$  complexes in order to make side-by-side structural comparisons. Selected bond lengths and angles for each structure can be found in Table 5.1. Around the equatorial plane, nitrogen atoms  $\text{N}_{2-5}$  of their respective pyridine subunits have been appropriately assigned with the nitrogen atom  $\text{N}_1$  being associated with the pyridine unit axial to the exogenous cyanide ligand labeled  $\text{C}_{30}$  and  $\text{N}_6$ .

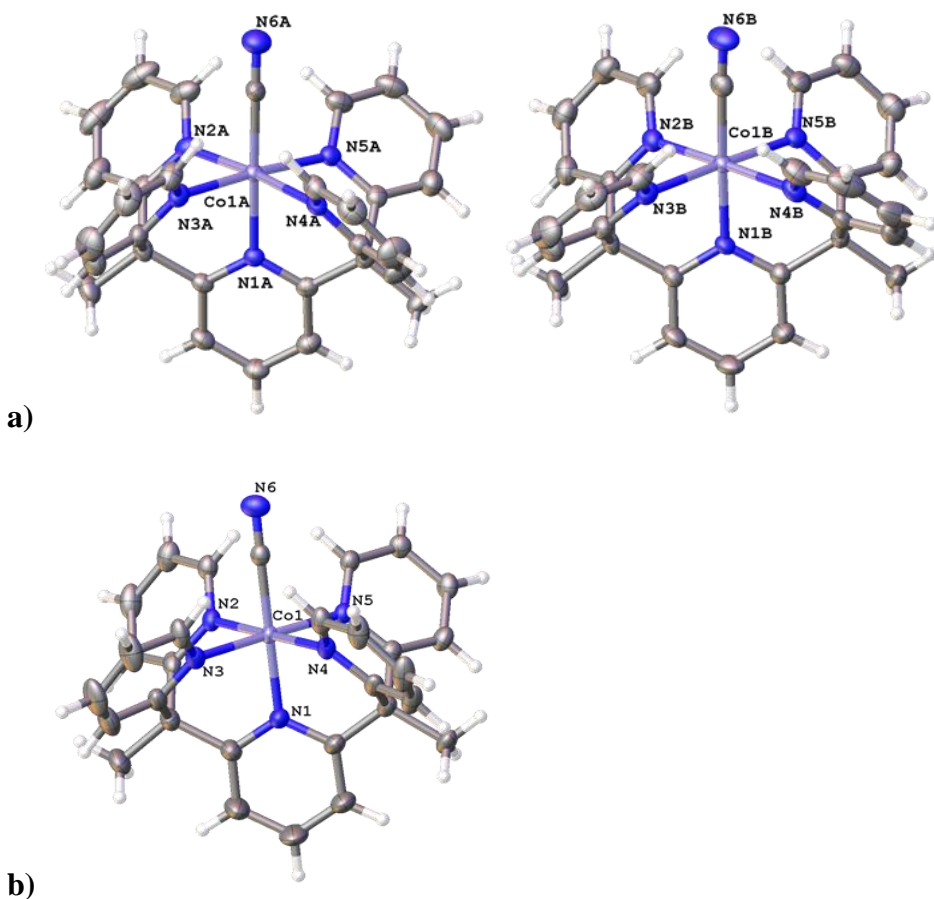


**Figure 5.1** Single crystal representations of **a)**  $[\text{Co}(\text{PY}_5\text{Me}_2)(\text{CN})](\text{OTf})$  and **b)**  $[\text{Co}(\text{PY}_5\text{Me}_2)(\text{CN})](\text{OTf})_2$  provided by Olex2 and structurally refined by ShelXT software. Note- the solvent and counter ions are excluded for clarity in each of the crystal structures above. Depicted ellipsoids are at the 50% probability level.

Upon inspection of the  $[\text{Co}(\text{PY}_5\text{Me}_2)(\text{CN})]^{2+/+}$  crystal structures, it appears that coordination of the exogenous cyanide to the sixth coordination site of the parent  $[\text{Co}(\text{PY}_5\text{Me}_2)(\text{MeCN})](\text{OTf})_2$  yields a distorted octahedral structure. In the case of the  $[\text{Co}(\text{PY}_5\text{Me}_2)(\text{CN})](\text{OTf})$  complex, two independent molecules make up the asymmetric unit and are both represented above. Superposition of these two molecules leads to nearly indistinguishable structures with minor bond angle and/or bond length changes, Table 5.1.

**Table 5.1** Selected bond lengths and angles for  $\text{Co}(\text{PY}_5\text{Me}_2)(\text{CN})(\text{OTf})$  and  $\text{Co}(\text{PY}_5\text{Me}_2)(\text{CN})(\text{OTf})_2$ . Note— bond lengths are reported in angstroms (Å) and bond angles are in degrees (°). The standard deviations of each value are shown in parenthesis. Each of the  $\text{N}_1 - \text{Co} - \text{N}_X$  ( $X = 2-5$ ) bond angles are not listed since each value is nearly  $90^\circ$  ( $\pm 1^\circ - 2^\circ$ ).

<b>Bond Distances &amp; Bond Angles</b>	<b><math>[\text{Co}(\text{PY}_5\text{Me}_2)(\text{CN})]^+</math> A</b>	<b><math>\text{Co}(\text{PY}_5\text{Me}_2)(\text{CN})^+</math> B</b>	<b><math>\text{Co}(\text{PY}_5\text{Me}_2)(\text{CN})^{2+}</math></b>
Co – N <sub>1</sub>	1.977(2)	1.964(3)	1.992(3)
Co – N <sub>2</sub>	2.127(3)	2.074(3)	1.981(3)
Co – N <sub>3</sub>	2.066(3)	2.123(3)	1.981(3)
Co – N <sub>4</sub>	2.138(3)	2.097(3)	1.980(3)
Co – N <sub>5</sub>	2.088(3)	2.115(3)	1.973(3)
Co – C <sub>30</sub>	1.913(3)	1.917(4)	1.891(3)
C <sub>30</sub> – N <sub>6</sub>	1.128(4)	1.133(4)	1.151(4)
N <sub>2</sub> – Co – N <sub>3</sub>	81.58(11)	82.77(11)	83.63(11)
N <sub>2</sub> – Co – N <sub>5</sub>	99.27(10)	95.64(11)	96.65(11)
N <sub>3</sub> – Co – N <sub>4</sub>	94.74(10)	98.31(11)	95.76(11)
N <sub>4</sub> – Co – N <sub>5</sub>	84.21(10)	83.15(11)	83.99(11)
N <sub>2</sub> – Co – N <sub>4</sub>	175.10(11)	177.23(11)	178.92(12)
N <sub>3</sub> – Co – N <sub>5</sub>	176.37(11)	176.54(11)	178.66(11)
N <sub>1</sub> – Co – C <sub>30</sub>	178.38(13)	177.86(13)	179.68(14)
N <sub>6</sub> – C <sub>30</sub> – Co	177.7(3)	177.3(3)	178.9(3)

The cobalt (II) metal center resides slightly above the equatorial plane as each of the pyridine units (N<sub>2</sub>-N<sub>5</sub>) are slightly less ( $\sim 1^\circ$ ) than  $90^\circ$  from the axial pyridine (N<sub>1</sub>). Constrictive bond angles are observed for the pyridine units bound through the ethyl bridge and are rather acute for the cobalt (II) ( $81.6^\circ - 82.8^\circ$ ). Oxidation of the cobalt (II) leads to a contraction of the equatorial pyridines, which widens the N<sub>2</sub> – Co – N<sub>3</sub> bond angle creating a more symmetric complex. The average Co-N bond length change of the four pyridines in the equatorial plane is  $\sim 0.124 - 0.126$  Å. A minor bond length change is observed for the axial pyridine unit upon oxidation. Also, as the axial pyridine (N<sub>1</sub>) of the PY<sub>5</sub>Me<sub>2</sub> expands, the more electropositive Co(III) causes the Co-C bond length of the cyanide (C<sub>30</sub>) to

contract by nearly the same distance. Consequently, the shorter Co-C bond length causes the C-N triple bond to become slightly longer ( $\sim 0.02$  Å).

As mentioned in the synthesis section above, the labile  $\text{CN}^-$  ligand of the  $[\text{Co}(\text{PY}_5\text{Me}_2)(\text{CN})](\text{OTf})$  complex in acetonitrile leads to the formation of a dimer complex, Figure 5.2. Dark red crystals of this complex were readily obtained for single crystal X-ray analysis and the resulting bond lengths and bond angles for this complex are reported in the Appendix, Table A5.4. Each of the nitrogen atoms,  $\text{N}_{1-5}$ , bound to  $\text{Co}_1$  are appropriately labeled to make side-by-side comparisons to the monomeric complex. Both of the axial bonds  $\text{Co}_1\text{-N}_1$  and  $\text{Co}_1\text{-C}_{30}$  appear to be longer than the monomer's by  $\sim 0.07$  Å and  $\sim 0.05$  Å, respectively. Around the equatorial plane the average  $\text{Co-N}_{2-5}$  bond lengths are nearly identical between the two complexes, deviating only by  $\sim 0.009$  Å. Interestingly, the average equatorial  $\text{Co-N}_{8-11}$  bond length around the  $\text{Co}_2$  is actually  $\sim 0.017$  Å shorter than the average bond length for nitrogen's bound to  $\text{Co}_1$ . Although the formal negative charge of the  $\text{CN}^-$  resides on the carbon atom, suggesting a tighter bond between  $\text{Co}_1$  and  $\text{C}_{30}$ , the bond length between these two atoms is only  $\sim 0.024$  Å shorter than the  $\text{Co}_2\text{-N}_6$  bond. The delocalized charge throughout the cyanide bridge also causes the  $\text{C}_{30}\text{-N}_6$  triple bond to weaken and expand. Both the  $\text{Co}_1\text{-C}_{30}\text{-N}_6$  and  $\text{Co}_2\text{-N}_6\text{-C}_{30}$  bond angles are measured to be the same ( $\sim 177.5^\circ\text{-}177.7^\circ$ ), however, the  $\text{N}_1\text{-Co}_1\text{-C}_{30}$  bond angle is slightly more acute ( $\sim 0.8^\circ$ ) than the  $\text{N}_6\text{-Co}_2\text{-N}_7$  bond angle. As with the monomeric complex, both cobalt metal centers lie slightly above the equatorial plane as each of the equatorial pyridines are less than  $90^\circ$  to the axial pyridines. Even though it is not shown in Figure 5.2, three triflates were found per dimer molecule, which would imply that each metal center is in its reduced state i.e.  $\text{Co(II)}$ .

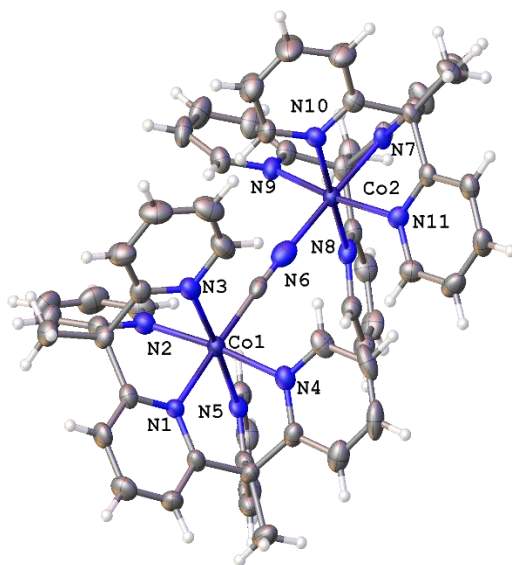


**Figure 5.9** Single crystal representation of the Dimer Complex provided by Olex2 and structurally refined by ShelXT software. Note– the solvent and counter ions are excluded for clarity in the crystal structure above. Depicted ellipsoids are at the 50% probability level.

#### 5.4.3 [Co(PY<sub>5</sub>Me<sub>2</sub>)(CN)](OTf) Magnetic Properties

Magnetic susceptibility of the paramagnetic [Co(PY<sub>5</sub>Me<sub>2</sub>)(CN)](OTf) complex was measured in acetonitrile-*d*<sub>3</sub> by <sup>1</sup>H NMR, Figure A5.10, using the Evans method.<sup>19,20</sup> Measurements were collected using a regular NMR tube containing a known concentration of [Co(PY<sub>5</sub>Me<sub>2</sub>)(CN)](OTf) dissolved in acetonitrile-*d*<sub>3</sub> along with a capillary insert filled with a saturated solution of Ferrocene (diamagnetic standard) also dissolved in acetonitrile-*d*<sub>3</sub>. The concentration of [Co(PY<sub>5</sub>Me<sub>2</sub>)(CN)](OTf) was varied at room temperature to provide the standard deviation in the calculated effective magnetic moment,  $\mu_{eff}$ . The  $\mu_{eff}$  for [Co(PY<sub>5</sub>Me<sub>2</sub>)(CN)](OTf) was calculated using Equations (5.1) and (5.2), where  $\chi_M$  is the molar susceptibility of the solute,  $\Delta\nu$  the observed frequency shift of the reference

resonance (hertz),  $\nu_0$  the spectrometer frequency (hertz),  $c$  is the concentration of [Co(PY<sub>5</sub>Me<sub>2</sub>)(CN)](OTf) (mol/L),  $\chi_p$  is the paramagnetic contribution to the molar susceptibility of the solute, and  $T$  is the temperature (K) of the sample.

$$\chi_M = \frac{3000\Delta\nu}{4\pi\nu_0c} \quad \text{Eq. (5.1)}$$

$$\mu_{eff} = 2.828\sqrt{\chi_p T} \quad \text{Eq. (5.2)}$$

Given the diamagnetic contribution,  $\chi_d$ , is generally small and negligible compared to the overall paramagnetic contribution,  $\chi_p$ , the  $\mu_{eff}$  was therefore determined directly from  $\chi_M$  providing a  $\mu_{eff} = 1.91 \pm 0.02 \mu_B$ .<sup>21</sup> The spin-only magnetic moment,  $\mu_{so}$ , for LS cobalt complexes is calculated to be  $\mu_{so} = 1.73 \mu_B$  suggesting that the experimentally determined value supports a LS cobalt complex.

#### 5.4.4 Vibrational Spectroscopy

Raman spectroscopy was used to further characterize the monomeric and dimer complexes, Figure 5.3. In both measurements single crystals of each complex were used. Of particular interest was to identify the CN vibrational frequencies for each complex. The dimer showed a single strong signal for the CN stretch at 2113 cm<sup>-1</sup> Figure 5.3b, which was slightly blue shifted from the primary CN vibrational signal of the Co(II) monomer at 2106 cm<sup>-1</sup>. Oxidation of the Co(II) monomer also resulted in a blue shifted cyano stretch frequency at 2140 cm<sup>-1</sup>. Looking at crystal structures of the monomeric complexes, it appears that the CN bond length elongates upon oxidation from Co(II) to Co(III). This may

seem counter-intuitive to a general statement that the longer bond length would result in a lower vibrational frequency at the same bond order, however, previous investigations concluded that the CN vibrational frequency increase is due to the force constant increase of the bond.<sup>22</sup> Oxidation of the Co(II) metal center leads to a higher energy signal due to the decreased  $\pi$  backbonding ability of the metal center leading to less antibonding character on the cyanide ligand, Table 5.2.

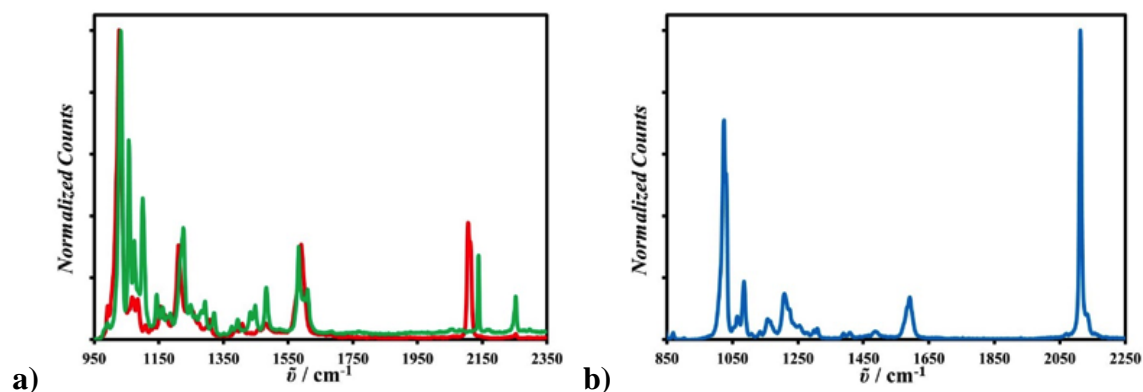


**Figure 5.10** Raman spectra using single crystals of **a)**  $[\text{Co}(\text{PY}_5\text{Me}_2)(\text{CN})](\text{OTf})$  (red line) and  $\text{Co}(\text{PY}_5\text{Me}_2)(\text{CN})](\text{OTf})_2$  (green line) as well as **b)** the Dimer complex (blue line).

Two additional CN signals from the expected arise in the Raman for both monomeric complexes, Figure 3a. These CN signals, at  $2254 \text{ cm}^{-1}$ , can be attributed to trapped acetonitrile in the crystal lattice and agree well with the crystal structures which show one molecule of acetonitrile per molecule of monomeric complex. In the case of the  $[\text{Co}(\text{PY}_5\text{Me}_2)(\text{CN})](\text{OTf})$  complex, splitting of the cyanide signal is also observed. Given there are two independent molecules in the asymmetric unit of the  $[\text{Co}(\text{PY}_5\text{Me}_2)(\text{CN})](\text{OTf})$  crystal, we speculate that the slight differences in localized environment i.e. solvent,

counterions, bond distances or bond angles could change the polarizability of the CN bond, which result in the two distinct vibrational signals at very similar wavenumbers.

**Table 5.2** Summary of cyano, CN, vibrational frequencies using Raman spectroscopy and single crystals of [Co(PY<sub>5</sub>Me<sub>2</sub>)(CN)](OTf), [Co(PY<sub>5</sub>Me<sub>2</sub>)(CN)](OTf) and the Dimer Complex.

Method	[Co(PY <sub>5</sub> Me <sub>2</sub> )(CN)](OTf)	[Co(PY <sub>5</sub> Me <sub>2</sub> )(CN)](OTf) <sub>2</sub>	Dimer Complex
Raman (cm <sup>-1</sup> )	2106	2140	2113
	2114		

#### 5.4.5 UV-Vis Spectroscopy

The UV-Vis of the monomeric [Co(PY<sub>5</sub>Me<sub>2</sub>)(CN)](OTf) (red line) and [Co(PY<sub>5</sub>Me<sub>2</sub>)(CN)](OTf)<sub>2</sub> (green line) complexes are shown in Figure 5.4. The cobalt (II) complex, [Co(PY<sub>5</sub>Me<sub>2</sub>)(CN)](OTf), contains two metal-to-ligand charge transfer (MLCT) bands in acetonitrile between 300 – 400 nm ( $\epsilon > 2000 \text{ M}^{-1} \text{ cm}^{-1}$ ). However, the only significant absorption feature of the [Co(PY<sub>5</sub>Me<sub>2</sub>)(CN)](OTf)<sub>2</sub> UV-Vis is a weak multifeatured d-d transition band at ~442 nm, see Figure 5.4 inset. Presumably this band resides in the [Co(PY<sub>5</sub>Me<sub>2</sub>)(CN)](OTf) UV-Vis spectrum, but is obscured by the onset of the MLCT band. In both spectra, below 300 nm a strong absorption band is present and is attributed to a metal independent ligand-based  $\pi$ - $\pi^*$  transition.<sup>14,23</sup> Such an assignment is made due to the absorption of the free PY<sub>5</sub>Me<sub>2</sub> ligand in acetonitrile, Figure A5.11, which has a  $\lambda_{\text{max}}$  at 263 nm and an  $\epsilon > 15000 \text{ M}^{-1} \text{ cm}^{-1}$ .

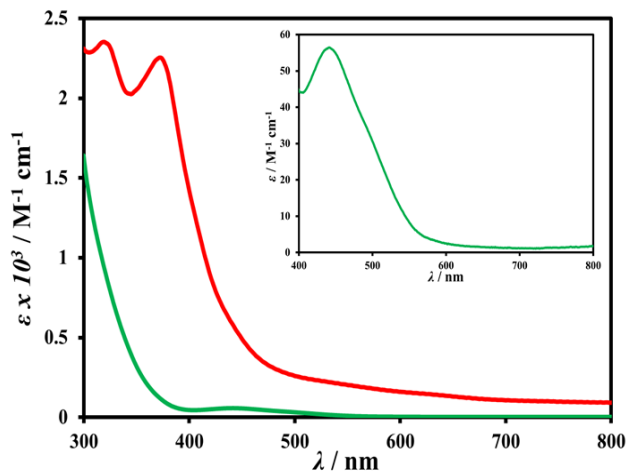


**Figure 5.11** UV-Vis spectra of  $[\text{Co}(\text{PY}_5\text{Me}_2)(\text{CN})](\text{OTf})$  (red line) and  $[\text{Co}(\text{PY}_5\text{Me}_2)(\text{CN})](\text{OTf})_2$  (green line) measured under air free conditions in acetonitrile. Inset– enhances the d-d transition of the  $[\text{Co}(\text{PY}_5\text{Me}_2)(\text{CN})](\text{OTf})_2$  complex.

#### 5.4.6 Electrochemical Properties

Cyclic voltammetry (CV) was used to probe the redox behavior of each cobalt pentapyridine complex synthesized. To avoid degradation or potential oxidation, each CV was measured under an  $\text{N}_2$  atmosphere. Similar to previous literature reports,  $[\text{Co}(\text{PY}_5\text{Me}_2)(\text{MeCN})](\text{OTf})_2$  reveals a quasi-reversible redox wave at 0.822 V vs. NHE, Figure 5.5 (dark blue dashed line), corresponding to the cobalt (II)/(III) oxidation.<sup>12</sup> Interestingly however, a small shoulder is also observed in the  $[\text{Co}(\text{PY}_5\text{Me}_2)(\text{MeCN})](\text{OTf})_2$  CV, though it is difficult to see in the Figure 5.5 below and never mentioned in prior reports. Previous electrochemical studies done on the free  $\text{PY}_5\text{Me}_2$  ligand reveal that the molecule is redox inactive, while the cobalt (I)/(II) transition is seen at -0.845 V vs. NHE, ruling out the possibility of these being the origin of the observed shoulder.<sup>11,12</sup> Given the simplicity of the system, it is speculated that the shoulder could be attributed to a counterion (CI) coordinated complex,  $[\text{Co}(\text{PY}_5\text{Me}_2)(\text{OTf})]$ , or the five coordinate  $[\text{Co}(\text{PY}_5\text{Me}_2)]^{2+}$  complex vacant of a species bound to the sixth

coordination site.<sup>11</sup> Mass spec data for the  $[\text{Co}(\text{PY}_5\text{Me}_2)(\text{MeCN})](\text{OTf})_2$  complex further supports this hypothesis as the two most intense peaks are for  $[\text{Co}(\text{PY}_5\text{Me}_2)]^{2+}$  and  $[\text{Co}(\text{PY}_5\text{Me}_2)(\text{OTf})]^+$ , Figure A5.1 respectively.

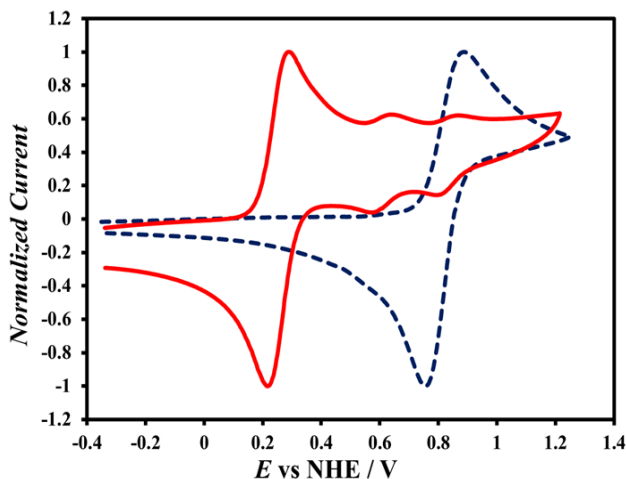


**Figure 5.12** Cyclic Voltammograms (CVs) of  $[\text{Co}(\text{PY}_5\text{Me}_2)(\text{CN})](\text{OTf})$  (red line) and  $[\text{Co}(\text{PY}_5\text{Me}_2)(\text{MeCN})](\text{OTf})_2$  (dark blue dashed line) measured in acetonitrile with 0.1 M TBAPF<sub>6</sub> using a platinum disk working electrode, a platinum mesh counter electrode and a homemade Ag/AgNO<sub>3</sub> (0.1 M TBAPF<sub>6</sub> acetonitrile) reference electrode.

Upon isolation of the  $[\text{Co}(\text{PY}_5\text{Me}_2)(\text{CN})](\text{OTf})$  complex, three quasi-reversible redox waves are observed when performing the electrochemistry in acetonitrile with 0.1M TBAPF<sub>6</sub>, Figure 5.5 (red line). The largest and most negative redox wave at 0.254 V vs. NHE is assigned to the cobalt (II)/(III) oxidation of the  $[\text{Co}(\text{PY}_5\text{Me}_2)(\text{CN})]^{+/2+}$  complex. Even with the use of single crystals, it appears that, after solvation and addition of a supporting electrolyte, small amounts of the  $[\text{Co}(\text{PY}_5\text{Me}_2)(\text{MeCN})]^{2+}$  and what we speculate to be the counterion (CI) coordinated,  $[\text{Co}(\text{PY}_5\text{Me}_2)(\text{OTf})]^+$ , exist in solution. This phenomenon becomes more evident upon overlaying the two CVs as in Figure 5.5. The equilibrium of these two species is observed in the electrochemistry of the dimer

complex as well, Figure A5.13. Although the cobalt (II)/(III) oxidation of the two metal centers is predominant and occurs successively between 0.2 – 0.4 V vs. NHE, upon further anodic sweeping the redox waves for both the  $[\text{Co}(\text{PY}_5\text{Me}_2)(\text{MeCN})]^{2+}$  and  $[\text{Co}(\text{PY}_5\text{Me}_2)(\text{OTf})]^+$  also appear. Unlike  $[\text{Co}(\text{PY}_5\text{Me}_2)(\text{CN})]^+$ , measuring the initial CV of the  $[\text{Co}(\text{PY}_5\text{Me}_2)(\text{CN})]^{2+}$  complex resulted in the observation of a single  $[\text{Co}(\text{PY}_5\text{Me}_2)(\text{CN})]^{2+/+}$  redox process, indicating stability of the oxidized monomer in supporting electrolyte. However, successive CVs of the  $[\text{Co}(\text{PY}_5\text{Me}_2)(\text{CN})]^{2+}$  complex led to the observed side-product formation shown in Figure 5.5, as the concentration of  $[\text{Co}(\text{PY}_5\text{Me}_2)(\text{CN})]^+$  built up in solution.

#### 5.4.7 Self-Exchange Kinetics of $[\text{Co}(\text{PY}_5\text{Me}_2)(\text{CN})]^{2+/+}$ via Stopped-Flow Spectroscopy

Stopped-flow spectroscopy was used to determine the homogeneous electron-transfer self-exchange rate constant for  $[\text{Co}(\text{PY}_5\text{Me}_2)(\text{CN})]^{2+/+}$ . Although stability has been demonstrated to be an issue with  $[\text{Co}(\text{PY}_5\text{Me}_2)(\text{CN})]^+$  while conducting electrochemical studies, short-term stability of the complex was confirmed in neat acetonitrile over the course of a day via  $^1\text{H}$  NMR studies, which validated the reliability of carrying out stopped-flow studies over the course of a few hours in neat acetonitrile. To isolate the self-exchange rate constant for  $[\text{Co}(\text{PY}_5\text{Me}_2)(\text{CN})]^{2+/+}$  using stopped-flow, a series of cross-exchange reactions between  $[\text{Co}(\text{PY}_5\text{Me}_2)(\text{CN})]^+$  and cobalt bis(2,2':6',2''-terpyridine),  $[\text{Co}(\text{terpy})_2]^{3+}$ , were performed, which provided the cross-exchange rate constant,  $k_{12}$ , for Reaction (1) below:



Selection of  $[\text{Co}(\text{terpy})_2]^{3+}$  for the cross-exchange with  $[\text{Co}(\text{PY}_5\text{Me}_2)(\text{CN})]^+$  was based on the complex's known outer-sphere one electron-transfer mechanism and slow electron-transfer kinetics.<sup>24</sup> Given the large potential difference between  $[\text{Co}(\text{terpy})_2]^{3+/2+}$  and  $[\text{Co}(\text{PY}_5\text{Me}_2)(\text{CN})]^{2+/+}$ , Table A5.5, the reaction was assumed to reach completion without an appreciable back reaction. Although the large driving force facilitates faster electron-transfer kinetics, low concentrations of the reactants provided sufficient signal and observable decays on the time scale of stopped-flow, which was a result of the large extinction coefficient of the  $[\text{Co}(\text{terpy})_2]^{2+}$  species formed in solution, Figure A5.12. Figure 5.6a shows a single exponential fit,  $A = A_\infty + (A_0 - A_\infty)e^{-k_{\text{obs}}t}$ , to a plot of the absorbance at 505 nm vs. time, which corresponds to the growth of the  $[\text{Co}(\text{terpy})_2]^{2+}$  species due to the reduction of  $[\text{Co}(\text{terpy})_2]^{3+}$  by  $[\text{Co}(\text{PY}_5\text{Me}_2)(\text{CN})]^+$ . In all reactions the  $[\text{Co}(\text{PY}_5\text{Me}_2)(\text{CN})]^+$  species was held in excess of  $[\text{Co}(\text{terpy})_2]^{3+}$ , which allowed the observed rate constants,  $k_{\text{obs}}$ , to be expressed by:

$$k_{\text{obs}} = k_{12}[\text{Co}(\text{PY}_5\text{Me}_2)(\text{CN})]^+ \quad \text{Eq. (5.3)}$$

Figure 5.6b shows a straight line fit of the  $k_{\text{obs}}$  values plotted as a function of the  $[\text{Co}(\text{PY}_5\text{Me}_2)(\text{CN})]^+$  concentration and provided the value for the forward rate constant,  $k_{12}$ , from the slope, respectively. The initial concentrations for the  $[\text{Co}(\text{PY}_5\text{Me}_2)(\text{CN})]^+$  and  $[\text{Co}(\text{terpy})_2]^{3+}$  reaction mixtures, as well as the observed pseudo-first order rate constants for each of these electron-transfer reactions can be found in Table A5.6.

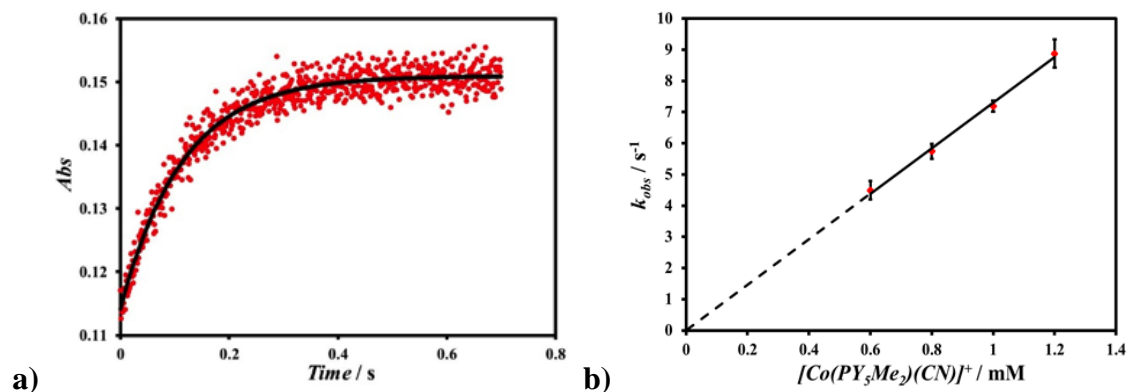


**Figure 5.13** **a)** Plot of absorbance at 505 nm vs. time, corresponding to the growth of the  $[Co(terpy)_2]^{2+}$  species (red dots) and the resulting single exponential fit (black line) for the reduction of  $[Co(terpy)_2]^{3+}$  ( $4.0 \times 10^{-5}$  M) by  $[Co(PY_5Me_2)(CN)]^+$  ( $1.2 \times 10^{-3}$  M). **b)** Pseudo-first order rate constants,  $k_{obs}$ , versus the excess concentration of  $[Co(PY_5Me_2)(CN)]^+$  for the reactions between  $[Co(PY_5Me_2)(CN)]^+$  and  $[Co(terpy)_2]^{3+}$ .

Using the experimentally determined cross-exchange rate constant,  $k_{12}$ , for Reaction (5.1) above, the Marcus cross-relation, Equation (5.4), was used to calculate the self-exchange rate constant,  $k_{11}$ , for  $[Co(PY_5Me_2)(CN)]^+$ :<sup>25,26</sup>

$$k_{12} \cong \sqrt{k_{11}k_{22}K_{12}} \quad \text{Eq. (5.4)}$$

where  $k_{22}$  is the self-exchange rate constant of  $[Co(terpy)_2]^{3+/2+}$ , and  $K_{12}$  is the equilibrium constant for the electron-transfer reaction. The Marcus cross-relation shown above has been modified to neglect the non-linear correction term,  $f_{12}$ , and the electrostatic work term,  $W_{12}$ . Both terms are a function of the reaction mixture's ionic strength and given the stability issues of the  $[Co(PY_5Me_2)(CN)]^+$  complex related to the dissociation and appearance of the  $[Co(PY_5Me_2)(MeCN)]^{2+}$  and  $[Co(PY_5Me_2)(OTf)]^+$  complexes upon introduction of a supporting electrolyte, Figures 5.5 and A5.8, stopped-flow solutions were made neat, as mentioned above, and the  $f_{12}$  and  $W_{12}$  terms ignored. Without supporting

electrolyte, however, it is expected that reduced coupling will result and an underestimate of the self-exchange rate constant,  $k_{11}$ , for  $[\text{Co}(\text{PY}_5\text{Me}_2)(\text{CN})]^+$  will be made. The equilibrium constant,  $K_{12}$ , for the electron-transfer reaction can be determined based on the free-energy difference of Reaction (1) and can be described by:

$$-nF\Delta E = -RT\ln K_{12} \quad \text{Eq. (5.5)}$$

where  $n$  is the number of electrons transferred ( $n = 1$ ),  $F$  is Faraday's constant,  $\Delta E$  is the formal potential difference between the oxidant and reductant in solution,  $R$  is the gas constant and  $T$  is the temperature. CVs shown in Figure A5.14 and summarized in Table A5.5 of the Appendix indicate a 285 mV formal potential difference between  $[\text{Co}(\text{PY}_5\text{Me}_2)(\text{CN})]^{2+/+}$  and  $[\text{Co}(\text{terpy})_2]^{3+/2+}$ . The calculated equilibrium constant for the cross-exchange Reaction (5.1) is therefore  $(6.6 \pm 0.9) \times 10^4$ . The self-exchange rate constant,  $k_{22}$ , for  $[\text{Co}(\text{terpy})_2]^{3+/2+}$  was measured independently by crossing the complex with 1,1'-dimethylferrocene  $[\text{Fe}(\text{C}_5\text{H}_4\text{CH}_3)]$  under similar conditions i.e. neat acetonitrile. Details regarding the reaction mixtures, experimental design and the resulting equilibrium and kinetic rate constants can be found in the Appendix and the experimental above. Based on these stopped-flow studies, the self-exchange rate constant,  $k_{22}$ , for  $[\text{Co}(\text{terpy})_2]^{3+/2+}$  was calculated to be  $41 \pm 9.9 \text{ M}^{-1}\text{s}^{-1}$ . Such a value matches well with prior literature reports.<sup>27,28</sup> Using this experimentally determined self-exchange rate constant,  $k_{22}$ , for  $[\text{Co}(\text{terpy})_2]^{3+/2+}$  and the calculated equilibrium constant,  $K_{12}$ , the self-exchange rate constant for  $[\text{Co}(\text{PY}_5\text{Me}_2)(\text{CN})]^{2+/+}$ ,  $k_{11}$ , was calculated to be  $20 \pm 5.5 \text{ M}^{-1}\text{s}^{-1}$ . This measured self-exchange value for  $[\text{Co}(\text{PY}_5\text{Me}_2)(\text{CN})]^{2+/+}$  is surprisingly small. Isoelectronic cobalt (II)

complexes such as  $[\text{Co}(\text{ttn})_2]^{2+}$  sustain self-exchange rate constants orders of magnitude large than  $[\text{Co}(\text{PY}_5\text{Me}_2)(\text{CN})]^{2+/+}$ .<sup>3,29</sup> A few explanations could reconcile the observed phenomenon and will be discussed in detail below. One explanation is that the slow self-exchange kinetics are due to a large inner-sphere reorganization that the complex undergoes upon oxidation. Looking at the crystal structures above, it appears that the equatorial pyridine units of the  $\text{PY}_5\text{Me}_2$  ligand significantly contract ( $\sim 0.1 \text{ \AA}$ ) when going from cobalt (II) to cobalt (III). The large structural change could inhibit the expected fast electron self-exchange, which results in a much smaller self-exchange rate constant.

#### 5.4.8 Recombination Kinetics

To mimic the recombination reactions at a  $\text{TiO}_2$  interface, as in operating DSSCs, half-cells were constructed as in Figure A5.17. The three-electrode setup provided the opportunity to conduct dark recombination studies to better understand the kinetics of interfacial charge-transfer. As depicted, the three-electrode setup was constructed such that a thin mesoporous film of  $\text{TiO}_2$ , deposited onto an FTO substrate, acted as a working electrode, while a platinum mesh was used as a counter electrode and a homemade  $\text{Ag}/\text{AgNO}_3$  electrode was used as a reference. Use of a reference electrode was important to these studies since it afforded a way to compare the current density,  $J$ , for each redox shuttle, at the same  $\text{TiO}_2$  potential, regardless of any differences in solution potential there may have been. By directly measuring  $J$  the differences in recombination rate constants,  $k_{et}$ , to the dissolved acceptor, at any given applied potential,  $E$ , could be identified, assuming the density of conduction band electrons,  $n_s$ , at any given applied potential and the initial acceptor/redox shuttle concentrations,  $[A]$ , were the same, Equation (6).<sup>29</sup>

$$J(E) = -qk_{et}[A]n_s \quad \text{Eq. (5.6)}$$

The measured current density plots as a function of applied potential,  $J$ - $E$ , for the half-cells employing  $[\text{Co}(\text{PY}_5\text{Me}_2)(\text{CN})](\text{OTf})_2$  (green dots) and  $[\text{Co}(\text{bpy})_3](\text{PF}_6)_3$  (light blue dots) OSRSs can be found in Figure 5.7 below.

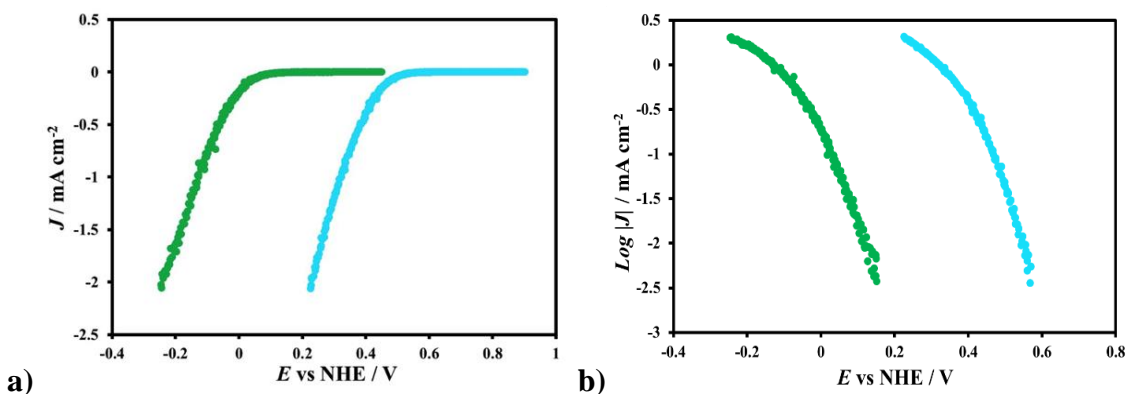


**Figure 5.14** a) Current density ( $J$ ) and b) log of current density ( $J$ ) versus applied potential ( $E$ ) plots for  $[\text{Co}(\text{PY}_5\text{Me}_2)(\text{CN})](\text{OTf})_2$  (green dots) and  $[\text{Co}(\text{bpy})_3](\text{PF}_6)_3$  (light blue dots) OSRSs measured using a mesoporous  $\text{TiO}_2$  working electrode, a platinum mesh counter electrode and a homemade  $\text{Ag}/\text{AgNO}_3$  (0.1M  $\text{TBAPF}_6$ ) reference electrode in an acetonitrile solution with 0.1M  $\text{LiOTf}$ .

Selection of  $[\text{Co}(\text{bpy})_3]^{3+}$  has become the benchmark for our side-by-side comparisons of new OSRSs as it has emerged as the champion redox shuttle, along with the fact that it is expected to employ the same one electron-transfer mechanism as  $[\text{Co}(\text{PY}_5\text{Me}_2)(\text{CN})]^{2+}$ . To ensure accurate measurements were being acquired, CVs were measured before and after the dark recombination studies, which indicated the reference was stable and the redox shuttles were well behaved. We note that carrying out a single dark recombination measurement using  $[\text{Co}(\text{PY}_5\text{Me}_2)(\text{CN})]^{2+}$  resulted in a negligible concentration of side-

products as  $[\text{Co}(\text{PY}_5\text{Me}_2)(\text{CN})]^+$  was produced. However, successive CV scans, as mentioned above, resulted in an obvious evolution of side-products, similar to the phenomena observed in Figure 5.5. Based on the CVs, the formal potentials of  $[\text{Co}(\text{PY}_5\text{Me}_2)(\text{CN})]^{2+/+}$  and  $[\text{Co}(\text{bpy})_3]^{3+/2+}$  were measured to be 0.254 V and 0.590 V vs. NHE, respectively. Given the dark  $J$ - $E$  curve for  $[\text{Co}(\text{bpy})_3]^{3+/2+}$  was characteristic of that previously measured for  $[\text{Co}(\text{Me}_2\text{bpy})_3]^{3+/2+}$  DSSCs further validated the  $J$ - $E$  behavior measured for  $[\text{Co}(\text{PY}_5\text{Me}_2)(\text{CN})]^{2+}$ .<sup>16</sup> Although rapid stirring was imparted during each measurement, the dark current density deviated from ideal behavior at more negative potentials due to solution resistance. A comparison of both  $J$ - $E$  curves indicates that the onset for recombination and the magnitude of dark current for  $[\text{Co}(\text{bpy})_3]^{3+}$  is more positive and significantly larger than  $[\text{Co}(\text{PY}_5\text{Me}_2)(\text{CN})]^{2+}$ . Since the current density is a direct measure of recombination, these measurements indicate that the kinetics for interfacial recombination is faster for  $[\text{Co}(\text{bpy})_3]^{3+}$  compared to  $[\text{Co}(\text{PY}_5\text{Me}_2)(\text{CN})]^{2+}$ .

## 5.5 Discussion

Rational design of new OSRSs is pivotal to the development of next generation DSSCs. Control over the coordination environment of cobalt OSRSs provides the ability to fine tune the charge-transfer kinetics of these complexes, which dictate the overall rates of regeneration and recombination in dye cells. Use of the pentadentate  $\text{PY}_5\text{Me}_2$  ligand affords a ligand periphery that enables the binding of a multitude of exogenous ligands, which can control the redox chemistry and spin-state of the cobalt metal center. In an effort to synthesize a new LS Co(II) OSRS that was expected to sustain fast electron-transfer kinetics and a more negative formal potential to inhibit recombination, cyanide,  $\text{CN}^-$ , was chosen as the exogenous ligand.

In principal, the synthesis of  $[\text{Co}(\text{PY}_5\text{Me}_2)(\text{CN})](\text{OTf})$  from the parent  $[\text{Co}(\text{PY}_5\text{Me}_2)(\text{MeCN})](\text{OTf})_2$  was expected to be facile and clean via the addition of a cyanide source. To our surprise, however, the cyanide ligand was observed to be much more labile than anticipated. Careful control over the reaction conditions was necessary in order to mitigate dimerization and/or subsequent cluster formation of a cobalt hexacyanide complex. If the reaction between  $[\text{Co}(\text{PY}_5\text{Me}_2)(\text{MeCN})](\text{OTf})_2$  and  $\text{CN}^-$  ( $> 1.5$  eq.) was allowed to stir for an extended period of time in an ice bath or was attempted at room temperature, the thermodynamically stable cluster complex was observed to crash out of solution. Structural support of the complex came from X-Ray crystallography, Figure A5.2. Similar structures, referred to as “star-like clusters”, have been reported in the literature by the Long group in an effort to study magnetic exchange.<sup>30</sup> Through the reaction of  $[(\text{PY}_5\text{Me}_2)\text{V}(\text{MeCN})]^{2+}$  with  $[\text{M}(\text{CN})_6]^{3-}$  ( $\text{M} = \text{Cr}, \text{Mo}$ ), a cis cyano cluster  $[(\text{PY}_5\text{Me}_2)_4\text{V}_4\text{M}(\text{CN})_6]^{5+}$  was obtained, which is structurally equivalent to the  $[(\text{PY}_5\text{Me}_2)_4\text{Co}_4\text{Co}(\text{CN})_6]^{4+}$  cluster complex that is isolated from our experiments. During  $^1\text{H}$  NMR measurements, used to probe the stability of  $[\text{Co}(\text{PY}_5\text{Me}_2)(\text{CN})](\text{OTf})$  over a couple day period, precipitation of what we expect to be free ligand and the cluster complex is observed, Figure A5.16, in neat acetonitrile and in acetonitrile with supporting electrolyte i.e. 0.1M TBAPF<sub>6</sub>. Interestingly, decomposition of  $[\text{Co}(\text{PY}_5\text{Me}_2)(\text{CN})](\text{OTf})$  is facilitated more rapidly upon addition of the TBAPF<sub>6</sub> supporting electrolyte and after several days the  $^1\text{H}$  NMR provides chemical shifts for the free  $\text{PY}_5\text{Me}_2$  ligand, the dimer complex, as well as the  $[\text{Co}(\text{PY}_5\text{Me}_2)(\text{CN})](\text{OTf})$  complex originally being studied, Figure A5.8. Formation of the dimer complex indicates free cyanide being liberated into solution as well as the presence of the solvato complex,  $[\text{Co}(\text{PY}_5\text{Me}_2)(\text{MeCN})]^{2+}$ . Given the lability

of Co(II) and the steric strain of the equatorial pyridines ( $N_2 - Co - N_3$ ), Table 5.1, the formation of  $[Co(CN)_6]^{4-}$  seems feasible by way of excess cyanide displacing the  $PY_5Me_2$  ligand. Any available  $[Co(PY_5Me_2)(MeCN)]^{2+}$  is then expected to coordinate via the accessible lone pair of the nitrogen Lewis base on the cyanide ligands of the  $[Co(CN)_6]^{4-}$  complex formed in solution. This would provide an explanation to the observed precipitate and the lack of appreciable  $[Co(PY_5Me_2)(MeCN)]^{2+}$  found in the  $^1H$  NMR spectrum.

Modification of the reaction conditions such that only one or less equivalents ( $\leq 1$  eq.) of  $CN^-$  are added to the  $[Co(PY_5Me_2)(MeCN)](OTf)_2$  reaction mixture at low temperature, results in the predominant isolation of a dimer complex. Single crystals were easily grown and the structural integrity was confirmed via X-Ray crystallography, Figure 5.2. Vibrational studies of the dimer complex revealed a single sharp CN signal in the Raman spectrum.  $^1H$  NMR studies using single crystals of the dimer complex, Figure A5.7, provided a unique spectrum to that measured for  $[Co(PY_5Me_2)(CN)](OTf)$ , Figure A5.5. With chemical shifts as far downfield as 80ppm, we speculate that the dimer complex is HS, however, any attempt to measure the magnetic susceptibility via the Evans method would be difficult as there are clearly multiple species that form in solution upon solvation of the pure complex. When overlaid, the chemical shifts of both the  $[Co(PY_5Me_2)(MeCN)](OTf)_2$  and  $[Co(PY_5Me_2)(CN)](OTf)$ , Figures A5.4 & A5.5, align well with the various chemical shifts found in the dimer spectrum, Figure A5.7. Electrochemical measurements of the dimer complex, Figure A5.13, rectify the phenomena observed by  $^1H$  NMR. Though it is difficult to assess the abundance of  $[Co(PY_5Me_2)(CN)](OTf)$ , as there are two successive redox waves atop the expected formal potential of  $[Co(PY_5Me_2)(CN)](OTf)$ , it is clear that the

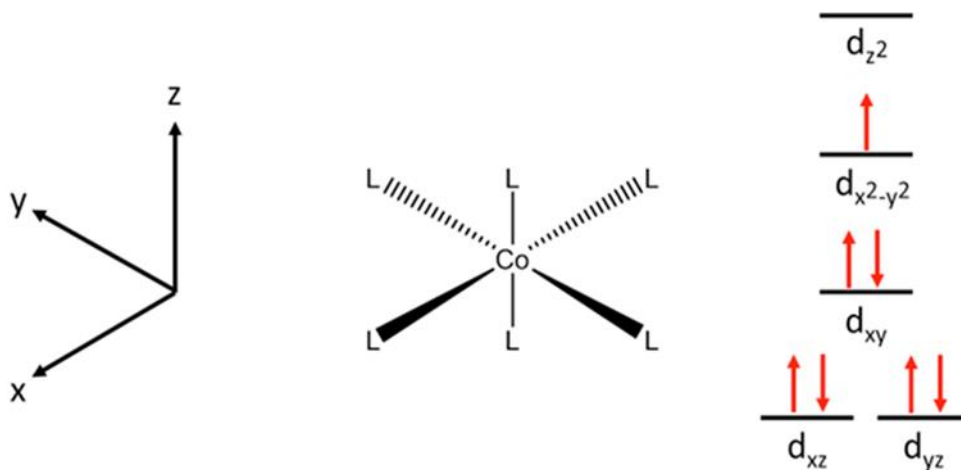
$[\text{Co}(\text{PY}_5\text{Me}_2)(\text{MeCN})](\text{OTf})_2$  and what is speculated to be the  $[\text{Co}(\text{PY}_5\text{Me}_2)(\text{OTf})](\text{OTf})$  complex are both present, which confirms the lability of the dimer complex in solution.

Isolation of the pure  $[\text{Co}(\text{PY}_5\text{Me}_2)(\text{CN})](\text{OTf})$  complex was tricky, though possible, by ensuring the reaction between  $[\text{Co}(\text{PY}_5\text{Me}_2)(\text{MeCN})](\text{OTf})_2$  and  $\text{CN}^-$  was carried out using a slight excess of  $\text{CN}^-$ , at low temperature and in a non-competitive solvent. After complexation of the exogenous cyanide, the complex was determined to be stable for several hours in neat acetonitrile, which enabled magnetic susceptibility measurements to be carried out. However, introduction of any supporting electrolyte immediately induced the dissociation of cyanide, Figure 5.5, and the conversion to the dimer and/or cluster complex. Surprisingly, even the synthesis of the oxidized  $[\text{Co}(\text{PY}_5\text{Me}_2)(\text{CN})](\text{OTf})_2$  complex needed to be carefully completed. Initial attempts to oxidize the parent  $[\text{Co}(\text{PY}_5\text{Me}_2)(\text{MeCN})](\text{OTf})_2$  complex with  $\text{Ag}^+$  resulted in unwanted side products that readily formed purple crystals suitable for X-Ray crystallography, Figure A5.3. As was previously observed, oxidation of the parent  $[\text{Co}(\text{PY}_5\text{Me}_2)(\text{MeCN})](\text{OTf})_2$  resulted in chemistry occurring with the counterion in solution, which liberated fluoride to produce a  $[\text{Co}(\text{PY}_5\text{Me}_2)(\text{F})](\text{OTf})_2$  complex.<sup>13</sup> Therefore, to obtain the pure  $[\text{Co}(\text{PY}_5\text{Me}_2)(\text{CN})](\text{OTf})_2$  complex, the synthesis was carried out by oxidizing  $[\text{Co}(\text{PY}_5\text{Me}_2)(\text{CN})](\text{OTf})$  with  $\text{AgOTf}$ . This yielded a clean product since any potential  $\text{AgCN}$  that precipitated out of solution was filtered off with the precipitated silver solid and any unreacted  $[\text{Co}(\text{PY}_5\text{Me}_2)(\text{CN})](\text{OTf})$  or  $[\text{Co}(\text{PY}_5\text{Me}_2)(\text{MeCN})](\text{OTf})_2$  could be neatly removed by washing the crude  $[\text{Co}(\text{PY}_5\text{Me}_2)(\text{CN})](\text{OTf})_2$  powder with dichloromethane,

An in-depth analysis of the  $[\text{Co}(\text{PY}_5\text{Me}_2)(\text{CN})]^{2+/+}$  crystal structures seemed to suggest the changes in bond distances upon oxidation or reduction support a LS Co(II) to LS Co(III) transition, which corroborate the data collected for magnetic susceptibility and  $^1\text{H}$  NMR. The average bond length change of the Co-N bonds of the pyridine units is only  $\sim 0.104 \text{ \AA}$ , which is significantly smaller than those reported for well-known HS Co(II) redox shuttles such as  $[\text{Co}(\text{bpy})_3]^{2+}$  and  $[\text{Co}(\text{phen})_3]^{2+}$  that have known Co-N bond length changes of  $\sim 0.19 \text{ \AA}$  upon oxidation.<sup>8,31,32</sup> Previously reported Co(II) redox shuttles with similar structures such as  $[\text{Co}(\text{PY}_5\text{Me}_2)(\text{NMBI})]^{2+}$ , where NMBI represents *N*-methylbenzimidazole, also contained larger average Co-N bond length changes of  $\sim 0.150 \text{ \AA}$ .<sup>13</sup> With such minor average Co-N bond length changes of the  $[\text{Co}(\text{PY}_5\text{Me}_2)(\text{CN})]^{2+/+}$  complex, one would expect intrinsically fast self-exchange kinetics, however, this doesn't appear to be the case. Using stopped-flow spectroscopy, the calculated self-exchange rate constant,  $k_{11}$ , for  $[\text{Co}(\text{PY}_5\text{Me}_2)(\text{CN})]^{2+/+}$  was only determined to be  $20 \pm 5.5 \text{ M}^{-1}\text{s}^{-1}$ . This is orders of magnitude lower than the value ( $\sim 9\text{-}13 \times 10^3 \text{ M}^{-1}\text{s}^{-1}$ ) determined for another isoelectronic LS Co(II) complex,  $[\text{Co}(\text{ttn})_2]^{3+/2+}$ , also measured using stopped-flow spectroscopy.<sup>3,8</sup> Slower self-exchange kinetics were expected for the  $[\text{Co}(\text{PY}_5\text{Me}_2)(\text{CN})]^{2+/+}$  cross-exchange reactions given the lack of supporting electrolyte, however, such a drastic difference in self-exchange rates is unlikely to be strictly due to the increased work function associated with electron-transfer. Thus, we reasoned from the crystal structures and UV-Vis data that the slower observed kinetics were likely due to a Jahn-Teller distortion of the  $[\text{Co}(\text{PY}_5\text{Me}_2)(\text{CN})]^+$  complex. As mentioned above, the equatorial pyridines go through a rather large contraction ( $\sim 0.124\text{-}0.126 \text{ \AA}$ ) upon oxidation,

while the axial bonds change minimally, suggesting the complex undergoes a Jahn-Teller compression, Scheme 2.

**Scheme 5.1** Splitting of the d-orbitals based on the hypothesized Jahn-Teller compression of the  $[\text{Co}(\text{PY}_5\text{Me}_2)(\text{CN})]^+$  complex.



It is difficult, however, to verify such phenomena using simple UV-Vis measurements of the  $[\text{Co}(\text{PY}_5\text{Me}_2)(\text{CN})]^+$  species. The strong broad visible absorption coupled with the MLCT transitions between 300-400 nm masks any noticeable d-d transitions. Interestingly, even though LS Co(III) isn't supposed to Jahn-Teller distort, the multifeatured d-d transition, Figure 5.4 inset, implies non-degenerate d-orbitals with more than one electronic transition. This is expected to be more obvious in the  $[\text{Co}(\text{PY}_5\text{Me}_2)(\text{CN})]^+$  UV-Vis, but again remains hidden by the broad visible absorption band. Aside from the complexes ability to go through a Jahn-Teller compression, another possible explanation for the smaller observed self-exchange rate constant could be that the complex transfers charge via an inner-sphere mechanism rather than an outersphere mechanism. In all assumptions above, it is thought that the activation-complexes are two separate entities; however, it is

difficult to rule out the possibility that  $[\text{Co}(\text{PY}_5\text{Me}_2)(\text{CN})]^{2+/+}$  doesn't complex to transfer electrons. The accessible lone pair of the nitrogen Lewis base has been shown to dimerize in solution, which would suggest it could pair with the acidic cobalt metal center of the  $[\text{Co}(\text{terpy})_2]^{3+/2+}$  complex when carrying out the cross-exchange reaction.

Although the self-exchange kinetics of  $[\text{Co}(\text{PY}_5\text{Me}_2)(\text{CN})]^{2+/+}$  are slower than expected, it still remains an interesting redox shuttle for regenerating IR absorbing sensitizers. Simple dark *J-E* measurements, Figure 5.7 above, comparing  $[\text{Co}(\text{PY}_5\text{Me}_2)(\text{CN})]^{2+}$  to  $[\text{Co}(\text{bpy})_3]^{3+}$  qualitatively demonstrates that the recombination rates to  $[\text{Co}(\text{PY}_5\text{Me}_2)(\text{CN})]^{2+}$  are much slower than to  $[\text{Co}(\text{bpy})_3]^{3+}$ . According to Equation (5.6), the dark current that is measured for each shuttle is directly proportional to the rate constant for recombination,  $k_{et}$ , at any given applied bias of the  $\text{TiO}_2$  electrode.<sup>29</sup> Thus, after comparing the dark currents between the two different redox shuttles at the same applied bias, it appears that at the formal potential of  $[\text{Co}(\text{PY}_5\text{Me}_2)(\text{CN})]^{2+}$  (0.254 V vs. NHE), the recombination rate constant is over three orders of magnitude larger for  $[\text{Co}(\text{bpy})_3]^{3+}$  than  $[\text{Co}(\text{PY}_5\text{Me}_2)(\text{CN})]^{2+}$ . Additionally, nearly 0.380 V must be applied past the formal potential of  $[\text{Co}(\text{PY}_5\text{Me}_2)(\text{CN})]^{2+}$ , while only ~0.270 V must be applied past the formal potential of  $[\text{Co}(\text{bpy})_3]^{3+}$  in order to reach the same magnitude of dark current,  $-1 \text{ mA cm}^{-2}$ . From these dark recombination measurements it seems clear that  $[\text{Co}(\text{bpy})_3]^{3+}$  is a much better acceptor than  $[\text{Co}(\text{PY}_5\text{Me}_2)(\text{CN})]^{2+}$ . Such a conclusion can be attributed to the reduced driving force for recombination of conduction band electrons and the intrinsically small self-exchange rate constant of  $[\text{Co}(\text{PY}_5\text{Me}_2)(\text{CN})]^{2+}$ . Given the observed kinetic behavior, if introduced into DSSCs, superior charge collection is expected for cells containing  $[\text{Co}(\text{PY}_5\text{Me}_2)(\text{CN})]^{2+/+}$  and the properly integrated IR absorbing sensitizer.

## 5.6 Conclusion

A new LS Co(II) redox shuttle has been synthesized and fully characterized for its potential application in DSSCs. The new class of cobalt redox shuttles shares the caveat that coordination of the pentapyridine ligand, PY<sub>5</sub>Me<sub>2</sub>, affords the opportunity to functionalize the sixth site of the cobalt metal center with a variety of exogenous ligands that can not only modulate the redox potential of the shuttle, but also manipulate the spin-state of the complex. In an effort to force Co(II) to become LS, cyanide was chosen as the exogenous ligand. Magnetic susceptibility measurements were used to confirm the Co(II) complex, [Co(PY<sub>5</sub>Me<sub>2</sub>)(CN)](OTf), was in fact LS upon isolating of the pure product. Interestingly, the cyanide ligand was much more labile than expected in a competitive coordinating solvent such as acetonitrile. Dissociation of the cyanide resulted in dimerization and the thermodynamically stable cluster complex. Without the use of a supporting electrolyte to help facilitate cyanide dissociation, the [Co(PY<sub>5</sub>Me<sub>2</sub>)(CN)](OTf) complex was stable enough in neat acetonitrile to collect kinetic measurements using stopped-flow spectroscopy. The unexpectedly slow self-exchange rate constant ( $k_{11} = 20 \pm 5.5 \text{ M}^{-1}\text{s}^{-1}$ ) was hypothesized to arise from either a Jahn-Teller compression observed by collecting single crystals of the [Co(PY<sub>5</sub>Me<sub>2</sub>)(CN)]<sup>2+/+</sup> complexes and/or a more complicated innersphere mechanism via complexation through the nitrogen lone pair of the exogenous cyanide ligand. Dark J-E measurements suggested that rates of recombination to the oxidized redox shuttle, [Co(PY<sub>5</sub>Me<sub>2</sub>)(CN)]<sup>2+</sup> is actually slower than the champion redox shuttle, [Co(bpy)<sub>3</sub>]<sup>3+</sup>, when compared side-by-side. As a result, the [Co(PY<sub>5</sub>Me<sub>2</sub>)(CN)]<sup>2+/+</sup> redox shuttle becomes an attractive candidate as a solid state hole

conductor for DSSCs with the promise of achieving quantitative charge collection, while also having the ability to successfully regenerate near IR and/or IR absorbing sensitizers.

## **APPENDIX**

## APPENDIX

**Table A5.1** Elemental analysis summary of the cobalt complexes under investigation. Note- Complex (0): [Co(PY<sub>5</sub>Me<sub>2</sub>)(MeCN)](OTf)<sub>2</sub>, Complex (1): [Co(PY<sub>5</sub>Me<sub>2</sub>)(CN)](OTf), Complex (2): [Co(PY<sub>5</sub>Me<sub>2</sub>)(CN)](OTf)<sub>2</sub> and Complex (3): Dimer Complex. Note- single crystals of the dimer complex were used for CHN assuming two acetonitrile molecules in the lattice. It was difficult, however, to isolate only Dimer crystals for the measurement. Presumably some [Co(PY<sub>5</sub>Me<sub>2</sub>)(MeCN)](OTf)<sub>2</sub> are present, which is the source of the larger error.

Complex		Calculated (%)			Found (%)		
		C	H	N	C	H	N
(0)	C <sub>33</sub> H <sub>28</sub> CoF <sub>6</sub> N <sub>6</sub> O <sub>6</sub> S <sub>2</sub>	47.09	3.35	9.99	45.33	3.03	8.56
(1)	C <sub>31</sub> H <sub>25</sub> CoF <sub>3</sub> N <sub>6</sub> O <sub>3</sub> S	54.95	3.72	12.40	54.47	3.71	11.90
(2)	C <sub>32</sub> H <sub>25</sub> CoF <sub>6</sub> N <sub>6</sub> O <sub>6</sub> S <sub>2</sub>	46.50	3.05	10.17	45.67	3.17	9.59
(3)	C <sub>66</sub> H <sub>56</sub> Co <sub>2</sub> F <sub>9</sub> N <sub>13</sub> O <sub>9</sub> S <sub>3</sub>	50.80	3.63	11.67	48.40	3.43	10.20

**Table A5.2** Single crystal X-ray diffraction data and refinement details. Note- Complex (1): [Co(PY<sub>5</sub>Me<sub>2</sub>)(CN)](OTf), Complex (2): [Co(PY<sub>5</sub>Me<sub>2</sub>)(CN)](OTf)<sub>2</sub>, Complex (3): Dimer Complex.

Parameter	Complex (1)	Complex (2)	Complex (3)
Formula	C <sub>33</sub> H <sub>28</sub> CoF <sub>3</sub> N <sub>7</sub> O <sub>3</sub> S	C <sub>35</sub> H <sub>31.5</sub> CoF <sub>6</sub> N <sub>6.5</sub> O <sub>6.5</sub> S <sub>2</sub>	C <sub>66</sub> H <sub>56</sub> Co <sub>2</sub> F <sub>9</sub> N <sub>13</sub> O <sub>9</sub> S <sub>3</sub>
Formula Weight	718.61	884.22	1560.27
Crystal System	triclinic	triclinic	triclinic
Space Group	P-1	P-1	P-1
a/Å	14.2538(2)	10.3672(2)	13.9383(2)
b/Å	15.6315(2)	11.2824(2)	14.8958(3)
c/Å	17.2705(3)	16.1555(3)	18.9651(3)
α/°	73.2243(9)	73.7610(10)	74.5330(10)
β/°	68.4389(9)	83.3770(10)	68.7280(10)
γ/°	63.4098(9)	88.0000(10)	77.0620(10)
V/Å <sup>3</sup>	3164.38(9)	1802.15(6)	3500.80(11)
Z	4	2	2
Z'	2	1	1
ρ <sub>calc.</sub> /g cm <sup>-3</sup>	1.508	1.629	1.480
abs. coeff., μ/mm <sup>-1</sup>	5.432	5.615	5.321
2θ range/°	2.782 to 72.212	2.866 to 72.075	2.554 to 72.578
Measured Refl.	43158	28673	40510
Independent Refl.	11856	6784	13184
Reflections Used	8910	5648	9046
R <sub>int</sub>	0.0639	0.0636	0.0892
Parameters	871	555	892
Restraints	0	50	44
Largest Peak	0.838	0.475	3.424
Deepest Hole	-0.563	-0.475	-2.031
Goodness of Fit	1.024	1.048	1.356
wR <sub>2</sub> (all data)	0.1374	0.1280	0.3655
wR <sub>2</sub> (I>2σI)	0.1219	0.1210	0.3334
R <sub>1</sub> (all data)	0.0773	0.0598	0.1535
R <sub>1</sub> (I>2σI)	0.0514	0.0475	0.1172

**Table A5.3** Single crystal X-ray diffraction data and refinement details. Note- Complex (4): Cluster Complex and Complex (5): [Co(PY<sub>5</sub>Me<sub>2</sub>)(F)](OTf)<sub>2</sub>.

Parameter	Complex (4)	Complex (5)
Formula	C <sub>125</sub> H <sub>112</sub> Co <sub>5</sub> F <sub>9</sub> N <sub>26</sub> O <sub>9</sub> S <sub>3</sub>	C <sub>33.5</sub> H <sub>29</sub> ClCoF <sub>7</sub> N <sub>6</sub> O <sub>6</sub> S <sub>2</sub>
Formula Weight	2684.23	903.13
Crystal System	monoclinic	triclinic
Space Group	P2 <sub>1</sub> /m	P-1
a/Å	16.3058(6)	8.777(6)
b/Å	22.1105(9)	14.193(10)
c/Å	18.9889(7)	16.408(11)
α/°	90	102.360(8)
β/°	92.703(3)	102.170(8)
γ/°	90	104.828(8)
V/Å <sup>3</sup>	6838.4(5)	1852(2)
Z	2	2
Z'	0.5	1
ρ <sub>calc.</sub> /g cm <sup>-3</sup>	1.304	1.619
abs. coeff., μ/mm <sup>-1</sup>	5.701	0.737
2θ range/°	2.329 to 58.948	1.324 to 25.408
Measured Refl.	30240	25141
Independent Refl.	10009	6795
Reflections Used	2071	5271
R <sub>int</sub>	0.3910	0.0435
Parameters	374	526
Restraints	78	0
Largest Peak	2.065	1.201
Deepest Hole	-0.689	-0.509
Goodness of Fit	1.504	1.051
wR <sub>2</sub> (all data)	0.5148	0.1648
wR <sub>2</sub> (I>2σI)	0.4541	0.1502
R <sub>1</sub> (all data)	0.4780	0.0717
R <sub>1</sub> (I>2σI)	0.2161	0.0537

**Table A5.4** Selected bond lengths and angles for the Dimer Complex. Note— bond lengths are reported in angstroms (Å) and bond angles are in degrees (°). The standard deviations of each value are shown in parenthesis.

<b>Bond Distances</b>	<b>Dimer Complex</b>	<b>Bond Angles</b>	<b>Dimer Complex</b>
Co1 – N1	2.042(5)	N1 – Co1 – N2	87.6(3)
Co1 – N2	2.096(6)	N1 – Co1 – N3	88.2(3)
Co1 – N3	2.120(8)	N1 – Co1 – N4	86.6(3)
Co1 – N4	2.115(7)	N1 – Co1 – N5	88.8(2)
Co1 – N5	2.119(7)	N1 – Co1 – C30	178.2(3)
Co1 – C30	1.963(9)	N2 – Co1 – N3	82.4(3)
C30 – N6	1.16(1)	N2 – Co1 – N4	173.9(3)
Co2 – N6	1.987(9)	N2 – Co1 – N5	95.9(3)
Co2 – N7	2.066(5)	N2 – Co1 – C30	94.2(3)
Co2 – N8	2.085(8)	N3 – Co1 – N4	99.2(3)
Co2 – N9	2.138(6)	N3 – Co1 – N5	176.6(3)
Co2 – N10	2.095(8)	N3 – Co1 – C30	92.0(3)
Co2 – N11	2.147(6)	N4 – Co1 – N5	82.2(3)
-	-	N4 – Co1 – C30	91.6(3)
-	-	N5 – Co1 – C30	91.1(3)
-	-	N6 – C30 – Co1	177.7(7)
-	-	C30 – N6 – Co2	177.5(7)
-	-	N6 – Co2 – N7	179.0(3)
-	-	N6 – Co2 – N8	90.7(3)
-	-	N6 – Co2 – N9	93.5(3)
-	-	N6 – Co2 – N10	91.8(3)
-	-	N6 – Co2 – N11	93.6(3)
-	-	N7 – Co2 – N8	89.0(2)
-	-	N7 – Co2 – N9	87.5(2)
-	-	N7 – Co2 – N10	88.5(2)
-	-	N7 – Co2 – N11	85.4(2)
-	-	N8 – Co2 – N9	81.3(3)
-	-	N8 – Co2 – N10	176.8(3)
-	-	N8 – Co2 – N11	98.6(3)
-	-	N9 – Co2 – N10	96.6(3)
-	-	N9 – Co2 – N11	172.9(3)
-	-	N10 – Co2 – N11	83.2(3)

**Table A5.5** Formal reduction potentials,  $E^\circ$ , of  $[\text{Co}(\text{PY}_5\text{Me}_2)(\text{X})]$  ( $\text{X} = \text{MeCN}$  or  $\text{CN}$ ),  $[\text{Co}(\text{terpy})_2]^{3+/2+}$  and 1,1'-dimethylferrocene,  $[\text{Fe}(\text{C}_4\text{H}_5\text{CH}_3)_2]^{+/0}$ , redox shuttles measured via CV. Ferrocene,  $[\text{Fe}(\text{C}_5\text{H}_5)_2]^{+/0}$ , is also included as a point of reference in converting from  $\text{Ag}/\text{AgNO}_3$  to NHE (Ferrocene: 0.40V vs. SCE).<sup>15</sup> All formal potentials were measured in acetonitrile with 0.1 M tetrabutylammonium hexafluorophosphate, TBAPF<sub>6</sub>, supporting electrolyte using a platinum working electrode, a platinum mesh counter electrode and a homemade  $\text{Ag}/\text{AgNO}_3$  (0.1 M TBAPF<sub>6</sub> acetonitrile) reference electrode.

Redox Couple	$E^\circ$ (V vs NHE)
$[\text{Co}(\text{PY}_5\text{Me}_2)(\text{MeCN})]^{3+/2+}$	$822 \pm 3$
$[\text{Co}(\text{PY}_5\text{Me}_2)(\text{CN})]^{2+/+}$	$254 \pm 3$
$[\text{Co}(\text{terpy})_2]^{3+/2+}$	$539 \pm 2$
$[\text{Fe}(\text{C}_4\text{H}_5\text{CH}_3)_2]^{+/0}$	$527 \pm 5$
$[\text{Fe}(\text{C}_5\text{H}_5)_2]^{+/0}$	$641 \pm 9$

**Table A5.6** Observed pseudo-first order rate constants,  $k_{\text{obs}}$ , and the initial reaction mixtures for the cross-exchange reactions between  $[\text{Co}(\text{PY}_5\text{Me}_2)(\text{CN})](\text{OTf})$  and  $[\text{Co}(\text{terpy})_2](\text{PF}_6)_3$ , Reaction (5.1) of the main text, in neat acetonitrile at  $25 \pm 0.1^\circ\text{C}$ .

$[\text{Co}(\text{PY}_5\text{Me}_2)(\text{CN})]^+ / \text{M}$	$[\text{Co}(\text{terpy})_2]^{3+} / \text{M}$	$k_{\text{obs}} / \text{s}^{-1}$
$6.00 \times 10^{-4}$	$4.00 \times 10^{-5}$	$4.5 \pm 0.3$
$8.00 \times 10^{-4}$		$5.7 \pm 0.2$
$1.00 \times 10^{-3}$		$7.2 \pm 0.2$
$1.20 \times 10^{-3}$		$8.9 \pm 0.5$

**Table A5.7** Observed pseudo-first order rate constants,  $k_{\text{obs}}$ , and the initial reaction mixtures for the cross-exchange between  $[\text{Fe}(\text{C}_5\text{H}_4\text{CH}_3)]$  and  $[\text{Co}(\text{terpy})_2](\text{PF}_6)_3$  in neat acetonitrile at  $25 \pm 0.1^\circ\text{C}$ .

$[\text{Fe}(\text{C}_5\text{H}_4\text{CH}_3)] / \text{M}$	$[\text{Co}(\text{terpy})_2]^{3+} / \text{M}$	$[\text{Fe}(\text{C}_5\text{H}_4\text{CH}_3)]^+ / \text{M}$	$k_{\text{obs}} / \text{s}^{-1}$
$3.00 \times 10^{-4}$	$3.00 \times 10^{-5}$	$3.00 \times 10^{-4}$	$7.6 \pm 0.2$
$4.00 \times 10^{-4}$			$10.3 \pm 0.4$
$5.00 \times 10^{-4}$			$12.4 \pm 0.2$
$6.00 \times 10^{-4}$			$14.4 \pm 0.3$
$7.00 \times 10^{-4}$			$17.2 \pm 0.5$

**Table A5.8** Kinetic summary of the cross-exchange rate constants,  $k_{23}$  and  $k_{32}$ , and the measured equilibrium constants for the forward reaction,  $K_{23}$ , between  $[\text{Fe}(\text{C}_5\text{H}_4\text{CH}_3)]$  and  $[\text{Co}(\text{terpy})_2](\text{PF}_6)_3$  in neat acetonitrile at  $25 \pm 0.1^\circ\text{C}$ .

Kinetic Parameter	Cross-exchange values
$K_{23}$ (Nernst)	$1.6 \pm 0.3$
$K_{23}$ ( $k_{23} / k_{32}$ )	$9.8 \pm 5.9$
$k_{23} / (\text{M}^{-1}\text{s}^{-1})$	$(2.3 \pm 0.8) \times 10^4$
$k_{32} / (\text{M}^{-1}\text{s}^{-1})$	$(2.4 \pm 1.4) \times 10^3$

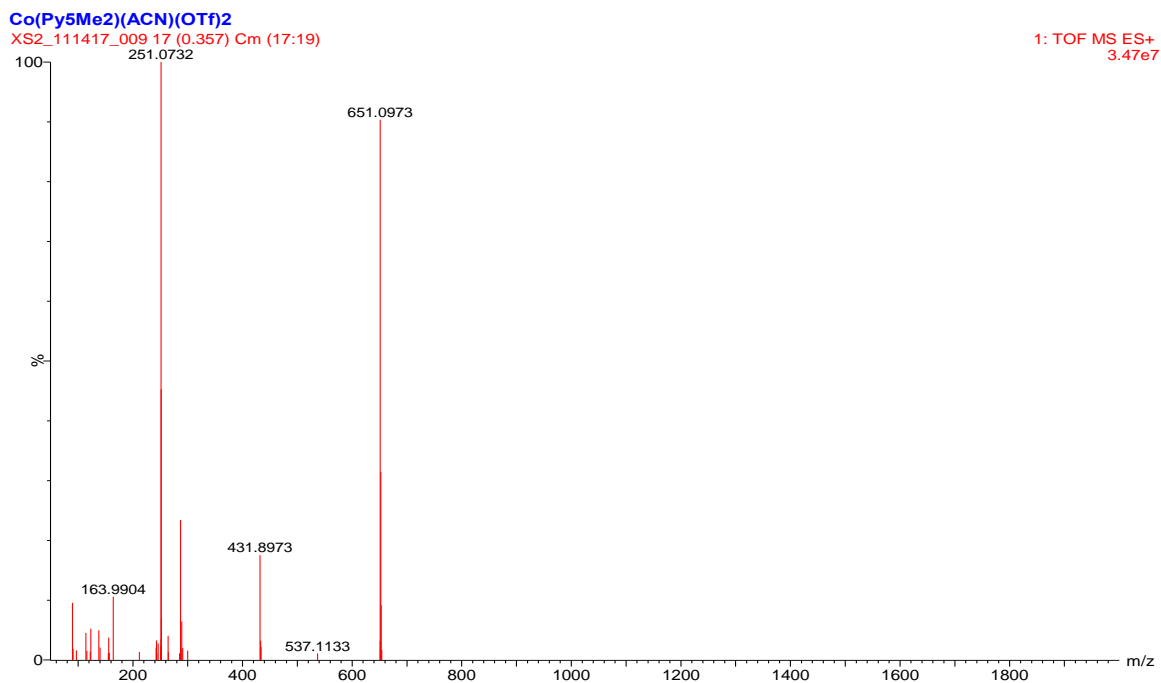


**Figure A5.1** Mass spectrum of  $[\text{Co}(\text{PY}_5\text{Me}_2)(\text{MeCN})](\text{OTf})_2$ .

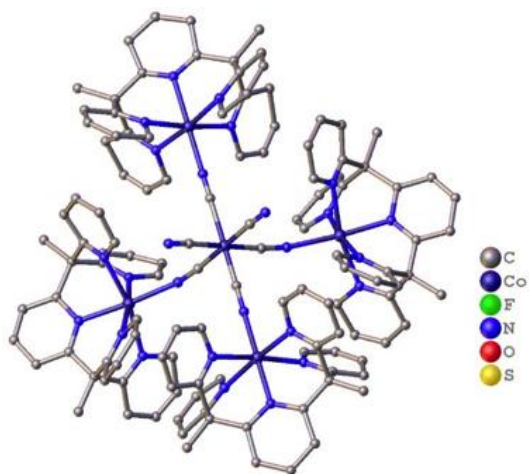


**Figure A5.2** Single crystal representation of the hexadentate Cobalt Cluster Complex provided by Olex2 and structurally refined by ShelXT software. Note- the protons, counterions and solvent are omitted for image clarity.

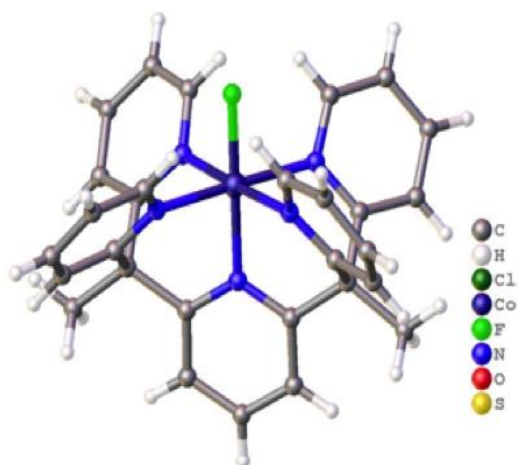


**Figure A5.3** Single crystal representation of [Co(PY<sub>5</sub>Me<sub>2</sub>)(F)](OTf)<sub>2</sub> provided by Olex2 and structurally refined by ShelXT software. Note- the counterions and solvent molecules are omitted for image clarity.

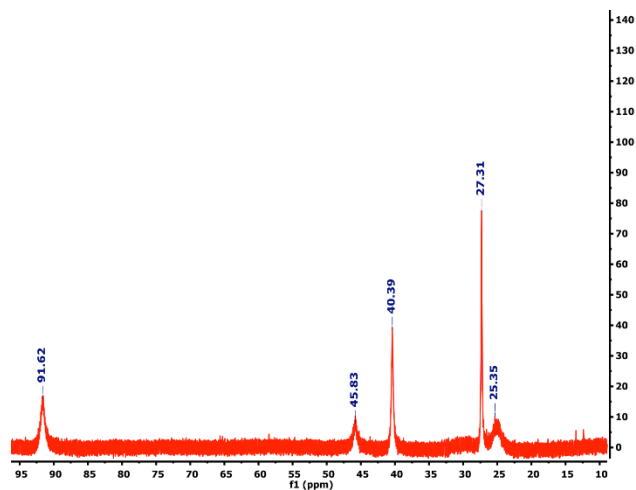


**Figure A5.4**  $^1\text{H}$  NMR of  $[\text{Co}(\text{PY}_5\text{Me}_2)(\text{MeCN})](\text{OTf})_2$  in acetonitrile- $d_3$ .

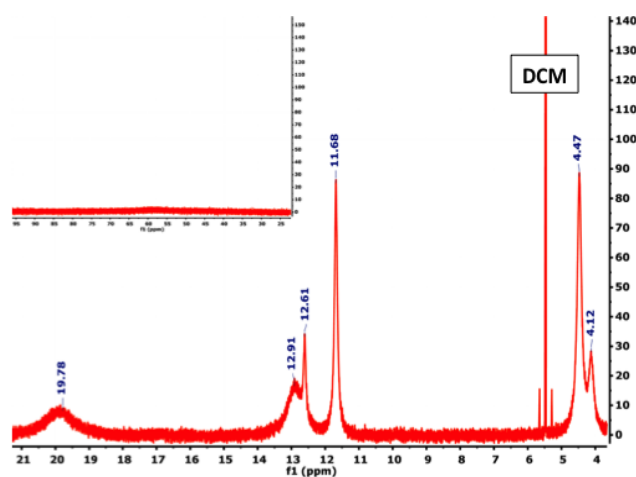


**Figure A5.23**  $^1\text{H}$  NMR of  $[\text{Co}(\text{PY}_5\text{Me}_2)(\text{CN})](\text{OTf})$  in acetonitrile- $d_3$ . Inset shows there are no chemical shifts downfield from 25 ppm.

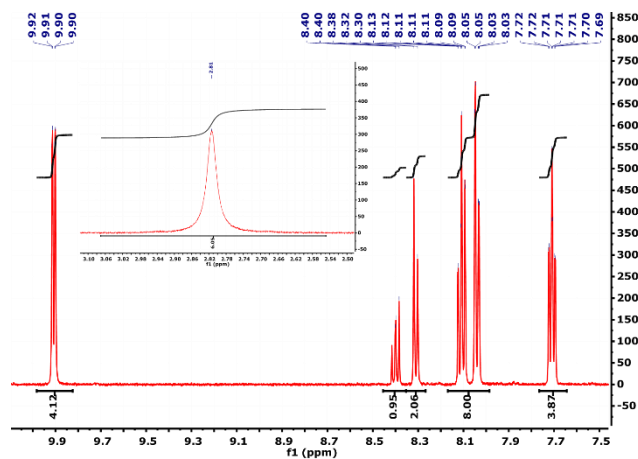


**Figure A5.24**  $^1\text{H}$  NMR of  $[\text{Co}(\text{PY}_5\text{Me}_2)(\text{CN})](\text{OTf})_2$  in acetonitrile- $d_3$ . Inset shows the chemical shift and integration for the methyl groups of the  $\text{PY}_5\text{Me}_2$  ligand.

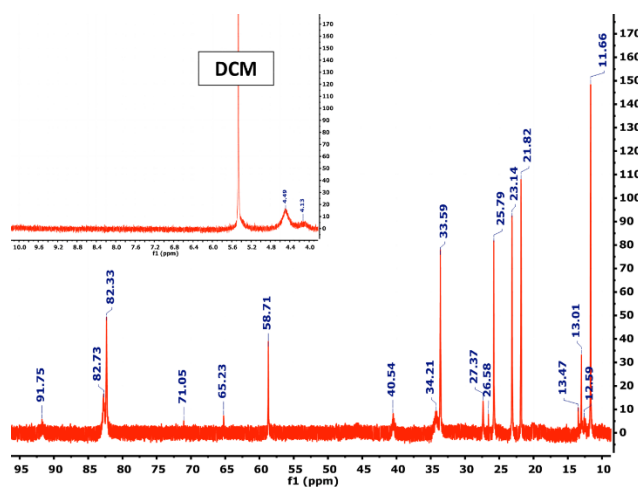


**Figure A5.25**  $^1\text{H}$  NMR of the Dimer Complex in acetonitrile- $d_3$ . Inset is meant to demonstrate that there are no chemical shifts in the aromatic region for the  $[\text{Co}(\text{PY}_5\text{Me}_2)(\text{CN})](\text{OTf})_2$  and/or free  $\text{PY}_5\text{Me}_2$  ligand.

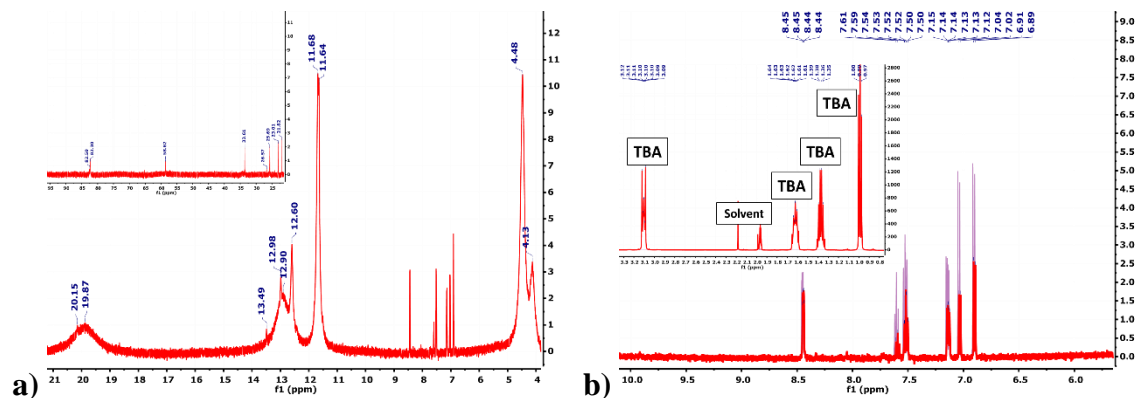


**Figure A5.26 a)**  $^1\text{H}$  NMR indicating the stability of  $[\text{Co}(\text{PY}_5\text{Me}_2)(\text{CN})](\text{OTf})$  with 0.1M  $\text{TBAPF}_6$  in acetonitrile- $d_3$  after several days and **b)** an enhancement of the aromatic region with the free  $\text{PY}_5\text{Me}_2$  ligand (purple line) overlaid on the  $[\text{Co}(\text{PY}_5\text{Me}_2)(\text{CN})](\text{OTf})$  (red line) spectrum. The inset of **a)** indicates the chemical shifts for the formation of the Dimer Complex. The inset of **b)** indicates the chemical shifts associated with the TBA.

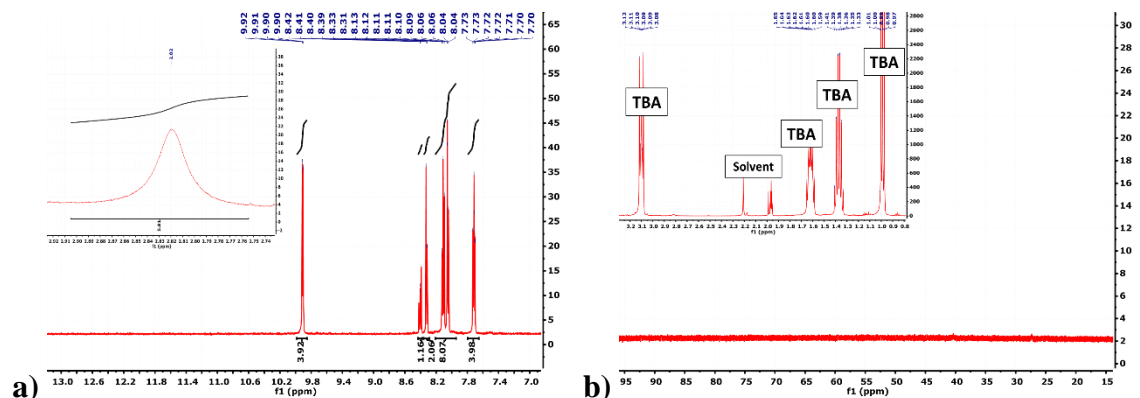


**Figure A5.27 a) & b)**  $^1\text{H}$  NMR indicating the stability of  $[\text{Co}(\text{PY}_5\text{Me}_2)(\text{CN})](\text{OTf})_2$  with 0.1M  $\text{TBAPF}_6$  in acetonitrile- $d_3$  after several days. The inset of **a)** indicates the chemical shift for the methyl groups of the  $\text{PY}_5\text{Me}_2$  ligand. The inset of **b)** indicates the chemical shifts associated with the TBA. Note-  $[\text{Co}(\text{PY}_5\text{Me}_2)(\text{CN})](\text{OTf})_2$  is sparingly soluble in acetonitrile with 0.1M  $\text{TBAPF}_6$  supporting electrolyte.

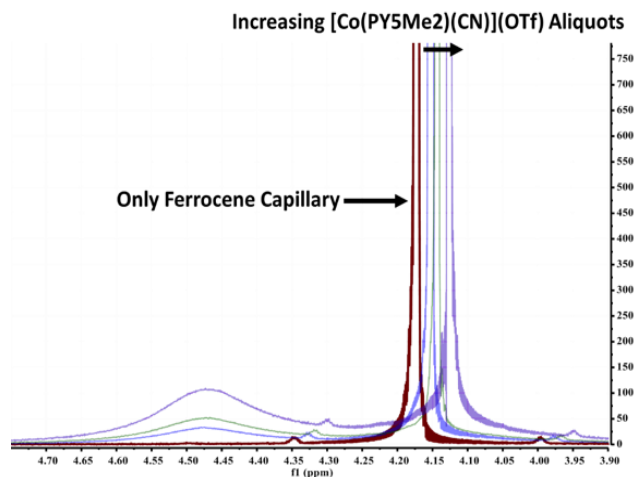


**Figure A5.28** Magnetic susceptibility measurements in acetonitrile- $d_3$  using the Evans Method and following the  $^1\text{H}$  chemical shift of Ferrocene,  $[\text{Fe}(\text{C}_5\text{H}_5)_2]$ , after additions of the paramagnetic  $[\text{Co}(\text{PY}_5\text{Me}_2)(\text{CN})](\text{OTf})$  complex.

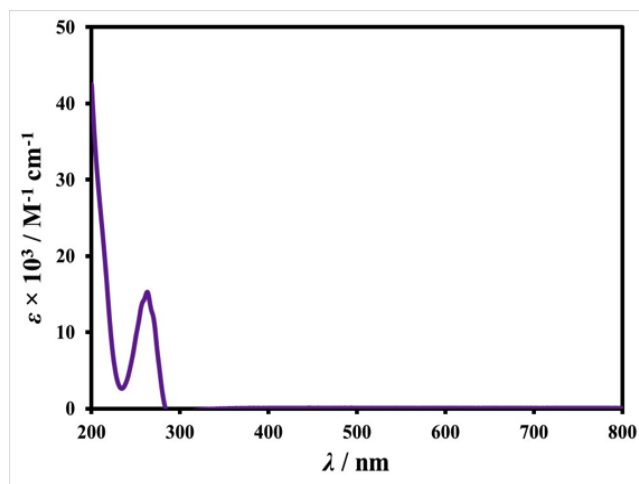


**Figure A5.29** UV-Vis spectrum of the  $\text{PY}_5\text{Me}_2$  ligand, where  $\text{PY}_5\text{Me}_2$  represents 2,6-bis(1,1-bis(2-pyridyl)ethyl)pyridine, in acetonitrile.

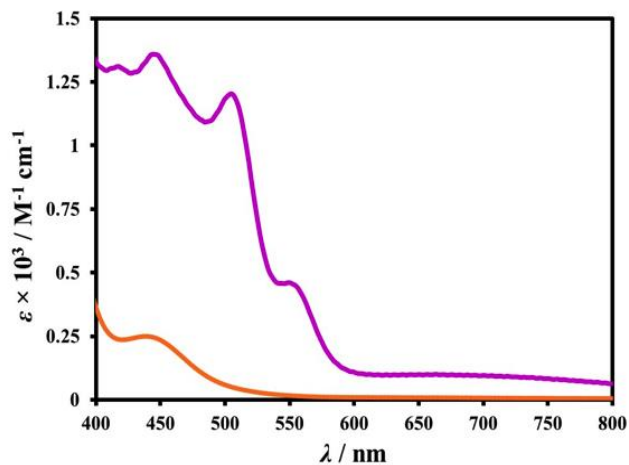


**Figure A5.30** UV-Vis spectra of the [Co(terpy)<sub>2</sub>](PF<sub>6</sub>)<sub>2</sub> (pink) and [Co(terpy)<sub>2</sub>](PF<sub>6</sub>)<sub>3</sub> (orange) complexes, where terpy represents 2,2':6',2''-terpyridine, in acetonitrile.

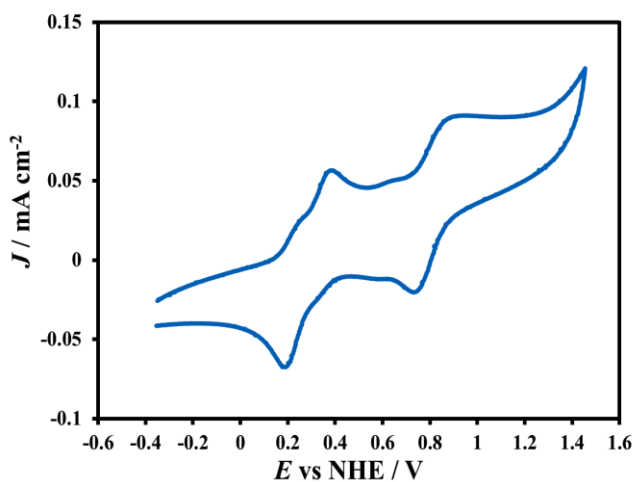


**Figure A5.31** Normalized CV of the Dimer Complex measured in acetonitrile with 0.1 M TBAPF<sub>6</sub> supporting electrolyte using a platinum disk working electrode, a platinum mesh counter electrode and a homemade Ag/AgNO<sub>3</sub> (0.1 M TBAPF<sub>6</sub> acetonitrile) reference electrode.

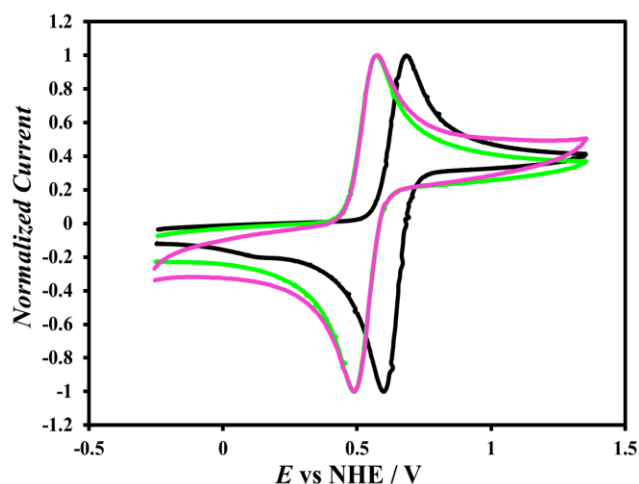


**Figure A5.32** Normalized CVs of  $[\text{Fe}(\text{C}_5\text{H}_5)_2]$  (black line),  $[\text{Fe}(\text{C}_5\text{H}_4\text{CH}_3)_2]$  (green line) and  $[\text{Co}(\text{terpy})_2](\text{PF}_6)_2$  (pink line) measured in acetonitrile with 0.1 M TBAPF<sub>6</sub> supporting electrolyte using a platinum disk working electrode, a platinum mesh counter electrode and a homemade Ag/AgNO<sub>3</sub> (0.1 M TBAPF<sub>6</sub> acetonitrile) reference electrode.

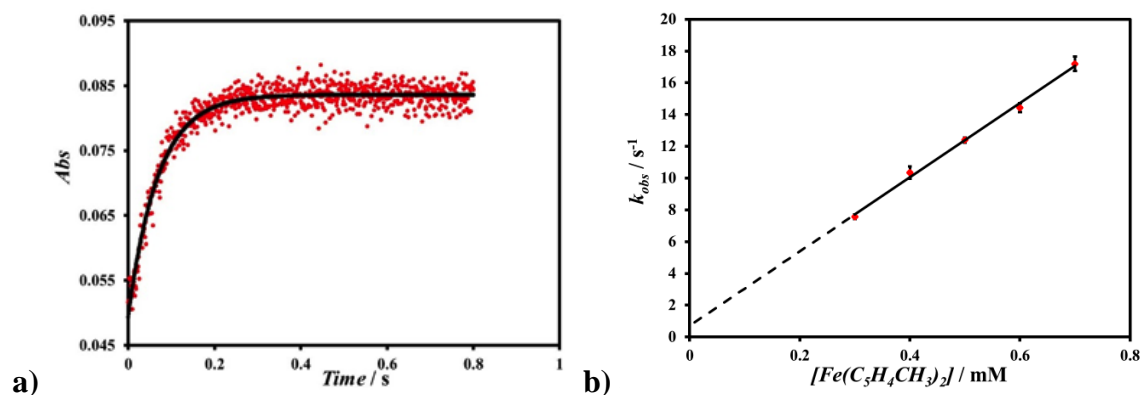


**Figure A5.33** **a)** Plot of absorbance at 505 nm vs. time, corresponding to the growth of the  $[\text{Co}(\text{terpy})_2]^{2+}$  species (red dot) and the resulting fit (black line) for the reduction of  $[\text{Co}(\text{terpy})_2]^{3+}$  ( $3.0 \times 10^{-5}$  M) by  $[\text{Fe}(\text{C}_5\text{H}_4\text{CH}_3)]$  ( $6.0 \times 10^{-4}$  M). **b)** Observed pseudo-first order rate constants,  $k_{\text{obs}}$ , versus the excess concentration of  $[\text{Fe}(\text{C}_5\text{H}_4\text{CH}_3)]$  for the reactions between  $[\text{Fe}(\text{C}_5\text{H}_4\text{CH}_3)]$  and  $[\text{Co}(\text{terpy})_2]^{3+}$ .



**Figure A5.34** NMR tubes displaying  $[\text{Co}(\text{PY}_5\text{Me}_2)(\text{CN})]$  degradation (precipitate) in neat acetonitrile- $d_3$  (right) and in acetonitrile- $d_3$  with 0.1 M TBAPF<sub>6</sub> supporting electrolyte (left).

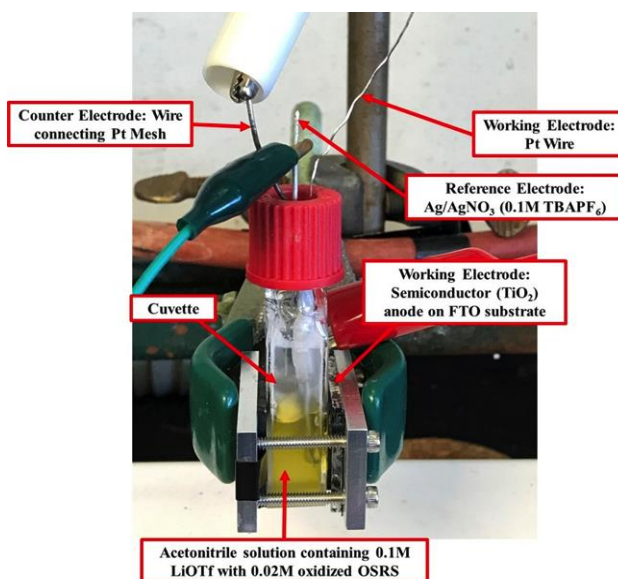


**Figure A5.35** Experimental three-electrode setup used to measure the recombination kinetics of  $[\text{Co}(\text{PY}_5\text{Me}_2)(\text{CN})](\text{OTf})_2$  and  $[\text{Co}(\text{bpy})_3](\text{PF}_6)_3$ . Depicted is a mesoporous  $\text{TiO}_2$  film sintered to an FTO substrate (working electrode) clamped to a cuvette cutout and exposed to 2mL of an acetonitrile containing 20mM of the oxidized redox shuttle and 0.1M LiOTf. A high surface area platinum (Pt) mesh was used as a counter electrode and a

homemade Ag/AgNO<sub>3</sub> (0.1M TBAPF<sub>6</sub>) was used as a reference electrode as well. CVs were taken with a Pt wire working electrode before and after the dark recombination studies in order to check that the redox potentials of [Co(PY<sub>5</sub>Me<sub>2</sub>)(CN)](OTf)<sub>2</sub> and [Co(bpy)<sub>3</sub>](PF<sub>6</sub>)<sub>3</sub> were stable and/or side products weren't forming.<sup>16</sup>

## **REFERENCES**

## REFERENCES

1. Mathew, S.; Yella, A.; Gao, P.; Humphry-Baker, R.; Curchod, B. F. E.; Ashari-Astani, N.; Tavernelli, I.; Rothlisberger, U.; Nazeeruddin, M. K.; Grätzel, M. Dye-Sensitized Solar Cells with 13% Efficiency Achieved through the Molecular Engineering of Porphyrin Sensitizers. *Nat. Chem.* **2014**, *6* (3), 242–247.
2. Baillargeon, J.; Xie, Y.; Hamann, T. W. Bifurcation of Regeneration and Recombination in Dye-Sensitized Solar Cells via Electronic Manipulation of Tandem Cobalt Redox Shuttles. *ACS Appl. Mater. Interfaces* **2017**, *9* (39), 33544–33548.
3. Xie, Y.; Baillargeon, J.; Hamann, T. W. Kinetics of Regeneration and Recombination Reactions in Dye-Sensitized Solar Cells Employing Cobalt Redox Shuttles. *J. Phys. Chem. C* **2015**, *119* (50), 28155–28166.
4. Hao, Y.; Yang, W.; Zhang, L.; Jiang, R.; Mijangos, E.; Saygili, Y.; Hammarstro, L.; Hagfeldt, A.; Boschloo, G. A Small Electron Donor in Cobalt Complex Electrolyte Significantly Improves Efficiency in Dye-Sensitized Solar Cells. *Nat. Commun.* **2016**, *7*, 1–8.
5. Yang, W.; Vlachopoulos, N.; Hao, Y.; Hagfeldt, A.; Boschloo, G. Efficient Dye Regeneration at Low Driving Force Achieved in Triphenylamine Dye LEG4 and TEMPO Redox Mediator Based Dye-Sensitized Solar Cells. *Phys. Chem. Chem. Phys.* **2015**, *17*, 15868–15875.
6. Hamann, T. W.; Ondersma, J. W. Dye-Sensitized Solar Cell Redox Shuttles. *Energy Environ. Sci.* **2011**, *4* (2), 370.
7. Chandrasekhar, S. .; McAuley, A. Syntheses, Structure, and Reactivity of Cobalt and Nickel Complexes of 1,4,7-Trithiacyclodecane: Self-Exchange Rates for Co(S6)2+/3+ Couples from 59Co NMR Spectroscopy. *Inorg. Chem.* **1992**, *31* (3), 480–487.
8. Kupperts, H. J.; Neves, A.; Pomp, C.; Ventur, D.; Wieghardt, K.; Nuber, B.; Weiss, J. Electron-Transfer Barriers in cobalt(III) and cobalt(II) Bis Complexes of 1,4,7-Triazacyclononane(tacn) and 1,4,7-Trithiacyclononane (Ttcn). Crystal Structures of [CoII(tacn)2]I2.2H2O and of [CoIII(ttcn)2](ClO4)3. *Inorg. Chem.* **1986**, *25* (14), 2400–2408.
9. Osvath, P.; Sargeson, A. M.; Skelton, B. W.; White, A. H. Cobalt (II) and cobalt(III) Complexes of a Novel Homoleptic Thioether Cage. *J. Chem. Soc. Chem. Commun.* **1991**, *23* (15), 1036–1038.
10. Zadrozny, J. M.; Freedman, D. E.; Jenkins, D. M.; Harris, T. D.; Iavarone, A. T.; Mathonière, C.; Clérac, R.; Long, J. R. Slow Magnetic Relaxation and Charge-Transfer in Cyano-Bridged Coordination Clusters Incorporating [Re(CN)7]3-/4-. *Inorg. Chem.* **2010**, *49* (19), 8886–8896.

11. Sun, Y.; Bigi, J. P.; Piro, N. A.; Tang, M. L.; Long, J. R.; Chang, C. J. Molecular Cobalt Pentapyridine Catalysts for Generating Hydrogen from Water. *J. Am. Chem. Soc.* **2011**, *133* (24), 9212–9215.
12. King, A. E.; Surendranath, Y.; Piro, N. A.; Bigi, J. P.; Long, J. R.; Chang, C. J. A Mechanistic Study of Proton Reduction Catalyzed by a Pentapyridine Cobalt Complex: Evidence for Involvement of an Anation-Based Pathway. *Chem. Sci.* **2013**, *4* (4), 1578–1587.
13. Kashif, M. K.; Axelson, J. C.; Duffy, N. W.; Forsyth, C. M.; Chang, C. J.; Long, J. R.; Spiccia, L.; Bach, U. A New Direction in Dye-Sensitized Solar Cells Redox Mediator Development: In Situ Fine-Tuning of the Cobalt(II)/(III) Redox Potential through Lewis Base Interactions. *J. Am. Chem. Soc.* **2012**, *134* (40), 16646–16653.
14. Goldsmith, C. R.; Jonas, R. T.; Cole, A. P.; Stack, T. D. P. A Spectrochemical Walk: Single-Site Perturbation within a Series of Six-Coordinate Ferrous Complexes. *Inorg. Chem.* **2002**, *41* (18), 4642–4652.
15. Connelly, N. G.; Geiger, W. E. Chemical Redox Agents for Organometallic Chemistry. *Chem. Rev.* **1996**, *96* (2), 877–910.
16. Ondersma, J. W.; Hamann, T. W. Measurements and Modeling of Recombination from Nanoparticle TiO<sub>2</sub> Electrodes. *J. Am. Chem. Soc.* **2011**, *133* (21), 8264–8271.
17. Bechlars, B.; D'Alessandro, D. M.; Jenkins, D. M.; Iavarone, A. T.; Glover, S. D.; Kubiak, C. P.; Long, J. R. High-Spin Ground States via Electron Delocalization in Mixed-Valence Imidazolate-Bridged Divanadium Complexes. *Nat. Chem.* **2010**, *2* (5), 362–368.
18. Sapp, S. A.; Elliott, C. M.; Contado, C.; Caramori, S.; Bignozzi, C. A. Substituted Polypyridine Complexes of Cobalt (II/III) as Efficient Electron-Transfer Mediators in Dye-Sensitized Solar Cells. *J. Am. Chem. Soc.* **2002**, *124* (37), 11215–11222.
19. Evans, D. F. 400. The Determination of the Paramagnetic Susceptibility of Substances in Solution by Nuclear Magnetic Resonance. *J. Chem. Soc.* **1959**, 2003–2005.
20. Schubert, E. M. Utilizing the Evans Method with a Superconducting NMR Spectrometer in the Undergraduate Laboratory. *J. Chem. Educ.* **1992**, *69* (1), 62.
21. Bain, G. A.; Berry, J. F. Diamagnetic Corrections and Pascal's Constants. *J. Chem. Educ.* **2008**, *85* (4), 532–536.
22. Jones, L. H. Nature of Bonding in Metal Cyanide Complexes as Related to Intensity and Frequency of Infrared Absorption Spectra. *Inorg. Chem.* **1963**, *2* (4), 777–780.
23. Klein Gebbink, R. J. M.; Jonas, R. T.; Goldsmith, C. R.; Stack, T. D. P. A Periodic Walk: A Series of First-Row Transition Metal Complexes with the Pentadentate Ligand PY5. *Inorg. Chem.* **2002**, *41* (18), 4633–4641.

24. Krivokapic, I.; Zerara, M.; Daku, M. L.; Vargas, A.; Enachescu, C.; Ambrus, C.; Tregenna-piggott, P.; Amstutz, N.; Krausz, E.; Hauser, A. Spin-Crossover in Cobalt (II) Imine Complexes. *Coord. Chem. Rev.* **2007**, *251* (3–4), 364–378.
25. Marcus, R. A.; Sutin, N. Electron Transfers in Chemistry and Biology. *Biochim. Biophys. Acta - Rev. Bioenerg.* **1985**, *811* (3), 265–322.
26. Sutin, N. Nuclear, Electronic, and Frequency Factors in Electron Transfer Reactions. *Acc. Chem. Res.* **1982**, *15* (9), 275–282.
27. Beattie, J. K.; Elsbernd, H. Electron Exchange Reaction of Bis (terpyridine)cobalt<sup>3+/2+</sup> Re-Examined by NMR. *Inorganica Chim. Acta* **1995**, *240* (1–2), 641–644.
28. Chow, H. S.; Constable, E. C.; Housecroft, C. E.; Kulicke, K. J.; Tao, Y. When Electron Exchange Is Chemical Exchange—assignment of <sup>1</sup>H NMR Spectra of Paramagnetic cobalt(II)-2,2':6',2"-Terpyridine Complexes. *Dalt. Trans.* **2005**, No. 2, 236–237.
29. Hamann, T. W.; Gstrein, F.; Brunschwig, B. S.; Lewis, N. S. Measurement of the Dependence of Interfacial Charge-Transfer Rate Constants on the Reorganization Energy of Redox Species at N-ZnO/H<sub>2</sub>O Interfaces. *J. Am. Chem. Soc.* **2005**, *127* (40), 13949–13954.
30. Freedman, D. E.; Jenkins, D. M.; Long, J. R. Strong Magnetic Exchange Coupling in the Cyano-Bridged Coordination Clusters [(PY5Me<sub>2</sub>)<sub>4</sub>V<sub>4</sub>M(CN)<sub>6</sub>]<sub>5</sub><sup>+</sup> (M = Cr, Mo). *Chem. Commun.* **2009**, *219* (32), 4829–4831.
31. Du, M.; Zhao, X.-J.; Cai, H. Crystal Structure of tris(2,2'-bipyridine)cobalt(III) Triperchlorate Dihydrate, [Co(C<sub>10</sub>H<sub>8</sub>N<sub>2</sub>)<sub>3</sub>](ClO<sub>4</sub>)<sub>3</sub>·2H<sub>2</sub>O. *Krist. New Cryst. Struct.* **2004**, *219*, 463–465.
32. Yao, J. C.; Ma, L. F.; Yao, F. J. Crystal Structure of Tris (2,2'-bipyridine)cobalt(II) Diperchlorate, [Co(C<sub>10</sub>H<sub>8</sub>N<sub>2</sub>)<sub>3</sub>](ClO<sub>4</sub>)<sub>2</sub>. *Krist. New Cryst. Struct.* **2005**, *220*, 483–484.

## Chapter 6. Considerations for the Future Directions of DSSCs

### 6.1 Integrating Near-IR Absorbing Sensitizers into Solid-State DSSC Devices for Potential Tandem Solar Cell Designs

Fast exchanging cobalt redox shuttles such as  $[\text{Co}(\text{ttn})_2]^{3+/2+}$  and  $[\text{Co}(\text{ptpy})_3]^{+/0}$  are difficult to integrate into conventional DSSC systems as they are plagued by fast recombination, see Chapters 3 & 4. Much of this can be attributed to the sensitizers these redox shuttles are being paired with. In an effort to enhance  $V_{oc}$  our group and others have invested time into seeking out redox shuttles with more positive redox potentials. By minimizing the driving force,  $-\Delta G^o$ , for the regeneration reaction between the OSRS and the dye, larger self-exchange rate constants, due to an increased activation energy, are necessary to ensure quantitative regeneration. However, as the driving force for the regeneration reaction becomes smaller a larger driving force is brought about for the recombination reaction. Coupling the larger driving force with the smaller reorganization energy of the fast exchanging redox shuttle, it becomes apparent as to why recombination is so fast, Equation (1.2).

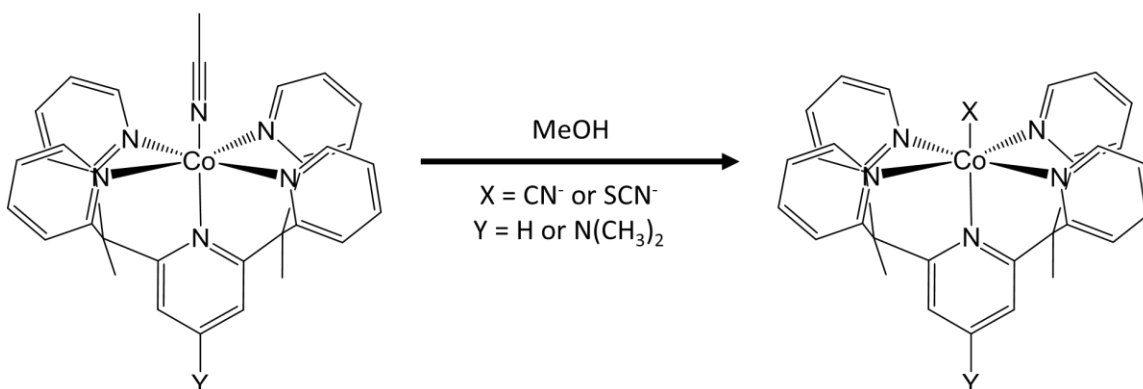
Our efforts to circumvent fast recombination to fast exchanging redox shuttles was addressed in Chapter 5. By cleverly designing a redox shuttle with a more negative redox potential than  $[\text{Co}(\text{ttn})_2]^{3+/2+}$ , we sought to minimize the driving force for the recombination reaction and slow back-electron transfer. Although we realize these systems will suffer losses in  $V_{oc}$ , dyes with smaller optical gaps will be able to be used, which can enhance the  $J_{sc}$  of these devices. The smaller driving force for the recombination to the oxidized dye, we hope, will also provide less demanding constraints on OSRSs to sustain large self-exchange rate constants in order to provide quantitative regeneration at minimal

driving forces. Efforts to synthesize the highly negative  $[\text{Co}(\text{PY}_5\text{Me}_2)(\text{CN})]^{2+/+}$  presented significant complications in stability due to the lability of the cyanide ligand in solution. The short-term stability of this complex, however, provides an interesting route to make solid-state DSSCs (ss-DSSCs) devices. Recent work by the groups of Bach *et. al.* and Hagfeldt *et. al.* has demonstrated that ss-DSSCs can be fabricated through the crystallization of OSRSs via slow evaporation of the liquid electrolyte.<sup>1-3</sup> The resulting semi-crystalline hole transport material (HTM) coupled with a variety of organic sensitizers has produced device efficiencies ranging from 5.7-11 %. Major advantages of these devices over traditional solution based DSSCs include their conductivity and long-term stability. Mass transport limitations at high carrier concentrations can be eliminated based on mitigating diffusion of the shuttle to and from the counter electrode, along with the issue of device shorting due to evaporation of the volatile solvent i.e. acetonitrile. Compared to other HTM such as spiro-MeOTAD, copper bipyridine HTMs demonstrated more than 10 times higher conductivity.<sup>3</sup> This would suggest that hole hopping, as a result of fast self-exchange kinetics, is quite rapid. Even dye regeneration appears to be nearly quantitative with only 0.2 eV of driving force. This is an exciting result as our motif for synthesizing fast exchanging cobalt redox shuttles has a distinct advantage over cobalt complexes with sluggish exchange kinetics such as  $[\text{Co}(\text{bpy})_3]^{3+/2+}$ . Indeed, poor performing ss-DSSCs have been constructed using  $[\text{Co}(\text{bpy})_3]^{3+/2+}$  compared to a hexadentate cobalt complex  $[\text{Co}(\text{bpyPY4})]^{3+/2+}$ , which was said to sustain faster exchange kinetics via investigation of spin-cross over.

Scheme 6.1 outlines several molecules that I believe would be interesting to study as future solid state HTM. Modification of the axial exogenous ligand and/or axial pyridine

for these complexes can provide a library of shuttles with varying potentials and spin-states that could be insightful for understanding regeneration and recombination. Aside from studying these kinetic pathways, we can also provide a quantitative assessment as to the conductivity of these cells based on the measured self-exchange rate constants using stopped-flow spectroscopy.

**Scheme 6.1** Synthetic route for creating new OSRSs using the pentacoordinated,  $\text{PY}_5\text{Me}_2$ , ligand



As previously mentioned in Chapter 5, a moderate self-exchange has already been measured for  $[\text{Co}(\text{PY}_5\text{Me}_2)(\text{CN})]^{2+/+}$ . Synthesis of  $[\text{Co}(\text{PY}_5\text{Me}_2)(\text{NCS})]^+$  has also previously been carried out and partially characterized, Figure 6.1.  $^1\text{H}$  NMR and CV studies, Figure 6.1b, using single crystals of  $[\text{Co}(\text{PY}_5\text{Me}_2)(\text{NCS})]^+$  reveal similar stability problems to  $[\text{Co}(\text{PY}_5\text{Me}_2)(\text{CN})]^+$  with and without the presence of a supporting electrolyte. However, short-term stability over the course of a day is verified via  $^1\text{H}$  NMR. The large chemical shifts observed in the preliminary  $^1\text{H}$  NMR studies seem to indicate the paramagnetic complex is HS Co(II), see Appendix A6.1, which could provide a good comparison to the LS  $[\text{Co}(\text{PY}_5\text{Me}_2)(\text{CN})]^+$  complex. Referring to Figures 5.8 and 6.1b,

there appears to be nearly 0.4 eV separating the two shuttles:  $[\text{Co}(\text{PY}_5\text{Me}_2)(\text{CN})]^{2+/+}$  and  $[\text{Co}(\text{PY}_5\text{Me}_2)(\text{NCS})]^{2+/+}$ . Use of the electron donating methylamine ( $\text{N}(\text{CH}_3)_2$ ) affords the opportunity to push both of the parent complexes to more negative potentials, which can provide a large range of driving forces for regeneration and recombination studies. Our group has already developed several osmium sensitizers that could be paired with each of these shuttles. Although the extinction coefficient of these sensitizers is large, competitive light absorption might be observed in the case of  $[\text{Co}(\text{PY}_5\text{Me}_2)(\text{CN})]^{2+/+}$  as a HTM, see Figure 5.7. Care will need to be taken to eliminate oxygen when developing a procedure to make these shuttles into HTM as they are susceptible to oxidation. However, if proper precautions are taken, these devices should provide exciting results for the design and development of next generation dye cells.

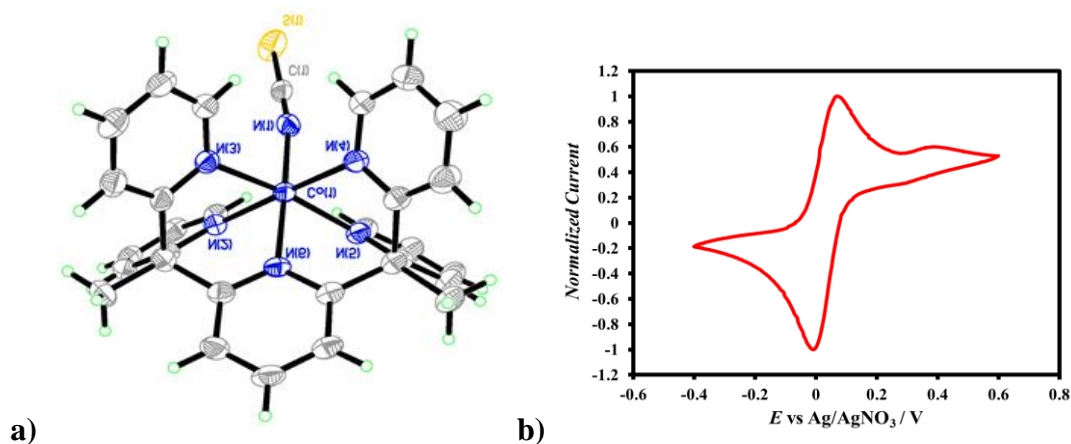


**Figure 6.1** a) Single crystal representation of  $[\text{Co}(\text{PY}_5\text{Me}_2)(\text{NCS})](\text{OTf})$  provided by Olex2 and structurally refined by ShelXT software. Note- the counterions and solvent molecules are omitted for image clarity. b) CV of  $[\text{Co}(\text{PY}_5\text{Me}_2)(\text{NCS})](\text{OTf})$  in acetonitrile with 0.1 M TBAPF<sub>6</sub> using a platinum working electrode, a platinum mesh counter electrode and a homemade (0.1 M TBAPF<sub>6</sub> in acetonitrile) Ag/AgNO<sub>3</sub> reference electrode.

## 6.2 Copper Redox Shuttles as Alternatives to Cobalt

Although  $[\text{Co}(\text{bpy})_3]^{3+/2+}$  has arisen as the champion redox shuttle, it still presents complications for dye cells reaching over 15% PCEs. The key problem with most cobalt bipyridyl redox shuttles, as alluded to throughout this dissertation, is the large reorganization energy these complexes need to overcome upon oxidation or reduction, which consequently require a large over potential for efficient regeneration.<sup>4,5</sup> Similar to cobalt polypyridyl OSRSs, copper complexes are also known to go through large structural changes upon electron exchange.<sup>6,7</sup> The four coordinate nature of copper lends itself to a unique conformational change going from a tetrahedral geometry to square planar upon oxidation. Such a conformational change can lead to large reorganization energies, however, by adding steric bulk to the ligand framework we can alter the degree to which these complexes change conformation. This is impactful for a two reasons. One, by forcing the redox shuttle to stay tetrahedral, the reorganization energy becomes minimized and the kinetics for electron-transfer become faster. And two, this synthetic modification helps to mitigate coordination of solvent molecules, electrolyte additives or counterions to the vacant axial sites of the four coordinate Cu(II).<sup>8,9</sup> At this point, as I will talk about below, it seems unclear if this coordination event is actually detrimental, preliminary studies suggest it might actually benefit the dye cell. The reason this might be good is that coordination and subsequent loss of these axial ligands can slow down the kinetics of charge-transfer. This can be advantageous in the outlook of recombination. The larger barrier to dissociate the extra ligand then transfer charge may in fact slow down recombination. On the other hand, this can also be detrimental in that changing the coordination sphere of the complex can lead to an unknown solution potential within the

dye cell ( $E_{f,0}$ ) and/or a possibly large overpotential for the reduction reaction at the counter electrode.

Recent work in our lab has provided some rather interesting results. Fundamental studies to try and understand the mechanism for charge-transfer using  $[\text{Cu}(\text{dmbpy})_2]^{2+/+}$  suggests that the Cu(II) complex is unstable when competitive, potentially coordinating additives, are introduced into the system. Similar to the phenomena observed by Hupp *et al.*, addition of the common electrolyte additive TBP to a solution of  $[\text{Cu}(\text{dmbpy})_2]^{2+}$  results in displacement of the dmbpy ligand and the formation of  $[\text{Cu}(\text{TBP})_x]^{2+}$ .<sup>10</sup> Crystal structures of this complex actually yields a six coordinate complex with the counterions bound to the axial sites of the copper,  $[\text{Cu}(\text{TBP})_4(\text{OTf})_2]$ . Interestingly, Cu(I) is inert to substitution, however, almost immediately after oxidation, displacement of dmbpy occurs resulting in what appears to be irreversible electrochemistry for the reduction of  $[\text{Cu}(\text{TBP})_x]^{2+}$  back to  $[\text{Cu}(\text{dmbpy})_2]^+$ . Bulk electrolysis coupled with spectrophotometry measurements conclude, however, that the process of dissociation and association of dmbpy after reduction to Cu(I) is in fact a reversible process. Scan rate dependence measurements of  $[\text{Cu}(\text{dmbpy})_2]^+$  in the absence of TBP reveal minimal peak separation over a 1 V window, which suggests the kinetics at the electrode surface are fast upon oxidation. With these results in mind, the fast electrode kinetics implies rapid and potentially quantitative regeneration is possible at low over potentials, as well as sluggish recombination kinetics to  $[\text{Cu}(\text{TBP})_x]^{2+}$  to form  $[\text{Cu}(\text{dmbpy})_2]^+$ . Indeed, quantitative regeneration has been observed at minimal overpotentials ( $< 0.2$  eV) with this redox shuttle paired with the organic sensitizer Y123 producing cell efficiencies over 10 %.<sup>11,12</sup>

An open and interesting question that remains in my mind to these systems is how the formation of  $[\text{Cu}(\text{TBP})_x]^{2+}$  affects the potential drop at the counter electrode. Not knowing the potential of the counter electrode leaves us in the dark in determining the maximum obtainable  $V_{oc}$ . Based on the reported redox potential for  $[\text{Cu}(\text{dmbpy})_2]^{2+/+}$  and measured potential of the  $\text{TiO}_2$  conduction band ( $E_{cb}$ ), one should expect a  $V_{oc}$  close to 2 V though the literature is only reporting 1 V. Maybe these cells are fully optimized as a result of the shift in solution potential upon the formation of  $[\text{Cu}(\text{TBP})_x]^{2+}$ . Obtaining this extra volt of open circuit potential would push dye cells to reach over 20% efficiencies. Another route to explore is to synthesize more robust ligands to withstand the displacement with TBP, along with creating enough steric hindrance to mitigate solvent coordination. This would create a true one-electron OSRS that can be fundamentally tested using the principals of Marcus theory. It would be interesting to see how these shuttles would fair at such positive potentials. Being in the inverted region, surface passivation might be pivotal to eliminating an onslaught of surface state recombination.<sup>13</sup> If recombination in these systems is a drastic issue, replacement of the liquid electrolyte for a HTM, as discussed above, could facilitate faster migration of the hole away from the surface via self-exchange rather than diffusion providing more efficient solar cells.

### **6.3 The Quest for New Semiconductor Materials**

The success of DSSCs has relied on a single material since Grätzel's seminal report in 1991. Much of this has to do with the fact that  $\text{TiO}_2$  is cheap and colloidal suspensions of these particles used as pastes are easy to fabricate. The wideband gap of anatase  $\text{TiO}_2$  is also advantageous for allowing only the sensitizer to absorb visible light. A major drawback to using this material is the intrinsic properties it sustains as a result of utilizing

a polycrystalline material. It is well known that a large distribution of intraband gap states are comprised within the nanoparticle  $\text{TiO}_2$  film.<sup>14,15</sup> These mid gap states along the surface of the nanoparticle i.e. surface states present a large problem within DSSCs as they tend to facilitate recombination. Recent studies from our lab has demonstrated that the high concentrations of these midgap states rapidly facilitate recombination under circumstances where electron-transfer should otherwise be slow if only restricted to charge-transfer from conduction band states. The realization as to the degree of surface state recombination has provided evidence for poor performing cells that utilize highly positive redox shuttles with low reorganization energies i.e. the recipe for observing Marcus inverted behavior.<sup>13</sup> As a result, there remains a pressing need to investigate new materials to alleviate the issues surrounding recombination.

In looking at alternative materials to  $\text{TiO}_2$ , the energetics and distribution of conduction bands states is critical to high performing dye cells. As a result, our group has spent the past several years developing novel spectroelectrochemical measurements to identify the band edge placement, as well as methods to study the trap state distribution of  $\text{TiO}_2$  in an effort to apply this methodology to new materials.<sup>16-18</sup> A major stipulation for carrying out such spectroelectrochemical experiments is the use of a highly transparent film. Development of colloidal pastes of new materials isn't a trivial task; however, it is an issue worth investigating for the implementation of new materials. Aside from spectroelectrochemical experiments requiring a transparent film, high efficiency cells require this as well in order to eliminate excess scattering of light from the film. Our group has been interested in investigating ternary oxides such as  $\text{SrTiO}_3$  and  $\text{SrSnO}_3$  as potential alternative materials to  $\text{TiO}_2$ . The band edge placement of  $\text{SrTiO}_3$  is said to be more

negative than TiO<sub>2</sub>, which can hinder injection. However, a major issue with that was identified was conductivity. Doping was demonstrated to enhance electron transport and thus the performance, however, many more studies are necessary to identify, in full, the limitations of this material and others similar to it.

#### **6.4 Mechanistic Insight as to the Pathway for Dye Recombination**

Throughout this dissertation only the dynamics of recombination to the oxidized redox shuttle have been considered for improving dye cell performance; however, dye recombination is also a very important pathway to understand. Depending on the mechanism for electron-transfer at the electrode surface i.e. surface state or conduction band recombination, the self-exchange rate constant and reorganization energy can have a significant influence on the kinetics of regeneration aside from the influence of the redox shuttles. Over the past few decades, several groups have looked at studying dye recombination through the use of transient spectroscopy. This approach, however, has a few major pitfalls and constraints. One such constraint is that extremely high laser intensities, some nearly 1000 times stronger than 1 Sun or standard solar cell illumination conditions, are necessary to acquire adequate signal-to-noise. With such high intensity laser light, it is common that dyes become degraded or ablated from the surface, which calls into question the validity of the collected data. Secondly, and most importantly, this approach only really yields experimental trends to the measured data rather than providing any meaningful mechanistic information.<sup>19-24</sup> Such trends have provided a qualitative picture of dye behavior relative to laser light intensity, electrolyte additives, applied potential, etc..., but limited quantitative information regarding recombination rate constants or the relative contribution of surface state or conduction band recombination falls out of these

measurements.<sup>21,22</sup> Time constants have been extracted via stretched exponential and/or multiexponential fits to the collected transient data, but, again, little explanation results from identifying the reasons as to why the stretch parameter was varied or why multiple time constants were generated.<sup>23,25</sup> Based on the experimental design, it is difficult to see how only dye recombination is being measured, which could answer why variable stretch parameters are used and why multiple time constants can be generated. If we rationalize the phenomena that occur while carrying out a transient measurement, aside from dye recombination, electrons are also able to diffuse through the TiO<sub>2</sub> film upon injection, while holes can hop on the electrode surface via self-exchanging dyes before finding an electron to recombine with.<sup>25,26</sup> Unfortunately, transient measurements do not take the latter two phenomena into consideration, which has indicated to us that a new approach must be developed to identify only the characteristics of dye recombination.

To eliminate the phenomena of hole hopping at the surface and the electron diffusion throughout the TiO<sub>2</sub> we are attempting to measure dye recombination kinetics under steady-state conditions. Our approach is an adopted technique developed by Hagfeldt and Boschloo known as photoinduced absorption spectroscopy (PIA).<sup>27,28</sup> PIA is a powerful technique in that the measurement can be carried out under conditions analogous to an operating dye cell and the experimental setup is relatively straightforward to design, see Figure 6.2.

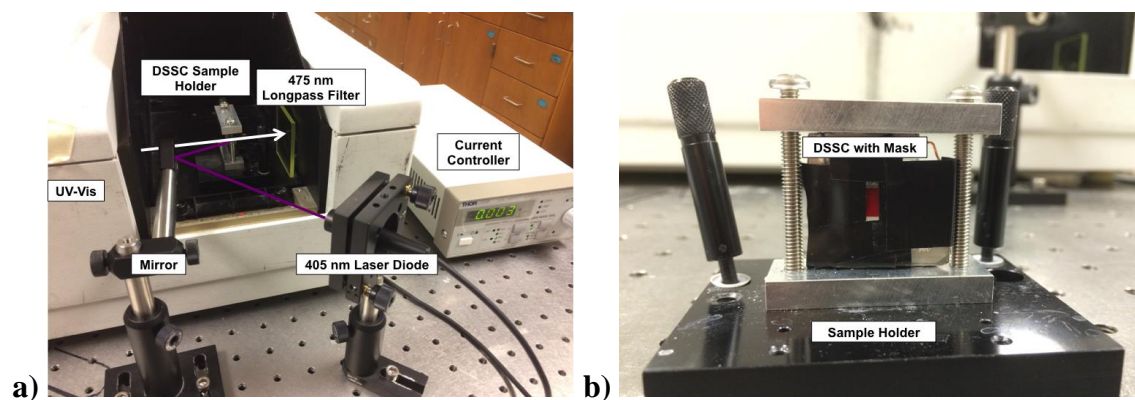


**Figure 6.1** a) A detailed image of the PIA setup. b) Sample holder for full DSSC PIA studies. Note- the laser and mirror are enclosed in a housing to eliminate any extraneous light.

The basic measurement is quite similar to the principals of transient laser spectroscopy, where a pump is used to photexcite the sample and a probe is used to measure the resulting photoaction spectra. However, unlike a transient measurement, which requires the pump and probe to simultaneously strike the sample one after another, our goal is to impart conditions where the pump constantly illuminates/excites the sample (i.e. steady-state conditions), while the probe measures the photoaction spectra of the dye. The low light photoexcitation can be imparted using a simple laser diode (405 nm) and the difference spectra can be measured using a UV-Vis spectrometer. An example of a collected data set can be seen in Figure 6.3a.

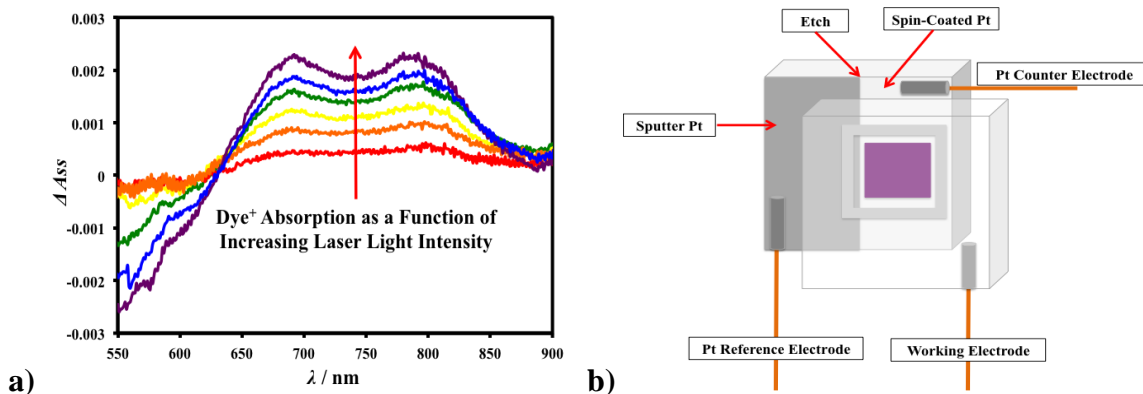


**Figure 6.2 a)** PIA of a complete DSSC containing a TiO<sub>2</sub> filmed sensitized with the D35cpdt interfaced with an inert acetonitrile electrolyte containing 0.1 M LiTFSI. **b)** Proposed three electrode setup for measuring PIA with fully constructed dye cells.

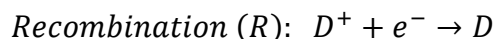
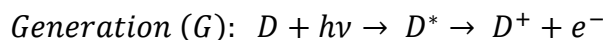
By quantifying the oxidized dye concentration as a function of either laser light intensity or potential modulation, we expect to gain insight as to the relative rates of recombination, see Scheme A6.1 of the Appendix. We hope to couple our knowledge of charge distribution and interfacial charge-transfer to provide a model that explains the observed experimental data.<sup>29</sup> Initial attempts at carrying out steady-state PIA measurements resulted in difficulties collecting reproducible data. It has been observed that dyes such as N3, N719 or Z907, when exposed to coordinating solvents such as acetonitrile, tend to be labile and lose their -NCS ligand.<sup>30</sup> More chemically robust dyes, which replace the -NCS substituents with heteroleptic bidentate ligands, provide much more stable measurements though the absorption of the oxidized sensitizer isn't always as significant and identifiable as the spectra displayed above in Figure 6.3a. Use of the organic sensitizer D35cpdt provides great stability and reproducible measurements, which makes the sensitizer very attractive for steady-state PIA studies. By introducing the sensitizer into the designed three-electrode cell shown above, Figure 6.3b, we hope to be able to control the potential of the TiO<sub>2</sub> film relative to the incident laser light intensity. The goal is to be able

to make direct comparisons of oxidized dye concentration as a function of applied potential and correlate directly to the model which identifies the relative contributions of surface-state and conduction band recombination relative to driving force and the reorganization energy of the sensitizer used.

## **APPENDIX**

## APPENDIX

**Scheme A6.1** Mathematical theory of steady-state PIA measurements.<sup>27</sup>



$$G = \phi_{inj} \frac{d[D^*]}{dt} = \phi_{inj} \frac{I_0}{N_A} (1 - \exp^{-\Gamma_D \varepsilon_D})$$

$\phi_{inj}$ : Injection Efficiency

$I_0$ : Laser Intensity (Power Density / Energy of Laser light) (Photons s<sup>-1</sup> cm<sup>-2</sup>)

$N_A$ : Avagadro's Number

$\Gamma_D$ : Dye Surface Coverage (mol cm<sup>-2</sup>)

$\varepsilon_D$ : Dye Extinction Coefficient (M<sup>-1</sup> cm<sup>-1</sup>)

$$R = -\frac{d[D^+]}{dt} = k_{rec}[D^+][n_s]$$

$k_{rec}$ : Recombination Rate Constant (M<sup>-1</sup> s<sup>-1</sup> or cm<sup>4</sup> s<sup>-1</sup>)

$[D^+]$ : Oxidized Dye Concentration (M<sup>-1</sup> or mol cm<sup>-3</sup>)

$[n_s]$ : Semiconductor Electron Concentration (M<sup>-1</sup> or mol cm<sup>-3</sup>)

Under Steady-State Conditions:

$$G = R$$

Condition 1: Electron concentration is not equal to the oxidized dye concentration:

$$[D^+] = [n_s] \frac{1}{k_{rec}} \phi_{inj} \frac{I_0}{N_A} (1 - \exp^{-\Gamma_D \varepsilon_D})$$

Condition 2: Electron concentration is equal to the oxidized dye concentration:

$$[D^+] = \sqrt{\frac{1}{k_{rec}} \phi_{inj} \frac{I_0}{N_A} (1 - \exp^{-\Gamma_D \varepsilon_D})}$$

Linking PIA Measurements to Theory:

$$\Delta A_{ss} = A_{pump\ on} - A_{pump\ off}$$

$$\Delta A_{ss} = (A_{D^+} + A_{e^-} + A_{D,off}) - (A_{D,on})$$

$$\Delta A_{ss} = (A_{D^+} + A_{e^-} + A_{D,off}) - (A_{D,on})$$

$$\Delta A_{ss} = (\varepsilon_{D^+}l[D^+] + \varepsilon_{e^-}l[n_s] + \varepsilon_Dl[D]_{off}) - (\varepsilon_Dl[D]_{on})$$

$$*\text{Note- } [D]_{off} = [D]_{on} - [D^+]$$

$$\Delta A_{ss} = [\varepsilon_{D^+}l[D^+] + \varepsilon_{e^-}l[n_s] + \varepsilon_Dl([D]_{on} - [D^+])] - (\varepsilon_Dl[D]_{on})$$

$$[D^+] = \frac{\Delta A_{ss} - \varepsilon_{e^-}l[n_s]}{\varepsilon_{D^+}l - \varepsilon_Dl}$$

\*Note- In the case of PIA studies  $[n_s]$  is the free electron concentration and  $\varepsilon_{e^-}$  is the extinction coefficient of the free electron in the conduction band.

\*An adjustment is made from the literature, which only assumes a single recombination rate constant,  $k_{rec}$ . For a complete kinetic picture, we have incorporated the contributions from surface state, ss, recombination as well as conduction band, cb, recombination:

$$R = k_{et,cb}[D^+][n_{cb}] + [D^+] \int_{E_{f,0}}^{E_{cb}} f(E - E_f)[g_{ss,exp}(E) + g_{ss,me}(E)]k_{et,ss}(E)dE$$

Under Steady-State Conditions we model:

$$[D^+](E_f) = \frac{\phi_{inj} \frac{I_0}{N_A} (1 - \exp^{-\Gamma_D \varepsilon_D})}{k_{et,cb}[n_{cb}] + \int_{E_{f,0}}^{E_{cb}} f(E - E_f)[g_{ss,exp}(E) + g_{ss,me}(E)]k_{et,ss}(E)dE}$$

\*Note- this derivation is assuming a constant light intensity and a changing potential. Under these circumstances we are imparting condition 1 above.

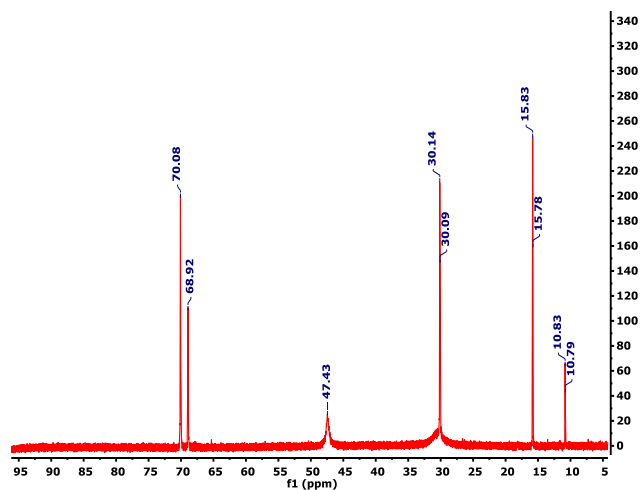


**Figure A6.1** <sup>1</sup>H NMR of [Co(PY<sub>5</sub>Me<sub>2</sub>)(NCS)](OTf) in acetonitrile-*d*<sub>3</sub>.

## REFERENCES

## REFERENCES

1. Freitag, M.; Daniel, Q.; Pazoki, M.; Sveinbjörnsson, K.; Zhang, J.; Sun, L.; Hagfeldt, A.; Boschloo, G. High-Efficiency Dye-Sensitized Solar Cells with Molecular Copper Phenanthroline as Solid Hole Conductor. *Energy Environ. Sci.* **2015**, *8* (9), 2634–2637.
2. Kashif, M. K.; Milhuisen, R. A.; Nippe, M.; Hellerstedt, J.; Zee, D. Z.; Duffy, N. W.; Halstead, B.; De Angelis, F.; Fantacci, S.; Fuhrer, M. S.; et al. Cobalt Polypyridyl Complexes as Transparent Solution-Processable Solid-State Charge Transport Materials. *Adv. Energy Mater.* **2016**, *6* (24), 1–7.
3. Cao, Y.; Saygili, Y.; Ummadisingu, A.; Teuscher, J.; Luo, J.; Pellet, N.; Giordano, F.; Zakeeruddin, S. M.; Moser, J.-E.; Freitag, M.; et al. 11% Efficiency Solid-State Dye-Sensitized Solar Cells with copper(II/I) Hole Transport Materials. *Nat. Commun.* **2017**, *8*, 15390.
4. Xie, Y.; Baillargeon, J.; Hamann, T. W. Kinetics of Regeneration and Recombination Reactions in Dye-Sensitized Solar Cells Employing Cobalt Redox Shuttles. *J. Phys. Chem. C* **2015**, *119* (50), 28155–28166.
5. Baillargeon, J.; Xie, Y.; Hamann, T. W. Bifurcation of Regeneration and Recombination in Dye-Sensitized Solar Cells via Electronic Manipulation of Tandem Cobalt Redox Shuttles. *ACS Appl. Mater. Interfaces* **2017**, *9* (39), 33544–33548.
6. Davies, K. M.; Byers, B. Kinetic Study of Electron-Transfer Reactions of Sterically Constrained Bis(diimine) Complexes of Copper(II) and Copper(I) with Ruthenium Ammine Complexes. *Inorg. Chem.* **1987**, *26* (22), 3823–3825.
7. Hattori, S.; Wada, Y.; Yanagida, S.; Fukuzumi, S. Blue Copper Model Complexes with Distorted Tetragonal Geometry Acting as Effective Electron-Transfer Mediators in Dye-Sensitized Solar Cells. *J. Am. Chem. Soc.* **2005**, *127* (26), 9648–9654.
8. Dunn, B. C.; Ochrymowycz, L. A.; Rorabacher, D. B. Electron-Transfer Kinetics of the Copper(II/I) Complex with 1,4,8,11-Tetrathiacyclotetradecane in Acetonitrile. *Inorg. Chem.* **1995**, *34* (7), 1954–1956.
9. Chaka, G.; Kandegedara, A.; Heeg, M. J.; Rorabacher, D. B. Comparative Study of Donor Atom Effects on the Thermodynamic and Electron-Transfer Kinetic Properties of copper(II/I) Complexes with Sexadentate Macrocyclic Ligands. [CuII/I([18]aneS4N2)] and [CuII/I([18]aneS4O2)]. *Dalt. Trans.* **2007**, *6* (4), 449–458.
10. Hoffeditz, W. L.; Katz, M. J.; Deria, P.; Cutsail, G. E.; Pellin, M. J.; Farha, O. K.; Hupp, J. T. One Electron Changes Everything. A Multispecies Copper Redox Shuttle for Dye-Sensitized Solar Cells. *J. Phys. Chem. C* **2016**, *120* (7), 3731–3740.

11. Saygili, Y.; Söderberg, M.; Pellet, N.; Giordano, F.; Cao, Y.; Munoz-García, A. B.; Zakeeruddin, S. M.; Vlachopoulos, N.; Pavone, M.; Boschloo, G.; et al. Copper Bipyridyl Redox Mediators for Dye-Sensitized Solar Cells with High Photovoltage. *J. Am. Chem. Soc.* **2016**, *138* (45), 15087–15096.
12. Freitag, M.; Teuscher, J.; Saygili, Y.; Zhang, X.; Giordano, F.; Liska, P.; Hua, J.; Zakeeruddin, S. M.; Moser, J. E.; Grätzel, M.; et al. Dye-Sensitized Solar Cells for Efficient Power Generation under Ambient Lighting. *Nat. Photonics* **2017**, *11* (6), 372–378.
13. Ondersma, J. W.; Hamann, T. W. Measurements and Modeling of Recombination from Nanoparticle TiO<sub>2</sub> Electrodes. *J. Am. Chem. Soc.* **2011**, *133* (21), 8264–8271.
14. Abayev, I.; Zaban, A.; Kytin, V. G.; Danilin, A. A.; Garcia-Belmonte, G.; Bisquert, J. Properties of the Electronic Density of States in TiO<sub>2</sub> Nanoparticles Surrounded with Aqueous Electrolyte. *J. Solid State Electrochem.* **2007**, *11* (5), 647–653.
15. Zaban, A.; Greenshtein, M.; Bisquert, J. Determination of the Electron Lifetime in Nanocrystalline Dye Solar Cells by Open-Circuit Voltage Decay Measurements. *Chemphyschem* **2003**, *4* (8), 859–864.
16. Mandal, D.; Hamann, T. W. Band Energies of Nanoparticle Semiconductor Electrodes Determined by Spectroelectrochemical Measurements of Free Electrons. *Phys. Chem. Chem. Phys.* **2015**, *17* (17), 11156–11160.
17. Ondersma, J. W.; Hamann, T. W. Conduction Band Energy Determination by Variable Temperature Spectroelectrochemistry. *Energy Environ. Sci.* **2012**, *5* (11), 9476.
18. Mandal, D.; Hamann, T. W. Charge Distribution in Nanostructured TiO<sub>2</sub> Photoanode Determined by Quantitative Analysis of the Band Edge Unpinning. *ACS Appl. Mater. Interfaces* **2016**, *8* (1), 419–424.
19. Clifford, J. N.; Palomares, E.; Nazeeruddin, M. K.; Grätzel, M.; Durrant, J. R. Dye Dependent Regeneration Dynamics in Dye Sensitized Nanocrystalline Solar Cells: Evidence for the Formation of a Ruthenium Bipyridyl Cation / Iodide Intermediate. *J. Phys. Chem. C* **2007**, *111* (17), 6561–6567.
20. Nelson, J.; Haque, S. A.; Klug, D. R.; Durrant, J. R. Trap-Limited Recombination in Dye-Sensitized Nanocrystalline Metal Oxide Electrodes. *Phys. Rev. B* **2001**, *63* (20), 205321.
21. Haque, S. A.; Tachibana, Y.; Willis, R. L.; Moser, J. E.; Grätzel, M.; Klug, D. R.; Durrant, J. R. Parameters Influencing Charge Recombination Kinetics in Dye-Sensitized Nanocrystalline Titanium Dioxide Films. *J. Phys. Chem. B* **2000**, *104* (3), 538–547.

22. Haque, S. A.; Tachibana, Y.; Klug, D. R.; Durrant, J. R. Charge Recombination Kinetics in Dye-Sensitized Nanocrystalline Titanium Dioxide Films under Externally Applied Bias. *J. Phys. Chem. B* **1998**, *102* (10), 1745–1749.
23. Kuciauskas, D.; Freund, M. S.; Gray, H. B.; Winkler, J. R.; Lewis, N. S. Electron Transfer Dynamics in Nanocrystalline Titanium Dioxide Solar Cells Sensitized with Ruthenium or Osmium Polypyridyl Complexes. *J. Phys. Chem. B* **2001**, *105* (2), 392–403.
24. Clifford, J. N.; Palomares, E.; Nazeeruddin, M. K.; Grätzel, M.; Nelson, J.; Li, X.; Long, N. J.; Durrant, J. R. Molecular Control of Recombination Dynamics in Dye-Sensitized Nanocrystalline TiO<sub>2</sub> Films: Free Energy vs Distance Dependence. *J. Am. Chem. Soc.* **2004**, *126* (16), 5225–5233.
25. Brigham, E. C.; Meyer, G. J. Ostwald Isolation to Determine the Reaction Order for TiO<sub>2</sub>(e<sup>-</sup>)|S<sup>+</sup> ↔ TiO<sub>2</sub>|S Charge Recombination at Sensitized TiO<sub>2</sub> Interfaces. *J. Phys. Chem. C* **2014**, *118* (15), 7886–7893.
26. Dimarco, B. N.; Motley, T. C.; Balok, R. S.; Li, G.; Siegler, M. A.; O'donnell, R. M.; Hu, K.; Meyer, G. J. A Distance Dependence to Lateral Self-Exchange across Nanocrystalline TiO<sub>2</sub>. A Comparative Study of Three Homologous Ru III/II Polypyridyl Compounds. *J Phys Chem C* **2016**, *120*, 14226–14235.
27. Boschloo, G.; Hagfeldt, A. Photoinduced Absorption Spectroscopy as a Tool in the Study of Dye-Sensitized Solar Cells. *Inorganica Chim. Acta* **2008**, *361* (3), 729–734.
28. Boschloo, G.; Hagfeldt, A. Photoinduced Absorption Spectroscopy of Dye-Sensitized Nanostructured TiO<sub>2</sub>. *Chem. Phys. Lett.* **2003**, *370* (3–4), 381–386.
29. Ondersma, J. W.; Hamann, T. W. Measurements and Modeling of Recombination from Nanoparticle TiO<sub>2</sub> Electrodes. *J. Am. Chem. Soc.* **2011**, *133* (21), 8264–8271.
30. Cecchet, F.; Gioacchini, A. M.; Marcaccio, M.; Paolucci, F.; Roffia, S.; Alebbi, M.; Bignozzi, C. A. Solvent Effects on the Oxidative Electrochemical Behavior of Cis-Bis(isothiocyanato)ruthenium(II)-Bis-2,2'-Bipyridine-4,4'-Dicarboxylic Acid. *J. Phys. Chem. B* **2002**, *106* (15), 3926–3932.